A GENERALIZED FINITE ELEMENT METHOD FOR THREE-DIMENSIONAL FRACTURES IN FIBER-REINFORCED COMPOSITES

BY

PHILLIPE DANIEL ALVES

DISSERTATION

Submitted in partial fulfillment of the requirements
for the degree of Doctor of Philosophy in Civil Engineering
in the Graduate College of the
University of Illinois at Urbana-Champaign, 2020

Urbana, Illinois

Doctoral Committee:

Professor Carlos Armando Duarte, Chair and Director of Research
Professor Philippe H. Geubelle
Professor Oscar Lopez-Pamies
Professor Angelo Simone, University of Padova

Abstract

Fiber reinforcements are used in a broad variety of materials in engineering. They increase the strength, stiffness, ductility, and resistance to fatigue of the unreinforced material. Computational simulations can reduce the cost of designing these materials, and improve the understanding of their failure mechanisms. However, modeling of damage evolution and the multiscale interactions in composite materials using standard Finite Element Methods (FEMs) face significant barriers in terms of model generation and problem size. This work presents recent advances of the Generalized Finite Element Method (GFEM) for three-dimensional modeling and simulation of crack propagation in fiber-reinforced composites. Fibers are discretely modeled using a modified formulation of the Embedded Reinforcement with bond Slip (mERS) that allows its combination with the GFEM where fractures are represented using enrichment functions instead of meshes fitting the crack surface. Matrix cracks are described using discontinuous and singular functions as in the GFEM for homogeneous materials. This procedure can address some of the limitations of existing FEMs by describing both cracks and fibers independently of the underlying FEM mesh. Examples illustrating the capabilities and robustness of the method are presented. Crack propagation simulations are compared to physical tests showing that the method can successfully reproduce the failure behavior of fiber-reinforced composites. The results show that several failure mechanisms of the composite can be reproduced by the model, including matrix crack propagation, fiber debonding, and failure. In addition a multiscale approach is proposed using the GFEM^{gl}, a framework that allows intercommunication between macro and micro scales of the material.

Acknowledgments

I would like to thank Prof. C. Armando Duarte for his help during my studies. His guidance, support, patience and motivation helped me develop my skills during my doctorate.

I also would like to thank my thesis committee (listed in alphabetical order of last name): Prof. Philippe H. Geubelle, Prof. Oscar Lopez-Pamies, and Prof. Angelo Simone, for their insightful comments and questions which made me see my research from various perspectives.

I want to acknowledge my colleagues and labmates who offered me much help and encouragement. Additionally, I am grateful to all current and previous group members for their contributions to the research in this group.

I would like to thank the Department of Civil & Environmental Engineering at the University of Illinois at Urbana-Champaign, the National Science Foundation (NSF), and the Conselho Nacional de Desenvolvimento Cientifico e Tecnologico (CNPq) for providing the resources.

Finally, of course, I am thankful to my friends and family for all the support.

Table of Contents

Chapter 1

Introduction

1.1 Background and motivation

Revolutionary design of future power generation systems, rockets, hypersonic missiles, and flight vehicles are contingent on the development of advanced composite materials. The design of composite structures [1] has long relied on physical testing to establish their effectiveness, while their modeling and computational simulations have been hindered by the available tools. In fact, the current methods imply high costs and protracted design process. Computational simulations can potentially reduce these costs and improve the understanding of failure mechanisms of this class of materials.

Many advanced materials like Ceramic Matrix Composites (CMCs) rely on crack bridging mechanisms to hold cracks together and resist their growth. As observed by Kruzic and co-workers [2, 3], cracks in CMCs are initially very small (at the micrometer scale) and can behave in a way that is vastly different from that of the millimeter-scale cracks studied in the laboratory. This difference is, in fact, a notable problem in predicting fatigue failures in modern advanced materials. In crack bridging problems, a small crack situated between reinforcing fibers or layers needs only to overcome the cracking resistance of the matrix in order to propagate. However, once the crack has propagated into the reinforcing phase, the crack is held and propagation resistance is increased. As many modern composites show similar behavior, the development of a reliable computational tool to characterize the interaction between an arbitrarily-oriented fiber and a three-dimensional crack has become necessary.

The main objective of this work is to develop a three-dimensional Generalized Finite Element Method (GFEM) [4–7] able to simulate fractures in fiber-reinforced materials, including crack bridging mechanisms. The proposed research offers an alternative for the difficult and costly fracture experiments needed to determine the fracture behavior of complex fiber-reinforced materials.

1.2 Relevance

Since the 1960s the use of composite materials has grown with an average of 15% per year, [8]. It has led the development of many different kinds of composites in order to supply every new demand. Hence, it becomes increasingly more important to be able to model these materials accurately, inexpensively, and quickly using computer models. In particular, for composites materials with fibers, it can be observed that the overall behavior of the composite is highly dependent on the fiber configuration. Specimens such as the one shown in Fig. 1.1 can present several fiber arrangements. To accurately describe the mechanical behavior of the composite it is necessary the appropriate description of the physics of the fibers, matrix, and their interfaces.

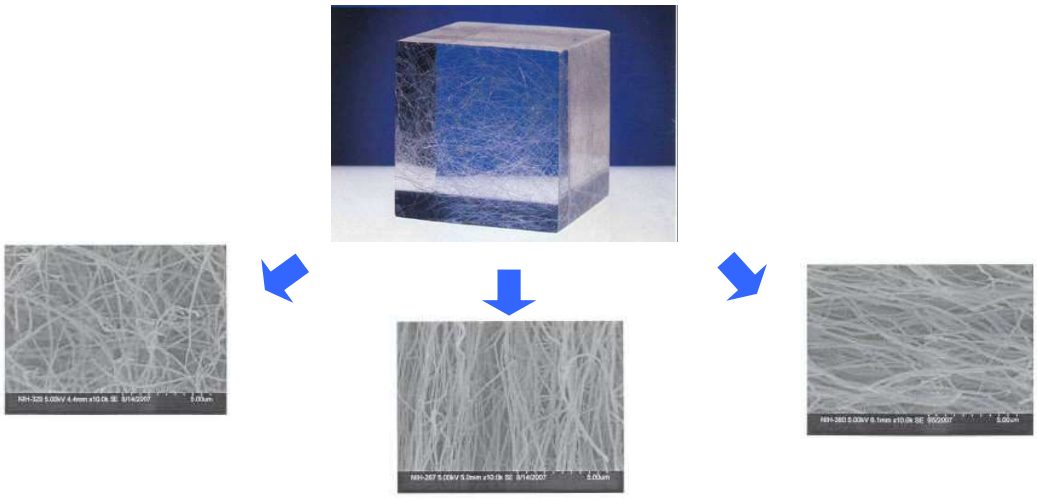

Figure 1.1: Several fiber configuration for a reinforced composite, adapted from [9]

The demand for high-temperature thermostructural materials continues to grow, fueled principally by power generation systems for aircraft engines, turbines, rockets, and most recently, hypersonic missiles and flight vehicles. Typical components include combustors, nozzles, and thermal insulation. With their high melting point, strength, low-density, and toughness, composites offer great potential for enabling elevations in the operating temperatures of these systems, [10]. Figure 1.2 shows the turbine inlet temperature in a jet engine and the corresponding nozzle component made of composite material (CMC).

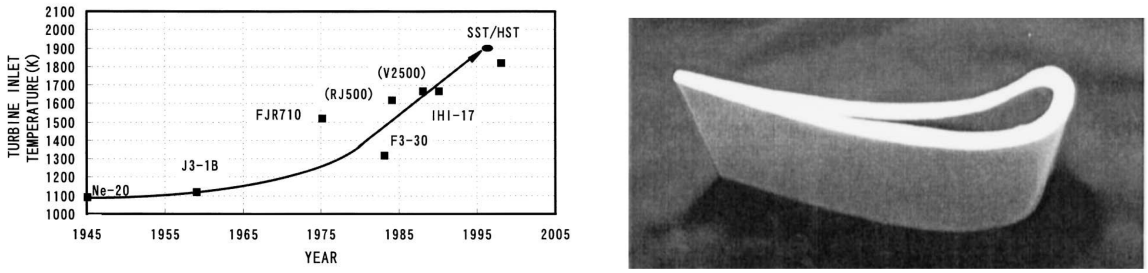

(a) (b)

Figure 1.2: (a)Trends of turbine inlet temperature in a jet engine. (b) Turbine nozzle component made of CMC [11]

Available methods are not able to efficiently model this class of material. The proposed computational methodology will enable validated simulations and improve the understanding of complex fiber configurations and behaviors. Complex physical models (such as the one shown in Fig. 1.3) have been arising in recent years and a reliable and powerful tool is necessary to help scientists and engineers to find solutions of important problems related to composite materials.

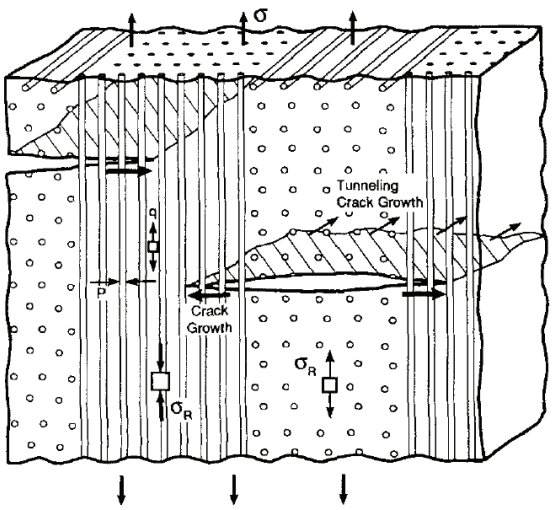

Figure 1.3: Modeling physical behavior (source: [12])

1.3 Critical issues and potential applications

1.3.1 Failure mechanisms in fiber-reinforced composites

Failure models in heterogeneous materials must take into account how they fail at the microscopic level. Advanced CMCs, for example, tend to break in a way that is intermediate between ductile and brittle materials. They can resist failure by cracking better than brittle materials, but like ductile metals, they are susceptible to fatigue failures over time. Because fatigue failures in these materials occur very differently than in ductile metals, traditional methods for fatigue predictions are not appropriate [13]. Many advanced materials rely on crack bridging mechanisms to hold cracks together and resist crack growth. Cracks in composite components are initially very small (micrometer scale) and can behave in a way that is vastly different from that of the millimeter-scale cracks studied in laboratory tests using standardized techniques developed for traditional metal alloys [2, 3]. This difference is a notable problem in predicting fatigue failures in modern materials.

In crack bridging, a small crack situated between reinforcing fibers or layers needs only to overcome the cracking resistance of the matrix in order to propagate. However, once the crack has propagated around the reinforcing phase, fibers can hold the crack together and increase crack propagation resistance. This rising fracture or fatigue resistance with crack extension, called a rising R-curve, is seen across a broad range of advanced materials. However, since the bridging only develops with crack extension, there is an inherent effect of crack size on the material toughness [14] and, as well, on the cyclic fatigue-crack growth resistance [15] for cracks shorter than the steady-state bridging-zone lengths. Such crack-size effects on fracture toughness are expressed in the form of a R-curve, which allows for failure predictions based on the loading conditions and initial flaw size [14]. This enhanced cracking resistance of materials with rising R-curves, should be utilized by designers when predicting whether fatigue cracks will arrest during cyclic loading or grow and lead to fracture. Otherwise, the design will be either far from optimal or non-conservative.

1.3.2 Limitations of experimental predictions: a potential application

The majority of fatigue-crack growth tests performed to date on many materials have used millimeter-scale (so called "large") cracks growing in standard fracture mechanics specimens [14]. These experiments are typically believed to represent the behavior of cracks with steady-state bridging zones. Crack-size effects on the fatigue threshold are thus ignored in such experiments, and the measured fatigue thresholds are non-conservative when compared to those from smaller cracks with developing, or transient, bridging zones [14]. Since relevant crack sizes (in CMCs, for example) for structural use will likely be several orders of magnitude smaller than those in such test specimens, effects of crack size must be addressed if the fatigue threshold is to be used as a design parameter.

Some of the most promising applications of CMCs, for example, are as replacement of traditional metal alloys in structural components subjected to high temperatures and very high cycling frequencies. These components will fail quickly if the fatigue threshold of the material is exceeded, providing limited useful service life. Because of this, the fatigue threshold, ΔK_{TH}, below which cracks are presumed not to propagate under cyclic loads, is often considered as a critical parameter in the fatigue of high-toughness ceramics. A major challenge in the application of CMCs in design is the crack-size dependence of the fatigue threshold R-curves during the bridging zone development. The precise definition of the fatigue threshold R-curves is a central issue for the adoption of CMCs by the industry.

Direct measurements of fatigue crack propagation resistance curves are usually costly and time consuming because of the difficulty and length of fatigue experiments [14]. In this research, a method is proposed to help modeling these materials. The proposed multiscale computational framework will also enable the study of the effect of matrix, fiber, and matrix-fiber interface properties. This will open many opportunities for optimization of the material performance of a large number of composites.

1.3.3 Numerical simulation

Although advanced materials such as CMCs can be used safely based on empirical experience and over-design strategies, optimizing their performance requires more sophisticated approaches to accurately predict their strength and fatigue life. The response prediction of advanced materials, like fiber-reinforced composites, requires addressing phenomena spanning multiple spatial and temporal scales. The behavior and performance of these materials is driven by the complex interactions and evolution of defects at microscales as illustrated in Fig. 3(a). These small-scale damages interact with the global response of the structure and may gradually evolve into a macro defect or damage mode. Many years of successful experiences at designing metallic components and structures cannot be directly transferred to composite structures. The current design of composite structures relies on tests of elements and sub-components to establish the effects of local details on structural behavior leading to high costs and time-consuming design processes [16].

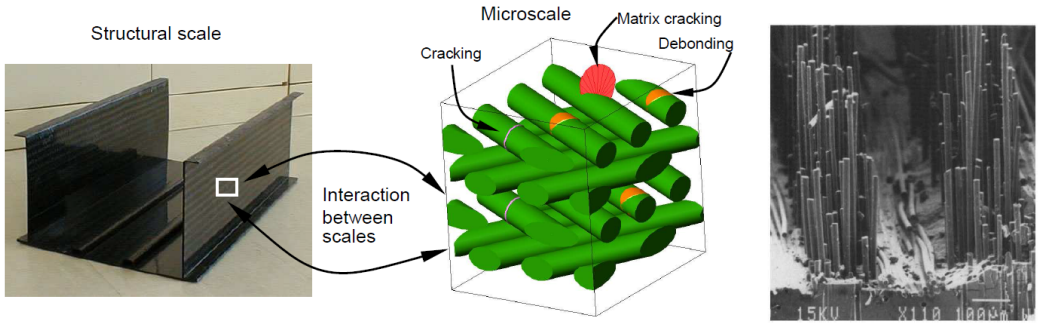

Figure 1.4: (a) Damage characterization in composite materials involves complex multiscale interactions. (b) Three dimensional fracture surface of a Continuous Fiber Ceramic Composite (CFCC) showing extensive fiber pullout [12]

The mathematical homogenization theory [17], has been used extensively since the 1970s as a tool for analyzing the multiscale response of materials. It uses asymptotic expansions of displacement, strain, and stress fields about macroscopic values. This method is based on the assumptions of the spatial periodicity of microscopic representative volume elements (RVEs) and local uniformity of macroscopic fields within each RVE [18]. These assumptions make physical sense when the goal of the analysis is to predict the on-set of damage. However, they become much less realistic as the various damage mechanisms progress.

1.4 Objectives

The objective of this research is the development of a finite element approach to accurate simulate fiber-reinforced composites. The approach must admit the inclusion of a large number of fibers and be mesh independent. The basic idea is shown in Fig. 1.5. The proposed model allows the superimposition of fibers on a matrix material mesh. In other words, fibers and background mesh do not need to coincide.

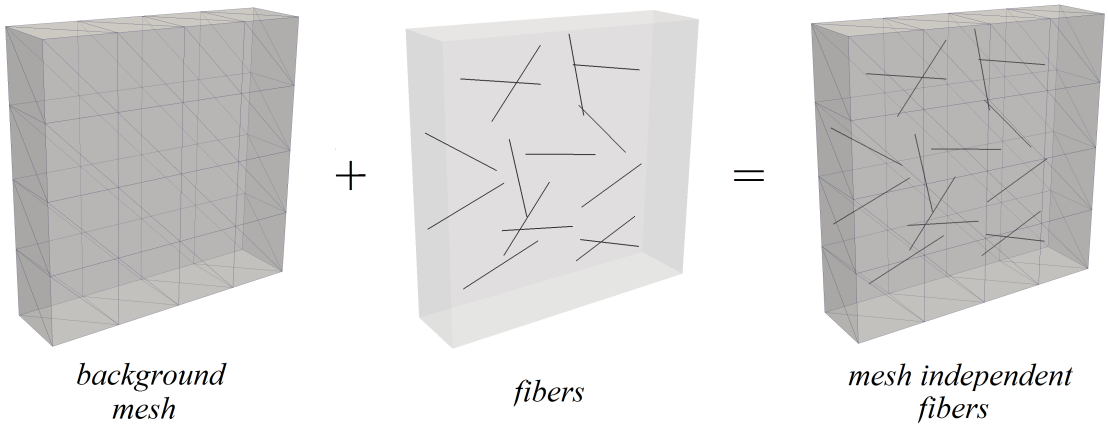

Figure 1.5: Modeling discrete fibers in a continuous matrix material, (figure adapted from [19])

The idea of modeling each individual fiber comes from the assumption that this is the most direct way of representing the influence of the fiber orientation and its mechanical properties in a continuum. The discrete modeling of individual fibers provides several advantages, including the ability to simulate the effects of fiber dispersion on pre and post cracking composite performance, as described by [20]. The ability of mesh independence is particularly important when solving a realistic problem in engineering. Realistic simulations of evolving crack surfaces require hundreds of small propagation steps and several different initial crack configurations. Thus, even the best available 3D mesh generator will eventually run into difficulties during a simulation and require user intervention. In addition, mapping of nonlinear or time-dependent solutions between meshes that are not nested invariably leads to loss of accuracy.

1.5 Literature review

There are many techniques to simulate cracks in fiber-reinforced composites. One effective approach is to smear the effects of the fibers using a traction-separation law as shown in, e.g., References [21–27]. Another common method uses a cohesive approach to model the effects of the reinforcement layer bridging the crack ([28] and references therein). This approach was recently combined with the GFEM in References [29–31]. Under the group of fully discrete models for fiber-reinforced composites, approaches based on the classical Finite Element Method (FEM) are the most straightforward. They are characterized by conformal discretizations of matrix and fiber regions, with nodes and edges of matrix elements connected to corresponding nodes and edges of fiber elements [32–35], and bond-slip mechanisms that can be introduced by means of matrix-fiber interface elements.

While these approaches can be very accurate as they can potentially produce a digital replica of the composite, their relatively high computational burden is a major drawback. Nonetheless, conformal FEM approaches offer the possibility of generating reference numerical solutions when analytical solutions are not available. A classical FEM approach is therefore adopted as a reliable method to obtain reference solution, as can be observed in the several numerical examples in this dissertation. This classical solution has, however, prohibitive cost or is unable to perform for some classes of problems.

The necessity of describing pre- and post-cracking behavior of fiber-reinforced materials has led to the development of several numerical techniques [20, 36–40], referred to as discrete fiber models, that can represent each individual fiber within the composite volume in an explicit manner and at a significantly lower computational burden compared to classical FEM approaches. Discrete fiber models provide the possibility of directly modeling the local behavior of the fibers, including their rupture, and the effects of non uniformity of fiber distribution within the material volume. These capabilities can be important when simulating failure of fiber-reinforced composites as shown in, e.g., References [20, 41–44].

Lattice models [40, 41, 44, 45] are probably the most impressive in terms of fiber densities that can be handled with a limited computational burden at the cost however of reduced control in terms of material properties (the Poisson's ratio of the material depends on the local arrangement of the lattice although recent developments [46] have addressed this shortcoming). Another limitation, albeit restricted to the context of

this work, is its incompatibility with classical FEM approximations for solids.

The discrete fiber approach closest to a classical FEM approach is the Embedded Reinforcement method with bond Slip (ERS) [36, 37, 47]. This method facilitates the discretization of high aspect ratio fibers by allowing their mesh-independent representation through the superposition of reinforcement bar or beam elements and matrix elements in a non-conformal manner. Zienkiewicz et al. [48] were the first to propose an approach to describe embedded reinforcements. In this approach, here referred to as Embedded Reinforcement Method (ERM), the reinforcement is represented by bar elements perfectly bonded to the matrix material. The capability of modeling slip and bonding between reinforcement and matrix was introduced by Balakrishnan and Murray [36]. For convenience, any approach that enables the modeling of embedded reinforcemnts with slip is hereafter referred to as ERS. In the ERS proposed by Elwi and Hrudey [37] the method was extended to model a generally curved reinforcing layer in a two-dimensional setting, while its three-dimensional extension is due to Hartl [47].

In these formulations, embedded reinforcements are added by means of extra contributions to the principle of virtual work and via relatively simple modifications to the classical FEM approximation. However, the ERS can only be used, in a consistent way, with low-order finite element approximations as shown in Sec. 3.3.1.

A methodology related to the one presented here is the Conforming Generalized Strong Discontinuity Approach (CGSDA) with Embedded Reinforcement [49]. In this method, discontinuities are discretized using the CGSDA [50]. As in the GFEM, the finite element mesh need not fit the crack surface, but the crack tip must end at an element boundary. Hence, the geometry of the crack front is mesh dependent in the case of three-dimensional fracture problems. This is also the case in the GFEM if only the Heaviside enrichment are adopted. The method of Octávio et al. [49] has only been formulated for linear elements and applied to 2D problems.

1.6 Outline

This dissertation is composed by seven chapters and outlined as follows:

- *Chapter 1:* Introduces fiber-reinforced composite materials and its relevance, describes objectives and gives a literature overview.
- *Chapter 2:* Presents the mathematical derivation of the problem with focus on the development of the mathematical background that governs the mechanical behavior of fiber-reinforced composite materials.
- *Chapter 3:* Introduces the GFEM-mERS and presents in details its formulation developed for fiber-reinforced materials.
- *Chapter 4:* Presents 3D numerical experiments of fiber-reinforced materials using the GFEM-mERS formulation developed in Chapter 3.
- *Chapter 5:* Introduces the theory for nonlinear debonding and crack propagation parameters. Performs numerical experiments combining advanced physics in fiber-reinforced composite materials.
- *Chapter 6:* Presents formulation and numerical experiments of multiscale problems using GFEM.
- *Chapter 7:* Conclusions and suggestions for future work are presented.

This document is also is composed by three appendices:

- *Appendix A:* Presents the Object Oriented Project for the GFEM-mERS.
- *Appendix B:* Presents a validation of a 3D adaptive GFEM for mixed-mode brittle fracture propagation.
- *Appendix C:* Presents parametric studies using numerical experiments for fracture mechanics in fiber-reinforced materials.

Chapter 2

A Fiber-Matrix Model

2.1 Introduction

This chapter [1] presents the mathematical model adopted for a continuum with one embedded fiber. The goal is develop a formulation able to simulate fiber-reinforced materials under the assumption of linear elastic materials.

2.2 Mathematical formulation

The assumptions adopted here follow those in Reference [52]. For simplicity, a single fiber is considered. Extension of the model to an arbitrary number of fibers is straightforward as shown by Radtke et al. [52].

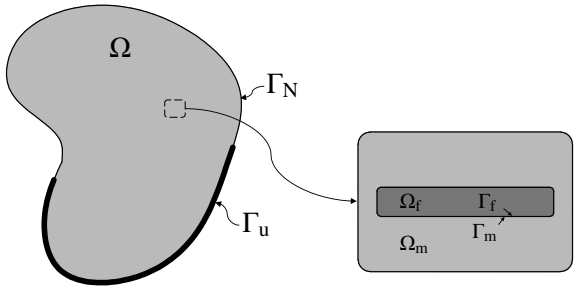

Figure 2.1: Continuum with one fiber

Consider a domain $\Omega \subset \mathbb{R}^3$ with an embedded fiber as shown in Fig. 2.1. Let Ω_f and Ω_m denote the domains occupied by the fiber and matrix, respectively, with $\Omega = \Omega_f \cup \Omega_m$. The matrix-fiber interface is denoted by Γ. For simplicity, we assume that the fiber is fully embedded in Ω. Thus, $\Gamma \cap \partial\Omega = \emptyset$, where $\partial\Omega$

[1] This chapter has been adapted from "P. Alves, A. Simone, C. A. Duarte, A generalized finite element method for three-dimensional fractures in fiber reinforced composites, Meccanica (2020), [51]"

is the boundary of Ω. The external surface of the fiber is denoted by Γ_f while the external surface of the matrix facing the fiber is denoted by Γ_m. The boundary $\partial\Omega$ is decomposed as $\partial\Omega = \Gamma_u \cup \Gamma_N$ with $\Gamma_u \cap \Gamma_N = \emptyset$. Dirichlet and Neumann boundary conditions are prescribed on Γ_u and Γ_N, respectively.

The equilibrium equations are given by

$$\nabla \cdot \boldsymbol{\sigma} = \mathbf{0} \qquad \text{in } \Omega \tag{2.1}$$

with boundary conditions

$$\boldsymbol{\sigma} \cdot \boldsymbol{n} = \bar{\boldsymbol{t}} \ \text{ on } \Gamma_N \qquad \text{and} \qquad \boldsymbol{u} = \bar{\boldsymbol{u}} \ \text{ on } \Gamma_u \tag{2.2}$$

prescribed on $\partial\Omega$, where $\boldsymbol{n}$ is the outward unit normal vector to $\partial\Omega$, $\bar{\boldsymbol{t}}$ are prescribed tractions, and $\bar{\boldsymbol{u}}$ are prescribed displacements.

The tractions at the fiber-matrix interface are denoted by

$$\boldsymbol{\sigma} \cdot \boldsymbol{n}_f = \boldsymbol{t}_f \ \text{ on } \Gamma_f \qquad \text{and} \qquad \boldsymbol{\sigma} \cdot \boldsymbol{n}_m = \boldsymbol{t}_m \ \text{ on } \Gamma_m, \tag{2.3}$$

where $\boldsymbol{n}_f$ and $\boldsymbol{n}_m$ are outward unit normal vectors to Γ_f and Γ_m, respectively, and $\boldsymbol{\sigma} \cdot \boldsymbol{n}_f = -\boldsymbol{\sigma} \cdot \boldsymbol{n}_m = \boldsymbol{t}_f$ by equilibrium.

The matrix and the fiber are assumed to behave as a linear elastic material, i.e.,

$$\boldsymbol{\sigma}_m = \boldsymbol{D}_m : \boldsymbol{\epsilon} \quad \text{and} \tag{2.4}$$

$$\boldsymbol{\sigma}_f = \boldsymbol{D}_f : \boldsymbol{\epsilon}, \tag{2.5}$$

where $\boldsymbol{D}_m$ and $\boldsymbol{D}_f$ denote the fourth order Hooke's tensor for matrix and fiber, respectively.

2.2.1 Kinematic Assumptions

The displacement field $\boldsymbol{u}$ over the entire body Ω is decomposed as

$$\boldsymbol{u} = \hat{\boldsymbol{u}} + \tilde{\boldsymbol{u}}, \tag{2.6}$$

where $\hat{\boldsymbol{u}}$ is a continuous function across the matrix-fiber interface Γ, but possibly discontinuous elsewhere in Ω (since there may be cracks in Ω), and $\tilde{\boldsymbol{u}}$ is continuous over the fiber subdomain Ω_f, discontinuous across the fiber-matrix interface Γ, and identically zero over the matrix subdomain Ω_m. The field $\tilde{\boldsymbol{u}} = \boldsymbol{u} - \hat{\boldsymbol{u}}$ is the relative displacement between fiber and matrix. Function $\tilde{\boldsymbol{u}}$ is also known as fiber slip [36, 37], and $\hat{\boldsymbol{u}}$, the non-slip component, is known as duct displacement [47] or concrete displacement [36] (this quantity is expressed in terms of the matrix displacement field of the element crossed by the fiber as shown in Sec. 3.3.1). Figure 2.2 illustrates these functions. Function $\hat{\boldsymbol{u}}|_{\Omega_\mathrm{m}}$ represents the matrix displacement over Ω_m, i.e.,

$$\boldsymbol{u}|_{\Omega_\mathrm{m}} = \hat{\boldsymbol{u}}|_{\Omega_\mathrm{m}} \tag{2.7}$$

while $\hat{\boldsymbol{u}}|_{\Omega_\mathrm{f}}$ is the matrix displacement over the fiber domain Ω_f.

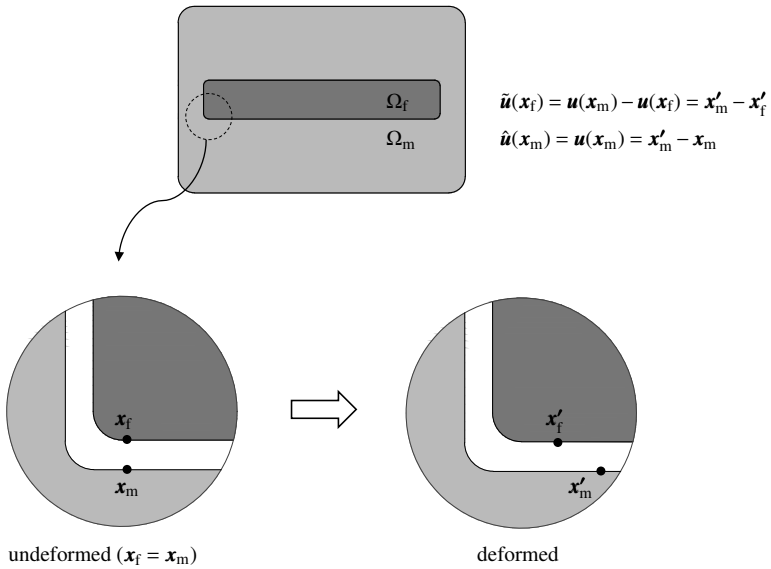

Figure 2.2: Zoom-in at a fiber-matrix interface at the undeformed (left) and deformed (right) configurations

In the spirit of ERS, the fiber displacement is decomposed in two components:

$$\boldsymbol{u}|_{\Omega_\mathrm{f}} = \hat{\boldsymbol{u}}|_{\Omega_\mathrm{f}} + \tilde{\boldsymbol{u}}|_{\Omega_\mathrm{f}}. \tag{2.8}$$

Based on the above decomposition, the displacement jump across the fiber-matrix interface is given by

$$[\![\boldsymbol{u}]\!]|_\Gamma = \boldsymbol{u}|_{\Gamma_\mathrm{f}} - \boldsymbol{u}|_{\Gamma_\mathrm{m}} = (\hat{\boldsymbol{u}} + \tilde{\boldsymbol{u}})|_{\Gamma_\mathrm{f}} - (\hat{\boldsymbol{u}} + \tilde{\boldsymbol{u}})|_{\Gamma_\mathrm{m}} = \tilde{\boldsymbol{u}}|_{\Gamma_\mathrm{f}} = [\![\tilde{\boldsymbol{u}}]\!]|_\Gamma \tag{2.9}$$

since $\hat{\boldsymbol{u}}$ is a continuous function over interface Γ and $\tilde{\boldsymbol{u}}$ is identically zero over the matrix subdomain Ω_m.

Based on decomposition (2.6), the small strain tensor is also decomposed as

$$\boldsymbol{\epsilon} = \nabla^s \boldsymbol{u} = \nabla^s \hat{\boldsymbol{u}} + \nabla^s \tilde{\boldsymbol{u}}. \tag{2.10}$$

where ∇^s is the symmetric part of the gradient operator.

The tractions $\boldsymbol{t}_\mathrm{f}$ at the fiber-matrix interface (Fig. 2.3) are related to the displacement jump (2.9) through the linear relation

$$\boldsymbol{t}_\mathrm{f} = \boldsymbol{D}_\mathrm{b}[\![\boldsymbol{u}]\!]|_\Gamma = \boldsymbol{D}_\mathrm{b}[\![\tilde{\boldsymbol{u}}]\!]|_\Gamma = \boldsymbol{D}_\mathrm{b}\tilde{\boldsymbol{u}}|_\Gamma, \tag{2.11}$$

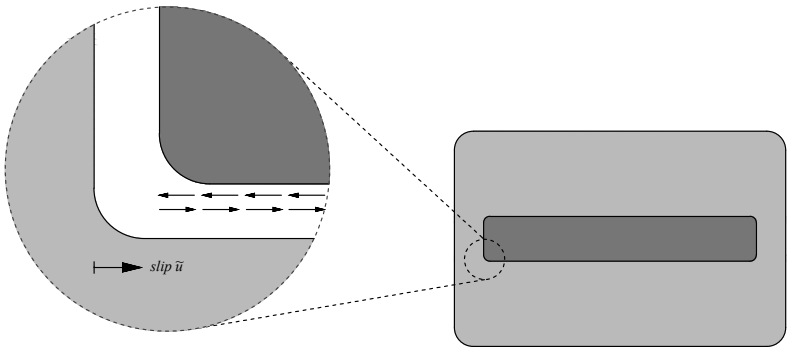

Figure 2.3: Tractions along the fiber boundary

where $\boldsymbol{D}_\mathrm{b}$ is a second order tensor for the bond between matrix and fiber. The last equality in the above equation is a consequence of $\tilde{\boldsymbol{u}}$ being identically zero over the matrix subdomain Ω_m as stated earlier. It is noted that a nonlinear traction separation law for the fiber-matrix interface is needed to model debonding at the fiber-matrix interface and it will be presented later in Chapter 5.

2.2.2 Principle of Virtual Work

The weak formulation of the problem described in the previous section is given by: Find $\boldsymbol{u} \in \mathcal{U}$, such that

$$\int_{\Omega} \nabla^s \delta\boldsymbol{u} : \boldsymbol{\sigma}\, \mathrm{d}\Omega + \int_{\Gamma_\mathrm{f}} [\![\delta\boldsymbol{u}]\!]|_\Gamma \cdot \boldsymbol{t}_\mathrm{f}\, \mathrm{d}\Gamma = \int_{\Gamma_\mathrm{N}} \delta\boldsymbol{u} \cdot \bar{\boldsymbol{t}}\, \mathrm{d}\Gamma_\mathrm{N} \quad \forall\ \delta\boldsymbol{u} \in \mathcal{U}_0, \tag{2.12}$$

where

$$\mathcal{U}(\Omega) = \left\{ \boldsymbol{u} : \boldsymbol{u}(\boldsymbol{x}) \in \mathbb{R}^3\ \forall\, \boldsymbol{x} \in \Omega;\ u_i \in H^1(\Omega), i = 1,2,3;\ \boldsymbol{u}|_{\Gamma_\mathrm{u}} = \bar{\boldsymbol{u}} \right\} \tag{2.13}$$

$$\mathcal{U}_0(\Omega) = \left\{ \boldsymbol{u} \in \mathcal{U}(\Omega) :\ \boldsymbol{u}|_{\Gamma_\mathrm{u}} = \boldsymbol{0} \right\} \tag{2.14}$$

The kinematic assumptions from Sec. 2.2.1 lead to

$$\int_{\Omega} \nabla^s \delta\hat{\boldsymbol{u}} : \boldsymbol{\sigma}\, \mathrm{d}\Omega + \int_{\Omega_\mathrm{f}} \nabla^s \delta\tilde{\boldsymbol{u}} : \boldsymbol{\sigma}\, \mathrm{d}\Omega + \int_{\Gamma_\mathrm{f}} [\![\delta\tilde{\boldsymbol{u}}]\!]|_\Gamma \cdot \boldsymbol{t}_\mathrm{f}\, \mathrm{d}\Gamma = \int_{\Gamma_\mathrm{N}} \delta\hat{\boldsymbol{u}} \cdot \bar{\boldsymbol{t}}\, \mathrm{d}\Gamma_\mathrm{N}. \tag{2.15}$$

It is noted that both $\delta\hat{\boldsymbol{u}}$ and $\delta\tilde{\boldsymbol{u}}$ belong to $\mathcal{U}_0$.

Since the virtual displacements $\delta\hat{\boldsymbol{u}}$ and $\delta\tilde{\boldsymbol{u}}$ are arbitrary, (2.15) can be split as

$$\int_{\Omega} \nabla^s \delta\hat{\boldsymbol{u}} : \boldsymbol{\sigma}\, \mathrm{d}\Omega = \int_{\Gamma_\mathrm{N}} \delta\hat{\boldsymbol{u}} \cdot \bar{\boldsymbol{t}}\, \mathrm{d}\Gamma_\mathrm{N} \quad \text{and} \tag{2.16}$$

$$\int_{\Omega_\mathrm{f}} \nabla^s \delta\tilde{\boldsymbol{u}} : \boldsymbol{\sigma}\, \mathrm{d}\Omega + \int_{\Gamma_\mathrm{f}} [\![\delta\tilde{\boldsymbol{u}}]\!]|_\Gamma \cdot \boldsymbol{t}_\mathrm{f}\, \mathrm{d}\Gamma = 0. \tag{2.17}$$

Using the decomposition of the strain tensor given in (2.10) and constitutive laws (2.4), (2.5), and (2.11), lead to

$$\begin{aligned} &\int_{\Omega_\mathrm{m}} \nabla^s \delta\hat{\boldsymbol{u}} : \boldsymbol{D}_\mathrm{m} : \nabla^s \hat{\boldsymbol{u}}\, \mathrm{d}\Omega + \int_{\Omega_\mathrm{f}} \nabla^s \delta\hat{\boldsymbol{u}} : \boldsymbol{D}_\mathrm{f} : \nabla^s \hat{\boldsymbol{u}}\, \mathrm{d}\Omega \\ &+ \int_{\Omega_\mathrm{f}} \nabla^s \delta\hat{\boldsymbol{u}} : \boldsymbol{D}_\mathrm{f} : \nabla^s \tilde{\boldsymbol{u}}\, \mathrm{d}\Omega = \int_{\Gamma_\mathrm{N}} \delta\hat{\boldsymbol{u}} \cdot \bar{\boldsymbol{t}}\, \mathrm{d}\Gamma_\mathrm{N}, \end{aligned} \tag{2.18}$$

since $\nabla^s \tilde{\boldsymbol{u}} = \boldsymbol{0}$ over Ω_m, and

$$\int_{\Omega_\mathrm{f}} \nabla^s \delta\tilde{\boldsymbol{u}} : \boldsymbol{D}_\mathrm{f} : \nabla^s \hat{\boldsymbol{u}} \, \mathrm{d}\Omega + \int_{\Omega_\mathrm{f}} \nabla^s \delta\tilde{\boldsymbol{u}} : \boldsymbol{D}_\mathrm{f} : \nabla^s \tilde{\boldsymbol{u}} \, \mathrm{d}\Omega + \int_{\Gamma_\mathrm{f}} \delta\tilde{\boldsymbol{u}}|_\Gamma \cdot (\boldsymbol{D}_\mathrm{b} \tilde{\boldsymbol{u}}|_\Gamma) \, \mathrm{d}\Gamma = 0. \tag{2.19}$$

since $[\![\delta\tilde{\boldsymbol{u}}]\!]|_\Gamma = \delta\tilde{\boldsymbol{u}}|_\Gamma$.

As the integral over the matrix domain Ω_m in Equation (2.18) is difficult to evaluate using a nonconformal discretization of matrix and fiber domains, it is converted to an integral over the whole domain Ω thus yielding

$$\begin{aligned} &\int_\Omega \nabla^s \delta\hat{\boldsymbol{u}} : \boldsymbol{D}_\mathrm{m} : \nabla^s \hat{\boldsymbol{u}} \, \mathrm{d}\Omega + \int_{\Omega_\mathrm{f}} \nabla^s \delta\hat{\boldsymbol{u}} : (\boldsymbol{D}_\mathrm{f} - \boldsymbol{D}_\mathrm{m}) : \nabla^s \hat{\boldsymbol{u}} \, \mathrm{d}\Omega \\ &+ \int_{\Omega_\mathrm{f}} \nabla^s \delta\hat{\boldsymbol{u}} : \boldsymbol{D}_\mathrm{f} : \nabla^s \tilde{\boldsymbol{u}} \, \mathrm{d}\Omega = \int_{\Gamma_\mathrm{N}} \delta\hat{\boldsymbol{u}} \cdot \bar{\boldsymbol{t}} \, \mathrm{d}\Gamma_\mathrm{N}. \end{aligned} \tag{2.20}$$

Hereafter the cross-sectional area of the fibers is assumed constant over its length. Furthermore, the stress state in each fiber is assumed to be one-dimensional – the fibers can only take axial deformation. This is valid for thin and flexible fibers. With these assumptions, equations (2.19) and (2.20) can be simplified as

$$\begin{aligned} &A_\mathrm{f} \int_{L_\mathrm{f}} \nabla^s \delta\tilde{\boldsymbol{u}} : \boldsymbol{D}_\mathrm{f} : \nabla^s \hat{\boldsymbol{u}} \, \mathrm{d}l + A_\mathrm{f} \int_{L_\mathrm{f}} \nabla^s \delta\tilde{\boldsymbol{u}} : \boldsymbol{D}_\mathrm{f} : \nabla^s \tilde{\boldsymbol{u}} \, \mathrm{d}l \\ &+ C_\mathrm{f} \int_{L_\mathrm{f}} \delta\tilde{\boldsymbol{u}}|_\Gamma \cdot (\boldsymbol{D}_\mathrm{b} \tilde{\boldsymbol{u}}|_\Gamma) \, \mathrm{d}l = 0 \end{aligned} \tag{2.21}$$

and

$$\begin{aligned} &\int_\Omega \nabla^s \delta\hat{\boldsymbol{u}} : \boldsymbol{D}_\mathrm{m} : \nabla^s \hat{\boldsymbol{u}} \, \mathrm{d}\Omega + A_\mathrm{f} \int_{L_\mathrm{f}} \nabla^s \delta\hat{\boldsymbol{u}} : (\boldsymbol{D}_\mathrm{f} - \boldsymbol{D}_\mathrm{m}) : \nabla^s \hat{\boldsymbol{u}} \, \mathrm{d}l \\ &+ A_\mathrm{f} \int_{L_\mathrm{f}} \nabla^s \delta\hat{\boldsymbol{u}} : \boldsymbol{D}_\mathrm{f} : \nabla^s \tilde{\boldsymbol{u}} \, \mathrm{d}l = \int_{\Gamma_\mathrm{N}} \delta\hat{\boldsymbol{u}} \cdot \bar{\boldsymbol{t}} \, \mathrm{d}\Gamma_\mathrm{N}, \end{aligned} \tag{2.22}$$

where A_f, C_f and L_f are the cross-section area, circumference, and length of the fiber, respectively. Equation (2.9) was used to arrive at the last term on the left had side of (2.21). With an abuse of notation, all quantities are kept in a general three-dimensional setting.

Chapter 3

Fiber and Matrix Discretization

3.1 Introduction

This chapter [1] combines a Generalized FEM for 3D static fractures with a modification of the Embedded Reinforcement with bond Slip method (mERS). The proposed GFEM-mERS inherits the benefits of both methods: It can simulate fractures in fiber-reinforced composites using meshes that do not fit the fractures or the fibers, thus bringing the potential to solve complex fractures problems with minimal user intervention in model creation.

A brief review of GFEM is presented in Sec. 3.2 and the modifications necessary for the combination of the ERS with this GFEM are presented in Sec. 3.3. These modifications allows the integration of the mERS with methods that adopt high-order polynomial or even non-polynomial shape functions. This, in turn, enables the proposed method to adopt discretization of fractures with fibers bridging across their faces and the use of high-order polynomial approximations. Hence, the FEM mesh does not need to fit fracture surfaces or fibers. This greatly facilitates the discretization of fractures in fiber-reinforced composites as shown in Chapter 4.

[1] This chapter has been adapted from "P. Alves, A. Simone, C. A. Duarte, A generalized finite element method for three-dimensional fractures in fiber-reinforced composites, Meccanica (2020), [51] and "P. Alves, C. A. Duarte, A GFEM for three-dimensional crack propagation in fiber-reinforced composites, conference paper awarded by the Engineering Mechanics Institute (EMI) - Ph.D. research competition on Computational Mechanics - UCSD (2017), [53]"

3.2 The Generalized Finite Element Method (GFEM)

The GFEM has its origins in the works of Babuška and co-workers, initially named as Special Finite Element Method (SFEM) [54] and later as Partition of Unity Method (PUM) [4, 55], and Duarte and Oden as a meshless formulation in the *hp*-Cloud Method [56, 57] and later as a hybrid approach with the FEM [6]. Indeed, it can be considered an instance of the PUM, in the sense that it employs a set of Partition of Unity (PU) functions to guarantee interelement continuity. Such strategy creates conforming approximations which are improved by a nodal enrichment scheme. This basic idea shares the same characteristics as the eXtended Finite Element Method (XFEM) proposed later in [58], as it is noted by [59].

A brief review of generalized FEM approximations is given in this section. Further details can be found in [5, 6, 55, 60]. In summary, the GFEM can be interpreted as the Finite Element Method hierarchically enriched with special functions that can approximate well the behavior of the solution of a given class of problems. The GFEM approximation $\boldsymbol{u}^{\text{GFEM}}$ of a vector field $\boldsymbol{u}$ (*e.g.*, displacements) is given by

$$\begin{aligned}\boldsymbol{u}^{\text{GFEM}}(\boldsymbol{x}) &= \boldsymbol{u}^{\text{FEM}}(\boldsymbol{x}) + \boldsymbol{u}^{\text{ENR}}(\boldsymbol{x}) \\ &= \sum_{\alpha\in I_h} \underline{\hat{\boldsymbol{u}}}_\alpha N_\alpha(\boldsymbol{x}) + \sum_{\alpha\in I_h^e} N_\alpha(\boldsymbol{x}) \sum_{i=1}^{m_\alpha} \underline{\tilde{\boldsymbol{u}}}_{\alpha i} E_{\alpha i}(\boldsymbol{x}), \\ \underline{\hat{\boldsymbol{u}}}_\alpha, \underline{\tilde{\boldsymbol{u}}}_{\alpha i} &\in \mathbb{R}^d,\ d = 1,2,3. \end{aligned} \tag{3.1}$$

In the above equation, $N_\alpha(\boldsymbol{x})$, $\alpha \in I_h = \{1,\cdots,\text{nnod}\}$, is the standard linear finite element shape function associated with node $\boldsymbol{x}_\alpha$ of a finite element mesh covering the analysis domain $\bar{\Omega}$ and with nnod nodes; $E_{\alpha i}$ is an *enrichment function* at the node with index $\alpha \in I_h^e \subset I_h$, and $i = \{1,\cdots,m_\alpha\}$ is the index of the enrichment function at the node with m_α being the total number of enrichments assigned to node $\boldsymbol{x}_\alpha$.

The enrichment functions $E_{\alpha i}$ are chosen such that they approximate the unknown solution $\boldsymbol{u}$ of the problem locally in the support ω_α of shape function $N_\alpha(\boldsymbol{x})$. This support, also denoted as a node patch or a node cloud, is given by the union of the finite elements sharing node $\boldsymbol{x}_\alpha$. Figure 3.1 illustrates the construction of a GFEM shape function using a discontinuous enrichment function as an example.

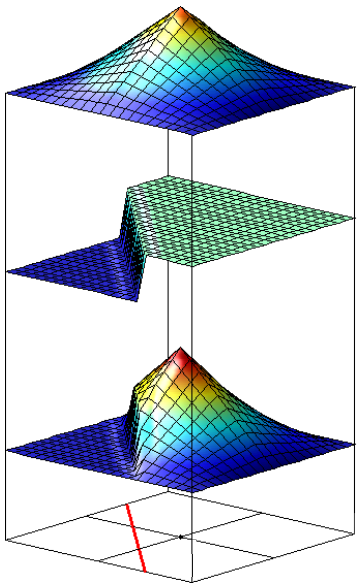

Figure 3.1: Partition of unity function $N_{\alpha i}$, enrichment function $E_{\alpha i}$, and resulting GFEM shape function $\phi_{\alpha i}$, [61]

The fracture problems analyzed in Chapter 4 are assumed to satisfy linear elastic fracture mechanics assumptions. Three types of enrichments are adopted here to solve this class of problems:

1) Polynomials $\hat{E}_{\alpha i}$, which are used at nodes in the set I_h^p. An example of polynomials of degree $p = 1$ in three dimensions is

$$\left\{\hat{E}_{\alpha i}\right\}_{i=1}^{m_\alpha=3} = \left\{\frac{(x-x_\alpha)}{h_\alpha}, \frac{(y-y_\alpha)}{h_\alpha}, \frac{(z-z_\alpha)}{h_\alpha}\right\} \tag{3.2}$$

with h_α being a scaling factor and $\boldsymbol{x}_\alpha = (x_\alpha, y_\alpha, z_\alpha)$ the coordinates of the node associated with patch ω_α;

2) The generalized Heaviside function [62, 63] is used at nodes whose support $\omega_\alpha = \omega_\alpha^+ \cup \omega_\alpha^-$ is fully cut by the crack surface. It is defined as

$$\mathcal{H}(\boldsymbol{x}) = \begin{cases} 1 & \text{if } \boldsymbol{x} \in \omega_\alpha^+, \alpha \in I_h^H \\ 0 & \text{otherwise} \end{cases} \tag{3.3}$$

Nodes enriched with $\mathcal{H}$ belong to set I_h^H. An example of GFEM p-hierarchical discontinuous enrichments based on (3.3) is

$$\left\{E_{\alpha i}^{\mathcal{H}}\right\}_{i=1}^{m_\alpha=4} = \left\{\mathcal{H}(\boldsymbol{x}), \mathcal{H}(\boldsymbol{x})\tfrac{(x-x_\alpha)}{h_\alpha}, \mathcal{H}(\boldsymbol{x})\tfrac{(y-y_\alpha)}{h_\alpha}, \mathcal{H}(\boldsymbol{x})\tfrac{(z-z_\alpha)}{h_\alpha}\right\} \tag{3.4}$$

3) Singular functions from the asymptotic expansion of the elasticity solution in the neighborhood of a crack front. In this dissertation, the singular enrichments proposed by Oden and Duarte [5, 64] are used. Let $(r,\theta,\bar{z})$ and $(\bar{x},\bar{y},\bar{z})$ denote the local crack front cylindrical and Cartesian coordinate system respectively at point (x,y,z) denoted in the global Cartesian coordinate system as shown in Fig. 3.2. Let κ denote the Kolosov constant defined as $\kappa = 3-4\nu$ for plane strain and $\kappa = \frac{3-\nu}{1+\nu}$ for plane stress, and ν the Poisson's ratio. The so-called OD singular enrichments are given by

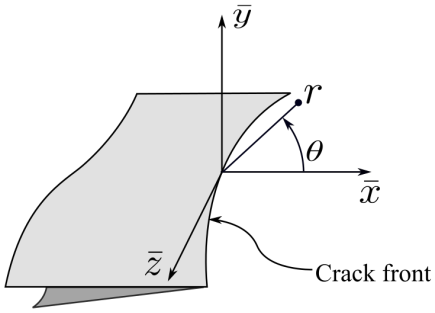

Figure 3.2: Crack front Cartesian and polar coordinate systems

$$\boldsymbol{E}^{\text{OD}}_{\text{front}}(\boldsymbol{x}) = \boldsymbol{R}_{\boldsymbol{x}\bar{\boldsymbol{x}}}(\boldsymbol{x}) \begin{bmatrix} \sqrt{r}\left[\left(\kappa-\frac{1}{2}\right)\cos\frac{\theta}{2}-\frac{1}{2}\cos\frac{3\theta}{2}\right] & \sqrt{r}\left[\left(\kappa+\frac{3}{2}\right)\sin\frac{\theta}{2}+\frac{1}{2}\sin\frac{3\theta}{2}\right] \\ \sqrt{r}\left[\left(\kappa+\frac{1}{2}\right)\sin\frac{\theta}{2}-\frac{1}{2}\sin\frac{3\theta}{2}\right] & \sqrt{r}\left[\left(\kappa-\frac{3}{2}\right)\cos\frac{\theta}{2}+\frac{1}{2}\cos\frac{3\theta}{2}\right] \\ \sqrt{r}\sin\frac{\theta}{2} & \sqrt{r}\cos\frac{\theta}{2} \end{bmatrix}, \tag{3.5}$$

where $\boldsymbol{R}_{\boldsymbol{x}\bar{\boldsymbol{x}}}(\boldsymbol{x})$ represents the rotation matrix from local crack Cartesian coordinate system to global Cartesian coordinate system at point $\boldsymbol{x}$ with entries given by

$$\boldsymbol{R}_{\boldsymbol{x}\bar{\boldsymbol{x}}}(\boldsymbol{x}) = \begin{bmatrix} R_{11} & R_{12} & R_{13} \\ R_{21} & R_{22} & R_{23} \\ R_{31} & R_{32} & R_{33} \end{bmatrix} \tag{3.6}$$

The columns of $\boldsymbol{R}_{\boldsymbol{x}\bar{\boldsymbol{x}}}(\boldsymbol{x})$ represent the components of the crack coordinate system base vectors with respect to the global base vector. The dimension of $\boldsymbol{E}^{\text{OD}}_{\text{front}}(\boldsymbol{x})$ is 3×2, with each row corresponding to an axis of the global coordinate system. These functions are used to enrich the displacement vector in the global coordinate directions x, y, and z, respectively, at a node belonging to set I_h^{front}. A scalar implementation of OD enrichments able to exactly reproduce the first term of the Mode I, II, and III of the asymptotic expansion of the elasticity solution is presented in [65].

Using the above enrichments, the GFEM approximation of the elastic solution for a cracked body is given by

$$\begin{aligned}\boldsymbol{u}^{\mathrm{GFEM}}(\boldsymbol{x}) = &\sum_{\alpha\in I_h} \underline{\hat{\boldsymbol{u}}}_\alpha N_\alpha(\boldsymbol{x}) + \sum_{\alpha\in I_h^p} N_\alpha(\boldsymbol{x}) \sum_{i=1}^{m_\alpha} \underline{\hat{\boldsymbol{u}}}_{\alpha i} \hat{E}_{\alpha i}(\boldsymbol{x}) \\ &+ \sum_{\alpha\in I_h^H} N_\alpha(\boldsymbol{x}) \sum_{i=1}^{m_\alpha} \underline{\tilde{\boldsymbol{u}}}_{\alpha i} E^{\mathcal{H}}_{\alpha i}(\boldsymbol{x}) \\ &+ \sum_{\alpha\in I_h^{\mathrm{front}}} N_\alpha(\boldsymbol{x}) \sum_{i=1}^{2} \underline{\breve{\boldsymbol{u}}}_{\alpha i} \odot \boldsymbol{E}^{\mathrm{OD}}_{\alpha i}(\boldsymbol{x}),\end{aligned} \tag{3.7}$$

where $\boldsymbol{E}^{\mathrm{OD}}_{\alpha i}(\boldsymbol{x})$ is the i-th column of $\boldsymbol{E}^{\mathrm{OD}}_{\mathrm{front}}(\boldsymbol{x})$ and $\odot$ stands for the entry-wise product of two vectors operator (Hadamard product). Equation (3.7) can also be written in matrix notation as

$$\boldsymbol{u}^{\mathrm{GFEM}}(\boldsymbol{x}) = \boldsymbol{N}^{\mathrm{GFEM}} \boldsymbol{U}^{\mathrm{GFEM}}, \tag{3.8}$$

where matrix $\boldsymbol{N}^{\mathrm{GFEM}}$ has standard and GFEM shape functions defined using polynomial, generalized Heaviside, and singular enrichments and $\boldsymbol{U}^{\mathrm{GFEM}}$ is the global vector of degrees of freedom. The GFEM approximation $\boldsymbol{u}^{\mathrm{GFEM}}$ is used in Sec. 3.3 in combination with the modified ERS approach to discretize the problem described in Chapter 2.

3.3 Discretization of fiber-reinforced composites with 3D fractures

This section presents the approximations for the components of the displacement field (2.6) for a fractured fiber-reinforced composite. Fibers are discretized with a modified version of the ERS, described next, while fractures are discretized with the GFEM presented in Sec. 3.2. After a short review of the assumptions and formulation of the ERS approach, the modifications necessary for its combination with the GFEM for fractures are presented. These modifications enable, for example, the discretization of fractures with fibers bridging across fracture faces.

3.3.1 The classical ERS formulation

In the ERS approach the displacement field of a fiber is decomposed into non-slip and slip components (2.8) as described next.

The non-slip component is obtained from the matrix displacement field and therefore is a derived quantity. This field is approximated using standard FEM shape functions as in

$$\hat{\boldsymbol{u}}(\boldsymbol{x}) = \boldsymbol{N}_{\mathrm{m}}(\boldsymbol{x})\boldsymbol{U}_{\mathrm{m}}, \tag{3.9}$$

where $\boldsymbol{N}_{\mathrm{m}}$ contains the shape functions for the matrix element and $\boldsymbol{U}_{\mathrm{m}}$ its degrees of freedom. As an example, in the case of a linear tetrahedron element (TET4), $\boldsymbol{N}_{\mathrm{m}}$ and $\boldsymbol{U}_{\mathrm{m}}$ are given, respectively, by

$$\boldsymbol{N}_{\mathrm{m}}(\boldsymbol{x}) = \begin{bmatrix} N_{\mathrm{m}_1}(\boldsymbol{x}) & 0 & 0 & \dots & N_{\mathrm{m}_4}(\boldsymbol{x}) & 0 & 0 \\ 0 & N_{\mathrm{m}_1}(\boldsymbol{x}) & 0 & \dots & 0 & N_{\mathrm{m}_4}(\boldsymbol{x}) & 0 \\ 0 & 0 & N_{\mathrm{m}_1}(\boldsymbol{x}) & \dots & 0 & 0 & N_{\mathrm{m}_4}(\boldsymbol{x}) \end{bmatrix} \quad \text{and} \tag{3.10}$$

$$\boldsymbol{U}_{\mathrm{m}} = \begin{bmatrix} u_{\mathrm{m1x}} & u_{\mathrm{m1y}} & u_{\mathrm{m1z}} & \dots & u_{\mathrm{m4x}} & u_{\mathrm{m4y}} & u_{\mathrm{m4z}} \end{bmatrix}^{\mathrm{T}}. \tag{3.11}$$

Let $\boldsymbol{x}_{\mathrm{f}1} = (x_{\mathrm{f}1}, y_{\mathrm{f}1}, z_{\mathrm{f}1})$ and $\boldsymbol{x}_{\mathrm{f}2} = (x_{\mathrm{f}2}, y_{\mathrm{f}2}, z_{\mathrm{f}2})$ denote the intersection points between the fiber and the element boundary as illustrated in Fig. 3.3. These points are hereafter denoted as fiber nodes. Using (3.9), the matrix displacement at these nodes is given by

$$\hat{\boldsymbol{u}}_{1,2} = \begin{bmatrix} \hat{\boldsymbol{u}}(\boldsymbol{x}_{\mathrm{f}1}) \\ \hat{\boldsymbol{u}}(\boldsymbol{x}_{\mathrm{f}2}) \end{bmatrix} = \begin{bmatrix} \boldsymbol{N}_{\mathrm{m}}(\boldsymbol{x}_{\mathrm{f}1}) \\ \boldsymbol{N}_{\mathrm{m}}(\boldsymbol{x}_{\mathrm{f}2}) \end{bmatrix} \boldsymbol{U}_{\mathrm{m}} = \boldsymbol{N}_{\mathrm{mf}}(\boldsymbol{x}_{\mathrm{f}1}, \boldsymbol{x}_{\mathrm{f}2})\boldsymbol{U}_{\mathrm{m}}. \tag{3.12}$$

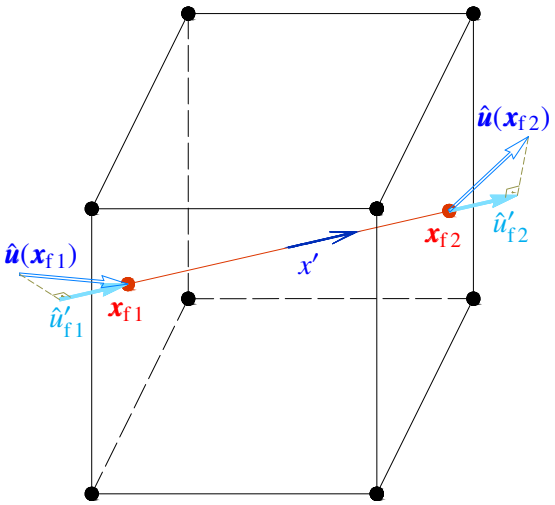

Figure 3.3: Intersection between the fiber and element boundary

In matrix $\boldsymbol{N}_{\mathrm{mf}}(\boldsymbol{x}_{\mathrm{f}1}, \boldsymbol{x}_{\mathrm{f}2})$, the matrix shape functions are evaluated at the fiber nodes. In the case of a TET4 element, this matrix is given by

$$\boldsymbol{N}_{\mathrm{mf}}(\boldsymbol{x}_{\mathrm{f}1}, \boldsymbol{x}_{\mathrm{f}2}) = \begin{bmatrix} N_{\mathrm{m}_1}(\boldsymbol{x}_{\mathrm{f}1}) & 0 & 0 & \cdots & N_{\mathrm{m}_4}(\boldsymbol{x}_{\mathrm{f}1}) & 0 & 0 \\ 0 & N_{\mathrm{m}_1}(\boldsymbol{x}_{\mathrm{f}1}) & 0 & \cdots & 0 & N_{\mathrm{m}_4}(\boldsymbol{x}_{\mathrm{f}1}) & 0 \\ 0 & 0 & N_{\mathrm{m}_1}(\boldsymbol{x}_{\mathrm{f}1}) & \cdots & 0 & 0 & N_{\mathrm{m}_4}(\boldsymbol{x}_{\mathrm{f}1}) \\ N_{\mathrm{m}_1}(\boldsymbol{x}_{\mathrm{f}2}) & 0 & 0 & \cdots & N_{\mathrm{m}_4}(\boldsymbol{x}_{\mathrm{f}2}) & 0 & 0 \\ 0 & N_{\mathrm{m}_1}(\boldsymbol{x}_{\mathrm{f}2}) & 0 & \cdots & 0 & N_{\mathrm{m}_4}(\boldsymbol{x}_{\mathrm{f}2}) & 0 \\ 0 & 0 & N_{\mathrm{m}_1}(\boldsymbol{x}_{\mathrm{f}2}) & \cdots & 0 & 0 & N_{\mathrm{m}_4}(\boldsymbol{x}_{\mathrm{f}2}) \end{bmatrix}. \tag{3.13}$$

The displacement vectors $\hat{\boldsymbol{u}}(\boldsymbol{x}_{\mathrm{f}1})$ and $\hat{\boldsymbol{u}}(\boldsymbol{x}_{\mathrm{f}2})$ are depicted in Fig. 3.3. The components of these vectors in the fiber direction are given by

$$\underline{\hat{\boldsymbol{u}}}'_{\mathrm{f}} = \begin{bmatrix} \hat{u}'_{\mathrm{f}1} \\ \hat{u}'_{\mathrm{f}2} \end{bmatrix} = \boldsymbol{R}_{\mathrm{mf}} \hat{\boldsymbol{u}}_{1,2} = \boldsymbol{R}_{\mathrm{mf}} \boldsymbol{N}_{\mathrm{mf}}(\boldsymbol{x}_{\mathrm{f}1}, \boldsymbol{x}_{\mathrm{f}2}) \boldsymbol{U}_{\mathrm{m}}, \tag{3.14}$$

where

$$\boldsymbol{R}_{\mathrm{mf}} = \begin{bmatrix} \cos(\theta_{x'x}) & \cos(\theta_{x'y}) & \cos(\theta_{x'z}) & 0 & 0 & 0 \\ 0 & 0 & 0 & \cos(\theta_{x'x}) & \cos(\theta_{x'y}) & \cos(\theta_{x'z}) \end{bmatrix} \tag{3.15}$$

with $\theta_{x'x}$, $\theta_{x'y}$, and $\theta_{x'z}$ the angles between the fiber axis x' and the global x, y, and z directions, respectively.

Matrix $\boldsymbol{R}_{\mathrm{mf}}$ projects the matrix displacements at the fiber nodes on the fiber direction x'. The displacement components $\hat{u}'_{\mathrm{f}1}$ and $\hat{u}'_{\mathrm{f}2}$ are also depicted in Fig. 3.3.

The matrix displacement along the fiber is further approximated using one-dimensional linear shape functions and nodal displacements $\hat{u}'_{\mathrm{f}1}$ and $\hat{u}'_{\mathrm{f}2}$, i.e.,

$$\hat{u}_{\Omega_{\mathrm{f}}}(x') = \boldsymbol{N}_{\mathrm{f}}(x')\,\underline{\hat{\boldsymbol{u}}}'_{\mathrm{f}} = \begin{bmatrix} N_{\mathrm{f}1}(x') & N_{\mathrm{f}2}(x') \end{bmatrix} \begin{bmatrix} \hat{u}'_{\mathrm{f}1} \\ \hat{u}'_{\mathrm{f}2} \end{bmatrix}, \tag{3.16}$$

where x' is the coordinate along the fiber as shown in Fig. 3.3. Inserting (3.14) into (3.16) leads to

$$\hat{u}_{\Omega_{\mathrm{f}}}(x') = \boldsymbol{N}_{\mathrm{f}}(x')\boldsymbol{R}_{\mathrm{mf}}\boldsymbol{N}_{\mathrm{mf}}(\boldsymbol{x}_{\mathrm{f}1}, \boldsymbol{x}_{\mathrm{f}2})\boldsymbol{U}_{\mathrm{m}}. \tag{3.17}$$

Equation (3.17) assumes that the FEM shape functions adopted for the discretization of the matrix displacement field *restricted to one-dimensional fibers crossing the element*, are identical to the 1D shape functions adopted for the discretization of the longitudinal displacement of the fibers. This is in general not correct. For example, if the matrix is discretized with 2D bilinear elements and the fibers are discretized with 1D linear elements, as broadly used in the ERS literature, the restriction of the 2D shape functions to 1D is not a linear function, except in special cases. This is also not the case for the GFEM approximation of a matrix with cracks. GFEM shape functions can be discontinuous and/or singular. Their restriction to 1D is clearly not a linear polynomial. This issue is addressed in the modified ERS described in the next section.

The approximation given by (3.17) is however not valid if the matrix displacement is approximated by the GFEM presented in Sec. 3.2. In this case the matrix displacement $\hat{\boldsymbol{u}}$ presents a discontinuity and possibly a singularity that can not be approximated by the 1D linear shape functions $\boldsymbol{N}_{\mathrm{f}}(x')$. The non-slip displacement component of the classical ERS formulation is modified in the next section so that it can be used together with the GFEM for fractures.

The approximation of the fiber slip (relative displacement between matrix and fiber) is given by

$$\tilde{u}_{\Omega_{\mathrm{f}}}(x') = \boldsymbol{N}_{\mathrm{f}}(x')\boldsymbol{U}_{\mathrm{f}}, \tag{3.18}$$

where the fiber shape functions and degrees of freedom are given, respectively, by

$$\boldsymbol{N}_{\mathrm{f}}(x') = \begin{bmatrix} N_{\mathrm{f}1}(x') & N_{\mathrm{f}2}(x') \end{bmatrix} \text{ and} \tag{3.19}$$

$$\boldsymbol{U}_{\mathrm{f}} = \begin{bmatrix} u_{\mathrm{f}1x'} & u_{\mathrm{f}2x'} \end{bmatrix}^{\mathrm{T}}. \tag{3.20}$$

A linear approximation is adopted for the slip leading to only two extra degrees of freedom for each fiber segment embedded in a 2D or 3D element. It is noted that the slip degrees of freedom $\boldsymbol{U}_{\mathrm{f}}$ are defined in the fiber direction x'. Further details regarding the final expression of the discretized system of equations can be found in references [36, 37, 47].

3.3.2 Modified ERS formulation (mERS)

In the proposed modified ERS (mERS), only the non-slip component of the fiber displacement is modified and the approximation of the fiber slip component is taken as in the original ERS. The non-slip component (i.e., the displacement of the matrix in the direction of the fiber) is given by

$$\hat{u}_{\Omega_{\mathrm{f}}}(x') = \boldsymbol{R}_{\mathrm{f}}\hat{\boldsymbol{u}}[\boldsymbol{x}(x')] = \boldsymbol{R}_{\mathrm{f}}\boldsymbol{N}_{\mathrm{m}}[\boldsymbol{x}(x')]\boldsymbol{U}_{\mathrm{m}}, \tag{3.21}$$

where the transformation matrix $\boldsymbol{R}_{\mathrm{f}}$ is given by

$$\boldsymbol{R}_{\mathrm{f}} = \begin{bmatrix} \cos(\theta_{x'x}) & \cos(\theta_{x'y}) & \cos(\theta_{x'z}) \end{bmatrix}. \tag{3.22}$$

The key difference between Equation (3.17) and Equation (3.21) is that in the latter the matrix shape functions are evaluated at each point x' on the fiber, while in the former the shape functions are evaluated at the fiber nodes only. The consequence of this is that Equation (3.21) can be used with any approximation space adopted for the matrix while Equation (3.17) cannot. Here, the GFEM approximation (3.8) for fractures presented in Sec. 3.2 is employed in place of the ERS approximation in Equation (3.9):

$$\hat{\boldsymbol{u}}(\boldsymbol{x}) = \boldsymbol{N}^{\mathrm{GFEM}}(\boldsymbol{x})\boldsymbol{U}^{\mathrm{GFEM}}. \tag{3.23}$$

In the above equation and hereafter in this dissertation, the matrix shape functions $\boldsymbol{N}_{\mathrm{m}}$ are taken as the GFEM shape functions $\boldsymbol{N}^{\mathrm{GFEM}}$. This leads to the equation

$$\hat{u}_{\Omega_{\mathrm{f}}}(x') = \boldsymbol{R}_{\mathrm{f}}\hat{\boldsymbol{u}}[\boldsymbol{x}(x')] = \boldsymbol{R}_{\mathrm{f}}\boldsymbol{N}^{\mathrm{GFEM}}[\boldsymbol{x}(x')]\boldsymbol{U}^{\mathrm{GFEM}} \tag{3.24}$$

for the matrix displacement in the direction of the fiber.

3.3.3 Matrix strain

The matrix strain is given by

$$\hat{\boldsymbol{\epsilon}} = \boldsymbol{\nabla}^s\hat{\boldsymbol{u}}. \tag{3.25}$$

Using (3.23) in the previous equation leads to

$$\hat{\boldsymbol{\epsilon}}^* = \boldsymbol{L}\boldsymbol{N}^{\mathrm{GFEM}}\boldsymbol{U}^{\mathrm{GFEM}} = \boldsymbol{B}^{\mathrm{GFEM}}\boldsymbol{U}^{\mathrm{GFEM}}, \tag{3.26}$$

where $\hat{\boldsymbol{\epsilon}}^*$ is the strain tensor $\hat{\boldsymbol{\epsilon}}$ in Voigt notation, $\boldsymbol{L}$ is the differential operator $\boldsymbol{\nabla}^s$ in matrix format and

$$\boldsymbol{B}^{\mathrm{GFEM}} = \boldsymbol{L}\boldsymbol{N}^{\mathrm{GFEM}}. \tag{3.27}$$

The matrix strain in the direction of the fiber is the component $\hat{\epsilon}'_{11}$ of the strain tensor

$$\hat{\boldsymbol{\epsilon}}' = \boldsymbol{Q}\hat{\boldsymbol{\epsilon}}\boldsymbol{Q}^T, \tag{3.28}$$

where $\hat{\boldsymbol{\epsilon}}'$ is the strain tensor in the fiber coordinate system, $\hat{\boldsymbol{\epsilon}}$ is the strain tensor in the matrix coordinate system and $\boldsymbol{Q}$ is the rotation matrix between these systems. The components of these tensors are given by

$$\hat{\boldsymbol{\epsilon}}' = \begin{bmatrix} \hat{\epsilon}'_{11} & \hat{\epsilon}'_{12} & \hat{\epsilon}'_{13} \\ \hat{\epsilon}'_{12} & \hat{\epsilon}'_{22} & \hat{\epsilon}'_{32} \\ \hat{\epsilon}'_{13} & \hat{\epsilon}'_{23} & \hat{\epsilon}'_{33} \end{bmatrix} \tag{3.29}$$

$$\hat{\boldsymbol{\epsilon}} = \begin{bmatrix} \hat{\epsilon}_{11} & \hat{\epsilon}_{12} & \hat{\epsilon}_{13} \\ \hat{\epsilon}_{12} & \hat{\epsilon}_{22} & \hat{\epsilon}_{32} \\ \hat{\epsilon}_{13} & \hat{\epsilon}_{23} & \hat{\epsilon}_{33} \end{bmatrix} \tag{3.30}$$

$$\boldsymbol{Q} = \begin{bmatrix} Q_{11} & Q_{12} & Q_{13} \\ Q_{21} & Q_{22} & Q_{23} \\ Q_{31} & Q_{32} & Q_{33} \end{bmatrix} = \begin{bmatrix} \cos(\theta_x^{x'}) & \cos(\theta_y^{x'}) & \cos(\theta_z^{x'}) \\ \cos(\theta_x^{y'}) & \cos(\theta_y^{y'}) & \cos(\theta_z^{y'}) \\ \cos(\theta_x^{z'}) & \cos(\theta_y^{z'}) & \cos(\theta_z^{z'}) \end{bmatrix} \tag{3.31}$$

In (3.31), θ is the angle between a fiber coordinate system direction and a global coordinate system direction. For example, $\theta_x^{x'}$, is the angle between coordinate axes x' and x. Equation (3.28) in index notation is given by

$$\hat{\epsilon}'_{ij} = Q_{ik}\hat{\epsilon}_{kl}Q^T_{lk} \tag{3.32}$$

Since the only component of interest is $\hat{\epsilon}'_{11}$ (strain in the fiber direction), from (3.32) we have

$$\hat{\epsilon}'_{11} = Q_{1k}\hat{\epsilon}_{kl}Q^T_{l1} = Q_{1k}\hat{\epsilon}_{kl}Q_{1l} \tag{3.33}$$

Expanding the previous expression

$$\begin{aligned} \hat{\epsilon}'_{11} = \; & Q_{11}\hat{\epsilon}_{11}Q_{11} + Q_{12}\hat{\epsilon}_{21}Q_{11} + Q_{13}\hat{\epsilon}_{31}Q_{11} + \\ & Q_{11}\hat{\epsilon}_{11}Q_{11} + Q_{12}\hat{\epsilon}_{21}Q_{11} + Q_{13}\hat{\epsilon}_{31}Q_{11} + \\ & Q_{11}\hat{\epsilon}_{11}Q_{11} + Q_{12}\hat{\epsilon}_{21}Q_{11} + Q_{13}\hat{\epsilon}_{31}Q_{11} \end{aligned} \tag{3.34}$$

Writing it in matrix notation leads to

$$\hat{\epsilon}'_{11} = \boldsymbol{R}\hat{\boldsymbol{\epsilon}}^* \tag{3.35}$$

where

$$\boldsymbol{R} = \begin{bmatrix} \cos^2(\theta_x^{x'}) \\ \cos^2(\theta_y^{x'}) \\ \cos^2(\theta_z^{x'}) \\ 2\cos(\theta_x^{x'})\cos(\theta_y^{x'}) \\ 2\cos(\theta_y^{x'})\cos(\theta_z^{x'}) \\ 2\cos(\theta_x^{x'})\cos(\theta_z^{x'}) \end{bmatrix}^T \tag{3.36}$$

and

$$\boldsymbol{\epsilon}^* = \begin{bmatrix} \epsilon_{11} \\ \epsilon_{22} \\ \epsilon_{33} \\ \epsilon_{12} \\ \epsilon_{13} \\ \epsilon_{23} \end{bmatrix} \tag{3.37}$$

Using the above, we have

$$\hat{\epsilon}'_{11}(x') = \boldsymbol{R}\hat{\boldsymbol{\epsilon}}^*[\boldsymbol{x}(x')], \tag{3.38}$$

The gradient of the 1D fiber slip is given by

$$\tilde{\epsilon}'(x') = \frac{d\tilde{u}_{\Omega_\mathrm{f}}(x')}{dx'} = \frac{d\boldsymbol{N}_\mathrm{f}(x')}{dx'}\boldsymbol{U}_\mathrm{f} = \boldsymbol{B}_\mathrm{f}(x')\boldsymbol{U}_\mathrm{f}, \tag{3.39}$$

where

$$\boldsymbol{B}_\mathrm{f}(x') = \begin{bmatrix} \dfrac{dN_{\mathrm{f}1}(x')}{dx'} & \dfrac{dN_{\mathrm{f}2}(x')}{dx'} \end{bmatrix}. \tag{3.40}$$

3.3.4 Constitutive relations

The constitutive relation (2.4) in matrix format is given by

$$\hat{\boldsymbol{\sigma}}^* = \mathbb{D}_\mathrm{m}\hat{\boldsymbol{\epsilon}}^* \tag{3.41}$$

where $\hat{\boldsymbol{\sigma}}^*$ and $\hat{\boldsymbol{\epsilon}}^*$ are the stress and strain tensors in Voigt notation, and

$$\mathbb{D}_\mathrm{m} = \frac{E_\mathrm{m}}{(1+\nu_\mathrm{m})(1-2\nu_\mathrm{m})}\begin{bmatrix} 1-\nu_\mathrm{m} & \nu_\mathrm{m} & \nu_\mathrm{m} & 0 & 0 & 0 \\ \nu_\mathrm{m} & 1-\nu_\mathrm{m} & \nu_\mathrm{m} & 0 & 0 & 0 \\ \nu_\mathrm{m} & \nu_\mathrm{m} & 1-\nu_\mathrm{m} & 0 & 0 & 0 \\ 0 & 0 & 0 & 1-2\nu_\mathrm{m} & 0 & 0 \\ 0 & 0 & 0 & 0 & 1-2\nu_\mathrm{m} & 0 \\ 0 & 0 & 0 & 0 & 0 & 1-2\nu_\mathrm{m} \end{bmatrix}. \tag{3.42}$$

Since the fiber is modeled as a truss, the constitutive relation (2.5) degenerates to the one-dimensional Hooke's law

$$\tilde{\sigma}' = E_\mathrm{f}\tilde{\epsilon}' \tag{3.43}$$

in the fiber coordinate system.

Only the longitudinal fiber displacement is considered when idealizing a fiber as a truss. Therefore, the traction-separation law (2.11) degenerates to

$$t_{\mathrm{f}x'}(x') = K_\mathrm{b}\tilde{u}_{\Omega_\mathrm{f}}(x') \tag{3.44}$$

where $t_{\mathrm{f}x'}$ is the shear traction along the fiber, $\tilde{u}_{\Omega_\mathrm{f}}$ is the fiber slip (relative displacement between matrix and fiber), and K_b is the stiffness of the fiber-matrix interface, taken as a constant unless stated otherwise.

3.3.5 GFEM-mERS discretization of cracks in fiber-reinforced composites

Each term in (2.22) and (2.21) is discretized using the GFEM approximation for a matrix with cracks and the modified ERS formulation for the fiber and matrix-fiber interaction presented in Secs. 3.2 and 3.3, respectively.

The first term in (2.22) is discretized using (3.26) and (3.41), leading to

$$\int_{\Omega} \nabla^s \delta\hat{\boldsymbol{u}} : \boldsymbol{D}_{\mathrm{m}} : \nabla^s \hat{\boldsymbol{u}} d\Omega \implies \int_{\Omega} (\boldsymbol{B}_{\mathrm{m}})^T \mathbb{D}_{\mathrm{m}} \boldsymbol{B}_{\mathrm{m}} \, \mathrm{d}\Omega \tag{3.45}$$

where $\boldsymbol{B}_{\mathrm{m}} \equiv \boldsymbol{B}^{\mathrm{GFEM}}$. The second term of (2.22), discretized using (3.26), (3.38), (3.41) and (3.43), leads to

$$A_{\mathrm{f}} \int_{L_{\mathrm{f}}} \nabla^s \delta\hat{\boldsymbol{u}} : (\boldsymbol{D}_{\mathrm{f}} - \boldsymbol{D}_{\mathrm{m}}) : \nabla^s \hat{\boldsymbol{u}} \, \mathrm{d}l \implies A_{\mathrm{f}} \int_{L_{\mathrm{f}}} (\boldsymbol{B}_{\mathrm{m}})^T \boldsymbol{R}^T (E_{\mathrm{f}} - E_{\mathrm{m}}) \boldsymbol{R} \boldsymbol{B}_{\mathrm{m}} \, \mathrm{d}l. \tag{3.46}$$

The third term of (2.22) discretized using (3.26), (3.38), (3.39) and (3.43) leads to

$$A_{\mathrm{f}} \int_{L_{\mathrm{f}}} \nabla^s \delta\hat{\boldsymbol{u}} : \boldsymbol{D}_{\mathrm{f}} : \nabla^s \tilde{\boldsymbol{u}} \, \mathrm{d}l \implies A_{\mathrm{f}} \int_{L_{\mathrm{f}}} (\boldsymbol{B}_{\mathrm{m}})^T \boldsymbol{R}^T E_{\mathrm{f}} \boldsymbol{B}_{\mathrm{f}} \, \mathrm{d}l. \tag{3.47}$$

The right hand side of (2.22) discretized using (3.23) leads to

$$\int_{\Gamma_{\mathrm{N}}} \delta\hat{\boldsymbol{u}} \cdot \bar{\boldsymbol{t}} \, \mathrm{d}\Gamma_{\mathrm{N}} \implies \int_{\Gamma_{\mathrm{N}}} (\boldsymbol{N}_{\mathrm{m}})^T \bar{\boldsymbol{t}} \, \mathrm{d}\Gamma \tag{3.48}$$

where $\boldsymbol{N}_{\mathrm{m}} \equiv \boldsymbol{N}^{\mathrm{GFEM}}$. The first term of (2.21) discretized using (3.26), (3.38), (3.39) and (3.43) leads to

$$A_{\mathrm{f}} \int_{L_{\mathrm{f}}} \nabla^s \delta\tilde{\boldsymbol{u}} : \boldsymbol{D}_{\mathrm{f}} : \nabla^s \hat{\boldsymbol{u}} \, \mathrm{d}l \implies A_{\mathrm{f}} \int_{L_{\mathrm{f}}} (\boldsymbol{B}_{\mathrm{f}})^T E_{\mathrm{f}} \boldsymbol{R} \boldsymbol{B}_{\mathrm{m}} \, \mathrm{d}l. \tag{3.49}$$

The second term of (2.21) discretized using (3.39) and (3.43) leads to

$$A_{\mathrm{f}} \int_{L_{\mathrm{f}}} \nabla^s \delta\tilde{\boldsymbol{u}} : \boldsymbol{D}_{\mathrm{f}} : \nabla^s \tilde{\boldsymbol{u}} \, \mathrm{d}l \implies A_{\mathrm{f}} \int_{L_{\mathrm{f}}} (\boldsymbol{B}_{\mathrm{f}})^T E_{\mathrm{f}} \boldsymbol{B}_{\mathrm{f}} \, \mathrm{d}l. \tag{3.50}$$

Finally, the third term of (2.21) discretized using (3.18) and (3.44) leads to

$$C_{\mathrm{f}} \int_{L_{\mathrm{f}}} \delta\tilde{\boldsymbol{u}} \cdot (\boldsymbol{D}_{\mathrm{b}}\tilde{\boldsymbol{u}})\, \mathrm{d}l \implies C_{\mathrm{f}} \int_{L_{\mathrm{f}}} (\boldsymbol{N}_{\mathrm{f}})^T K_{\mathrm{b}} \boldsymbol{N}_{\mathrm{f}}\, \mathrm{d}l. \tag{3.51}$$

The above yields the following system of equilibrium equations

$$\begin{bmatrix} \boldsymbol{K}_{\mathrm{mm}} & \boldsymbol{K}_{\mathrm{mf}} \\ \boldsymbol{K}_{\mathrm{fm}} & \boldsymbol{K}_{\mathrm{ff}} \end{bmatrix} \begin{bmatrix} \boldsymbol{U}^{\mathrm{GFEM}} \\ \boldsymbol{U}_{\mathrm{f}} \end{bmatrix} = \begin{bmatrix} \boldsymbol{f} \\ \boldsymbol{0} \end{bmatrix} \tag{3.52}$$

where the terms in (3.52) are given by

$$\boldsymbol{K}_{\mathrm{mm}} = \int_{\Omega} (\boldsymbol{B}_{\mathrm{m}})^T \mathbb{D}_{\mathrm{m}} \boldsymbol{B}_{\mathrm{m}} d\Omega + A_{\mathrm{f}} \int_{L_{\mathrm{f}}} (\boldsymbol{B}_{\mathrm{m}})^T \boldsymbol{R}^T (E_{\mathrm{f}} - E_{\mathrm{m}}) \boldsymbol{R} \boldsymbol{B}_{\mathrm{m}}\, \mathrm{d}l, \tag{3.53}$$

$$\boldsymbol{K}_{\mathrm{mf}} = A_{\mathrm{f}} \int_{L_{\mathrm{f}}} (\boldsymbol{B}_{\mathrm{m}})^T \boldsymbol{R}^T E_{\mathrm{f}} \boldsymbol{B}_{\mathrm{f}}\, \mathrm{d}l, \tag{3.54}$$

$$\boldsymbol{K}_{\mathrm{fm}} = A_{\mathrm{f}} \int_{L_{\mathrm{f}}} (\boldsymbol{B}_{\mathrm{f}})^T E_{\mathrm{f}} \boldsymbol{R} \boldsymbol{B}_{\mathrm{m}}\, \mathrm{d}l, \tag{3.55}$$

$$\boldsymbol{K}_{\mathrm{ff}} = A_{\mathrm{f}} \int_{L_{\mathrm{f}}} (\boldsymbol{B}_{\mathrm{f}})^T E_{\mathrm{f}} \boldsymbol{B}_{\mathrm{f}}\, \mathrm{d}l + C_{\mathrm{f}} \int_{L_{\mathrm{f}}} (\boldsymbol{N}_{\mathrm{f}})^T K_{\mathrm{b}} \boldsymbol{N}_{\mathrm{f}}\, \mathrm{d}l, \tag{3.56}$$

$$\boldsymbol{f} = \int_{\Gamma_{\mathrm{N}}} (\boldsymbol{N}_{\mathrm{m}})^T \bar{\boldsymbol{t}}\, \mathrm{d}\Gamma. \tag{3.57}$$

The derivations presented in this section, leading to (3.52), assume that there is a single fiber in the analysis domain. The extensions to the case of multiple fibers is straightforward due to the hierarchical nature of (3.52): the GFEM discretization of a cracked domain is simply augmented by the discretization of each fiber based on the mERS. Thus, the system of equations for the case of n fibers is of the form

$$\begin{bmatrix} \boldsymbol{K}_{\mathrm{mm}} & \boldsymbol{K}_{\mathrm{mf}_1} & \boldsymbol{K}_{\mathrm{mf}_2} & \cdots & \boldsymbol{K}_{\mathrm{mf}_n} \\ \boldsymbol{K}_{\mathrm{f}_1\mathrm{m}} & \boldsymbol{K}_{\mathrm{f}_1\mathrm{f}_1} & \boldsymbol{0} & \cdots & \boldsymbol{0} \\ \boldsymbol{K}_{\mathrm{f}_2\mathrm{m}} & \boldsymbol{0} & \boldsymbol{K}_{\mathrm{f}_2\mathrm{f}_2} & \cdots & \boldsymbol{0} \\ \vdots & \vdots & \vdots & \ddots & \vdots \\ \boldsymbol{K}_{\mathrm{f}_n\mathrm{m}} & \boldsymbol{0} & \boldsymbol{0} & \cdots & \boldsymbol{K}_{\mathrm{f}_n\mathrm{f}_n} \end{bmatrix} \begin{bmatrix} \boldsymbol{U}^{\mathrm{GFEM}} \\ \boldsymbol{U}_{\mathrm{f}_1} \\ \boldsymbol{U}_{\mathrm{f}_2} \\ \vdots \\ \boldsymbol{U}_{\mathrm{f}_n} \end{bmatrix} = \begin{bmatrix} \boldsymbol{f} \\ \boldsymbol{0} \\ \boldsymbol{0} \\ \vdots \\ \boldsymbol{0} \end{bmatrix}. \tag{3.58}$$

Chapter 4

Numerical Experiments with the GFEM-mERS

4.1 Introduction

This chapter [1] presents several verification examples and one validation problem for the proposed GFEM-mERS. Reference 3D solutions are provided by standard FEM models in which fibers are discretized with 3D elements and the fiber-matrix interface is modeled using cohesive elements. The reference solutions, denoted 3DFEM in the following, are computed using Abaqus [66]. Consistent units are adopted in all examples but they are only explicitly provided for the problems in Secs 4.5 and 4.5.2.

4.2 Prismatic bar with two parallel fibers

The fiber-reinforced prismatic bar shown in Figs 4.1 and 4.2 is solved in this section. The bar is constrained at $x = 0.0$ and subjected to an axial traction of magnitude $\sigma = 40.0\ N/mm^2$ at $x = 10.0\ mm$. Two fibers are embedded into the bar as shown in Fig. 4.2. They are defined by the following segments: $f_1 = [(1.0, 0.25, -0.375), (9.0, 0.25, -0.375)]$, and $f_2 = [(1.0, 0.25, -0.625), (9.0, 0.25, -0.625)]$.

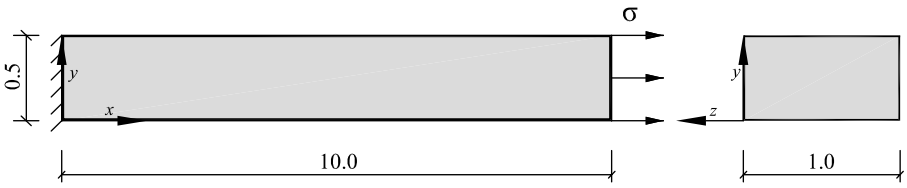

Figure 4.1: Prismatic bar with axial load (units in *mm*)

The moduli of elasticity of matrix and fiber are $E_{\mathrm{m}} = 1.0 \times 10^4\ N/mm^2$ and $E_{\mathrm{f}} = 5.0 \times 10^5\ N/mm^2$, respectively. The matrix Poisson's ratio is $\nu = 0.0$, and the fiber-matrix bond stiffness as $K_{\mathrm{b}} = 5.0 \times 10^4\ N/mm^3$.

[1] This chapter has been adapted from "P. Alves, A. Simone, C. A. Duarte, A generalized finite element method for three-dimensional fractures in fiber-reinforced composites, Meccanica (2020), [51]"

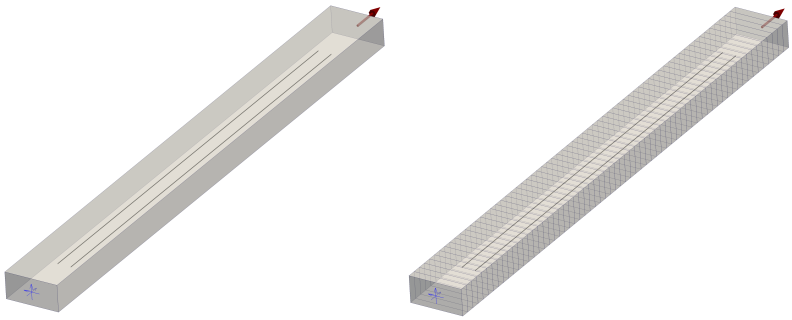

(a) Fiber orientation.

(b) Fibers and hexahedral GFEM mesh.

Figure 4.2: Fiber-reinforced bar. Blue arrows represent constraints applied to the displacement field at $x = 0$ while the red arrow represents the traction boundary condition prescribed at $x = 10$

Next, the effect of E_f, K_b, and the cross-section area, A_f, of each fiber on the axial stiffness of the bar is investigated. In all cases, the GFEM-mERS solution is compared with a reference 3D standard FEM solution. If the fibers are removed, the axial displacement of the bar is given by

$$u_x = 4.0 \times 10^{-3} x. \tag{4.1}$$

The GFEM mesh adopted in the next sub-sections is shown in Fig. 4.2(b). The mesh is refined only in the axial direction since the Poisson's ratio of $\nu = 0.0$ leads to a 1D solution. Tri-linear hexahedral elements are adopted for the GFEM discretization of the matrix while 1D linear elements are adopted for the mERS discretization of the fibers. The GFEM-mERS model has 780 matrix and 106 fiber DOFs, while the reference 3DFEM model has 8,022 DOFs. Fig. 4.2(b) also shows that a GFEM element can have more than one embedded fiber. It is noted that a new (sub)fiber is created every time a fiber crosses an element, and therefore the number of fiber degrees of freedom (DOFs) increases as the 3D mesh is refined.

4.2.1 Reference 3DFEM model

Figure 4.3 shows the prescribed boundary conditions in Abaqus. They are identical to the prescribed boundary conditions for the mERS model described earlier. The figure also shows the mesh corresponding to the 3DFEM model.

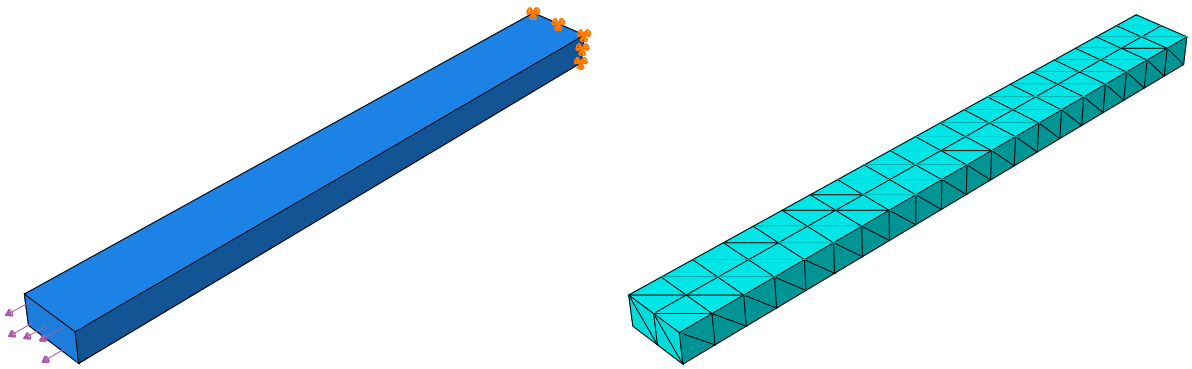

(a) Prescribed boundary conditions **(b)** Mesh refinement with tetrahedrons

Figure 4.3: Prismatic bar with parallel fibers computed with Abaqus

Figure 4.4 shows the final deformed shape (green) compared to the original configuration of the bar (black) for this problem. Mesh generation is highly simplified using mERS because the fibers do not need to match the matrix mesh.

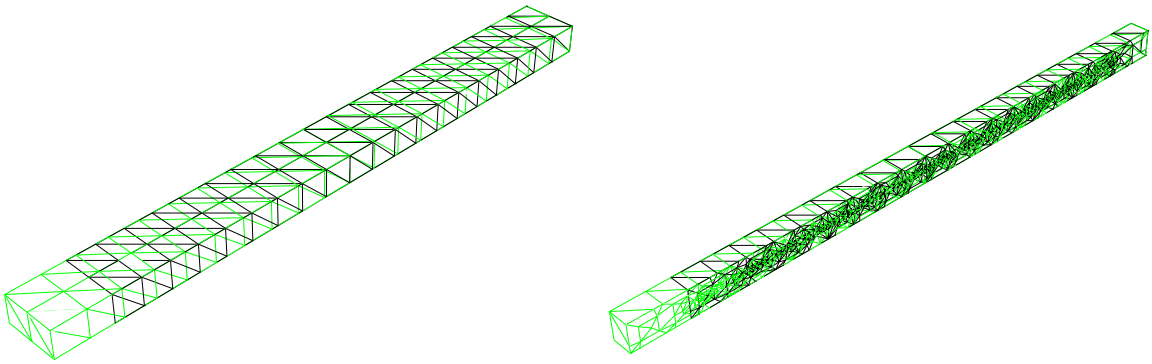

(a) Original (black) and deformed (green) shape **(b)** Cut view at the mid span of one of the fibers

Figure 4.4: Deformed shape of prismatic bar with parallel fibers computed with Abaqus

Because for this problem the main stress is in the x-direction and the largest dimension of fiber is oriented in this direction, both fibers are stressed equally. Figure 4.5 shows the stress for these 2 fibers. It is important to note the difference in magnitude between fiber and matrix meshes.

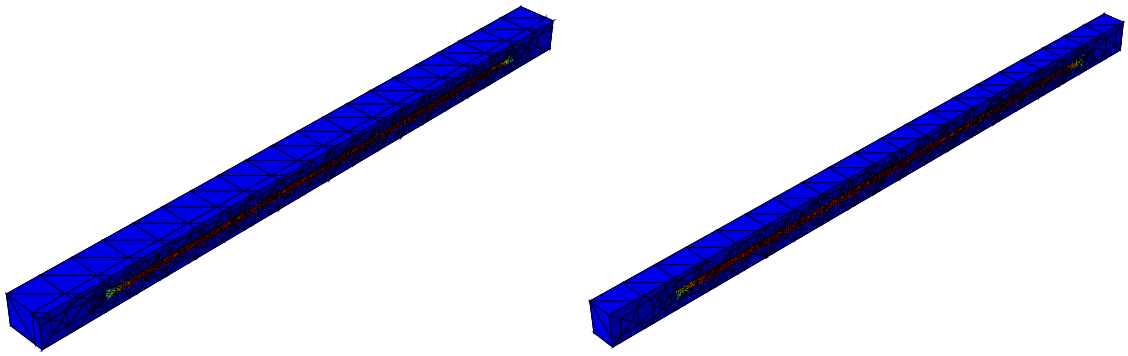

(a) Stress along fiber 1 **(b)** Stress along fiber 2

Figure 4.5: Stress at the fibers computed with Abaqus

4.2.2 Effect of modulus of elasticity of fibers

The effect of the modulus of elasticity of the fibers on the stiffness of the bar is analyzed in this section. Parameter E_f is taken in the range $[0.0, 1.0 \times 10^6]$ N/mm^2 while all other parameters remain the same as in Sec. 4.2. Figure 4.6 shows the displacement at $x = 10.0$ computed with the GFEM-mERS and the reference 3D FEM model. As expected, the axial displacement reduces as E_f increases and matches the value given by Eq. 4.1 when $E_f = 0$. The agreement of the GFEM-mERS with the 3D FEM reference solution is excellent.

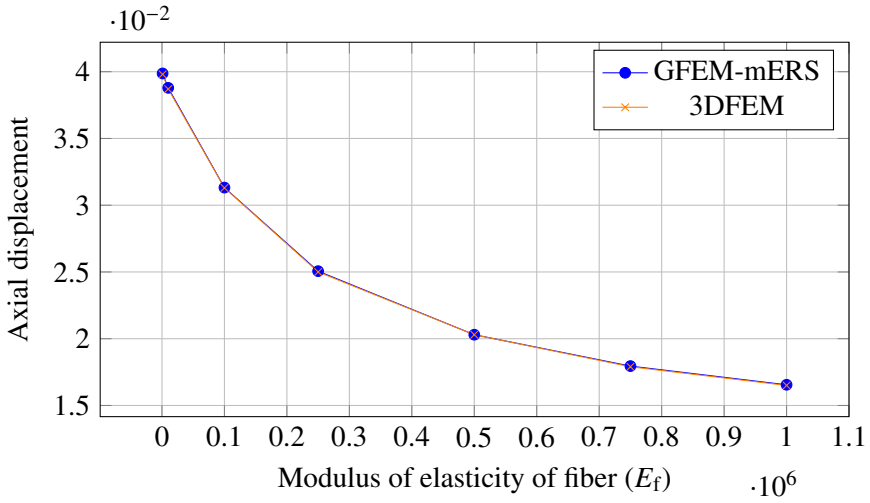

Figure 4.6: Axial displacement at the right end of a prismatic bar as a function of E_f

4.2.3 Effect of cross-section area of fibers

In this section, the cross-section area of each fiber is taken in the range $1.0 \times 10^{-7} \leq A_f \leq 0.1\ mm^2$, while all other parameters remain the same as in Sec. 4.2. The axial displacement at $x = 10.0$ is plotted in Fig. 4.7. A nearly zero cross-section area leads to a displacement of $u_x = 0.04$, matching the solution without fibers. A good agreement between the GFEM-mERS and the 3DFEM reference solution is observed for all values of A_f.

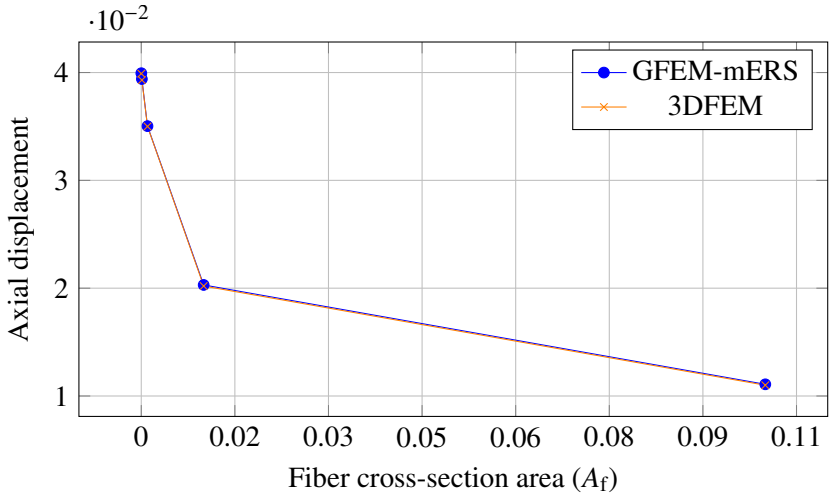

Figure 4.7: Axial displacement at the right end of a prismatic bar as a function of A_f

4.2.4 Effect of matrix-fiber bond stiffness

In this section, the effect of the matrix-fiber bond stiffness on the axial displacement of the bar is analyzed. Parameter K_b is taken in the range $[1.0, 1.0 \times 10^7]\ N/mm^3$ while all other parameters remain the same as in Sec. 4.2. The results are shown in Fig. 4.8. A low value of K_b leads to the same displacement as in a bar without fibers while higher values lead, as expected, to an increase of the bar stiffness. A good agreement between the GFEM-mERS and the 3DFEM reference solution is again observed.

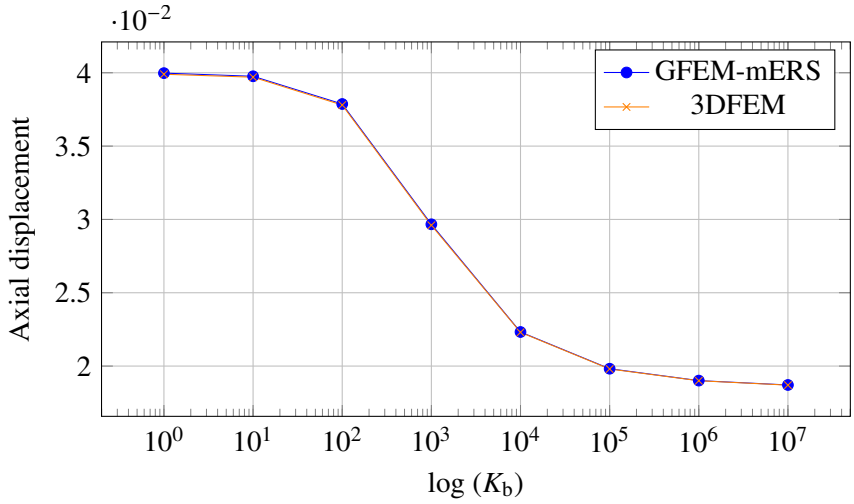

Figure 4.8: Axial displacement at the right end of a prismatic bar as a function of matrix-fiber bond stiffness K_b

4.3 Prismatic bar with diagonal fiber

The fiber-reinforced prismatic bar analyzed in Sec. 4.2 is considered again in this section. Here, however, only one fiber, defined by segment $f_1 = [(0.2, 0.1, -0.1), (9.8, 0.4, -0.9)]$, is embedded into the bar. The same material properties as in Sec. 4.2 are adopted. Figure 4.9 shows the problem setup and the GFEM mesh. Linear tetrahedral elements are adopted in order to show that the proposed mERS can be used with any type of element. The mesh is created by first meshing the domain with hexahedrons and then dividing each element into six tetrahedral elements. The GFEM-mERS model has 780 matrix and 185 fiber DOFs, while the reference 3DFEM model has 154,065 DOFs. In contrast with the previous problem, the fiber orientation adopted here leads to a non-constant displacement at each section of the prismatic bar, leading to a fully 3D deformed configuration as shown in Fig. 4.10. Axial displacements reported in this section are extracted at nodes A, B, C, and D shown in Fig. 4.9.

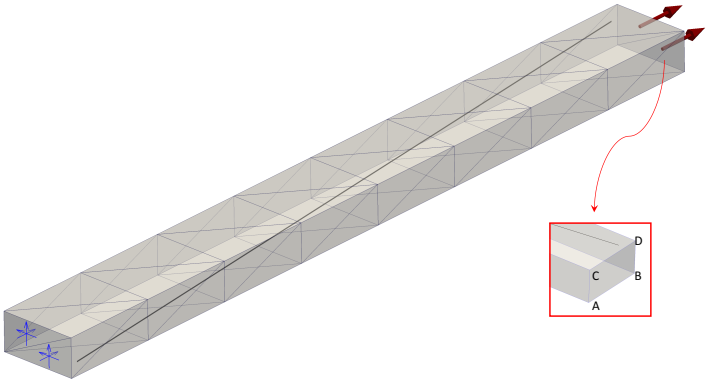

Figure 4.9: Fiber-reinforced bar and vertex nodes where axial displacement is reported. Blue arrows represent constraints applied to the displacement field at $x = 0$ while the red arrows represent the traction boundary condition prescribed at $x = 10$

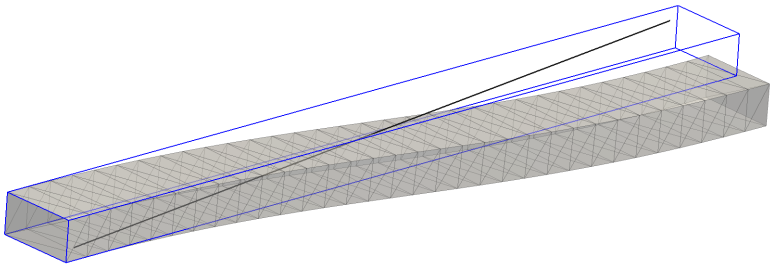

(a) Perspective view.

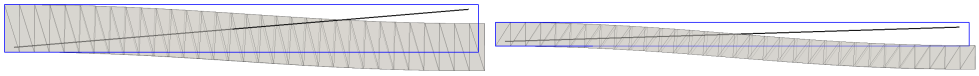

(b) Top view.

(c) Lateral view.

Figure 4.10: Deformed shape of prismatic bar with diagonal fiber

Figure 4.11 shows the final configuration and the stress of the fiber for the problems solved using the 3DFEM approach. It can be observed that the bar displaces in all three directions (x, y, z).

The same parametric studies presented in Secs. 4.2.2, 4.2.3, and 4.2.4 are reported in Figs. 4.12, 4.13, and 4.14, respectively. The axial displacements reported in these figures are computed at node *D* shown in Fig. 4.9. A very good agreement between the GFEM-mERS and the 3DFEM reference solution is again observed in all cases.

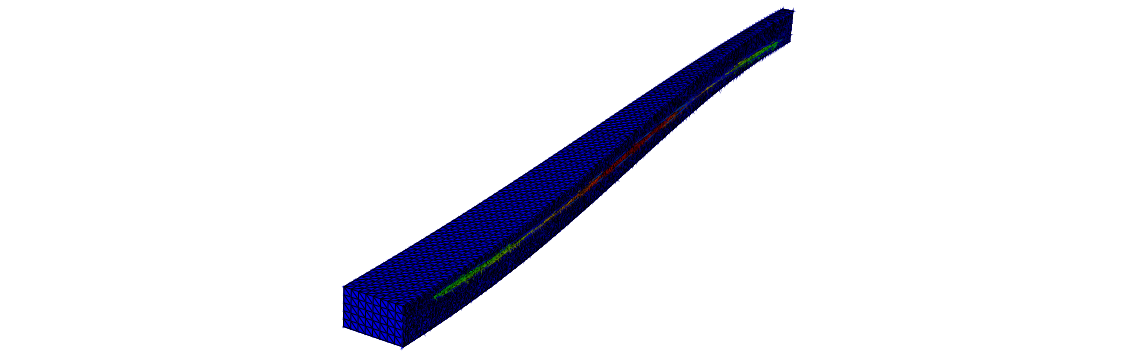

(a) Perspective view.

(b) Top view.

(c) Lateral view.

Figure 4.11: Deformed shape of prismatic bar with diagonal fiber (3DFEM reference solution)

4.3.1 Modulus of elasticity of the fiber

The problem is performed changing gradually the modulus of elasticity E_f (N/mm^2) of the fiber. It can be observed that as the stiffness of the fiber increases, the overall displacement of the composite reduces. Figure 4.12 compares mERS and 3DFEM results.

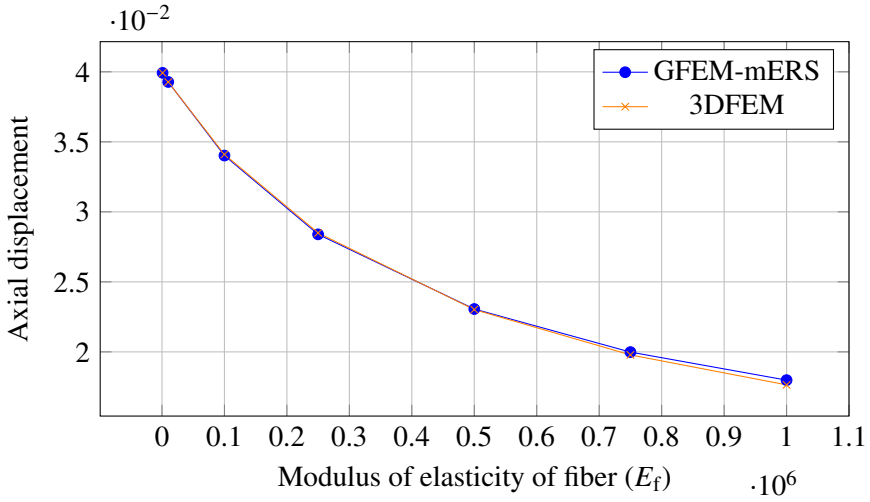

Figure 4.12: Axial displacement at the right end of the fiber-reinforced bar shown in Fig. 4.9 as a function of E_f

4.3.2 Cross section area of the fiber

This section studies how the area of the fiber A_f (mm^2) affects the displacement. As A_f increases the displacement of the problem reduces. Figure 4.13 compares the results mERS and 3DFEM for displacement at the bottom of the problem.

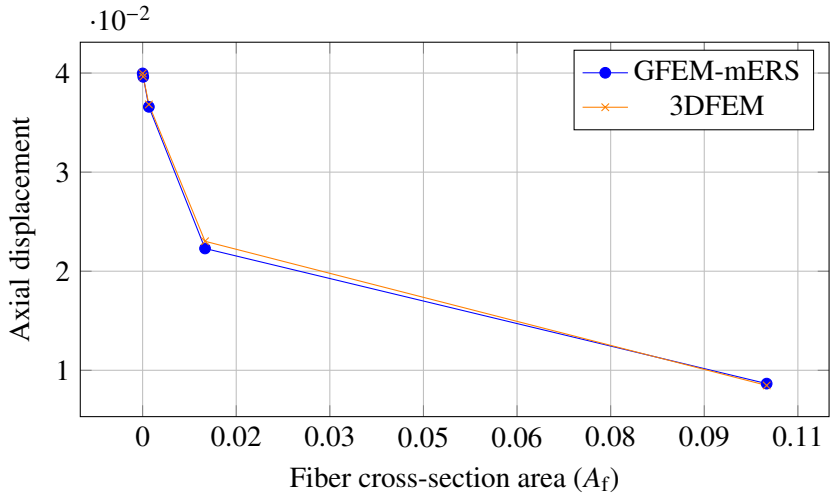

Figure 4.13: Axial displacement at the right end of the fiber-reinforced bar shown in Fig. 4.9 as a function of A_f.

4.3.3 Bond stiffness matrix-fiber

Bond stiffness K_b (N/mm^3) is gradually increased. Small K_b means soft interaction between fiber and matrix. Large K_b means strong interaction between materials.

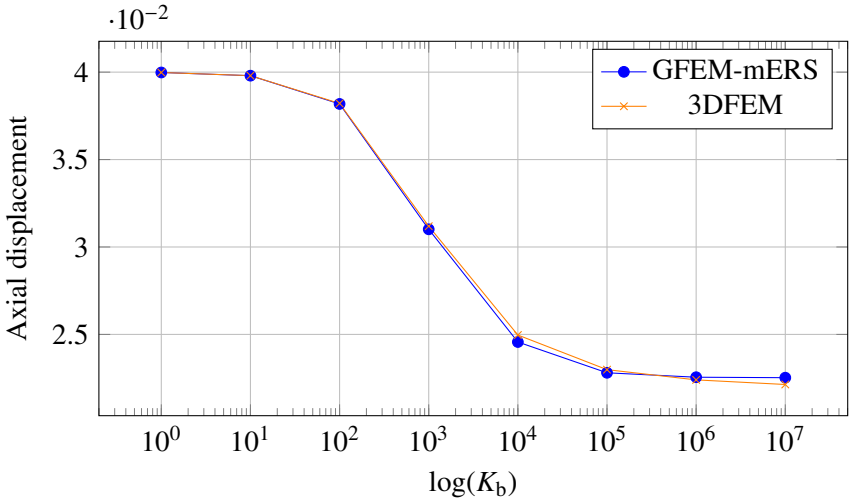

Figure 4.14: Axial displacement at the right end of the fiber-reinforced bar shown in Fig. 4.9 as a function of K_b

4.3.4 Convergence study

This section presents a convergence study of the GFEM-mERS using the prismatic bar shown in Fig. 4.9. Both the h- and p-version of the method are considered. In the first case a sequence of linear tetrahedral meshes is adopted. The mesh is refined only in the x-direction. They are created from hexahedral elements as described earlier. A mesh in this sequence is denoted as $n \times 1 \times 1$, where n is the number of hexahedral elements in the x-direction used to generate the mesh of tetrahedrons. The mesh $8 \times 1 \times 1$ is shown in Fig. 4.9. In the case of the p-version, the tetrahedral mesh $4 \times 1 \times 1$ is adopted and the polynomial order of the 3D GFEM shape functions is increased from $p = 1$ to $p = 4$. These GFEM shape functions are defined using a linear tetrahedral partition of unity and enrichment functions of polynomial degree 0, 1, 2, 3, respectively. The enrichment is isotropic meaning that the same polynomial order is used in all directions. Two-node linear elements are used for the mERS elements in all cases. The reference solution is again taken as the 3DFEM solution described earlier. The error of the GFEM-mERS is computed using the discrete L^2-norm

$$e^r(u_x) := \frac{\| e_x \|_{L^2}}{\| \breve{u}_x \|_{L^2}} = \frac{\sqrt{\sum_{i=a,b,c,d}(u_{xi} - \breve{u}_{xi})^2}}{\sqrt{\sum_{i=a,b,c,d}(\breve{u}_{xi})^2}}, \tag{4.2}$$

The term $u_{xi}, i = a, b, c, d$, is the component of the GFEM-mERS displacement in the x-direction, evaluated at vertex nodes A, B, C, D shown in Fig. 4.9, and $\breve{u}_{xi}, i = a, b, c, d$, are the corresponding 3DFEM reference values. Table 4.1 shows the results for the h-version of the GFEM-mERS. The relative error is computed using Eq. 4.2. Table 4.2 reports the results for the p-version of the GFEM-mERS. They show that the GFEM-mERS converges to the 3DFEM with mesh refinement or enrichment – the relative error is 0.15% and 0.07% for the last row in these tables. This indicates that the assumptions of the fiber-matrix model presented in Chapter 2 hold for the problem shown in Fig. 4.9.

Table 4.1: Displacements computed with the *h*-version of the GFEM-mERS. The first column lists the number of elements in the longitudinal direction of the bar. Column DOFs lists both matrix (GFEM) and fiber (mERS) degrees of freedom

$n\times1\times1$	u_{xa}	u_{xb}	u_{xc}	u_{xd}	DOFs	e^r [%]
4	0.0230	0.0234	0.0232	0.0230	73	18.8
8	0.0240	0.0243	0.0242	0.0239	133	15.5
16	0.0255	0.0257	0.0257	0.0254	251	10.3
32	0.0269	0.0271	0.0270	0.0269	491	5.40
64	0.0280	0.0281	0.0281	0.0280	965	1.65
128	0.0284	0.0286	0.0286	0.0283	1919	0.15

Table 4.2: Displacements computed with the *p*-version of the GFEM-mERS on a $4\times1\times1$ tetrahedral mesh. The first column lists the polynomial order of the 3D GFEM shape functions. Column DOFs lists both matrix (GFEM) and fiber (mERS) degrees of freedom

p	u_{xa}	u_{xb}	u_{xc}	u_{xd}	DOFs	e^r [%]
1	0.0230	0.0234	0.0232	0.0230	73	18.8
2	0.0266	0.0272	0.0271	0.0266	253	5.78
3	0.0280	0.0283	0.0283	0.0282	613	1.15
4	0.0284	0.0286	0.0286	0.0283	1213	0.07

Figure 4.15 shows the nodal values of the GFEM-mERS solution versus the number of degrees of freedom for both the *h*- and *p*-version. It can be observed that the *p*-version converges quicker than the *h*-version. One reason for this is that the number of fiber DOFs does not increase in the case of the *p*-version. In contrast, new sub-fiber elements are created as the mesh is refined.

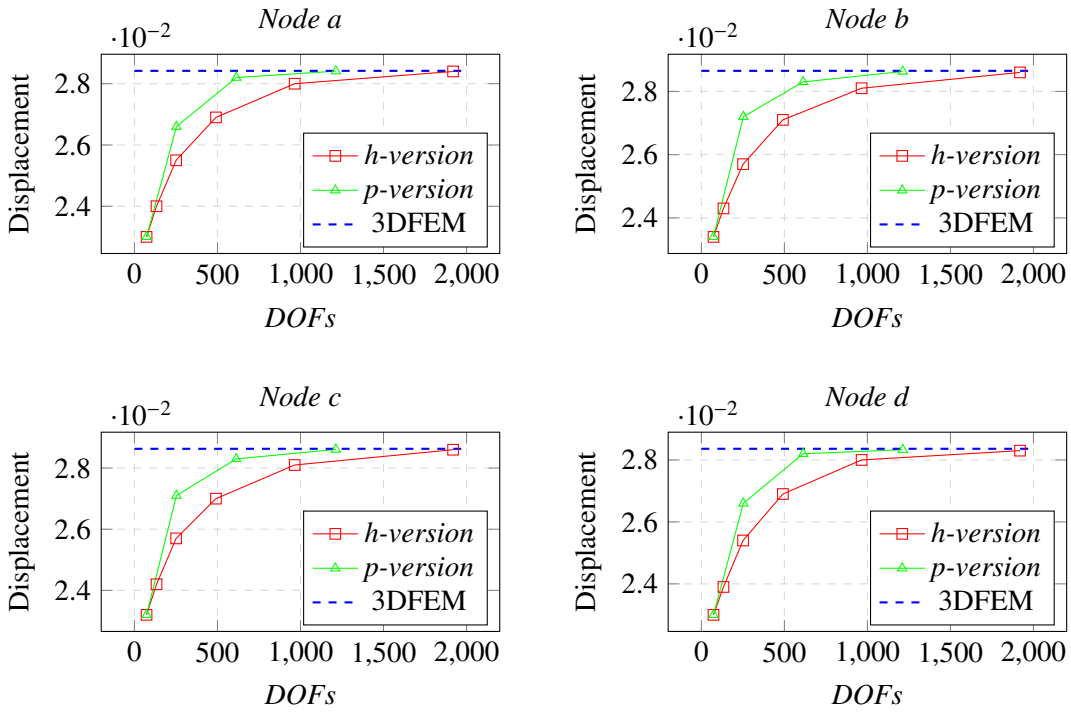

Figure 4.15: Convergence of the *h*- and *p*-version of the GFEM-mERS. The *h*-version adopts linear shape functions and the *p*-version adopts GFEM shape functions of degree $p = 1, 2, 3, 4$. The horizontal lines labeled 3DFEM correspond to the reference value computed with a 3D FEM model

The process of sub-fiber creation is illustrated in Fig. 4.16. As shown in that figure, every time a fiber crosses a 3D element, a new sub-fiber is generated. As a result, the ratio between the number of fiber and 3D DOFs is much higher in the *h*-version than in the *p*-version. These ratios are listed in Tabs. 4.3 and 4.4 for the *h*-version and the *p*-version, respectively. It is noted that the original ERS cannot be used with high-order approximations for the matrix displacement as explained at the end of Sec. 3.3.1. Such limitation is removed in the proposed mERS (cf. Sec. 3.3.2).

Table 4.3: Ratio between the number of fiber and matrix DOFs for the *h*-version of the GFEM-mERS

$n \times 1 \times 1$	Fiber DOFs	Matrix DOFs	$\frac{\text{Fiber DOFs}}{\text{Matrix DOFs}}$ [%]
4	13	60	21.67
8	25	108	23.15
16	47	204	23.04
32	95	396	23.99
64	185	780	23.72
128	371	1548	23.97

Table 4.4: Ratio between the number of fiber and matrix DOFs for the p-version of the GFEM-mERS

p	Fiber DOFs	Matrix DOFs	$\frac{\text{Fiber DOFs}}{\text{Matrix DOFs}}$ [%]
1	13	60	21.67
2	13	240	5.42
3	13	600	2.17
4	13	1200	1.08

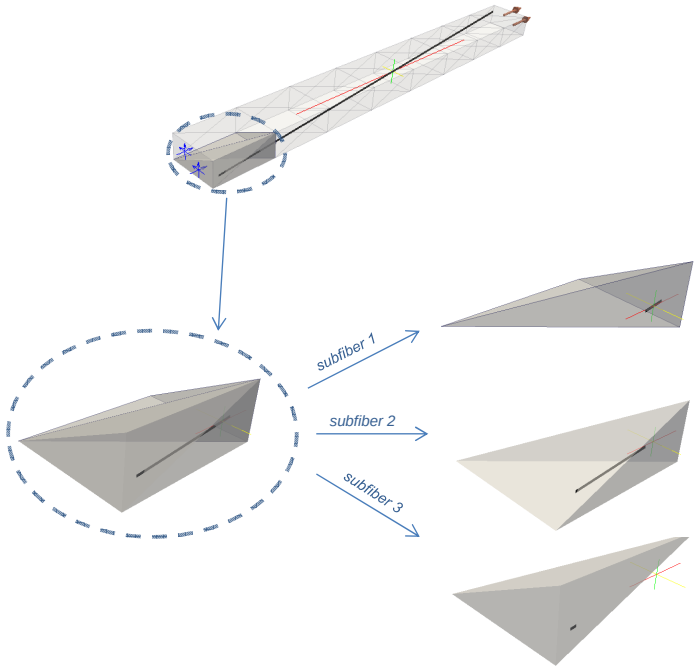

Figure 4.16: Process of creating sub-fibers in a 3D GFEM mesh. One sub-fiber is created for each tetrahedral element intersected by the fiber. This leads to an increase in fiber DOFs with refinement of the 3D mesh

4.4 Prismatic tensile specimen with a pre-defined crack

The cracked prismatic tensile specimen shown in Fig. 4.17 is analyzed in this section using the 3D GFEM-mERS. The predefined crack is at the middle plane of the specimen. A single fiber bridges the crack faces. This problem was proposed and solved in Kang et al. [20] using a lattice method. The following parameters are adopted, with consistent units: Modulus of elasticity of the matrix $E_m = 2.0 \times 10^4\ N/mm^2$; Poisson's ratio of the matrix $\nu = 0.2$; Modulus of elasticity of the fiber $E_\mathrm{f} = 6.0 \times 10^4\ N/mm^2$; Area of the fiber $A_\mathrm{f} = 3.2 \times 10^{-5}\ mm^2$; Fiber length $L_\mathrm{f} = 1.0\,m$; Matrix-fiber bond stiffness $K_\mathrm{b} = 5.0 \times 10^4\ N/mm^3$; Magnitude of traction prescribed at end faces of the specimen $\sigma = 600.0\ N/mm^2$. It is noted that the maximum load applied in the simulations reported in Kang et al. [20] is higher than the one adopted here (leading therefore

to a nonlinear load-displacement response in Kang et al. [20], while the specimen remains linear elastic for the maximum load adopted here. The specimen thickness is $L_f/30\ m$. The goal of this example is to demonstrate that the mERS combined with the GFEM is able to model a cracked domain with a fiber bridging the crack faces.

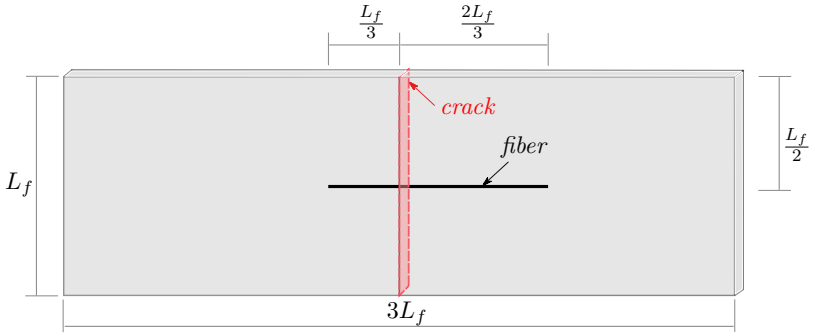

Figure 4.17: Prismatic tensile specimen with a pre-defined crack.

The GFEM-mERS solution is compared with a reference 3D standard FEM solution (denoted 3DFEM). Figure 4.18 shows a zoom in at the FEM mesh near the fiber-matrix interface. A very refined 3D mesh has to be used in order to have a conforming discretization at the interface leading to a model with 265,905 DOFs.

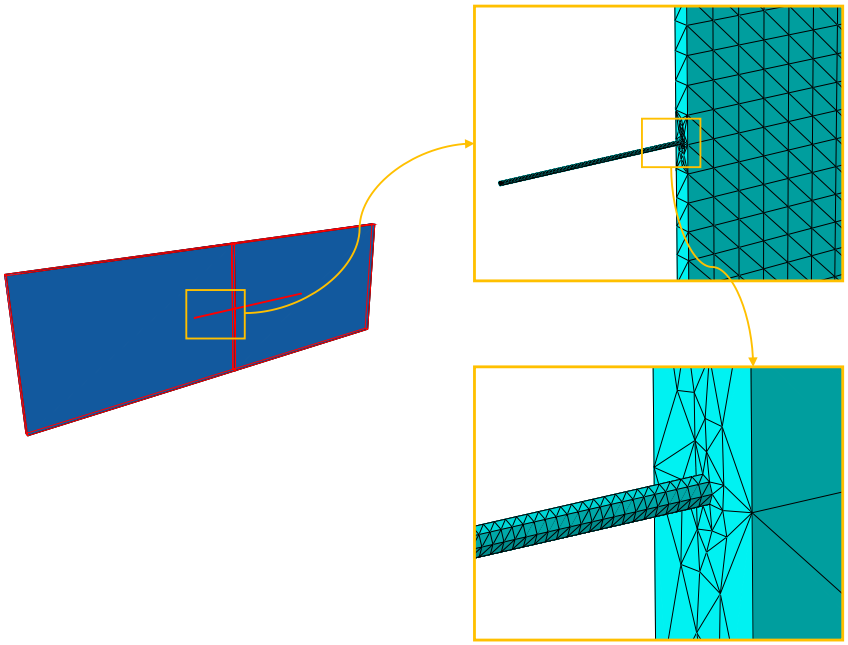

Figure 4.18: Reference 3D standard FEM model with zoom in showing the FEM mesh at the fiber-matrix interface

Figure 4.19 shows a 2D schematic of the GFEM discretizations adopted in this section. A 2D mesh is shown in the figure for simplicity, the actual problem is solved using the tetrahedral meshes shown in Fig. 4.21. It is noted that the crack is inside matrix elements and is represented by a Heaviside enrichment function (3.3), as described in Chapter 3. Furthermore, the crack surface intersects a sub-fiber element. This configuration is the most challenging case in terms of fiber description since the discontinuity of the displacement field is inside of both the matrix and sub-fiber element. The numerical integration over cracked 3D elements is performed using sub-element division as described in [67]. The 1D integration over sub-fibers cut by the crack (a single one in this problem) is performed using a Simpson quadrature rule [68] with 21 points. This is required to handle the discontinuity of the 3D GFEM shape functions at the point of intersection between the fiber and the crack surface. Since this is a 1D integration, its cost is small compared with the cost of the integration over the 3D domain. Sub-division of the fiber for numerical integration can also be used but it is not adopted in this research.

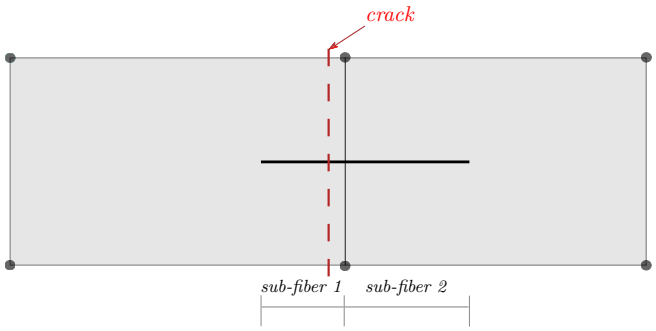

Figure 4.19: Schematic showing the location of the crack relative to matrix and sub-fiber elements. The left sub-fiber bridges the crack faces

Linear tetrahedral elements enriched with the Heaviside function (3.3) are adopted for matrix discretization, and linear 1D elements are used for sub-fiber elements. Three levels of refinement are used: level 1 ($3 \times 1 \times 2$), level 2 ($5 \times 3 \times 2$) and level 3 ($7 \times 5 \times 2$) as shown in Fig. 4.20.

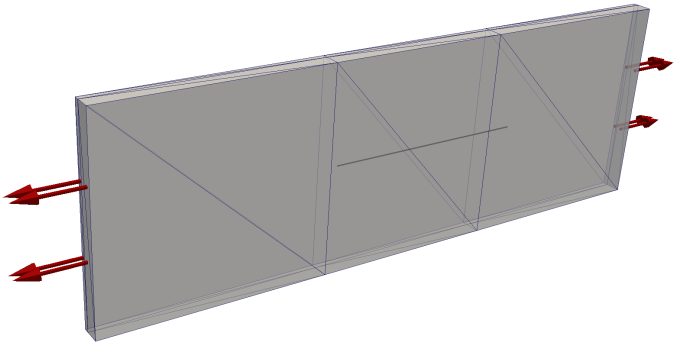

(a) Mesh refinement level 1

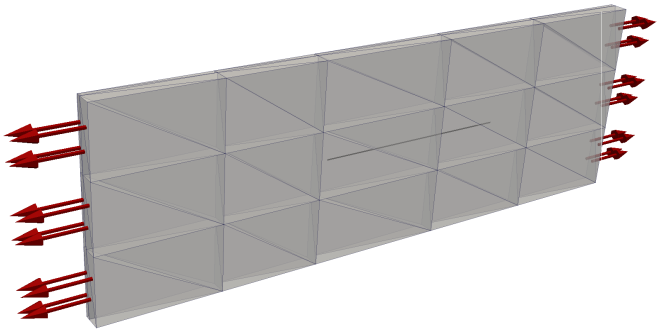

(b) Mesh refinement level 2

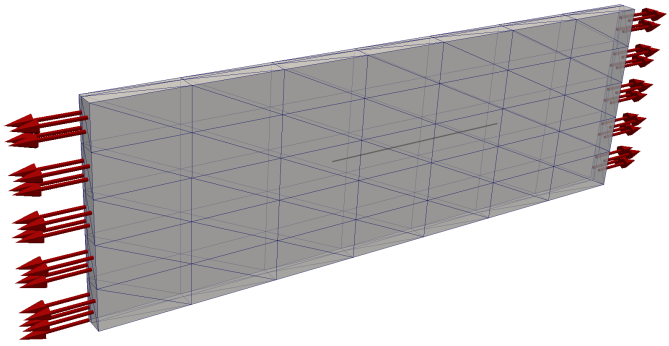

(c) Mesh refinement level 3

Figure 4.20: GFEM-mERS meshes used in convergence study. The red arrows represent the prescribed tractions

Figure 4.21 shows a representative GFEM-mERS mesh adopted to solve this problem with the corresponding boundary conditions. In all cases, there are two layers of elements in the direction normal to the plane of the specimen and nodes are positioned in order to have crack and fiber reproducing the most challenging case in terms of fiber description as schematically shown in Fig. 4.19.

As described earlier, the crack cuts both the 3D and 1D elements. The red arrows represent the prescribed tractions. Point Dirichlet boundary conditions are prescribed in order to prevent rigid body motions. It is noted that even the finest GFEM mesh is much coarser than the one shown in Fig. 4.18 for the reference 3DFEM model.

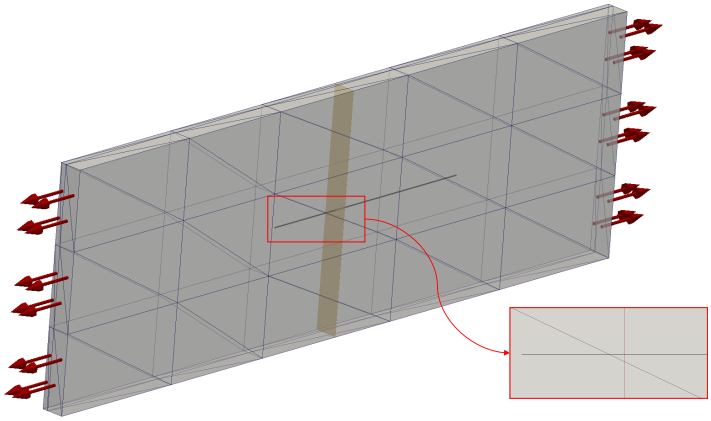

Figure 4.21: GFEM-mERS mesh (refinement level 2) used in convergence study. The red arrows represent the prescribed tractions. Detail shows the most challenged case in terms of fiber description as schematically described in Fig. 4.19

Table 4.5 shows the computed pullout displacement of sub-fiber 1 for the prescribed traction $\sigma = 600.0$. The pullout is taken as the slip displacement at the left end of sub-fiber 1. This same assumption is adopted in [20]. The table lists the GFEM-mERS results for the three meshes adopted and the relative difference with respect to the 3DFEM reference solution. The GFEM-mERS solution clearly approaches the reference values as the mesh is refined even though the finest GFEM-mERS mesh is much coarser than the one adopted in the 3DFEM model. The relative error in this case is 2.49%, which is small but larger than in the previous problems. This is likely caused by the presence of the crack which leads to 3D effects not present in the previous problems.

Table 4.5: Pullout of sub-fiber 1 computed with GFEM-mERS and relative difference with respect to the 3DFEM reference solution

Mesh	DOFs	Pullout ($\cdot 10^{-6}$)	Rel. Diff. [%]
1	77	0.9818	18.05
2	223	1.1279	5.85
3	441	1.1682	2.49

4.5 Fiber-reinforced compact tension specimen

This example consists of a composite specimen with discrete glass fiber tows in an epoxy matrix. This problem was proposed and solved experimentally by Jones [69]. Other examples of tow-level tests can be found, for example, in Zhao and Botsis [70] and in Zhang et al. [71]. The Compact Tension (CT) specimen geometry is based on the ASTM D5045 Standard. Fibers tows are perpendicular to the crack plane as shown in Fig. 4.22. Each tow is idealized as a single fiber in the computational models adopted here. Three variations of the specimen shown in Fig. 4.22 are studied in this section: (1) No fibers (denoted hereafter as the unreinforced specimen); (2) One-fiber specimen, with the fiber located 5 *mm* ahead of the crack front; (3) Five-fibers specimen, with fibers 5 *mm* apart from each other and 5 *mm* ahead of the crack front, as shown in Fig. 4.22. The goal of considering these three cases is to show whether the proposed GFEM-mERS can accurately capture the change in stiffness of the specimen as fibers are embedded in the matrix.

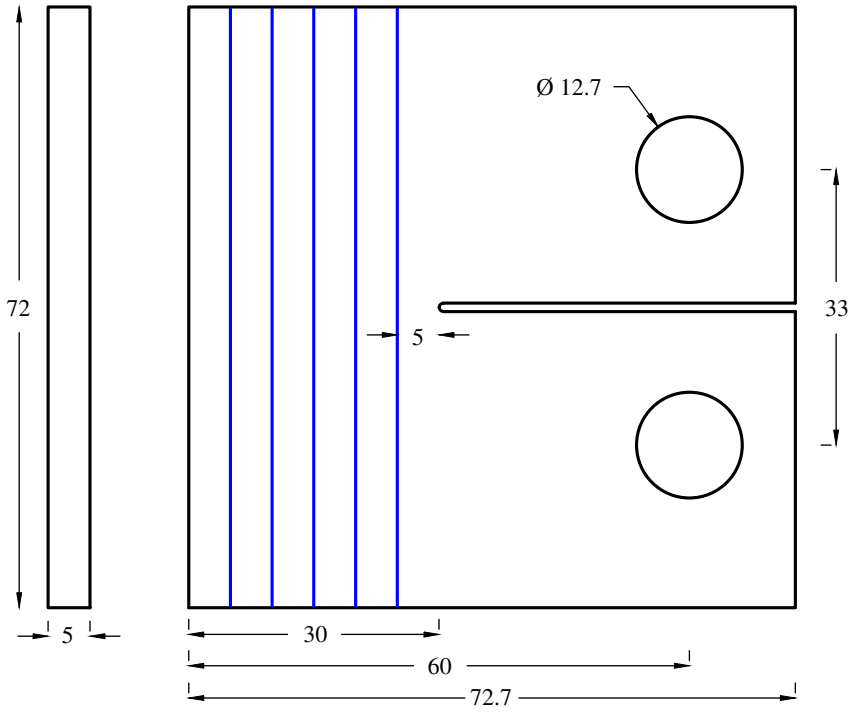

Figure 4.22: Compact Tension specimen with five fiber tows embedded in an epoxy matrix. All dimensions are in mm

The experiment performed by Jones [69] consisted of propagation and healing of fractures. Here, however, only a static fracture is considered. The GFEM-mERS results are compared to experimental data from [69] up to the load that leads to a stress intensity factor at the crack front equal to the fracture toughness of the matrix as described below.

The following parameters are adopted for this problem. Modulus of elasticity of the epoxy matrix $E_{\mathrm{m}} = 0.82\ GPa$; Poisson's ratio of the matrix $\nu = 0.35$; Modulus of elasticity of fibers $E_{\mathrm{f}} = 72.4\ GPa$; Area of each fiber tow (type 158B-AA-675) $A_{\mathrm{f}} = 0.33\ mm^2$; Matrix-fiber bond stiffness $K_{\mathrm{b}} = 1.0 \times 10^4\ N/mm^3$; and Fracture toughness $K_{\mathrm{Ic}} = 20\ N/\sqrt{mm}$. The material properties of matrix, fiber and interfacial bond are obtained from Miller-Stephenson [72], Owens Corning [9], Blaiszik [73], and Jones [69].

The GFEM-mERS solutions are also compared with 3D standard FEM results (denoted 3DFEM). The experimental setup and the numerical models are illustrated in Fig. 4.23. Fig. 4.24 shows the 3DFEM discretization of the fibers and CT specimen. Matrix and fibers are meshed using tetrahedral elements and the fiber-matrix bond is modeled using cohesive elements. The fiber and matrix meshes match each other along their interfaces. The crack is discretized using a mesh with double nodes along the crack surface.

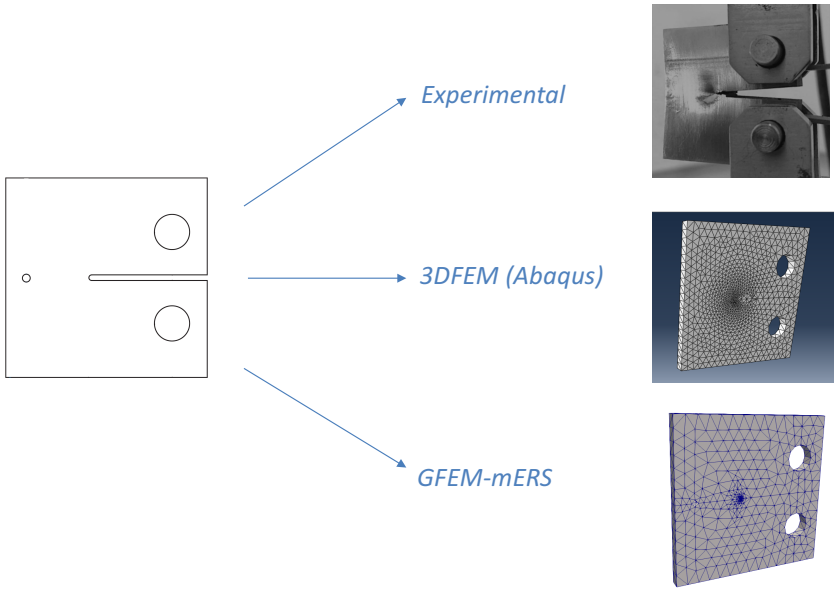

Figure 4.23: Experiment from [69], 3DFEM, and GFEM-mERS schematic models

The fibers and the matrix are independent Abaqus *Parts* of the problem. Each *Part* of the geometry is assembled into the *Model* as a second step in Abaqus. Therefore, the final model is composed by the two components. As an example, Fig. 4.24 depicts these two components (fibers and matrix) for the specimen.

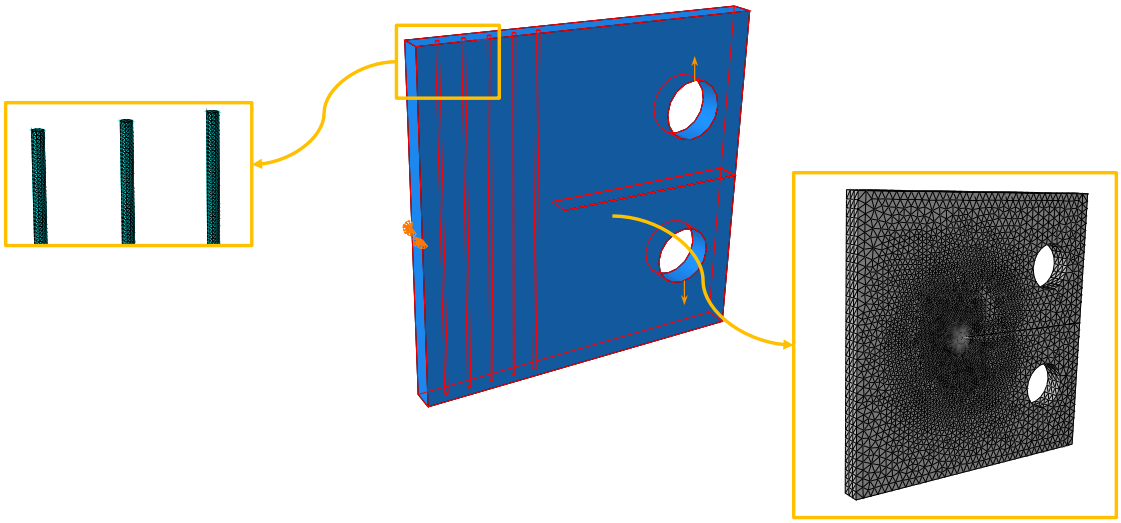

Figure 4.24: Reference 3D standard FEM model solved with Abaqus [66]

After creating the geometry and setting up the material properties, boundary conditions are applied. Nodal Dirichlet boundary conditions are prescribed at the specimen openings. Additional point constraints are used to prevent rigid body motions. Other approaches to model the boundary conditions at the specimen openings are available in the literature [74, 75]. Numerical experiments not reported here show that they lead to nearly identical results as those from the adopted approach. After prescribing the boundary conditions, the tetrahedron mesh of the matrix domain is refined. Fiber and matrix meshes are conforming along their interface. Abaqus cohesive elements COH3D4 are used at the interface between 3D matrix and fiber elements. The crack is modeled using double nodes in order to represent the displacement discontinuity across the crack surface. The singular behavior at the crack front is approximated using a highly refined mesh around the crack front.

Figure 4.25 shows the GFEM-mERS discretization of the specimen with five embedded fibers. Quadratic tetrahedral elements enriched with the Heaviside and singular functions defined in Eqs. 3.3 and 3.5, respectively, are used to discretize the cracked specimen. A convergence study not shown here was performed to verify that the results presented in this section are not affected by GFEM-mERS discretization errors. The crack surface is defined using an explicit triangulation as shown in Fig. 4.25. This triangulation has

no degrees of freedom and is defined independently of the 3D GFEM mesh [76]. Linear 1D elements are used for sub-fiber elements. Recall that a sub-fiber is created from the intersection between a fiber and a 3D element as illustrated in Fig. 4.16.

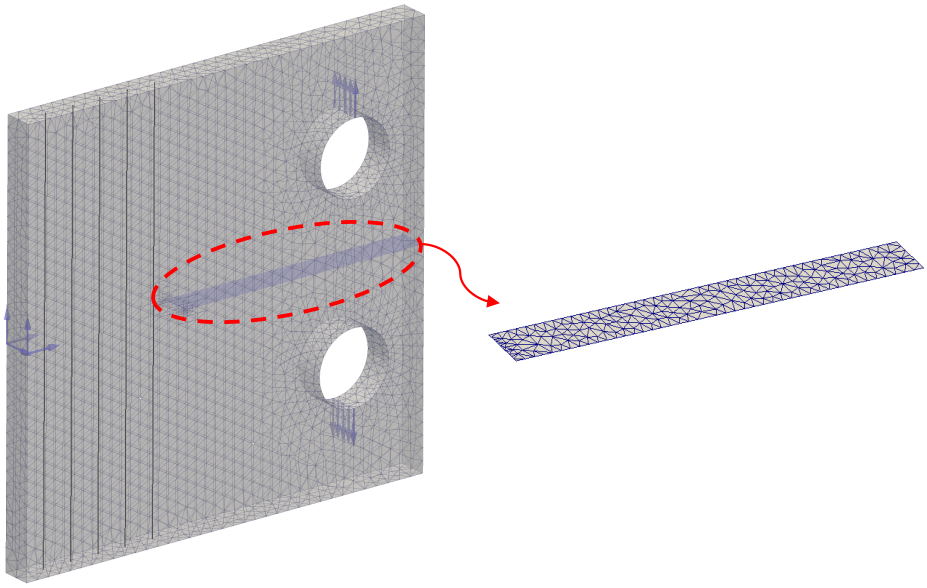

Figure 4.25: GFEM discretization of specimen. Fibers are discretized with mERS and an explicit representation of the crack surface is adopted

The prescribed nodal displacements at the openings of the CT specimen are shown in Fig. 4.25. Nodal displacements used to prevent rigid body motions are also shown in the figure. Table 4.6 lists the number of DOFs of the 3DFEM and GFEM-mERS discretizations of the specimens with 0, 1 and 5 fibers – configurations (1), (2), (3), respectively, in the table.

Table 4.6: Number of DOFs of the 3DFEM and GFEM-mERS discretizations of the specimens with 0, 1, and 5 fibers

Configuration	GFEM-mERS DOFs	3DFEM DOFs
1	265,932	695,490
2	270,725	1,090,434
3	287,049	1,108,848

4.5.1 Computation of critical load

This section presents the approach used to find the CT specimen load that leads to a Mode I stress intensity factor (K_{I}) at the crack front equal to the fracture toughness of the matrix K_{Ic}. This is done by first finding, as described below, the magnitude of the prescribed displacement D_c that leads to $K_{\mathrm{I}} = K_{\mathrm{Ic}}$ at the center of the crack front. Next, displacements with magnitude D_c are prescribed at the openings of the specimen and the magnitude of the resultant load at each opening (Fc) is computed using both GFEM-mERS and 3DFEM models. These results are compared with experimental data provided by Jones [69].

Computation of D_c

The magnitude of the prescribed displacement that leads to $K_{\mathrm{I}} = K_{\mathrm{Ic}}$ at the center of the crack front is found as follows. The problem is solved with the GFEM-mERS for two values of the magnitude of the prescribed displacements at the openings of the specimen: D_A and D_B. Let $K_{\mathrm{I},A}$ and $K_{\mathrm{I},B}$ be the corresponding values of K_{I} at the center of the crack front.

The magnitude of the prescribed displacement D_c that leads to $K_{\mathrm{I}} = K_{\mathrm{Ic}}$ is then given by

$$D_c = c_1 + c_2 K_{\mathrm{Ic}}. \tag{4.3}$$

Parameters c_1 and c_2 are found using the linear relation between K_{I} and the magnitude of the applied displacement. This leads to the following system of equations

$$\begin{bmatrix} 1 & K_{\mathrm{I},A} \\ 1 & K_{\mathrm{I},B} \end{bmatrix} \begin{Bmatrix} c_1 \\ c_2 \end{Bmatrix} = \begin{Bmatrix} D_A \\ D_B \end{Bmatrix}. \tag{4.4}$$

Displacement magnitude D_c for the three specimen configurations (1), (2), and (3) described earlier are listed in Tab. 4.7. The GFEM-mERS results agree well with the experimental data. The relative errors for specimen configurations (1), (2), and (3) are 1.08%, 3.78%, 2.72%, respectively.

Table 4.7: The magnitude of the prescribed displacement $D_c(\cdot 10^{-6}\text{m})$ that leads to $K_\text{I} = K_\text{Ic}$ at the center of the crack front. Experimental results are from [69]

Configuration	Experiment	GFEM-mERS
1	380.9	385.0
2	372.9	387.0
3	338.8	348.0

Computation of critical load Fc

Displacements with magnitude D_c computed with the approach described above are prescribed at the openings of the GFEM-mERS and 3DFEM models. The magnitude of the resultant reaction forces (F_c) at each opening of the three specimen configurations are listed in Tab. 4.8. Experimental data provided by Jones [69] is also listed in the table.

Table 4.8: Critical loads F_c(N) for analyzed models. Experimental results are from [69]

Configuration	Experiment	GFEM-mERS	3DFEM
1	73.1	75.2	76.5
2	68.3	77.0	81.6
3	85.6	95.0	101.5

The GFEM-mERS and 3DFEM results are also compared with the experimental results of Jones [69] in Figs. 4.26(a)–(c). They show the load-displacement curves for the three specimen configurations. In all simulations, displacement with magnitude D_c given in Tab. 4.7 are applied as boundary conditions. Reactions at nodes with prescribed displacements are extracted as a post-processing result. This procedure is analogous to the one adopted in the experiments reported in [69]. The experimental curves exhibit a linear relation between load and displacement until the first peak load. After that point, the crack rapidly advances (for all three specimen configurations). Since only static crack behavior is considered in this research, only the first part of the experiment is taken into account in our analysis, i.e., until the peak load is reached.

Figure 4.26(a) shows nearly identical results for the GFEM-mERS and 3DFEM. This is consistent with the results shown in Tab. 4.8 for the unreinforced specimen (Configuration 1). Figure 4.26(b) shows the results for the specimen with a single fiber tow. The peak load is higher than in the unreinforced specimen. Numerical and experimental results are similar. Both numerical methods predict a higher peak load than the experimental value. The peak load for the 3DFEM model is 5.97% higher than for the GFEM-mERS.

Identical results are not expected since the fiber is represented using 3D elements in the 3DFEM model while a 1D truss is used the GFEM-mERS model.

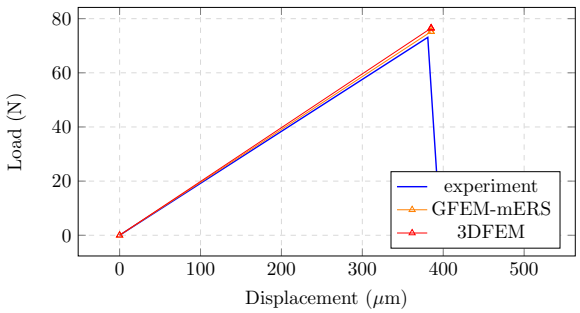

(a) Unreinforced specimen.

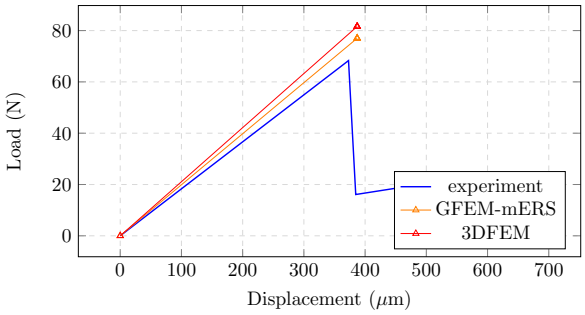

(b) Specimen with one fiber.

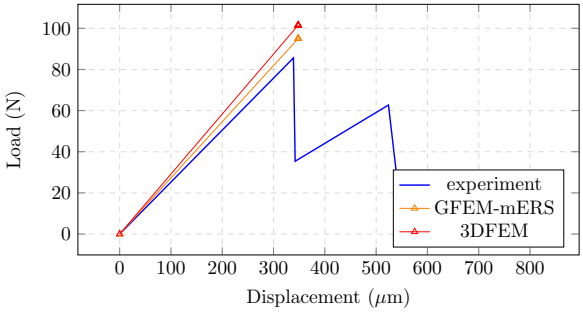

(c) Specimen with five fibers.

Figure 4.26: Load-displacement curve for the specimen with zero, one and five fibers. Experimental results are from [69]

Figure 4.26(c) shows the results for the specimen with five fiber tows. Both numerical models capture the effect of the added fiber tows, predicting a higher peak load than in the specimen with a single fiber. As in the previous case, both numerical methods predict a higher peak load than the experimental value. The peak load for the 3DFEM model is 6.84% higher than for the GFEM-mERS. As in the case with one fiber, identical results are not expected since the fiber is represented using 3D elements in the 3DFEM model while a 1D truss is used the GFEM-mERS model. The observed difference in peak load predicted by 3DFEM and GFEM-mERS models is further discussed later .

4.5.2 Compact tension specimen with fibers bridging crack faces

In this section, the fiber-reinforced specimen analyzed in the previous section is modified such that the crack surface is intersected by two fibers. The crack front is now located 17.5 *mm* from the left face of the specimen as shown in Fig. 4.27(a). Two fiber directions are considered. In the first case, the fibers are perpendicular to the crack surface plane like in the previous section, leading to a Mode I deformation. The distance between fibers is the same as in the previous section (5 *mm*). In the second case, the fibers are inclined 112.5° relative to the crack surface as shown in Fig. 4.27(b). This leads to a mixed mode deformation of the specimen. The distance between the left face of the specimen and the bottom end of the fibers are: 18.0, 23.5, 29.0, 34.5 and 40.0 *mm*.

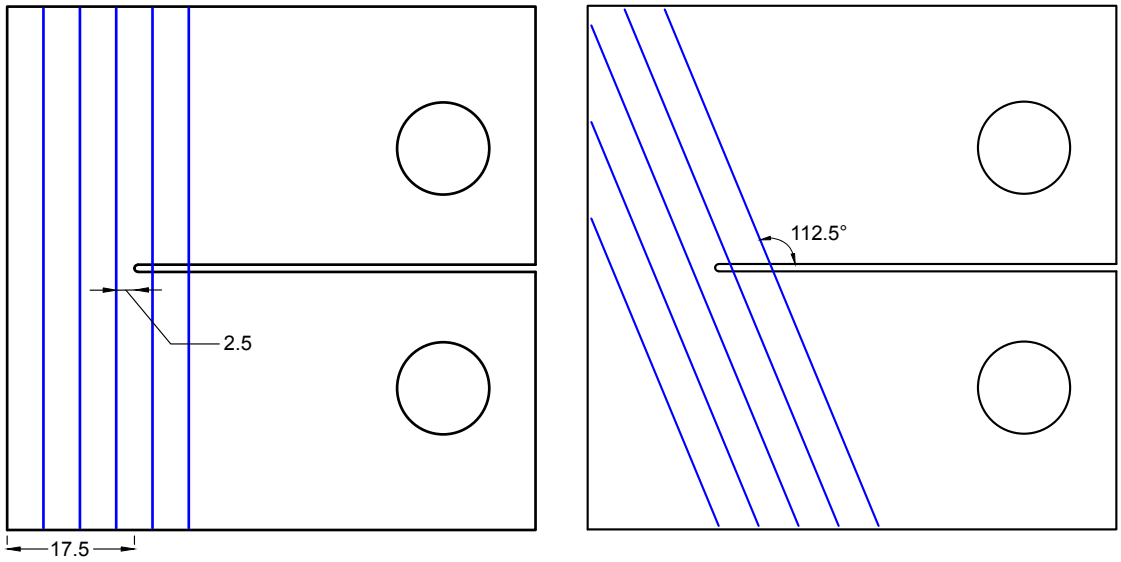

(a) Fibers perpendicular to the crack **(b)** Fibers inclined relative to the crack

Figure 4.27: Compact tension specimen with fibers bridging the crack faces. All dimensions are in mm

All material properties and dimensions are the same as in the previous section. The case of the specimen without fibers is also considered. The specimens are loaded with forces applied at nodes in the specimen openings. These are the same nodes shown in Fig. 4.25 subjected to prescribed displacements.

No experimental data is available for the specimens shown in Fig. 4.27. The GFEM-mERS results are compared with those provided by 3D standard FEM models. The 3DFEM model is similar to the one described in the previous section.

The Abaqus [66] geometry of the FEM model for unreinforced specimen, fibers perpendicular and inclined to the crack are shown in Fig. 4.28. Figure 4.29 depicts these two components (fibers and matrix) in details.

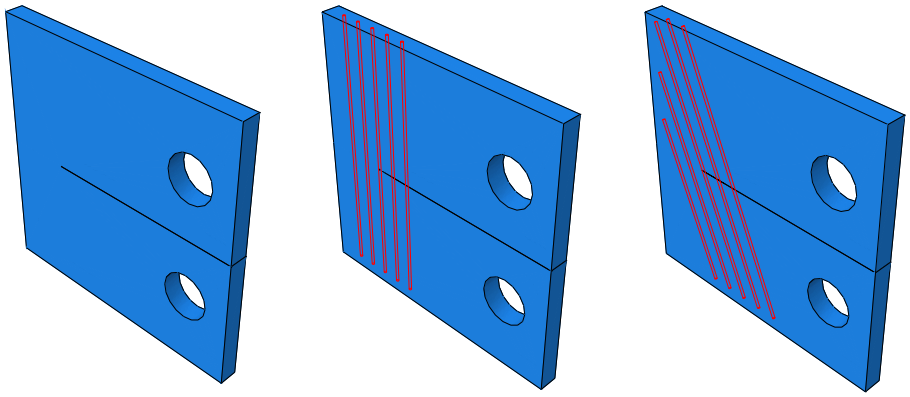

Figure 4.28: Abaqus Model of CT specimen with inclined fibers.

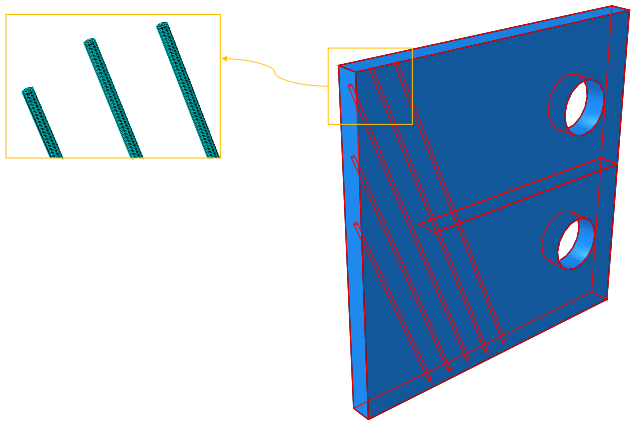

Figure 4.29: Three-dimensional FEM model of specimen with fibers inclined relative to the crack surface

Figure 4.30 shows the GFEM-mERS discretization of the specimen with vertical and inclined fibers, respectively. The same element types, approximation order and enrichment functions as in Sec. 4.5 are adopted.

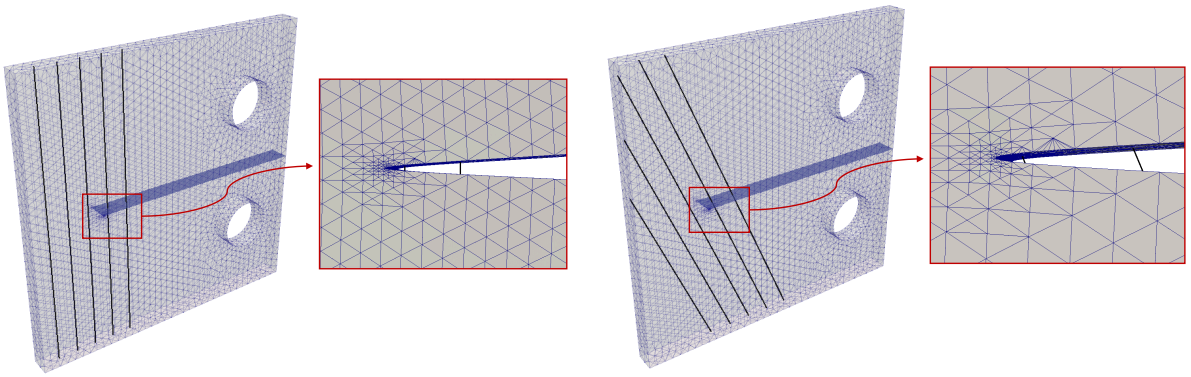

(a) Model with vertical fibers **(b)** Model with inclined fibers

Figure 4.30: GFEM-mERS discretizations of models with fibers bridging the crack faces. The deformed configurations show two fibers bridging the crack faces

Table 4.9 lists the displacement at a node in the specimen opening for the maximum prescribed load (50 N) and the relative difference with respect to the 3DFEM solution. The table lists results for the three fiber configurations considered: (1) No fibers; (2) Fibers perpendicular to the crack; (3) Fibers inclined relative to the crack. Load and displacement are prescribed and measured at the same point as in the previous problem – at the node with coordinates $(60.0,\ 58.85,\ 2.5)$.

Table 4.9: GFEM-mERS and 3DFEM displacement at a node in the specimen opening for the maximum prescribed load.

Specimen	GFEM-mERS displ. $(\cdot 10^{-6})$	3DFEM displ. $(\cdot 10^{-6})$	Rel. Diff. [%]
No fibers	605.32	606.01	0.11
Five inclined fibers	509.45	524.21	2.81
Five vertical fibers	461.33	482.06	4.30

The GFEM-mERS and 3DFEM results for the specimen without fibers are nearly identical. This shows that any difference in results for the specimens with fibers is due to the different models adopted for the fibers in GFEM-mERS and 3DFEM. The introduction of fibers in the specimens clearly increases their stiffness. The specimen with fibers perpendicular to the crack is stiffer than the one with inclined fibers as expected. In both cases, the GFEM-mERS and 3DFEM results are quite close, with the GFEM-mERS model being slightly stiffer than the 3DFEM. This is mainly due to the different approaches adopted to model the fiber-matrix interfaces. The 3DFEM model adopts a linear cohesive surface while the GFEM-mERS adopts a linear cohesive line. The difference between these two approaches is expected to decrease as the stiffness of the fiber-matrix interface is increased in both models. A higher matrix-fiber bond stiffness leads to no

slip between the matrix and the fibers. Thus the geometrical details of the interface become less important. To verify this hypothesis, the specimens are solved again using a very high bond stiffness – five orders of magnitude higher than the original K_b. The results are shown in Tab. 4.10. It can be observed that the GFEM-mERS and 3DFEM results for the very stiff matrix-fiber interfaces are closer than for the case of an interface that allows slip between the matrix and the fibers.

Table 4.10: GFEM-mERS and 3DFEM displacement at a node in the specimen opening for the maximum prescribed load

Specimen	GFEM-mERS displ. ($\cdot 10^{-6}$)	3DFEM displ. ($\cdot 10^{-6}$)	Rel. Diff. [%]
Five inclined fibers (compliant interface)	509.45	524.21	2.81
Five inclined fibers (stiff interface)	479.01	487.89	1.82
Five vertical fibers (compliant interface)	461.33	482.06	4.30
Five vertical fibers (stiff interface)	425.10	432.50	1.71

4.5.3 Computational cost and user time

This section presents the required computational cost and user time to solve the CT specimen with and without fibers using either the GFEM-mERS or the FEM. Problem size is taken as a proxy for the computational cost. Table 4.11 shows a comparison between problem size and user time for the 3DFEM and for the GFEM-mERS. The difference in problem size for 3DFEM compared to the GFEM-mERS is expected to grow further as the fiber volume fraction increases.

While computational time is important when comparing two methods, the cost of a simulation is often much lower than the cost of the user performing the simulation. Therefore the user time is also listed in Tab. 4.11 for both methods. In the table, "mesh generation" time is defined as the one that takes to generate the 3D FEM or the GFEM-mERS mesh for a problem. This includes, in the case of the FEM, the generation of a mesh fitting the crack surface and the fiber-matrix interfaces. In the case of the GFEM-mERS, the mesh needs only to fit the geometry of the CT specimen. Therefore the crack surface and fibers can be ignored at the time of mesh generation. Refinement around these features can be done as if they do not exist when solving the problem with the GFEM-mERS. In practice, the number and location of fibers change during the design process. Thus, Tab. 4.11 also includes the "mesh modification" time. This is defined as the time required to change a 3D FEM mesh to accommodate a different number of fibers or to change their location. As an example, this can represent the amount of time required to change the 3D FEM mesh for

the specimen with five vertical fibers to the one for the specimen with five inclined fibers. In the case of the 3DFEM, the mesh generation process often has to re-start from scratch when any of these changes happen, while in the GFEM-mERS the same user-generated mesh can be used to solve both problems – the change in fiber orientation or location does not require another user-defined mesh since it does not need to fit the fibers. Generating the 3DFEM mesh in Abaqus requires several iterations at regions where the matrix and fiber meshes do not fit well. Depending on the meshing parameters, like element type and mesh density, the mesh generator fails. Multiple trial and error iterations are often needed. The Abaqus mesh generator usually works well when the element size does not change quickly in the domain. Handling the local mesh refinements around each fiber is much more challenging.

Table 4.11 shows that the user time for mesh generation in the GFEM-mERS is at least one order of magnitude smaller than in the case of the FEM. This is the case since the mesh for GFEM-mERS does not have to handle the 3D fiber-matrix interface as in the case of the FEM. Furthermore, adding fibers to the model does not require additional user time in the case of the GFEM-mERS since the same user-defined mesh can be used for the problem with or without fibers.

Table 4.11: Problem size and user time for the GFEM-mERS and the 3DFEM. All times are in minutes. Missing entries correspond to negligible time

Specimen	DOFs	User time	
		Mesh generation	Mesh modification
No fibers 3DFEM	551,277	~40	~20
No fibers GFEM-mERS	302,493	~10	-
Five vertical fibers 3DFEM	576,291	~150	~120
Five vertical fibers GFEM-mERS	307,935	~10	-
Five inclined fibers 3DFEM	624,744	~150	~120
Five inclined fibers GFEM-mERS	325,092	~10	-

4.5.4 Local behavior study

The opening along the crack surface is examined in order to evaluate how the GFEM-mERS performs in the neighborhood of the region where fibers cross a discontinuity. Figure 4.31 shows the GFEM mesh used for the computations presented in this section. It is noted that the mesh is refined as it approaches the crack front in order to capture the behavior of the solution in this region. Refinement along the fiber directions is also performed and aims to capture the deformation of the matrix in the neighborhood of the

fibers. Although not presented in this chapter, a convergence study was performed to verify the accuracy of the adopted mesh. It is be noted that refinement along the fiber is important since the GFEM space is not enriched with functions able to approximate the behavior of the exact solution along the fibers. A study on the benefits of this class of enrichment can be found in [38, 77].

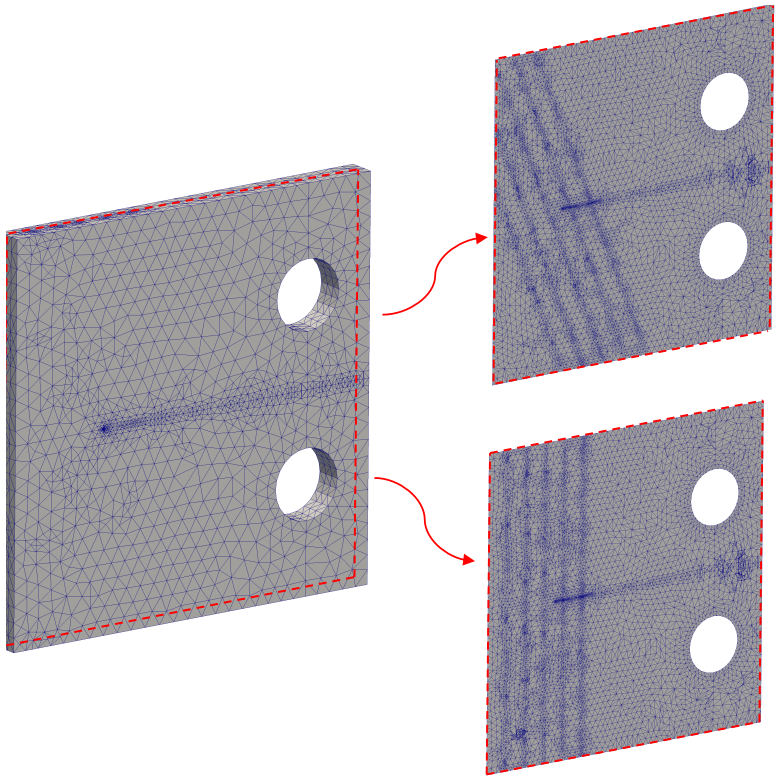

Figure 4.31: GFEM mesh for the compact tension specimen with fibers bridging the crack faces (left). Cuts showing the mesh refinement along the two fiber configurations considered in this section (right)

Figure 4.32 shows the magnitude of the crack opening along the centerline of the crack surface in the direction perpendicular to the crack front. This line coincides with the x-coordinate line. The blue curve in the figure represents the crack opening for the specimen without fibers. The full orange line represents the crack opening of the specimen with five vertical fibers, while the dashed line represents the 3DFEM for the same problem. The arrows in the figure show the location of the two fibers that cross the crack surface. From the results shown in the figure, it can be observed that the fibers affect not only the global behavior of the specimen (since the opening of the specimen is reduced, as demonstrated in previous sections), but more importantly, it also affects the displacements at a local level. Figure 4.32 shows small bumps near the location where the fibers cross the crack surface.

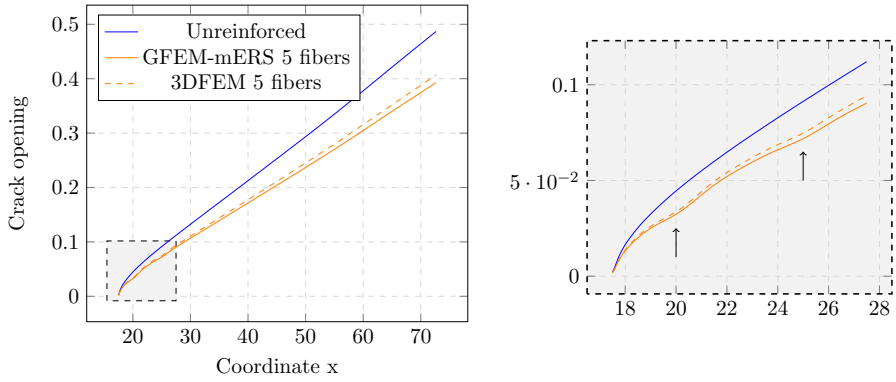

Figure 4.32: Magnitude of crack opening along the x-coordinate line for specimen with and without fibers.The arrows in the figure show the location of the two fibers that cross the crack surface

In order to study how the effect of fiber stiffness affects the crack opening, a series of simulations are performed varying this parameter. Figure 4.33 shows how the opening changes as the stiffness of the fiber increases. The blue and orange curves are the same as in Fig. 4.32. The green and purple curves correspond to cases of fibers with twice and three times, respectively, the stiffness of the fibers associated with the orange curve. It can be observed that as the stiffness of the fibers increase, the bump at the region where the fibers are located becomes more pronounced as expected.

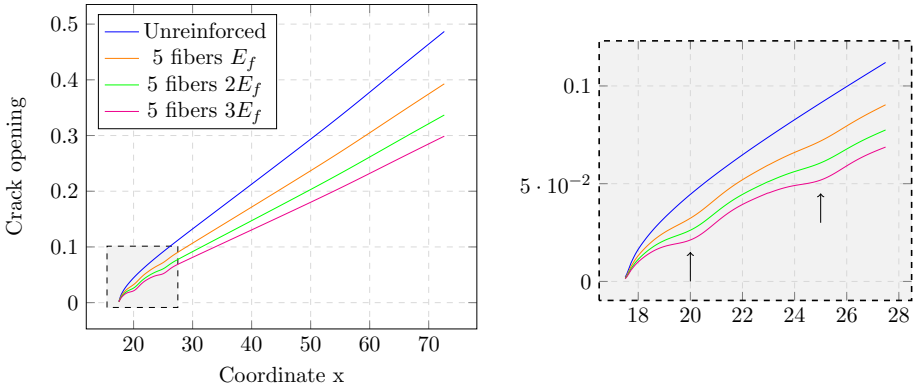

Figure 4.33: Magnitude of crack opening along the x-coordinate line for specimen with fibers of increasing stiffness

Figure 4.34 is analogous to Fig. 4.32 but with fibers inclined relative to the crack surface (same case as in Sec. 4.5.2). The bumps in the crack opening curve are less noticeable in this case.

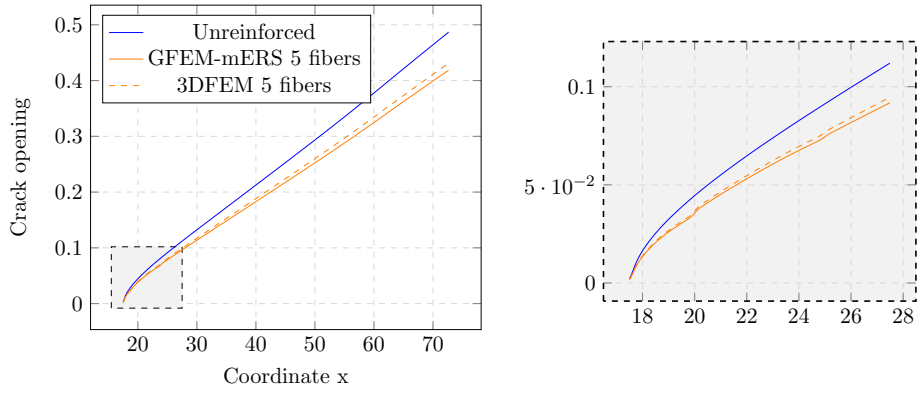

Figure 4.34: Magnitude of crack opening along the x-coordinate line for specimen with and without inclined fibers

4.5.5 Effect of fiber reinforcements on stress intensity factor

Stress Intensity Factors (SIFs) are fundamentally important parameters for linear elastic fracture mechanics. They are used to predict the crack growth speed, direction, and whether a crack will propagate under a given load. In this section, the effect of fiber reinforcements on the SIFs along the crack front of the CT specimen is investigated. SIFs extracted from GFEM-mERS solutions are compared with those provided by the 3DFEM model solved in Abaqus [66]. The Displacement Correlation Method (DCM) presented in [78] is used for SIF extraction in the GFEM-mERS while the J integral is used for 3DFEM model solved in Abaqus.

The relative difference between GFEM-mERS and 3DFEM SIFs is measure using the following discrete L^2-norm:

$$e^r(K_i) := \frac{\| e_i \|_{L^2}}{\| \breve{K}_i \|_{L^2}} = \frac{\sqrt{\sum_{j=1}^{N_{ext}} (K_i^j - \breve{K}_i^j)^2}}{\sqrt{\sum_{j=1}^{N_{ext}} (\breve{K}_i^j)^2}}, \tag{4.5}$$

The term N_{ext} is the number of extraction points along the crack front, $\breve{K}_i^j$ are the reference stress intensity factor obtained using Abaqus and K_i^j are the GFEM-mERS SIFs. The quantity $e^r(K_i)$ is referred to as the relative error of K_i.

Figure 4.35 (a) shows K_{I} along the crack front for the specimen without fibers. The crack front is the segment $\{(x,y,z) \mid x = \bar{x}, y = \bar{y}, z \in [0.0, 5.0]\}$ with $\bar{x}$ and $\bar{y}$ constants. The SIF curves extracted from GFEM-mERS and 3DFEM solutions are in very good agreement with a relative difference $e^r = 0.0532\%$. Mode II and III SIFs are not shown since this is a Mode I problem.

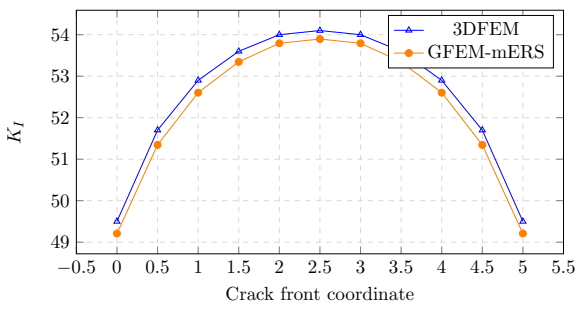

(a) Specimen without fibers

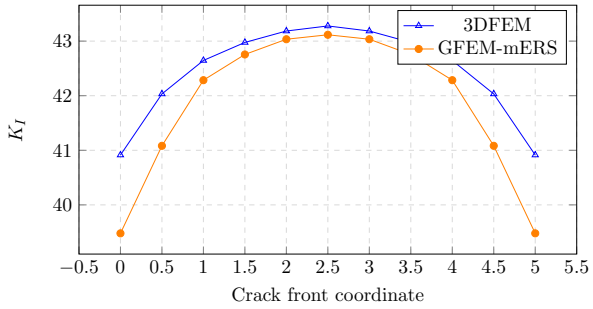

(b) Specimen with five fibers perpendicular to the crack

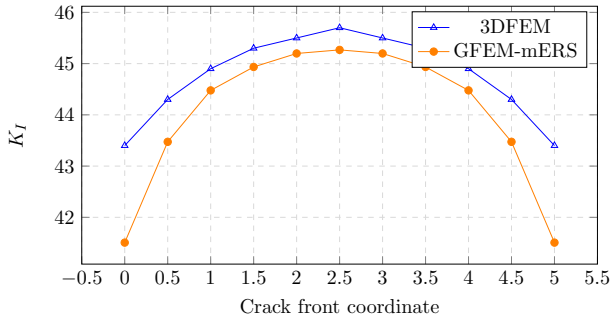

(c) Specimen with five fibers inclined relative to the crack

Figure 4.35: K_{I} along the crack front for the three specimen analyzed

Figures 4.35(b) and (c) show K_{I} along the crack front for the specimen with five fibers perpendicular and inclined with respect to the crack plane, respectively. These models are shown in Fig. 4.30. The relative difference between GFEM-mERS and 3DFEM SIFs is $e^r = 1.79\%$ and $e^r = 2.08\%$ for the models with vertical and inclined fibers, respectively. The difference between the two curves is larger at extraction points close to the domain boundary. Comparing the plots in Fig. 4.35, it can be observed that the model without fibers has the highest K_{I} and the one with fibers perpendicular to the crack plane has the lowest K_{I}. As expected, the later model is the most efficient in bridging the crack faces.

The effect of the bond slip stiffness K_{b} on the relative difference between GFEM-mERS and 3DFEM SIFs is studied next. The models for the specimen with fibers are solved with K_{b} five times the magnitude of the one used earlier. This procedure intends to mimic a perfect bonding between the matrix and fibers. The

plots for K_{I} are shown in Fig. 4.36. Comparing these curves with those shown in Figs 4.35(b) and 4.35(c), respectively, the difference between GFEM-mERS and 3DFEM results is smaller in the case of a high bond slip stiffness. The relative difference for the specimen with vertical and inclined fibers is reduced to $e^r = 1.53\%$ and $e^r = 1.73\%$, respectively.

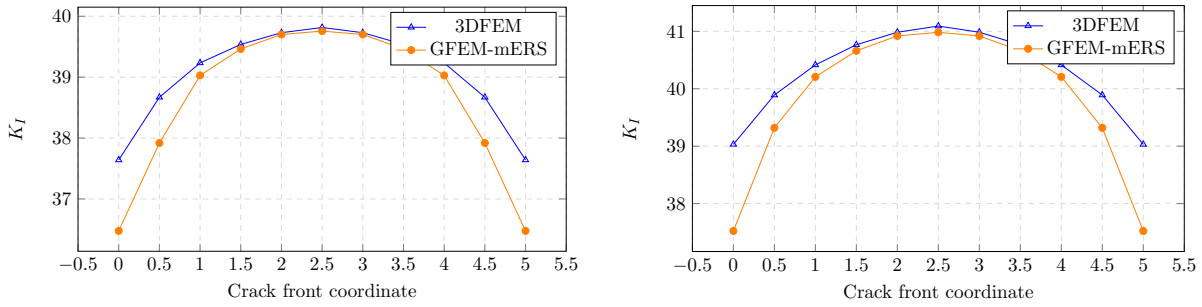

(a) Specimen with fibers perpendicular to the crack

(b) Specimen with fibers inclined relative to the crack

Figure 4.36: K_{I} along the crack front for the specimen with a high bond slip stiffness

4.6 Summary

Parametric studies for a range of fiber cross-section area, fiber stiffness, and fiber-matrix bond are presented in Sec. 4.1. A good agreement between the GFEM-mERS and 3DFEM reference solutions is observed for all parameter values considered. Convergence studies of the h- and p-version of the method are also presented. They show that the p-version of the GFEM-mERS converges quicker than the h-version. New sub-fiber elements are created as the 3D GFEM mesh is refined while the number of sub-fiber elements remains unchanged as the polynomial order of the GFEM approximation changes. As a result, the ratio between the number of fiber and 3D degrees of freedom is much higher in the h-version than in the p-version.

It is recalled that high-order approximations for the matrix displacement field are inconsistent with the original ERS formulation, while such limitation is removed in the proposed mERS, as shown in Sec. 3.3.2.

The GFEM-mERS is verified against fully 3D FEM solutions based on meshes that fit both the crack surfaces and fiber boundaries. The numerical experiments presented in Sec. 4.1 show that the GFEM-mERS solution clearly approaches the 3D FEM reference values as the GFEM mesh are refined even though the

finest GFEM-mERS mesh is much coarser than those adopted in the 3D FEM models.

The accuracy and robustness of the method are tested on a 3D problem with non-trivial geometry – a fiber-reinforced compact tension specimen. A range of fiber reinforcement configurations is considered, including the cases with fibers crossing the fracture and fibers with different orientations relative to the crack surface.

The simulations show that the GFEM-mERS can capture the change in specimen stiffness and stress intensity factor values as a function of the fiber orientation relative to the crack surface. The GFEM-mERS and 3DFEM results are quite close, with the GFEM-mERS model being slightly stiffer than the 3DFEM one. Local effects of the fiber reinforcements on the displacement field along the crack surface are also captured well by the GFEM-mERS. These effects cannot be predicted if homogenized material properties are adopted. The effect of fiber stiffness on these displacement perturbations along the crack surface is also studied in Sec. 4.1.

Quantities of interest provided by or extracted from GFEM-mERS solutions were compared with those provided by 3D FEM reference models solved using Abaqus [66]. They include the critical load for crack propagation, i.e., the magnitude of the CT specimen load that leads to a Mode I stress intensity factor at the crack front equal to the fracture toughness of the matrix. The relative difference between the critical load predicted by the GFEM-mERS and 3DFEM models was less than 6%.

Another quantity of interest considered was the Mode I stress intensity factor, K_{I}, along the crack front of the CT specimen. The relative difference between GFEM-mERS and 3DFEM K_{I} is $e^r = 1.79\%$ and $e^r = 2.08\%$ for the models with vertical and inclined fibers, respectively. This is a very good agreement given how much simpler the GFEM-mERS model is compared with the 3DFEM one. The effect of the fiber reinforcement and their orientation relative to the crack surface on extracted K_{I} was also captured well with the proposed GFEM-mERS.

Chapter 5

Three-Dimensional Crack Propagation in Fiber-Reinforced Composites Using a Nonlinear Debonding Law for Fiber-Matrix Interface

5.1 Introduction

This chapter [1] shows the recent advances on the GFEM-mERS for the solution of three-dimensional crack propagation in fiber-reinforced composites. The mechanical behavior theory developed here is built on top of the framework developed in the Chapter 2. Two additional features are proposed in this chapter:

- The definition of the constitutive behavior of the matrix, fiber and the fiber-matrix debonding. Matrix and fibers are considered linear elastic while the fiber-matrix interaction is modeled using a nonlinear constitutive relation.
- Crack propagation capabilities for fiber-reinforced composite materials using Linear Elastic Fracture Mechanics (LEFM). The main aspects of the theory are discussed in this chapter. Additional capabilities (with examples) are explained in appendix B [2].

5.2 A nonlinear fiber-matrix model

This section presents the mathematical model adopted for a continuum with an embedded fiber in a cracked domain. The assumptions adopted here follow those in [51] and [80]. A nonlinear cohesive law is

[1] This chapter has been adapted from "P. Alves and C. A. Duarte, Three-dimensional crack propagation in fiber-reinforced composites, in preparation, [79]

[2] Appendix B has been adapted from the paper by "F. Mukhtar, P. Alves and C. A. Duarte, Validation of a 3D Adaptative Stable Generalized/eXtended Finite Element Method for Mixed-Mode Brittle Fracture Propagation, International Journal of Fracture (2020), [80]"

adopted at fiber-matrix interface and, for simplicity, a single fiber is considered one more time. Extension of the model to an arbitrary number of fibers is straightforward. Linear Elastic Fracture Mechanics (LEFM) assumptions are adopted for matrix cracks. Inertial effects and gravity load are neglected.

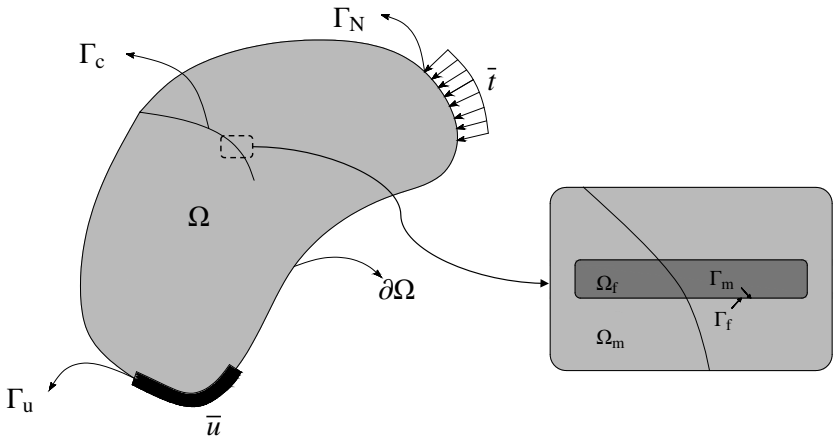

Figure 5.1: Continuum with one fiber and a crack

Consider a domain $\Omega \subset \mathbb{R}^3$, in which a fiber is included. Let Ω_f and Ω_m denote the domains occupied by the fiber and matrix, respectively, with $\Omega = \Omega_f \cup \Omega_m$. A crack surface Γ_c with crack front γ_F as shown in Fig. 5.1. The matrix-fiber interface is denoted by Γ, where Γ_m and Γ_f are the different sides of this interface. For simplicity, it is assumed that the fiber is fully embedded in Ω. Thus, $\Gamma \cap \partial\Omega = \emptyset$, where $\partial\Omega$ is the boundary of Ω. The external surface of the fiber is denoted by Γ_f while the external surface of the matrix facing the fiber is denoted by Γ_m. The boundary $\partial\Omega$ is decomposed as $\partial\Omega = \Gamma_u \cup \Gamma_N$ with $\Gamma_u \cap \Gamma_N = \emptyset$. Similarly to Chapter 2, Dirichlet and Neumann boundary conditions are prescribed on Γ_u and Γ_N.

$$\nabla \cdot \boldsymbol{\sigma} = \mathbf{0} \qquad \text{in } \Omega \tag{5.1}$$

where $\boldsymbol{\sigma}$ denotes the Cauchy stress tensor. The boundary conditions are given by

$$\boldsymbol{\sigma} \cdot \boldsymbol{n} = \bar{\boldsymbol{t}} \ \text{ on } \Gamma_N \qquad \text{and} \qquad \boldsymbol{u} = \bar{\boldsymbol{u}} \ \text{ on } \Gamma_u \tag{5.2}$$

where $\bar{\boldsymbol{u}}$ prescribed on $\partial\Omega$, where $\boldsymbol{n}$ is the outward unit normal vector to $\partial\Omega$, $\bar{\boldsymbol{t}}$ are prescribed tractions, and $\bar{\boldsymbol{u}}$ are prescribed displacements. The tractions at the fiber-matrix interface are denoted by

$$\boldsymbol{\sigma} \cdot \boldsymbol{n}_f = \boldsymbol{t}_f \ \text{ on } \Gamma_f \qquad \text{and} \qquad \boldsymbol{\sigma} \cdot \boldsymbol{n}_m = \boldsymbol{t}_m \ \text{ on } \Gamma_m, \tag{5.3}$$

where $\boldsymbol{n}_\mathrm{f}$ and $\boldsymbol{n}_\mathrm{m}$ are outward unit normal vectors to Γ_f and Γ_m, respectively, and $\boldsymbol{\sigma}\cdot\boldsymbol{n}_\mathrm{f} = -\boldsymbol{\sigma}\cdot\boldsymbol{n}_\mathrm{m} = \boldsymbol{t}_\mathrm{f}$ by equilibrium. Matrix and the fiber are assumed to behave as a linear elastic material, which are the same assumptions as assumed in Chapter 2.

$$\boldsymbol{\sigma}_\mathrm{m} = \boldsymbol{D}_\mathrm{m} : \boldsymbol{\epsilon} \quad \text{and} \tag{5.4}$$

$$\boldsymbol{\sigma}_\mathrm{f} = \boldsymbol{D}_\mathrm{f} : \boldsymbol{\epsilon} \tag{5.5}$$

where $\boldsymbol{D}_\mathrm{m}$ and $\boldsymbol{D}_\mathrm{f}$ denote the fourth order Hooke's tensor for matrix and fiber, respectively.

5.2.1 Kinematic assumptions

As developed by [51] and described in details in Chapter 2, the displacement field $\boldsymbol{u}$ over the entire body Ω is decomposed as

$$\boldsymbol{u} = \hat{\boldsymbol{u}} + \tilde{\boldsymbol{u}} \tag{5.6}$$

As in Chapter 2, functions here are generic and still valid for a cracked domain described in Fig. 5.1. Functions $\hat{\boldsymbol{u}}$ is a continuous function across the matrix-fiber interface Γ, but possibly discontinuous elsewhere in Ω, and $\tilde{\boldsymbol{u}}$ is continuous over the fiber subdomain Ω_f, discontinuous across the fiber-matrix interface Γ, and identically zero over the matrix subdomain Ω_m. The functions for matrix displacement, fiber displacement and the displacement jump across the fiber-matrix are the same as defined in Chapter 2, and given respectively by $\boldsymbol{u}|_{\Omega_\mathrm{m}}$ in Eq. 5.7, $\boldsymbol{u}|_{\Omega_\mathrm{f}}$ in Eq. 5.8 and $[\![\boldsymbol{u}]\!]|_\Gamma$ in Eq. 5.9.

$$\boldsymbol{u}|_{\Omega_\mathrm{m}} = \hat{\boldsymbol{u}}|_{\Omega_\mathrm{m}} \tag{5.7}$$

$$\boldsymbol{u}|_{\Omega_\mathrm{f}} = \hat{\boldsymbol{u}}|_{\Omega_\mathrm{f}} + \tilde{\boldsymbol{u}}|_{\Omega_\mathrm{f}} \tag{5.8}$$

$$[\![\boldsymbol{u}]\!]|_\Gamma = \boldsymbol{u}|_{\Gamma_\mathrm{f}} - \boldsymbol{u}|_{\Gamma_\mathrm{m}} = (\hat{\boldsymbol{u}} + \tilde{\boldsymbol{u}})|_{\Gamma_\mathrm{f}} - (\hat{\boldsymbol{u}} + \tilde{\boldsymbol{u}})|_{\Gamma_\mathrm{m}} = \tilde{\boldsymbol{u}}|_{\Gamma_\mathrm{f}} = [\![\tilde{\boldsymbol{u}}]\!]|_\Gamma \tag{5.9}$$

5.2.2 Principle of virtual work

The weak formulation of the problem described in the Chapter 2 is given one more time. Find $\boldsymbol{u} \in \mathcal{U}$, such that

$$\int_{\Omega} \nabla^s \delta\boldsymbol{u} : \boldsymbol{\sigma}\, \mathrm{d}\Omega + \int_{\Gamma_\mathrm{f}} [\![\delta\boldsymbol{u}]\!]|_\Gamma \cdot \boldsymbol{t}_\mathrm{f}\, \mathrm{d}\Gamma = \int_{\Gamma_\mathrm{N}} \delta\boldsymbol{u} \cdot \bar{\boldsymbol{t}}\, \mathrm{d}\Gamma_\mathrm{N} \quad \forall\ \delta\boldsymbol{u} \in \mathcal{U}_0, \tag{5.10}$$

where

$$\mathcal{U}(\Omega) = \left\{ \boldsymbol{u} : \boldsymbol{u}(\boldsymbol{x}) \in \mathbb{R}^3\ \forall\, \boldsymbol{x} \in \Omega;\ u_i \in H^1(\Omega), i = 1,2,3;\ \boldsymbol{u}|_{\Gamma_\mathrm{u}} = \bar{\boldsymbol{u}} \right\} \tag{5.11}$$

$$\mathcal{U}_0(\Omega) = \left\{ \boldsymbol{u} \in \mathcal{U}(\Omega) :\ \boldsymbol{u}|_{\Gamma_\mathrm{u}} = \boldsymbol{0} \right\} \tag{5.12}$$

The kinematic assumptions from Sec. 5.2.1 lead to

$$\int_{\Omega} \nabla^s \delta\hat{\boldsymbol{u}} : \boldsymbol{\sigma}\, \mathrm{d}\Omega + \int_{\Omega_\mathrm{f}} \nabla^s \delta\tilde{\boldsymbol{u}} : \boldsymbol{\sigma}\, \mathrm{d}\Omega + \int_{\Gamma_\mathrm{f}} [\![\delta\tilde{\boldsymbol{u}}]\!]|_\Gamma \cdot \boldsymbol{t}_\mathrm{f}\, \mathrm{d}\Gamma = \int_{\Gamma_\mathrm{N}} \delta\hat{\boldsymbol{u}} \cdot \bar{\boldsymbol{t}}\, \mathrm{d}\Gamma_\mathrm{N}. \tag{5.13}$$

As stated earlier, it is noted that both $\delta\hat{\boldsymbol{u}}$ and $\delta\tilde{\boldsymbol{u}}$ belong to $\mathcal{U}_0$. Therefore the virtual displacements $\delta\hat{\boldsymbol{u}}$ and $\delta\tilde{\boldsymbol{u}}$ are arbitrary, Eq. 5.13 can be split as

$$\int_{\Omega} \nabla^s \delta\hat{\boldsymbol{u}} : \boldsymbol{\sigma}\, \mathrm{d}\Omega = \int_{\Gamma_\mathrm{N}} \delta\hat{\boldsymbol{u}} \cdot \bar{\boldsymbol{t}}\, \mathrm{d}\Gamma_\mathrm{N} \quad \text{and} \tag{5.14}$$

$$\int_{\Omega_\mathrm{f}} \nabla^s \delta\tilde{\boldsymbol{u}} : \boldsymbol{\sigma}\, \mathrm{d}\Omega + \int_{\Gamma_\mathrm{f}} [\![\delta\tilde{\boldsymbol{u}}]\!]|_\Gamma \cdot \boldsymbol{t}_\mathrm{f}\, \mathrm{d}\Gamma = 0. \tag{5.15}$$

Up to this point these equations are the same governing equations as described in Chapter 2. The constitutive laws for matrix, fiber and interface are introduced and developed as follows. Here, it is chosen to present the derivation in its generic form, similarly as presented in [19]. The implementation and numerical examples in this research, however, consider the nonlinearity only at the interface, not at the matrix material. Material nonlinearities for advanced materials (including damage models with matrix degradation, as in [19]) can be easily introduced using the proposed formulation here presented.

The constitutive relations corresponding to the matrix (linear elastic), fiber (linear elastic) and interface (nonlinear) of the problems are presented in details in Sec. 5.3.2. The linearisation of Eqs. 5.14 and 5.15 leads to the following two linearised equilibrium statements:

$$\int_{\Omega} \nabla^s \delta\hat{\boldsymbol{u}} : \boldsymbol{\sigma}\, \mathrm{d}\Omega + \int_{\Omega} \nabla^s \delta\hat{\boldsymbol{u}} : \frac{\partial \boldsymbol{\sigma}}{\partial \boldsymbol{\epsilon}}\, \mathrm{d}\Omega = \int_{\Gamma_\mathrm{N}} \delta\hat{\boldsymbol{u}} \cdot \bar{\boldsymbol{t}}\, \mathrm{d}\Gamma_\mathrm{N} \tag{5.16}$$

$$\int_{\Omega_\mathrm{f}} \nabla^s \delta\tilde{\boldsymbol{u}} : \boldsymbol{\sigma}\, \mathrm{d}\Omega + \int_{\Omega_\mathrm{f}} \nabla^s \delta\tilde{\boldsymbol{u}} : \frac{\partial \boldsymbol{\sigma}}{\partial \boldsymbol{\epsilon}}\, \mathrm{d}\Omega + \int_{\Gamma_\mathrm{f}} \delta\tilde{\boldsymbol{u}} \cdot \boldsymbol{t}_\mathrm{f}\, \mathrm{d}\Gamma + \int_{\Gamma_\mathrm{f}} \delta\tilde{\boldsymbol{u}} \cdot \frac{\partial \boldsymbol{t}_\mathrm{f}}{\partial \tilde{u}}\, \mathrm{d}\Gamma = 0. \tag{5.17}$$

Considering that $\Omega = \Omega_\mathrm{m} + \Omega_\mathrm{f}$, using the decomposition of the strain tensor, and the constitutive laws, it can be found the following equations:

$$\begin{aligned}
&\int_{\Omega_\mathrm{m}} \nabla^s \delta\hat{\boldsymbol{u}} : \boldsymbol{D}_\mathrm{m} : \nabla^s \hat{\boldsymbol{u}}\, \mathrm{d}\Omega + \int_{\Omega_\mathrm{f}} \nabla^s \delta\hat{\boldsymbol{u}} : \boldsymbol{D}_\mathrm{f} : \nabla^s \hat{\boldsymbol{u}}\, \mathrm{d}\Omega + \int_{\Omega_\mathrm{f}} \nabla^s \delta\hat{\boldsymbol{u}} : \boldsymbol{D}_\mathrm{f} : \nabla^s \tilde{\boldsymbol{u}}\, \mathrm{d}\Omega \\
&+ \int_{\Omega_\mathrm{m}} \nabla^s \delta\hat{\boldsymbol{u}} : \boldsymbol{D}_\mathrm{m} : \nabla^s \Delta\hat{\boldsymbol{u}}\, \mathrm{d}\Omega + \int_{\Omega_\mathrm{f}} \nabla^s \delta\hat{\boldsymbol{u}} : \boldsymbol{D}_\mathrm{f} : \nabla^s \Delta\hat{\boldsymbol{u}}\, \mathrm{d}\Omega + \int_{\Omega_\mathrm{f}} \nabla^s \delta\hat{\boldsymbol{u}} : \boldsymbol{D}_\mathrm{f} : \nabla^s \Delta\tilde{\boldsymbol{u}}\, \mathrm{d}\Omega = \int_{\Gamma_\mathrm{N}} \delta\hat{\boldsymbol{u}} \cdot \bar{\boldsymbol{t}}\, \mathrm{d}\Gamma_\mathrm{N},
\end{aligned} \tag{5.18}$$

$$\begin{aligned}
&A_\mathrm{f} \int_{L_\mathrm{f}} \nabla^s \delta\tilde{\boldsymbol{u}} : \boldsymbol{D}_\mathrm{f} : \nabla^s \hat{\boldsymbol{u}}\, \mathrm{d}l + A_\mathrm{f} \int_{L_\mathrm{f}} \nabla^s \delta\tilde{\boldsymbol{u}} : \boldsymbol{D}_\mathrm{f} : \nabla^s \tilde{\boldsymbol{u}}\, \mathrm{d}l \\
&+ A_\mathrm{f} \int_{L_\mathrm{f}} \nabla^s \delta\tilde{\boldsymbol{u}} : \boldsymbol{D}_\mathrm{f} : \nabla^s \Delta\hat{\boldsymbol{u}}\, \mathrm{d}l + A_\mathrm{f} \int_{L_\mathrm{f}} \nabla^s \delta\tilde{\boldsymbol{u}} : \boldsymbol{D}_\mathrm{f} : \nabla^s \Delta\tilde{\boldsymbol{u}}\, \mathrm{d}l \\
&+ C_\mathrm{f} \int_{L_\mathrm{f}} \delta\tilde{\boldsymbol{u}}|_\Gamma \cdot (\boldsymbol{D}_\mathrm{b} \Delta\tilde{\boldsymbol{u}}|_\Gamma)\, \mathrm{d}l + C_\mathrm{f} \int_{L_\mathrm{f}} \delta\tilde{\boldsymbol{u}}|_\Gamma \cdot (\boldsymbol{D}_\mathrm{b} \tilde{\boldsymbol{u}}|_\Gamma)\, \mathrm{d}l = 0
\end{aligned}$$

where Δ denotes an increment of the corresponding quantity. After some arrangement the following equations are obtained:

$$\int_{\Omega} \nabla^s \delta\hat{\boldsymbol{u}} : \boldsymbol{D}_{\mathrm{m}} : \nabla^s \hat{\boldsymbol{u}} \, \mathrm{d}\Omega + A_{\mathrm{f}} \int_{L_{\mathrm{f}}} \nabla^s \delta\hat{\boldsymbol{u}} : (\boldsymbol{D}_{\mathrm{f}} - \boldsymbol{D}_{\mathrm{m}}) : \nabla^s \hat{\boldsymbol{u}} \, \mathrm{d}l$$
$$+ A_{\mathrm{f}} \int_{L_{\mathrm{f}}} \nabla^s \delta\hat{\boldsymbol{u}} : \boldsymbol{D}_{\mathrm{f}} : \nabla^s \tilde{\boldsymbol{u}} \, \mathrm{d}l + \int_{\Omega} \nabla^s \delta\hat{\boldsymbol{u}} : \boldsymbol{D}_{\mathrm{m}} : \nabla^s \Delta\hat{\boldsymbol{u}} \, \mathrm{d}\Omega$$
$$+ A_{\mathrm{f}} \int_{L_{\mathrm{f}}} \nabla^s \delta\hat{\boldsymbol{u}} : (\boldsymbol{D}_{\mathrm{f}} - \boldsymbol{D}_{\mathrm{m}}) : \nabla^s \Delta\hat{\boldsymbol{u}} \, \mathrm{d}l + A_{\mathrm{f}} \int_{L_{\mathrm{f}}} \nabla^s \delta\hat{\boldsymbol{u}} : \boldsymbol{D}_{\mathrm{f}} : \nabla^s \Delta\tilde{\boldsymbol{u}} \, \mathrm{d}l$$
$$= \int_{\Gamma_{\mathrm{N}}} \delta\hat{\boldsymbol{u}} \cdot \bar{\boldsymbol{t}} \, \mathrm{d}\Gamma_{\mathrm{N}}, \tag{5.19}$$

$$A_{\mathrm{f}} \int_{L_{\mathrm{f}}} \nabla^s \delta\tilde{\boldsymbol{u}} : \boldsymbol{D}_{\mathrm{f}} : \nabla^s \hat{\boldsymbol{u}} \, \mathrm{d}l + A_{\mathrm{f}} \int_{L_{\mathrm{f}}} \nabla^s \delta\tilde{\boldsymbol{u}} : \boldsymbol{D}_{\mathrm{f}} : \nabla^s \tilde{\boldsymbol{u}} \, \mathrm{d}l$$
$$+ C_{\mathrm{f}} \int_{L_{\mathrm{f}}} \delta\tilde{\boldsymbol{u}}|_{\Gamma} \cdot (\boldsymbol{D}_{\mathrm{b}} \tilde{\boldsymbol{u}}|_{\Gamma}) \, \mathrm{d}l + A_{\mathrm{f}} \int_{L_{\mathrm{f}}} \nabla^s \delta\tilde{\boldsymbol{u}} : \boldsymbol{D}_{\mathrm{f}} : \nabla^s \Delta\hat{\boldsymbol{u}} \, \mathrm{d}l$$
$$+ A_{\mathrm{f}} \int_{L_{\mathrm{f}}} \nabla^s \delta\tilde{\boldsymbol{u}} : \boldsymbol{D}_{\mathrm{f}} : \nabla^s \Delta\tilde{\boldsymbol{u}} \, \mathrm{d}l + C_{\mathrm{f}} \int_{L_{\mathrm{f}}} \delta\tilde{\boldsymbol{u}}|_{\Gamma} \cdot (\boldsymbol{D}_{\mathrm{b}} \Delta\tilde{\boldsymbol{u}}|_{\Gamma}) \, \mathrm{d}l = 0 \tag{5.20}$$

It can be observed that Eqs. 5.20 and 5.19 are very similar to Eqs. 2.21 and 2.22 presented in Chapter 2. Now, however, it is noted some terms due to the adopted cohesive law. As mentioned earlier, the nonlinear terms related to the matrix material can be simplified in this study, since linear elastic matrix is considered. More sophisticated models, including damage for example, can be easily introduced in this formulation for both matrix and fiber, as shown in [19]. The A_{f}, C_{f} and L_{f} are the cross-section area, circumference, and length of the fiber, respectively. With an abuse of notation, all quantities are kept in a general three-dimensional setting. One-dimensional relations are introduced, where appropriate, in Sec. 5.3.2.

5.3 Discretization of fiber-reinforced composites with 3D fractures for nonlinear models

5.3.1 GFEM-mERS

As in Chapter 3 the displacement field shown in Eq. 5.6 can be approximated using the GFEM-mERS defined earlier. In short, the GFEM approximation $\boldsymbol{u}^{\text{GFEM}}$ of a vector field $\boldsymbol{u}$ is given by

$$\begin{aligned}\boldsymbol{u}^{\text{GFEM}}(\boldsymbol{x}) &= \boldsymbol{u}^{\text{FEM}}(\boldsymbol{x}) + \boldsymbol{u}^{\text{ENR}}(\boldsymbol{x}) \\ &= \sum_{\alpha\in I_h} \underline{\hat{\boldsymbol{u}}}_{\alpha} N_{\alpha}(\boldsymbol{x}) + \sum_{\alpha\in I_h^e} N_{\alpha}(\boldsymbol{x}) \sum_{i=1}^{m_{\alpha}} \underline{\tilde{\boldsymbol{u}}}_{\alpha i} E_{\alpha i}(\boldsymbol{x}), \\ \underline{\hat{\boldsymbol{u}}}_{\alpha}, \underline{\tilde{\boldsymbol{u}}}_{\alpha i} &\in \mathbb{R}^d, d = 1,2,3. \end{aligned} \tag{5.21}$$

In this equation, the $N_{\alpha}(\boldsymbol{x})$, $\alpha \in I_h = \{1,\cdots,\text{nnod}\}$, is the standard linear finite element shape function associated with node $\boldsymbol{x}_{\alpha}$ of a finite element mesh covering the analysis domain $\bar{\Omega}$ and with nnod nodes; $E_{\alpha i}$ is the enrichment function at the node with index $\alpha \in I_h^e \subset I_h$, and $i = \{1,\cdots,m_{\alpha}\}$ is the index of the enrichment function at the node with m_{α} being the total number of enrichments assigned to node $\boldsymbol{x}_{\alpha}$. Using the parameters previously defined in Chapter 3, the GFEM approximation is therefore defined as for a cracked domain as in Eq. 5.22. Recall that $\hat{E}_{\alpha i}$, $E_{\alpha i}^{\mathcal{H}}$ and $E_{\alpha i}^{\text{OD}}$ are, respectively, the polynomials, generalized Heaviside and singular enrichments as defined previously. It is important to note that the enrichments are suitable for LEFM, and assume linear elastic matrix material. Equations 5.20 and 5.19 presented earlier can be simplified and the terms related to the nonlinearity of the matrix material can be dropped.

$$
\begin{aligned}
\boldsymbol{u}^{\mathrm{GFEM}}(\boldsymbol{x}) &= \sum_{\alpha\in I_h}\begin{bmatrix} N_\alpha\hat{E}_{\alpha i} & & \\ & N_\alpha\hat{E}_{\alpha i} & \\ & & N_\alpha\hat{E}_{\alpha i}\end{bmatrix}\hat{\underline{\boldsymbol{u}}}_{\alpha i} + \sum_{\alpha\in I_h^H}\begin{bmatrix} N_\alpha E^{\mathcal{H}}_{\alpha i} & & \\ & N_\alpha E^{\mathcal{H}}_{\alpha i} & \\ & & N_\alpha E^{\mathcal{H}}_{\alpha i}\end{bmatrix}\tilde{\underline{\boldsymbol{u}}}_{\alpha i} \\
&\quad + \sum_{\alpha\in I_h^{\mathrm{front}}}\sum_{i=1}^{2}\begin{bmatrix} N_\alpha\check{E}^{\mathrm{OD},x}_{\alpha i} & & \\ & N_\alpha\check{E}^{\mathrm{OD},y}_{\alpha i} & \\ & & N_\alpha\check{E}^{\mathrm{OD},z}_{\alpha i}\end{bmatrix}\check{\underline{\boldsymbol{u}}}_{\alpha i} \\
&= \sum_{\alpha\in I_h}\boldsymbol{N}_\alpha\hat{\underline{\boldsymbol{u}}}_{\alpha i} + \sum_{\alpha\in I_h^H}\boldsymbol{N}^H_\alpha\tilde{\underline{\boldsymbol{u}}}_{\alpha i} + \sum_{\alpha\in I_h^{\mathrm{front}}}\sum_{i=1}^{2}\boldsymbol{N}^{\mathrm{OD}}_{\alpha i}\check{\underline{\boldsymbol{u}}}_{\alpha i} \\
&= \boldsymbol{N}^{\mathrm{GFEM}}\boldsymbol{U}^{\mathrm{GFEM}},
\end{aligned}
\tag{5.22}
$$

where $\check{\underline{\boldsymbol{u}}}_{\alpha i} = [\check{\underline{u}}_{\alpha i}\ \check{\underline{v}}_{\alpha i}\ \check{\underline{w}}_{\alpha i}]^{\mathrm{T}}$, matrix $\boldsymbol{N}^{\mathrm{GFEM}}$ is simply the concatenation of $\boldsymbol{N}_\alpha$ ($\alpha\in I_h$), $\boldsymbol{N}^H_\alpha$ ($\alpha\in I_h^H$), and $\boldsymbol{N}^{\mathrm{OD}}_{\alpha i}$ ($\alpha\in I_h^{\mathrm{front}}$, $i=1,2$), and $\boldsymbol{U}^{\mathrm{GFEM}}$ is the global vector of degrees of freedom.

The mERS to be combined with the GFEM approximation follows the definition described in Chapter 3, where the displacement field can be divided in two non-slip components and slip component as shown earlier. The intersection between the fiber and element boundary is done as shown in Fig. 5.2. This formulation is necessary for the discretization of fractures (and propagation) with fibers bridging fracture faces using the GFEM-mERS.

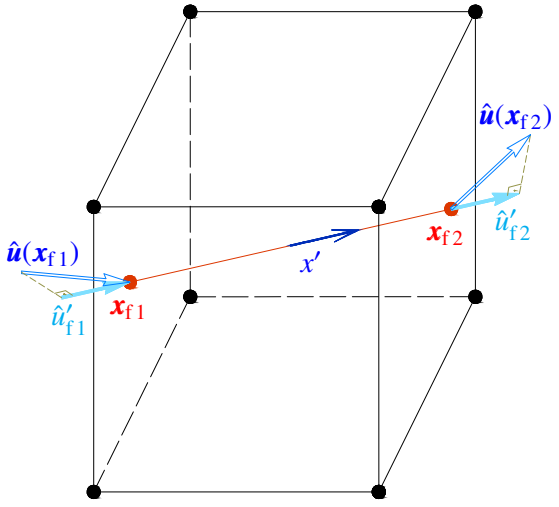

Figure 5.2: Intersection between the fiber and element boundary

Non-slip component The non-slip component is obtained from the matrix displacement field. They are the same as the GFEM approximation (Eq. 5.22) for fractures presented earlier in Sec. 3.2:

$$\hat{\boldsymbol{u}}(\boldsymbol{x}) = \boldsymbol{N}_{\mathrm{m}}(\boldsymbol{x})\boldsymbol{U}_{\mathrm{m}} = \boldsymbol{N}^{\mathrm{GFEM}}(\boldsymbol{x})\boldsymbol{U}^{\mathrm{GFEM}}. \tag{5.23}$$

The displacement of the matrix in the direction of the fiber is given by

$$\hat{u}_{\Omega_{\mathrm{f}}}(x') = \boldsymbol{R}_{\mathrm{f}}\hat{\boldsymbol{u}}[\boldsymbol{x}(x')] = \boldsymbol{R}_{\mathrm{f}}\boldsymbol{N}_{\mathrm{m}}[\boldsymbol{x}(x')]\boldsymbol{U}_{\mathrm{m}} = \boldsymbol{R}_{\mathrm{f}}\boldsymbol{N}^{\mathrm{GFEM}}[\boldsymbol{x}(x')]\boldsymbol{U}^{\mathrm{GFEM}} \tag{5.24}$$

where the transformation matrix $\boldsymbol{R}_{\mathrm{f}}$ is given by

$$\boldsymbol{R}_{\mathrm{f}} = \begin{bmatrix} \cos(\theta_{x'x}) & \cos(\theta_{x'y}) & \cos(\theta_{x'z}) \end{bmatrix} \tag{5.25}$$

with $\theta_{x'x}$, $\theta_{x'y}$, and $\theta_{x'z}$ the angles between the fiber axis x' and the global x, y, and z directions, respectively.

Slip component The approximation of the fiber slip (relative displacement between matrix and fiber) is given by

$$\tilde{u}_{\Omega_{\mathrm{f}}}(x') = \boldsymbol{N}_{\mathrm{f}}(x')\boldsymbol{U}_{\mathrm{f}}, \tag{5.26}$$

where the fiber shape functions and degrees of freedom are given, respectively by a linear approximation at the coordinate

$$\boldsymbol{N}_{\mathrm{f}}(x') = \begin{bmatrix} N_{\mathrm{f}1}(x') & N_{\mathrm{f}2}(x') \end{bmatrix} \text{ and} \tag{5.27}$$

$$\boldsymbol{U}_{\mathrm{f}} = \begin{bmatrix} u_{\mathrm{f}1x'} & u_{\mathrm{f}2x'} \end{bmatrix}^{\mathrm{T}}. \tag{5.28}$$

It is noted that the slip degrees of freedom $\boldsymbol{U}_{\mathrm{f}}$ are defined in the fiber direction x', as shown in Fig. 3.3.

5.3.2 Constitutive relations

The constitutive relation Eq. 5.4 in matrix format is given by

$$\hat{\boldsymbol{\sigma}} = \mathbb{D}_{\mathrm{m}}\hat{\boldsymbol{\epsilon}} \tag{5.29}$$

where

$$\mathbb{D}_{\mathrm{m}} = \frac{E_{\mathrm{m}}}{(1+\nu_{\mathrm{m}})(1-2\nu_{\mathrm{m}})}\begin{bmatrix} 1-\nu_{\mathrm{m}} & \nu_{\mathrm{m}} & \nu_{\mathrm{m}} & 0 & 0 & 0 \\ \nu_{\mathrm{m}} & 1-\nu_{\mathrm{m}} & \nu_{\mathrm{m}} & 0 & 0 & 0 \\ \nu_{\mathrm{m}} & \nu_{\mathrm{m}} & 1-\nu_{\mathrm{m}} & 0 & 0 & 0 \\ 0 & 0 & 0 & 1-2\nu_{\mathrm{m}} & 0 & 0 \\ 0 & 0 & 0 & 0 & 1-2\nu_{\mathrm{m}} & 0 \\ 0 & 0 & 0 & 0 & 0 & 1-2\nu_{\mathrm{m}} \end{bmatrix}. \tag{5.30}$$

and

$$\hat{\boldsymbol{\epsilon}} = \boldsymbol{\nabla}^s\hat{\boldsymbol{u}} = \boldsymbol{B}^{\mathrm{GFEM}}\boldsymbol{U}^{\mathrm{GFEM}} \tag{5.31}$$

as defined in Chapter 3

Since the fiber is modeled as a truss, the constitutive relation Eq. 5.5 degenerates to the one-dimensional Hooke's law

$$\tilde{\sigma}' = E_{\mathrm{f}}\tilde{\epsilon}' \tag{5.32}$$

The gradient of the 1D fiber slip in the fiber coordinate system is given by

$$\tilde{\epsilon}'(x') = \frac{d\tilde{u}_{\Omega_{\mathrm{f}}}(x')}{dx'} = \frac{d\boldsymbol{N}_{\mathrm{f}}(x')}{dx'}\boldsymbol{U}_{\mathrm{f}} = \boldsymbol{B}_{\mathrm{f}}(x')\boldsymbol{U}_{\mathrm{f}}, \tag{5.33}$$

For the matrix-fiber interface, only the longitudinal fiber displacement is considered when idealizing a fiber as a truss. Therefore, the traction-separation law degenerates to the following

$$D_{\mathrm{b}}(x') = \frac{\partial t_{\mathrm{f}}(x')}{\partial\tilde{u}_{\Omega_{\mathrm{f}}}(x')} \tag{5.34}$$

The term $t_{fx'}$ is the traction along the fiber boundary, $\tilde{u}_{\Omega_f}$ is the fiber slip (relative displacement between matrix and fiber), and $D_b(x')$ is the tangential component that comes from the stress-slip relation between matrix and fiber. Figure 5.3 shows (for a generic cohesive law) a nonlinear function that describes the traction $t_{fx'}$ due to the slip $\tilde{u}_{\Omega_f}$.

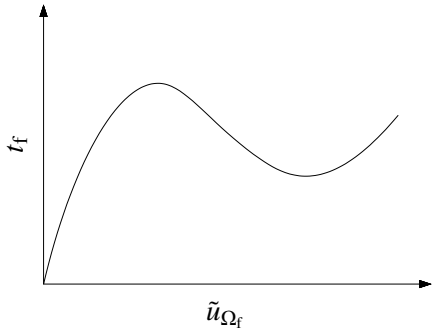

Figure 5.3: Generic bond stress-slip relation for the interaction of matrix and fiber

Two bond-slip relation are studied in this chapter. The bilinear law is used for verification of GFEM-mERS against several numerical examples using 3DFEM. The Piecewise Cubic Hermite Interpolating Polynomial (PCHIP) law [81], which is more complex and uses more parameters than the bilinear law, is used for validation of GFEM-mERS against laboratory experiments.

Bilinear law

The debonding law at the fiber-matrix interface is given by a bilinear law illustrated in Fig. 5.4. The bond-slip law consists of an initial elastic branch followed by a softening branch. The constitutive law is defined by a peak value (s^{ini}_{max}, τ^{ini}_{max}) and a load level (s^{ini}_{res1}, τ^{ini}_{res1}). This law is very simple, can be easily implemented and can be found in many commercial software.

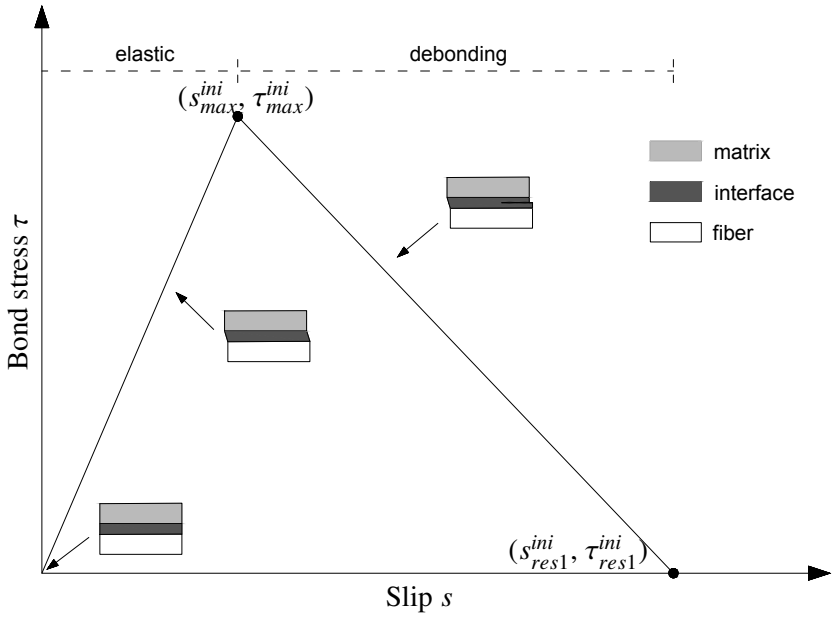

Figure 5.4: Bilinear bond stress-slip relation for the interaction of matrix fiber

Piecewise Cubic Hermite Interpolating Polynomial (PCHIP) law

A more accurate description of the nonlinear matrix-fiber interaction for many composites is described using the bond-slip law proposed by [81]. This law is very versatile and can be used to describe a large variety of composites, including reinforced concrete, [81], short glass fiber composites, [82], polypropylene composites, [83], and many others. Similarly to the bilinear law described earlier, this relation describes a traction τ due to the slip s. As shown in Fig. 5.5, this bond slip law consists of an initial elastic branch followed by a debonding and a final frictional pull-out branch. The constitutive law is defined by a peak value $(s^{ini}_{max}, \tau^{ini}_{max})$ and a residual load level $(s^{ini}_{res1}, \tau^{ini}_{res1})$. To control the frictional part of the law a control point $(s^{ini}_{res2}, \tau^{ini}_{res2})$ is defined. As suggested by [84], the parameter τ^{ini}_{res2} is set slightly smaller than τ^{ini}_{res1} to avoid a zero stiffness in the residual load part. The interpolation between points is realized by Piecewise Cubic Hermite Interpolating Polynomial Procedure (PCHIP) based on [85]. It uses a subset of cubic polynomials, which show monotonicity and continuity in the first derivatives between consecutive intervals. This reduces numerical problems during computations on the transitions between the intervals of the bond law.

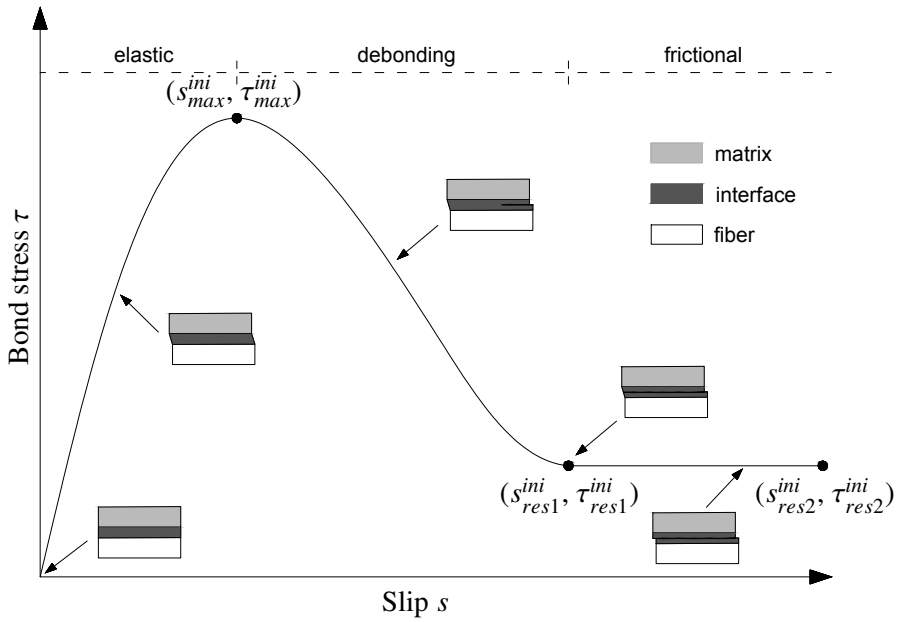

Figure 5.5: PCHIP bond stress-slip relation for the interaction of matrix fiber

The law is defined using four control points: P0 $(0,0)$, P1 $(s^{ini}_{max}, \tau^{ini}_{max})$, P2 $(s^{ini}_{res1}, \tau^{ini}_{res1})$, P3 $(s^{ini}_{res2}, \tau^{ini}_{res2})$. Therefore there are four points and three interpolation intervals. Withing these intervals function $\tau(s)$ is defined by

$$\tau(s) = \tau_l H_1(s) + (s_u - s_l) m H_2(s) + \tau_u H_3(s) + (s_u - s_l) m H_4(s) \tag{5.35}$$

The subscripts l and u indicate the neighbors of the interpolation interval. The terms H_1, H_2, H_3, H_4, m are defined as:

$$H_1(s) = 2(\frac{s - s_l}{s_u - s_l})^3 - 3(\frac{s - s_l}{s_u - s_l})^2 + 1 \tag{5.36}$$

$$H_2(s) = (\frac{s - s_l}{s_u - s_l})^3 - 2(\frac{s - s_l}{s_u - s_l})^2 + (\frac{s - s_l}{s_u - s_l}) \tag{5.37}$$

$$H_3(s) = -2(\frac{s - s_l}{s_u - s_l})^3 + 3(\frac{s - s_l}{s_u - s_l})^2 \tag{5.38}$$

$$H_4(s) = (\frac{s - s_l}{s_u - s_l})^3 - (\frac{s - s_l}{s_u - s_l})^2 \tag{5.39}$$

$$m = \frac{\tau_u - \tau_l}{s_u - s_l} \tag{5.40}$$

5.3.3 Nonlinear system of equilibrium equations

Each term in Eqs. 5.19 and 5.20 is discretized using a GFEM approximation for the matrix and the modified ERS formulation for the fiber and matrix-fiber interaction. They are done as in [51]. The above leads to the following system of equilibrium equations

$$\begin{bmatrix} \boldsymbol{K}_{\mathrm{mm}} & \boldsymbol{K}_{\mathrm{mf}} \\ \boldsymbol{K}_{\mathrm{fm}} & \boldsymbol{K}_{\mathrm{ff}} \end{bmatrix} \begin{bmatrix} \Delta \boldsymbol{U}^{\mathrm{GFEM}} \\ \Delta \boldsymbol{U}_{\mathrm{f}} \end{bmatrix} = \begin{bmatrix} \boldsymbol{f} \\ \boldsymbol{0} \end{bmatrix} - \begin{bmatrix} \boldsymbol{f}_{intU^{\mathrm{GFEM}}} \\ \boldsymbol{f}_{intU_{\mathrm{f}}} \end{bmatrix} \tag{5.41}$$

where the terms in Eq. 5.41 are given by

$$\boldsymbol{K}_{\mathrm{mm}} = \int_{\Omega} (\boldsymbol{B}_{\mathrm{m}})^T \mathbb{D}_{\mathrm{m}} \boldsymbol{B}_{\mathrm{m}} d\Omega + A_{\mathrm{f}} \int_{L_{\mathrm{f}}} (\boldsymbol{B}_{\mathrm{m}})^T \boldsymbol{R}^T (E_{\mathrm{f}} - E_{\mathrm{m}}) \boldsymbol{R} \boldsymbol{B}_{\mathrm{m}} \, \mathrm{d}l, \tag{5.42}$$

$$\boldsymbol{K}_{\mathrm{mf}} = A_{\mathrm{f}} \int_{L_{\mathrm{f}}} (\boldsymbol{B}_{\mathrm{m}})^T \boldsymbol{R}^T E_{\mathrm{f}} \boldsymbol{B}_{\mathrm{f}} \, \mathrm{d}l, \tag{5.43}$$

$$\boldsymbol{K}_{\mathrm{fm}} = A_{\mathrm{f}} \int_{L_{\mathrm{f}}} (\boldsymbol{B}_{\mathrm{f}})^T E_{\mathrm{f}} \boldsymbol{R} \boldsymbol{B}_{\mathrm{m}} \, \mathrm{d}l, \tag{5.44}$$

$$\boldsymbol{K}_{\mathrm{ff}} = A_{\mathrm{f}} \int_{L_{\mathrm{f}}} (\boldsymbol{B}_{\mathrm{f}})^T E_{\mathrm{f}} \boldsymbol{B}_{\mathrm{f}} \, \mathrm{d}l + C_{\mathrm{f}} \int_{L_{\mathrm{f}}} (\boldsymbol{N}_{\mathrm{f}})^T D_{\mathrm{b}} \boldsymbol{N}_{\mathrm{f}} \, \mathrm{d}l, \tag{5.45}$$

$$\boldsymbol{f} = \int_{\Gamma_{\mathrm{N}}} (\boldsymbol{N}_{\mathrm{m}})^T \bar{\boldsymbol{t}} \, \mathrm{d}\Gamma. \tag{5.46}$$

$$\boldsymbol{f}_{intU^{\mathrm{GFEM}}} = \int_{\Omega} (\boldsymbol{B}_{\mathrm{m}})^T \mathbb{D}_{\mathrm{m}} \boldsymbol{B}_{\mathrm{m}} \boldsymbol{U}^{\mathrm{GFEM}} d\Omega \tag{5.47}$$

$$+ A_{\mathrm{f}} \int_{L_{\mathrm{f}}} (\boldsymbol{B}_{\mathrm{m}})^T \boldsymbol{R}^T (E_{\mathrm{f}} - E_{\mathrm{m}}) \boldsymbol{R} \boldsymbol{B}_{\mathrm{m}} \boldsymbol{U}^{\mathrm{GFEM}} \mathrm{d}l + A_{\mathrm{f}} \int_{L_{\mathrm{f}}} (\boldsymbol{B}_{\mathrm{m}})^T \boldsymbol{R}^T E_{\mathrm{f}} \boldsymbol{B}_{\mathrm{f}} \boldsymbol{U}_{\mathrm{f}} \, \mathrm{d}l \tag{5.48}$$

$$\boldsymbol{f}_{intU_{\mathrm{f}}} = A_{\mathrm{f}} \int_{L_{\mathrm{f}}} (\boldsymbol{B}_{\mathrm{f}})^T E_{\mathrm{f}} \boldsymbol{R} \boldsymbol{B}_{\mathrm{m}} \boldsymbol{U}^{\mathrm{GFEM}} \, \mathrm{d}l + A_{\mathrm{f}} \int_{L_{\mathrm{f}}} (\boldsymbol{B}_{\mathrm{f}})^T E_{\mathrm{f}} \boldsymbol{B}_{\mathrm{f}} \boldsymbol{U}_{\mathrm{f}} \, \mathrm{d}l + C_{\mathrm{f}} \int_{L_{\mathrm{f}}} (\boldsymbol{N}_{\mathrm{f}})^T D_{\mathrm{b}} \boldsymbol{N}_{\mathrm{f}} \boldsymbol{U}_{\mathrm{f}} \, \mathrm{d}l \tag{5.49}$$

The derivations presented in this section, leading to Eq. 5.41, assume that there is a single fiber in the analysis domain. The extensions to the case of multiple fibers is straightforward due to the hierarchical nature of Eq. 5.41: the GFEM discretization of a cracked domain is simply augmented by the discretization of each fiber based on the GFEM-mERS. Thus, the system of equations for the case of n fibers is of the form:

$$\begin{bmatrix} \boldsymbol{K}_{\mathrm{mm}} & \boldsymbol{K}_{\mathrm{mf}_1} & \boldsymbol{K}_{\mathrm{mf}_2} & \cdots & \boldsymbol{K}_{\mathrm{mf}_n} \\ \boldsymbol{K}_{\mathrm{f}_1\mathrm{m}} & \boldsymbol{K}_{\mathrm{f}_1\mathrm{f}_1} & \boldsymbol{0} & \cdots & \boldsymbol{0} \\ \boldsymbol{K}_{\mathrm{f}_2\mathrm{m}} & \boldsymbol{0} & \boldsymbol{K}_{\mathrm{f}_2\mathrm{f}_2} & \cdots & \boldsymbol{0} \\ \vdots & \vdots & \vdots & \ddots & \vdots \\ \boldsymbol{K}_{\mathrm{f}_n\mathrm{m}} & \boldsymbol{0} & \boldsymbol{0} & \cdots & \boldsymbol{K}_{\mathrm{f}_n\mathrm{f}_n} \end{bmatrix} \begin{bmatrix} \Delta \boldsymbol{U}^{\mathrm{GFEM}} \\ \Delta \boldsymbol{U}_{\mathrm{f}_1} \\ \Delta \boldsymbol{U}_{\mathrm{f}_2} \\ \vdots \\ \Delta \boldsymbol{U}_{\mathrm{f}_n} \end{bmatrix} = \begin{bmatrix} \boldsymbol{f} \\ \boldsymbol{0} \\ \boldsymbol{0} \\ \vdots \\ \boldsymbol{0} \end{bmatrix} - \begin{bmatrix} \boldsymbol{f}_{intU^{\mathrm{GFEM}}} \\ \boldsymbol{f}_{intU_{\mathrm{f}1}} \\ \boldsymbol{f}_{intU_{\mathrm{f}2}} \\ \vdots \\ \boldsymbol{f}_{intU_{\mathrm{n}}} \end{bmatrix}. \tag{5.50}$$

5.3.4 Computational geometry issues for cracks and fibers

The implementation of the GFEM and GFEM-mERS requires efficient and robust computational geometry strategies. For the crack representation using GFEM the main challenges are the description of non-planar crack surfaces, the definition of based vectors of coordinate systems used in the computation of singular enrichment functions, and algorithms for automatic generation of elements used for the numerical integration of the weak form. For the fiber representation using GFEM-mERS the main challenge is the description of the 1D element (fiber) crossing 3D elements and its boundaries. This is essential to create the sub-fiber elements used for integration purposes.

Here, crack surfaces are represented using surface meshes like those shown in Figs. 5.6. These triangulations are known as *geometrical crack surfaces*. The surface mesh is independent of the 3D mesh used to solve the problem and composed of a set of triangles (facets) that represent the crack geometry and location. It is noted that these triangulations have no degrees of freedom. They serve only for computational geometry purposes. Figure 5.6 shows base vectors of coordinate systems defined at crack front vertices of a geometrical crack surface. Besides the computation of singular enrichments, these base vectors are also used for the extraction of stress intensity factors at crack front vertices, and for the crack front advancement as described in Sec. 5.4.1.

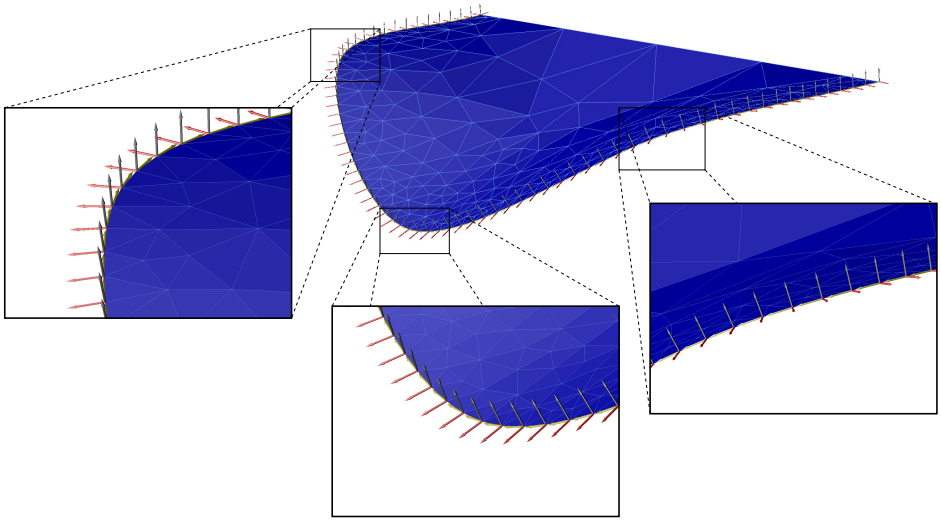

Figure 5.6: Non-planar crack surface and base vectors at crack front vertices [86]

Although the fibers do not need to be fit with matrix elements and crack surfaces, it is still required to map the matrix elements where fibers are inserted. The process, however, is substantially less complex when compared to the classical FEM method where both fiber and matrix meshes need to fit. The subfibers are essential for numerical integration and the process of creating is illustrated in Fig. 4.16 and described in details in [51]. Every time a fiber crosses a 3D element, a new sub-fiber is generated.

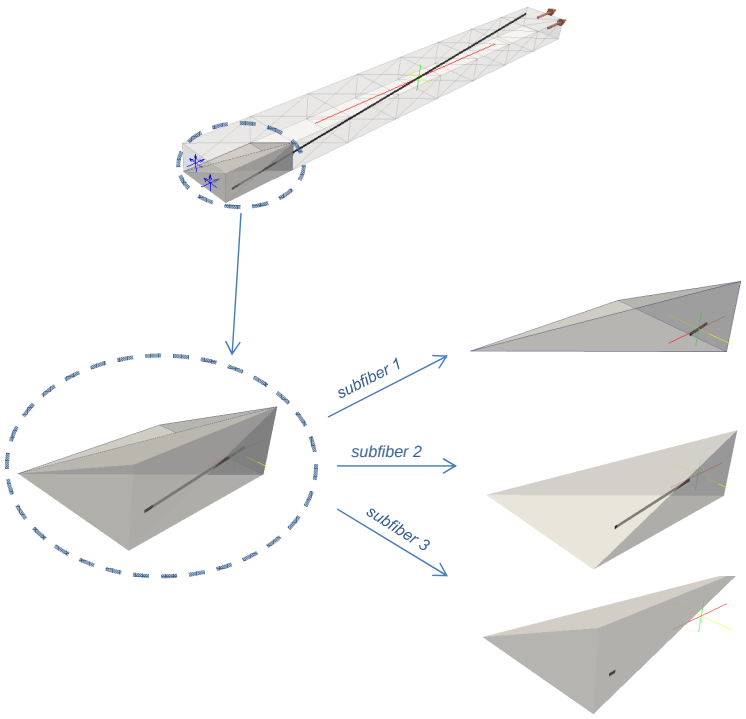

Figure 5.7: Process of creating sub-fibers in a 3D GFEM mesh. One sub-fiber is created for each tetrahedral element intersected by the fiber. This leads to an increase in fiber DOFs with refinement of the 3D mesh

Regarding fibers crossing the crack, there are three possible cases from the computational point of view. The 2D schematics of these cases are described in Fig. 5.8. For case (a), cracks are represented by double nodes and do not cross any subfiber; for case (b) cracks are represented by GFEM functions and do not cross any subfiber; and for case (c) cracks are represented by GFEM and cross a subfiber. As expected, the most challenging (and generic) case from the geometrical and numerical point of view occurs for case (c). The 1D integration over the subfibers cut by the crack is performed using a Simpson quadrature rule [68] with a large number of points as described in Chapter 4.

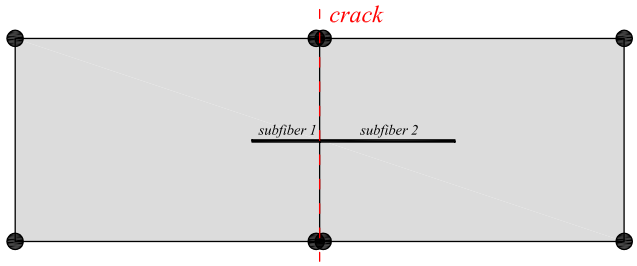

(a) Double nodes describing cracks

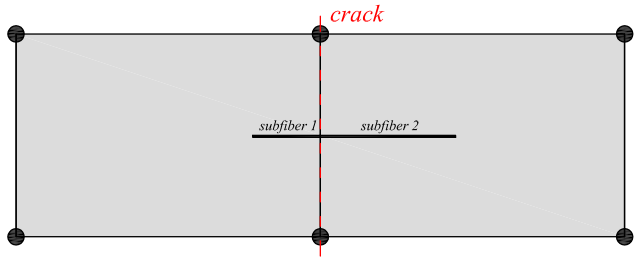

(b) GFEM describing cracks

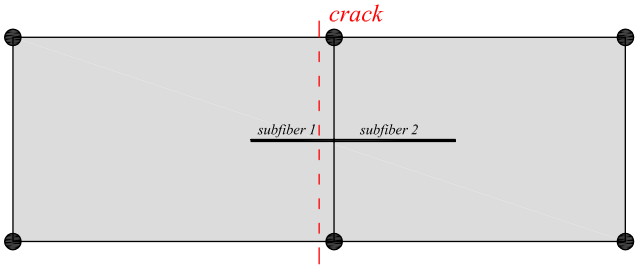

(c) GFEM describing cracks crossing subfibers

Figure 5.8: Schematic showing the location of the crack relative to matrix and sub-fiber elements

5.4 Crack propagation algorithm with mesh adaptivity for fiber-reinforced composites

This section presents the main steps of a 3D GFEM-mERS simulation of fracture propagation for fiber-reinforced composites. For this research linear elastic fracture mechanics is adopted. The propagation algorithm is based on those proposed in [76, 80, 87, 88] and is implemented in the 3D adaptive GFEM software ISET [89]. The algorithm enables automated, efficient, and accurate simulations of 3D fracture propagation in fiber composites as demonstrated in Sec. 4.1. Given the representation of the crack surface at propagation step (cf. Sec. 5.3.4), the following is performed:

1. Refine the 3D GFEM mesh around the crack front and fiber line such that the element size meets user-prescribed criteria. Example of this mesh is shown in Fig. 5.9. It can observe that the region where crack and fibers are located is highly refined. Details on the refinement algorithm can be found in [88] and [89].

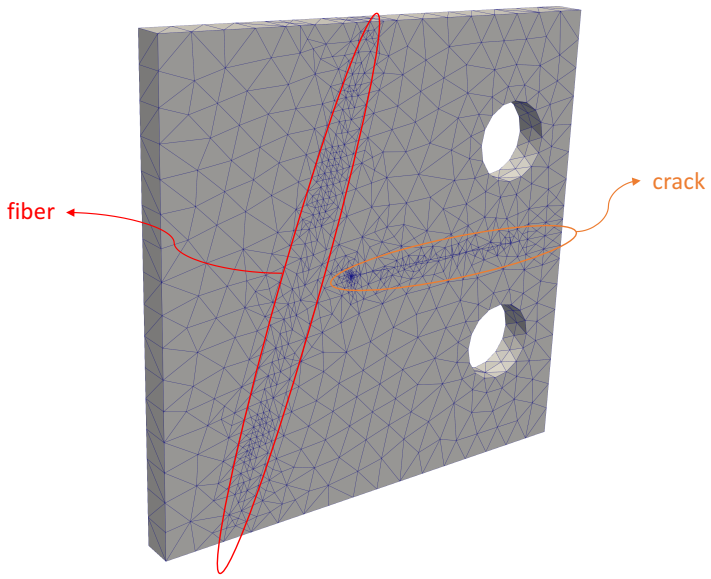

Figure 5.9: Mesh refinement of a representative problem containing fiber and crack

2. Compute the intersection between the geometrical crack surface and the GFEM mesh. The Computational Geometry Algorithms Library (CGAL) [90] implementation of AABB trees (trees of axis-aligned bounding boxes) is adopted for these computations. These intersections are in turn used for the generation of integration sub-elements as described in [65, 67].

3. Compute the intersection between the fibers and the GFEM mesh. AABB trees is also adopted for these computations. These intersections generate the sub-fibers as shown in Fig. 5.8 and presented in details in [51]. The algorithm is presented in Appendix A.

4. Enrich the finite element nodes with singular, Heaviside, and polynomial functions, as described in Sec. 3.2.

5. Integrate the stiffness matrix and load vector associated with the GFEM discretization of Eq. 5.1. This is performed with the aid of integration sub-elements and the sub-fibers generated previously.

6. Solve the linearized elastic problem Eq. 5.1 discretized with the GFEM. Due to the nonlinear aspect of Eq. 5.34, an iterative process is necessary.

7. Extract Mode I, II and III Stress Intensity Factors (SIFs) at every vertex on the crack front of the geometrical crack surface. The extraction method adopted is described in 5.5. The SIFs are used to determine, at each crack front vertex, if the crack will propagate and the direction and magnitude of propagation as described in Sec. 5.4.1.

8. Calculate the axial tensile strength of the fibers. This factor will indicate, for each fiber, if the ultimate strength σ_{ult} has been reached. Fiber stiffness is no longer considered after axial strenght hits σ_{ult} and fiber is considered broken (area of the fiber is considered null for future steps).

9. The propagation vectors are used to define the position of the crack front vertices at the next propagation step. The geometrical crack surface is updated by adding a new layer of triangular facets to the current crack front or by stretching the current crack front vertices. The strategy used depends on the magnitude of the crack front advancement vector at each front vertex. After several propagation steps, the crack surface triangulation may be remeshed to reduce the number of facets and speed up computational geometry operations. Details on these algorithms for geometrical crack surface updating and remeshing are described in [76]. Figure 5.41 shows the evolution of a crack surface and its update.

10. After updating the geometrical crack surface, the 3D GFEM mesh is unrefined to the initial mesh provided by the user. The algorithm is then repeated until no crack front vertex meet the propagation criterion or the user-prescribed number of propagation steps is reached.

5.4.1 A computational fracture growth model for linear elastic fracture mechanics

As described in details in [80], the propagation algorithm described earlier is based on linear elastic fracture mechanics assumptions and requires, at a crack propagation step, the following information at each crack front vertex of the geometrical fracture surface:

1. The crack propagation *direction*. In this work, the Schöllmann's criterion [91] is adopted.

2. The *magnitude* of the crack front advancement. A Paris-type law is used to compute this at each front vertex based on the maximum advancement magnitude, $\Delta a_{\max}$, prescribed by the user and other law-specific parameters.

Crack propagation direction: Schöllmann's criterion

Crack front deflection can be represented by the kinking angle θ_0 and the twisting angle ψ_0, as shown in Fig. 5.10. These quantities are computed using Schöllmann's criterion [91]. It assumes, like in the 2D Maximum Tangential Stress (MTS) criterion [92], that the crack growth direction is perpendicular to the maximum principal stress.

The kinking angle θ_0 is a non-linear function of all three SIFs and is determined by the conditions

$$\frac{\partial \sigma_1}{\partial \theta} = 0\Big|_{\theta=\theta_0} \qquad \frac{\partial^2 \sigma_1}{\partial \theta^2} < 0\Big|_{\theta=\theta_0}$$

where σ_1 is the maximum principal stress. Once the kinking angle θ_0 is calculated, the twisting angle, ψ_0, is given by the direction of σ_1 and can be computed using

$$\psi_0 = \frac{1}{2} \arctan\left(\frac{2\tau_{\theta z}(\theta_0)}{\sigma_\theta(\theta_0) - \sigma_z(\theta_0)}\right) \tag{5.51}$$

where σ_θ, $\tau_{\theta z}$ and σ_z are components of the stress tensor in a cylindrical coordinate system defined at the crack front. For further details, the reader is referred to [91, 93].

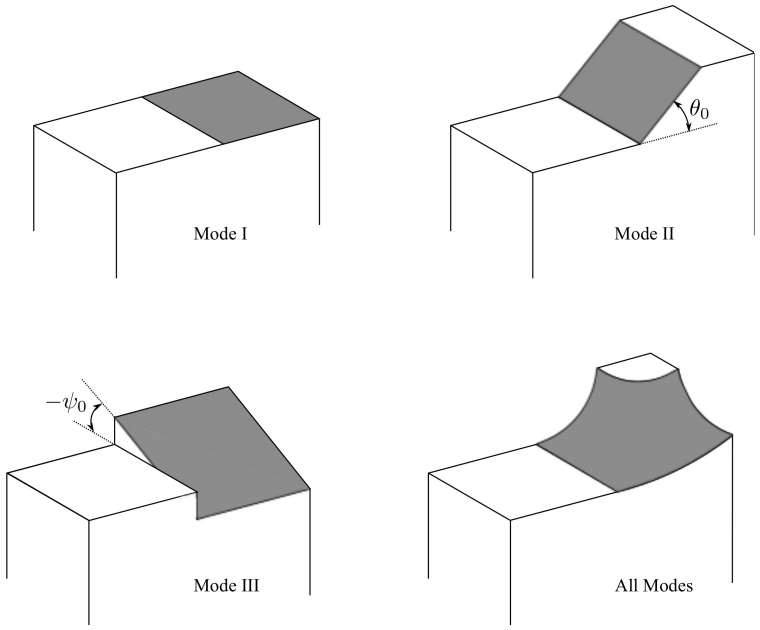

Figure 5.10: Crack growth under each mode and their superposition. The kinking angle θ_0 and the twisting angle ψ_0 define the direction of crack front propagation [88]

The kinking and twisting angles are used to prescribe the direction of crack propagation at each crack front vertex of the geometrical crack surface [87]. An effective crack front propagation direction θ^* is defined based on θ_0 and an increment accounting for the twisting angle ψ_0, and thus the effect of K_{III}. Details on the procedure to compute this increment are provided in [94].

Schöllmann's criterion degenerates to Erdogan and Sih's MTS criterion [92] if $K_{III} = 0$. In this case, the kinking angle θ_0 is given by [95]

$$\theta_0 = \begin{cases} 2\arctan\left[\frac{1}{4}\frac{K_I}{K_{II}} - \frac{1}{4}\sqrt{\left(\frac{K_I}{K_{II}}\right)^2 + 8}\right], & \text{if } K_{II} \neq 0 \\ 0, & \text{if } K_{II} = 0 \end{cases} \tag{5.52}$$

and the twisting angle $\psi_0 = 0$.

Crack front advancement magnitude

Crack growth in linear elastic fracture mechanics is dependent on the stress intensity factors or, equivalently, on the energy release rate [95, 96]. Griffith's criterion is commonly used for brittle fracture growth [95, 97, 98]. It is given by,

$$\Delta a(j) = \begin{cases} 0, & \text{if } \mathcal{G}_{\text{mixed}}(j) < \mathcal{G}_c \\ > 0, & \text{if } \mathcal{G}_{\text{mixed}}(j) = \mathcal{G}_c \end{cases} \tag{5.53}$$

where $\Delta a(j)$ is the magnitude of crack advancement at crack front vertex j, $\mathcal{G}_{\text{mixed}}(j)$ is the energy release rate in the direction of crack propagation at front vertex j, and $\mathcal{G}_c$ is the critical energy release rate of the material. In the case of plane strain conditions, $\mathcal{G}_c$ is given by

$$\mathcal{G}_c = \frac{1-\nu^2}{E} K_{Ic}^2 \tag{5.54}$$

where K_{Ic} is the fracture toughness of the material under Mode I loading.

The energy release rate at each crack front vertex is used to determine whether the crack front propagates or not. The crack propagates when the energy release rate at any crack front vertex *in the direction of crack propagation*, $\mathcal{G}_{\text{mixed}}$, reaches the critical energy release rate of the material [97, 98]. $\mathcal{G}_{\text{mixed}}$ is computed using [98],

$$\mathcal{G}_{\text{mixed}} = \mathcal{G}_{I/II} + \mathcal{G}_{III} \tag{5.55}$$

where $\mathcal{G}_{I/II}$ and $\mathcal{G}_{III}$ are given by [98],

$$\mathcal{G}_{I/II} = \frac{1-\nu^2}{E}\left\{\frac{1}{2}\cos\left(\frac{\theta^*}{2}\right)\left[K_I\left(1+\cos\theta^*\right)-3K_{II}\sin\theta^*\right]\right\}^2 \tag{5.56}$$

$$\mathcal{G}_{III} = \frac{1+\nu}{E}\left[K_{III}\cos\left(\frac{\theta^*}{2}\right)\right]^2 \tag{5.57}$$

It is noted that the criterion given by Eq. 5.53 does not provide the magnitude of the crack front advancement along the crack front once the condition $\mathcal{G}_{\text{mixed}} = \mathcal{G}_c$ is met at a crack front vertex. The criterion as stated in Eq. 5.53 is not suitable for computational implementation.

Lazarus [99] presented a regularization of Irwin's criterion – which is equivalent to Griffith's criterion – based on a Paris-type law with a high exponent. This law provides the magnitude of the crack front advancement along the crack front. It scales the magnitude of the advancement such that the point on the crack front with the largest Mode I stress intensity factor advances the most. It is adopted a similar strategy which is suitable for the simulation of 3D crack propagation in brittle materials. The magnitude of crack advancement, $\Delta a(j)$, at a crack front vertex j is taken as,

$$\Delta a(j) = \begin{cases} 0, & \text{if } K_{I,eq}(j) \leq K_{Ic} \\ \Delta a_{max}\left(\frac{K_{I,eq}(j)-K_{Ic}}{K_{I,eq}^{max}-K_{Ic}}\right)^m, & \text{if } K_{I,eq}(j) > K_{Ic} \end{cases} \tag{5.58}$$

where m and Δa_{max} are model parameters. A model similar to Eq. 5.58 is adopted in [100]. The *equivalent Mode I stress intensity factor*, $K_{I,eq}(j)$, at crack front vertex j is computed using the expression proposed by Schöllmann et al. [91] and Richard et al. [93],

$$K_{I,eq}(j) = \frac{1}{2}\cos\left(\frac{\theta_0}{2}\right)\left\{K_I\cos^2\left(\frac{\theta_0}{2}\right) - \frac{3}{2}K_{II}\sin(\theta_0) + \sqrt{\left[K_I\cos^2\left(\frac{\theta_0}{2}\right) - \frac{3}{2}K_{II}\sin(\theta_0)\right]^2 + 4K_{III}^2}\right\} \tag{5.59}$$

where K_I, K_{II}, K_{III}, and θ_0 are computed at crack front vertex j with θ_0 computed using Schöllmann's criterion as described earlier.

If $K_{III} = 0$, then

$$K_{I,eq}(j) = \cos^2\frac{\theta_0}{2}\left(K_I\cos\frac{\theta_0}{2} - 3K_{II}\sin\frac{\theta_0}{2}\right) \tag{5.60}$$

$$= \frac{1}{2}\cos\left(\frac{\theta_0}{2}\right)[K_I(1+\cos\theta_0) - 3K_{II}\sin\theta_0] \tag{5.61}$$

$$= \sqrt{\frac{E}{1-\nu^2}\mathcal{G}_{I/II}(\theta_0)} \tag{5.62}$$

Parameter Δa_{max} represents the maximum displacement magnitude among all front vertices. It is applied to the crack front vertex with the highest equivalent stress intensity factor $K_{I,eq}^{max}$. Parameter m is taken as unity in all problems solved here. It is noted that a crack front advancement is prescribed at a front vertex only if the crack growth criterion Eq. 5.53 is satisfied.

5.5 The Displacement Correlation Method (DCM)

This section presents the expression for the extraction of SIFs based on the Displacement Correlation Method (DCM) [101, 102]. This method is used to extract the SIFs for the problems described in this document. A more detailed derivation can be found in [103]. For this method, the approximation of K_I can be computed as follows

$$K_I^*(r) = \sqrt{\frac{2\pi}{r}}\frac{G}{\kappa+1}[\![u_y(r)]\!], \tag{5.63}$$

where $[\![u_y(r)]\!]$ is the displacement jump in the $\hat{y}$-direction of the crack front coordinate system as in shown in Fig. 5.11.

$$[\![u_y(r)]\!] = u_y(r,\pi) - u_y(r,-\pi) \tag{5.64}$$

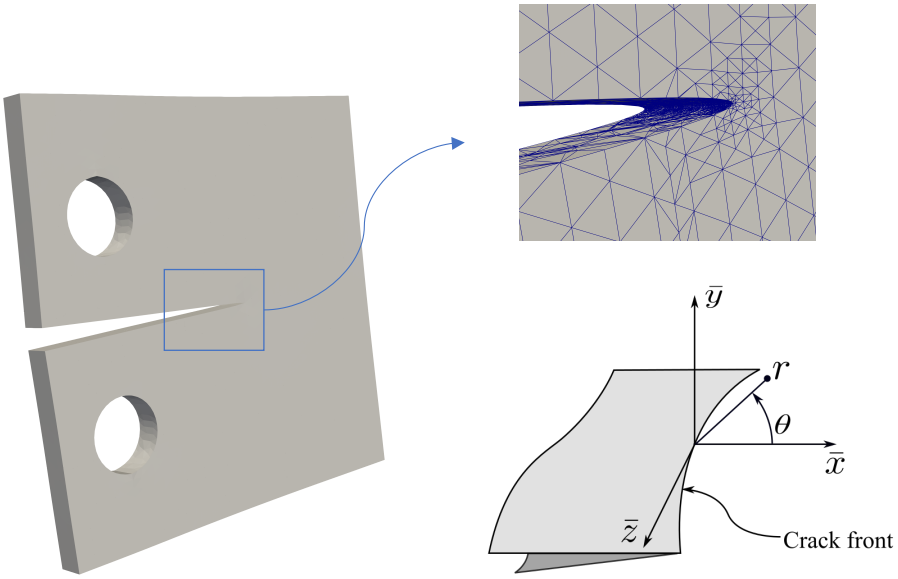

Figure 5.11: Crack front coordinate for fracture mechanics problems

The error of this approximation is $O(r)$. It can be improved using Richardson extrapolation [68] which is given by:

$$\begin{aligned} K_I^*(r_a) &= K_I + \tilde{C} r_a \\ K_I^*(r_b) &= K_I + \tilde{C} r_b, \end{aligned} \tag{5.65}$$

where r_a and r_b define the location of sampling points with $r_a < r_b$. The above equations can be solved for K_I as

$$K_I = \frac{r_b}{r_b - r_a}\left(K_I^*(r_a) - \frac{r_a}{r_b} K_I^*(r_b)\right). \tag{5.66}$$

This approximation of K_I has an error of $O(r^2)$ instead of $O(r)$. Analogous expressions can be derived to calculate approximations for K_{II} and K_{III}.

The averaging scheme is adopted in this work. In this strategy, several pairs of sampling points at r_a and r_b are used to compute approximations of K_I with Eq. 5.66. The final approximation of K_I is taken as the average of those approximations.

Let $K_I^*(r_k)$ be an approximation of K_I evaluated at r_k using Eq. 5.63, $k = 1, ..., N_{\text{sampl}}$, with $r_k < r_{k+1}$. N_{sampl} denotes the total number of sampling points used in the averaging scheme. Let $K_{I,k}$, be an approximation of K_I computed using Eq. 5.66 with $r_a = r_k$ and $r_b = r_{k+1} = r_k + \Delta_k$, i.e.,

$$K_{I,k} = \frac{r_{k+1}}{\Delta_k}\left(K_I^*(r_k) - \frac{r_k}{r_{k+1}}K_I^*(r_{k+1})\right). \tag{5.67}$$

A simple average of $K_{I,k}$, $k = 1, \ldots, N_{\text{sampl}} - 1$, gives the final approximation for K_I

$$K_I = \frac{1}{N_{\text{sampl}} - 1}\sum_{k=1}^{N_{\text{sampl}}-1} K_{I,k}. \tag{5.68}$$

Analogous averaging procedures are used for K_{II} and K_{III}.

In this work, the same distance between two consecutive sampling points is adopted, i.e., $\Delta_k = \Delta = 0.1 h_{\text{min}}$ where h_{min} is the minimum edge size of the elements cut by the crack front. The location of the first sampling point is defined by $\bar{\rho} = r_1 / h_{\text{min}} = 0.4$. The total number of sampling point used for the averaging scheme is $N_{\text{sampl}} = 10$. These parameters are selected based on recommendations from [78].

5.6 Numerical examples

This section presents several examples to illustrate the proposed approach. Reference 2D/3D solutions are provided by standard FEM models in which fibers are discretized with 2D/3D elements and the fiber-matrix interface is modeled using a cohesive law. The nonlinear fiber-matrix model and the propagation criteria adopted here were presented in details earlier in this chapter. The reference solutions are either obtained using Abaqus [66] or given by laboratory experiments as described in the next subsections.

5.6.1 Square domain with horizontal fiber

The problem consists in a square domain of length 4×10^{-3} m (all units are consistent). The fiber is located at coordinates $(0.2 \times 10^{-3}, 2 \times 10^{-3})$, $(3.8 \times 10^{-3}, 2 \times 10^{-3})$, as shown in Fig. 5.12. The displacement is restricted to zero at the left edge ($x = 0$) and a prescribed displacement p_d is applied at the right edge ($x = 4 \times 10^{-3}$ m).

The goal of this problem is to verify the implementation of the formulation presented in the previous chapters, in particular the nonlinear cohesive law at the fiber-matrix interface. Two different approaches are used to solve this problem: 2D GFEM-mERS and 2DFEM. The GFEM-mERS uses the formulation presented earlier in this chapter. The 2DFEM uses the classical FEM formulation built in Abaqus, and the modeling strategies described in [51]. The problem has the following material properties: Young's modulus of the matrix $E_m = 20 \times 10^9$ N/m^2; Poisson ratio of the matrix $\nu = 0.2$; Young's modulus of the fiber $E_f = 500 \times 10^9$ N/m^2. Diameter of the fiber $d_f = 0.1 \times 10^{-3}$ m.

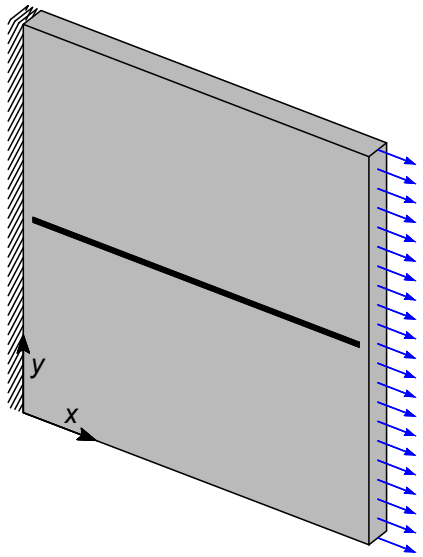

Figure 5.12: Geometry and boundary conditions of the specimen

The debonding law at the fiber-matrix interface is given by a bilinear law illustrated in Fig. 5.4. The bond-slip law consists of an initial elastic branch followed by a softening branch. The constitutive law has the following parameters: $s^{ini}_{max} = 1 \times 10^{-6}$ mm, $\tau^{ini}_{max} = 10 \times 10^7$ N/mm, $s^{ini}_{res1} = 1 \times 10^{-2}$ mm.

A refinement study is performed to investigate the dependence of results on the discretization. Two levels of structured refinements are used for the GFEM-mERS as shown in Fig. 5.13. A *coarse* 3×3 mesh (three bilinear quadrilateral elements each direction) and a *refined* 99×99 mesh. The fiber is parallel to the edges with respect to the background mesh. A similar study is performed in [84].

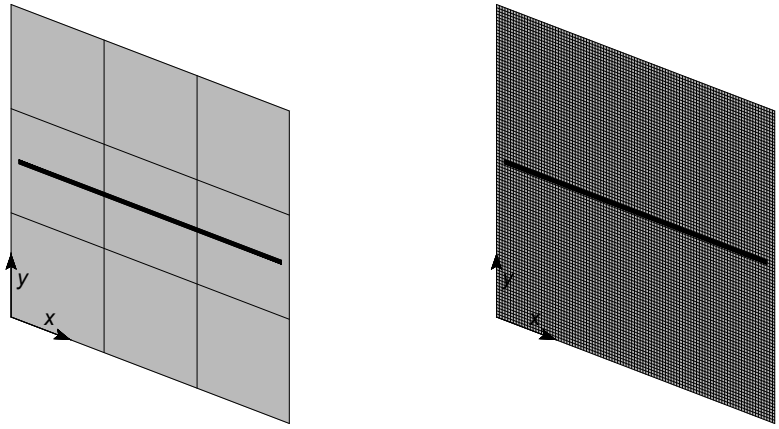

Figure 5.13: 2D meshes used to solve this problem. At the left a 3×3 mesh and at the right a 99×99 mesh

The prescribed displacement p_d is incrementally increased. The reaction force at the left edge is then calculated. Figure 5.14 shows applied displacement (x-axis) vs. resultant force (y-axis). The reaction force is calculated by the summation of the nodal forces of all the nodes located at the left edge of the domain.

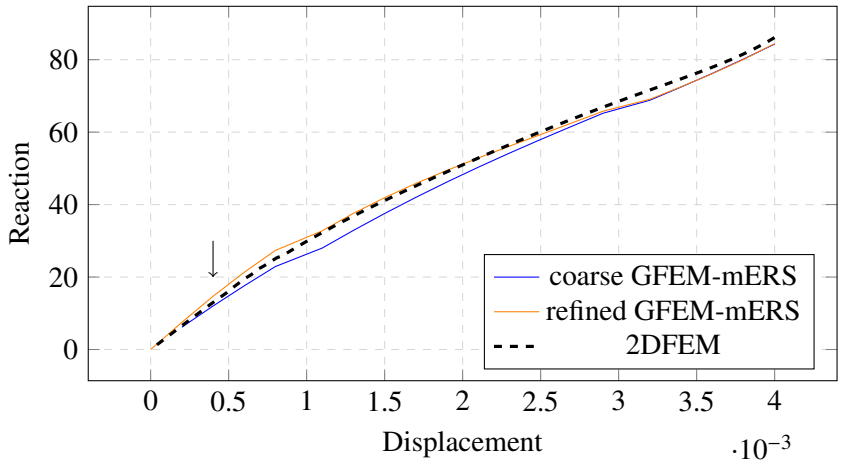

Figure 5.14: Comparative reactions between GFEM-mERS (coarse and refined) and 2DFEM analysis

Results are reported in Fig. 5.14 in terms of load-displacement curves. The curves show the effect of the non-linear fiber-matrix bond slip on the mechanical response (the arrow indicates when the first integration point on fiber-matrix interface experiences a nonlinear slip). Both *coarse* and *refined* meshes are able to capture the nonlinearity of the problem. Further studies are performed in the next sections to explore the effect of different parameters and how they affect the solution using GFEM-mERS and 2DFEM.

The 2DFEM model is solved using bilinear two-dimensional elements using a similar strategy previously reported in Chapter 4 and shown in details in [51]. Cohesive elements are used to implement the cohesive law at the fiber-matrix interface. A very refined mesh is used to obtain the reference 2DFEM solution. An x-y plane view of this mesh is shown in Fig. 5.15, where the von Misses stresses of the final step can also be visualized.

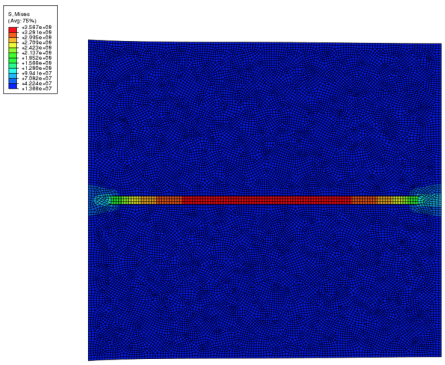

Figure 5.15: A representative von Misses stresses for bidimensional problem solved in Abaqus. It can be observed the difference of the stress magnitude for fiber and matrix

The effect of the diameter of the fiber

This section studies the effect of the diameter of the fiber d_f when comparing GFEM-mERS and 2DFEM models. Because in GFEM-mERS fibers are discretized using 1D elements, the ratio between diameter and length of the fiber should be small in order for the physics of the problem to be correctly captured. For problems where the ratio between diameter and length of the fiber are considerable, it is necessary the 2D representation of both fiber and matrix. This was previously studied by [104] with several numerical experiments. Table 5.1 shows the relative error e (Eq. 5.69) between the two models as d_f increases, where the error is calculated by relative difference between the reaction force of GFEM-mERS (R_{mERS}) and 2DFEM (R_{2DFEM}) measured as in the previous section.

$$e = \frac{|R_{2DFEM} - R_{mERS}|}{|R_{2DFEM}|} \tag{5.69}$$

Table 5.1: Comparative of reactions for different diameters d_f of the fiber

d_f	GFEM-mERS	2DFEM	$e(\%)$
0.1	84.3097	86.0149	1.98
0.05	78.7361	79.0259	0.37
0.025	74.1156	74.3098	0.26
0.01	70.2934	70.3808	0.12
0.001	67.4173	67.5187	0.12

Table 5.1 shows that the error becomes greater as d_f (mm) increases. The difference between models grows from $d_f = 0.05$ to $d_f = 0.1$ and it is expected to grow even faster for larger d_f. This highlights an important aspect to be observed when solving fiber-reinforced composite problems using the GFEM-mERS. This particular detail was taken into account for the other problems solved in this work.

Ratio between Young‘s modulus of fiber and matrix

The ratio between fiber and matrix Young‘s modulus is studied here. This is given by the variable $r_{fm} = \frac{E_f}{E_m}$. Because the stress magnitude can be very different for both materials, this can be a source of error between FEM and the GFEM-mERS models. The e is calculated as in the previous section.

Table 5.2: Comparative of reactions for different r_{fm}

r_{fm}	GFEM-mERS	2DFEM	$e(\%)$
25	84.3097	86.0149	1.98
50	89.6337	91.5213	2.06
100	94.3004	96.4069	2.19
200	97.9834	100.3928	2.22
400	100.5059	103.3373	2.15

Table 5.2 shows that higher values of r_{fm} slightly increase the numerical error for GFEM-mERS models when compared to 2DFEM. Although the reaction (global variable) is not entirely affected by r_{fm}, the enormous contrast of variables at the interface fiber-matrix for GFEM-mERS is the potential (and dangerous) source of error to be considered. This behavior was also noticed by [104].

Since the r_{fm} strongly affects quantities nearby the interface (where the different materials are located), it also affects the convergence of the nonlinear scheme. This will be quantified and studied later in this section when the slip at the interface is measured.

Effect of prescribed displacements magnitude

This section compares the error for some prescribed displacements p_d for two diameters of the fiber ($d_f = 0.1$ and $d_f = 0.001$). The values for p_d are 0.001, 0.002, 0.003 and 0.004. The experiments are performed using a refined 99×99 mesh. Error e is calculated using Eq. 5.69.

Table 5.3: Error for different prescribed displacements p_d for diameter of the fiber $d_f = 0.1$

p_d	GFEM-mERS	2DFEM	e (%)
0.001	30.96	30.275	2.26
0.002	51.15	52.548	2.66
0.003	66.86	68.425	2.29
0.004	84.41	86.015	1.87

Table 5.4: Error for different prescribed displacements p_d for diameter of the fiber $d_f = 0.001$

p_d	GFEM-mERS	2DFEM	e_r (%)
0.001	23.884	23.767	0.49
0.002	42.154	42.041	0.27
0.003	53.821	53.710	0.21
0.004	67.420	67.519	0.15

As observed earlier, it can be seen that problems with a smaller diameter d_f have a lower error. Here, however, it can be also observed that this error is relatively constant through the entire nonlinear process. It is clear the difference in the magnitude of the error between Tabs. 5.3 and 5.4. It is also shown the greatest error is not necessarily for the largest p_d. This shows the influence of the nonlinear fiber-matrix bond-slip law on the mechanical response for the problem. The initial stiffening effect of the fiber reduces with increasing p_d. As also observed by [84], the relative error is larger during the initial loading phase since the fiber-matrix bond-slip law develops a very steep and nonlinear behavior during this stage.

Study of the slip behavior

The slip along the fiber is computed and studied in this section. The slip is a particularly important variable for the nonlinear cohesive law at the matrix-fiber interface. Figure 5.16 shows the slips for the different prescribed displacements p_d. The parameters are the same as in Sec. 5.6.1.

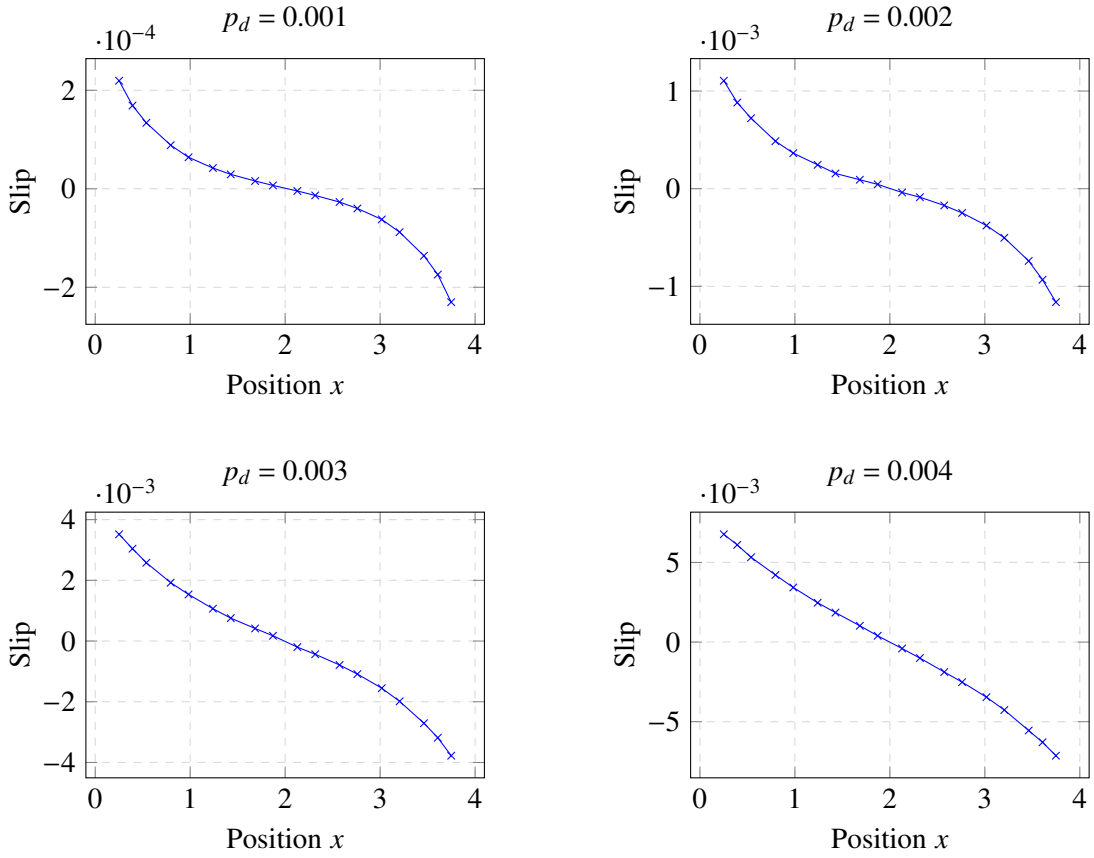

Figure 5.16: Slip for different d prescribed applied

After the peak load is achieved the shape of the slip rapidly changes as can be observed in Fig. 5.16. The largest absolute value of the slip at the ends of the fiber is also increased. In order to study how the peak load in the cohesive law affects the slip of the problem at $p_d = 0.001$, the variable τ_{max}^{ini} (N/mm) in Fig. 5.4 is parametrized. Figure 5.17 shows the results for different values of τ_{max}^{ini}. A larger τ_{max}^{ini} for matrix-fiber interface makes fiber and matrix displace together and, consequently, a smaller slip.

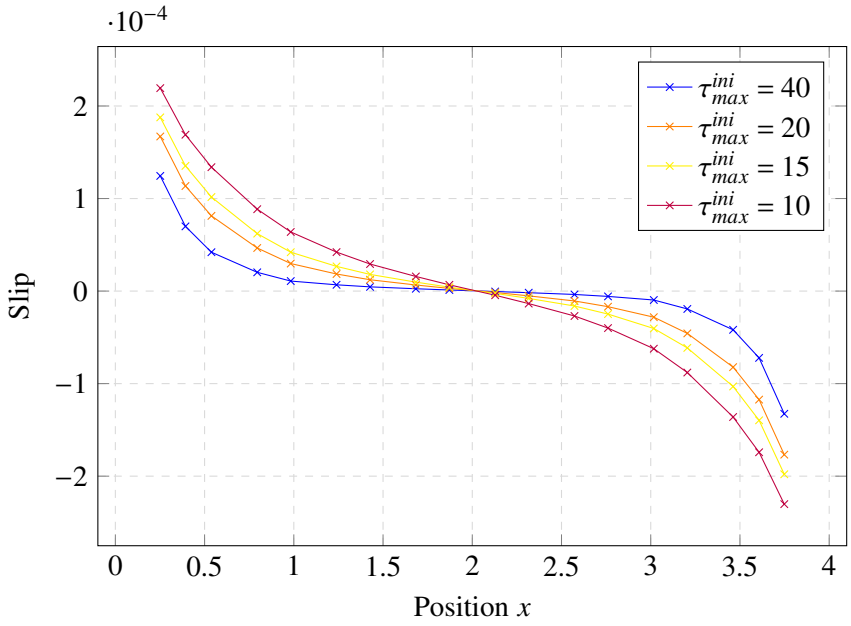

Figure 5.17: Slip for the fiber for different τ_{max}^{ini}

The ratio between fiber and matrix Yong's modulus r_{fm} previously studied in Sec. 5.6.1 is now studied in the slip point of view. Figure 5.18 shows the slip of the fiber for a large ratio of Young's modulus of the fiber and matrix ($r_{fm} = 10^6$). A smooth representation of the fiber slip is particularly important for the nonlinear process of the analysis. For this investigation, it can be observed the arise of oscillations when the coarse mesh is used to solve problems with very large r_{fm}.

The oscillations are observed especially near the extremities of the fiber as pointed by the dashed square in Fig. 5.18. Although this seems to be an extreme case, it is a problem to be aware when using the method. This issue (for problems solved in this chapter) can be addressed by refining the region around the fiber. A similar numerical instability was observed in [104] for problems with very large bond stiffness parameters.

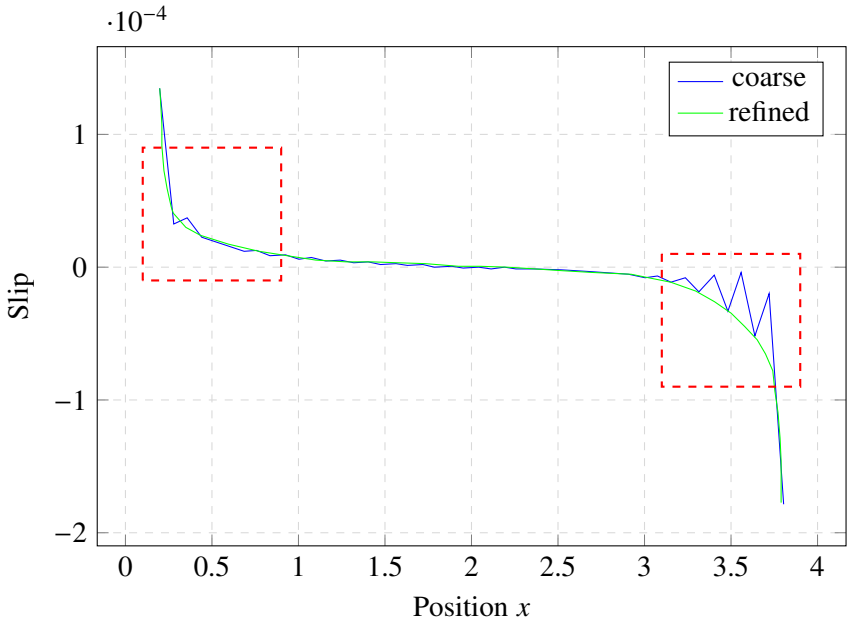

Figure 5.18: Slip for the fiber for different peak

A smooth representation of the quantities at the interface between two different materials is particularly important for the nonlinear analysis. For the problems solved in this research, a mesh refinement around the region of the fiber was able to fix possible issues regarding this topic.

Study of volume fraction

In order to study the volume fraction of fiber-reinforced composites, a large number of fibers is added to a unitary specimen. The material properties for matrix and fiber are the same as the previous problem, fibers have diameter $d_f = 0.005\ mm$ and bilinear cohesive law is used one more time at the fiber-matrix interface (same parameters as the previous section). The goal is to measure the error between GFEM-mERS against 2DFEM model as the number of fibers increases in a representative volume of the specimen. As a boundary condition, a prescribed displacement with linear variation across axis y is applied as shown in Fig. 5.19 (maximum absolute prescribed displacement equal to $d = 0.1\ mm$ and a relative angle θ).

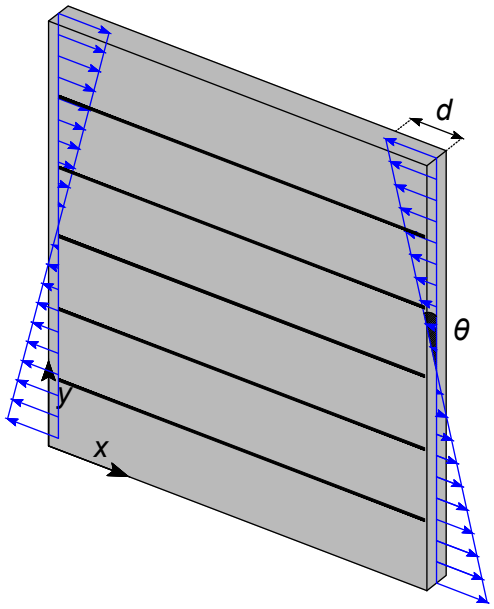

Figure 5.19: Geometry and boundary conditions of the specimen for volume fraction study

Fibers are equally spaced in the y direction as shown in Fig. 5.20. Five different fiber volumes are studied here: 5, 10, 20, 50, and 100 fibers. The fiber volume ratio can be calculated as: $V_f = \frac{v_f}{v_c}$, where v_f is the volume of fibers and v_c is the volume of the composite. Therefore the problems here analyzed enclose fiber volume ratio of 50%, which has many applications in engineering, [105].

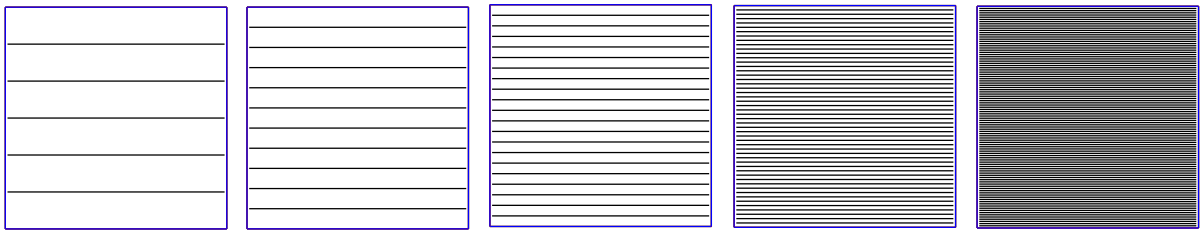

Figure 5.20: Fiber volumes tested in this experiment: 5, 10, 20, 50 and 100 fibers

Figure 5.21 shows how the composite is modeled using Abaqus. The figure shows two representative volumes: the specimen with 5 fibers (left) and the specimen with 100 fibers (right). The geometries of the models are shown at the top of the figure while the corresponding meshes are shown at the bottom of the figure. The figure also shows the fiber modeling details for the specimen with 100 fibers. It can be seen that fibers are modeled as 2D elements (with cohesive elements at the fiber-matrix interface). The mesh in Abaqus is automatically generated by setting the maximum dimension of the element (very small elements are used in order to obtain an overkill mesh solution).

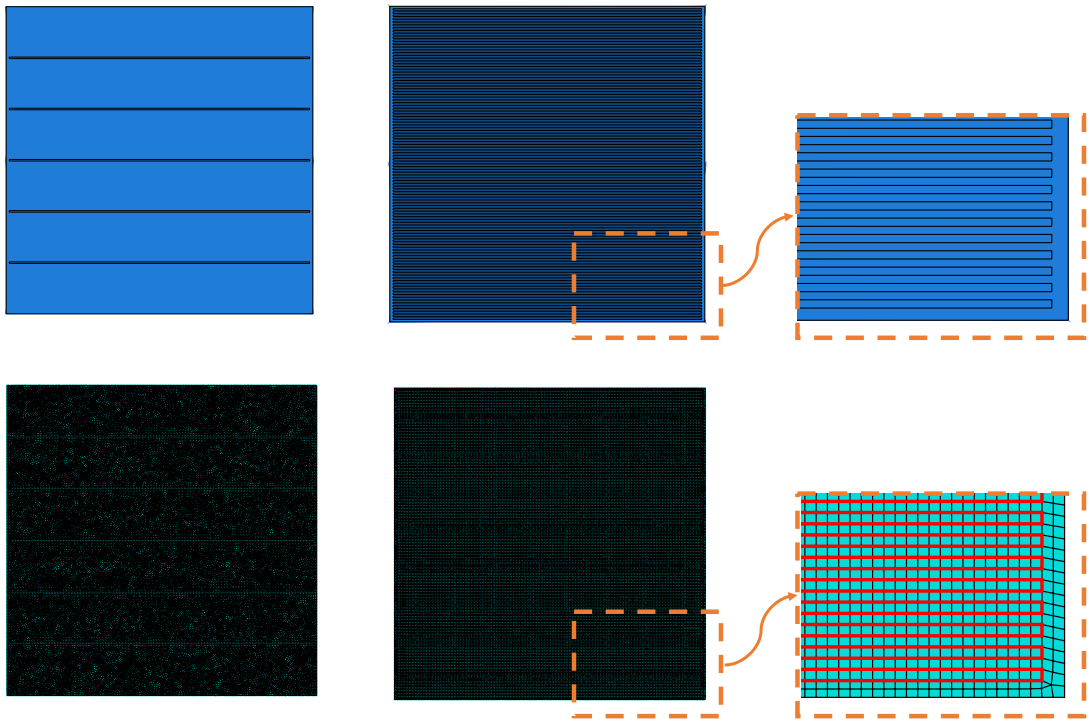

Figure 5.21: Fiber modeling using Abaqus. Model with 5 fibers (left) and 100 fibers (right). Fibers are modeled as 2D elements with cohesive elements at the fiber-matrix interface

.

Figure 5.22 shows the applied boundary condition in Abaqus (left), the deformed shape for the GFEM-mERS analysis (specimen with 5 fibers), and the deformed shape for the 2DFEM (also specimen with 5 fibers).

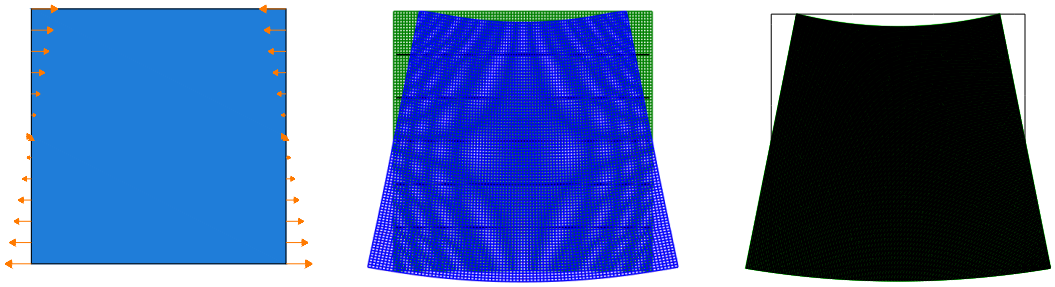

Figure 5.22: Deformed shape for the specimen. Boundary conditions at the left, deformed shape using the GFEM-mERs at the center and the deformed shape for the 2DFEM simulation at the right

The error e_s corresponding to the slip is measured by the relative difference between fiber slip computed with the GFEM-mERS (s) and 2DFEM ($\hat{s}$). The e_s is measured using the following discrete L^2-norm at $N = 5$ points through the first fiber (from the bottom).

$$e_s = \frac{\sqrt{\sum_{i=1}^{N}(s_i - \hat{s}_i)^2}}{\sqrt{\sum_{i=1}^{N}(\hat{s}_i)^2}} \tag{5.70}$$

Figure 5.23 shows how the error e_s progresses as the number of fibers increases. It can be observed that the error increases as the number of fibers increases, but they is still relatively small even for $V_f = 50\%$.

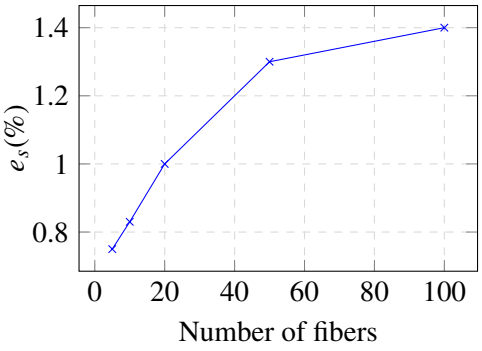

Figure 5.23: Error e_s for several volume fraction of fibers

Two others quantities of interest are measured for the specimen with 5 fibers (lowest volume ratio among the specimens presented in this section) and specimen with 100 fibers (highest volume ratio among the specimens presented in this section): the moment M along the edges (calculated using the reaction forces along the domain edge) and strain energy U of the problem. The goal here is to show how these quantities progress for two different fiber volumes as the angle θ increases (through displacement control applied at the edge). Figure 5.24 shows how the moment changes as a rotation θ is applied for specimens with different fiber volumes.

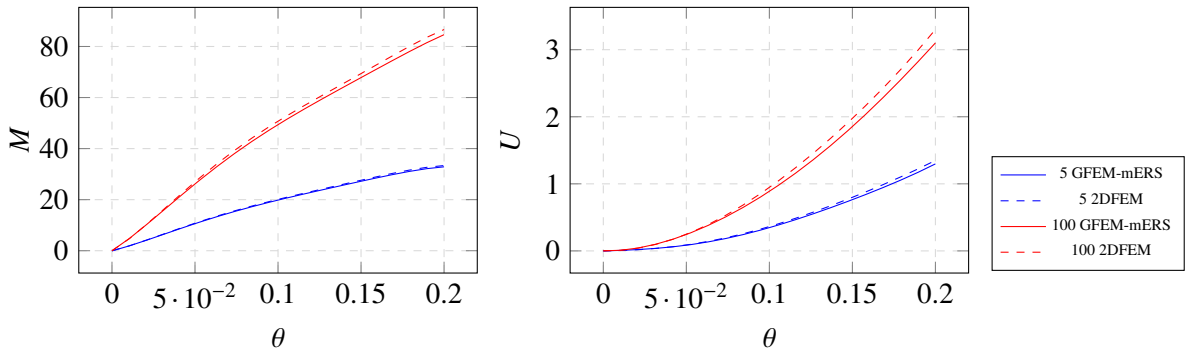

Figure 5.24: Quantities of interest (M and U) for two fiber volume fractions

The experiments show that the GFEM-mERS and 2DFEM slightly deviate as the rotation θ increases (for both specimens). This deviation is slightly bigger for the model with 100 fibers, which shows that the volume of fibers can potentially be a source of error in the model. The analysis in Fig. 5.23 and 5.24, however, indicate that error is relatively small even for a high volume fraction of fibers ($V_f = 50\%$). This shows that the error due to this variable is not significant for the numerical experiments henceforth performed in this research. An extension to randomly oriented fibers, higher fiber volume fractions, higher dimensional spaces, or different boundary conditions (including periodic boundary condition, for example) is indicated and can be the object of future studies.

5.6.2 Prismatic bar with fibers

After extensively solved a bidimensional problem in the previous sections, the following problems have three-dimensional domain composed of tetrahedral elements. The problem is solved using the GFEM-mERS theory described in this chapter and later compared to a 3DFEM model solved in Abaqus.

Two parallel fibers

The fiber-reinforced prismatic bar shown in Fig. 5.25 is solved in this section. The bar is constrained at one of the extremities and incrementally prescribed displacement is applied at the other end of the bar. Two fibers are embedded into the bar and they are defined by the following segments:
$f_1 = [(1.0, 0.25, -0.375), (9.0, 0.25, -0.375)]$, and $f_2 = [(1.0, 0.25, -0.625), (9.0, 0.25, -0.625)]$.

The moduli of elasticity of matrix and fiber are taken as $E_{\mathrm{m}} = 1.0 \times 10^4\ N/mm^2$ and $E_{\mathrm{f}} = 5.0 \times 10^5\ N/mm^2$, respectively. The matrix Poisson's ratio is set to $\nu = 0.0$, and the debonding law at the fiber-matrix interface is given by the bilinear law described previously .

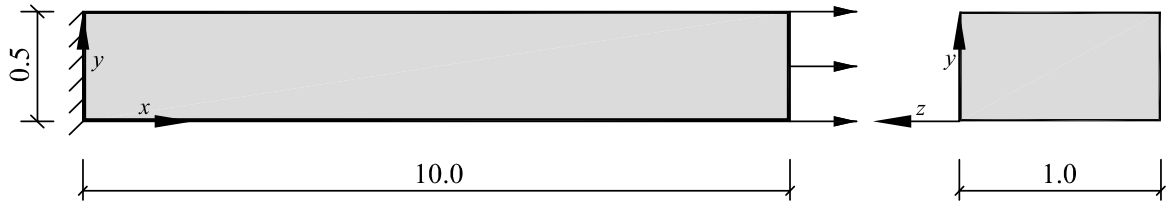

Figure 5.25: Prismatic bar with axial displacement

This problem is incrementally more complex compared to the problem presented in Sec. 5.6.1 since now two fibers are located into a 3D domain. Figure 5.25 shows the prescribed boundary conditions for both Abaqus and GFEM-mERS model. Figure 5.26 shows the mesh used for this problem (mERS and 3DFEM).

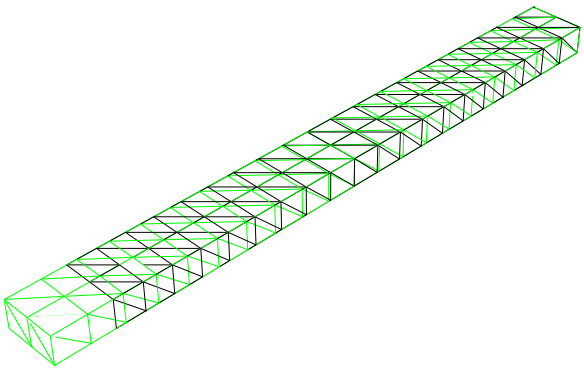

(a) Mesh for the 3DFEM mesh

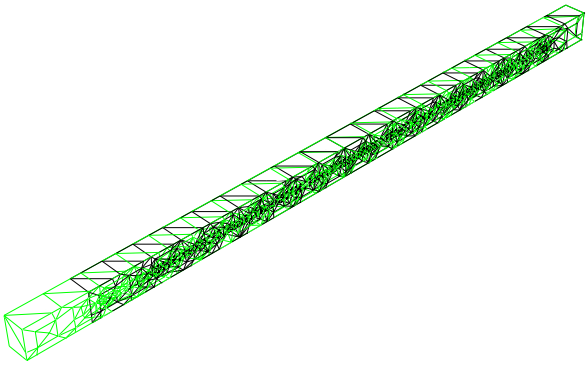

(b) Cut view for 3DFEM at the mid span of one of the fibers

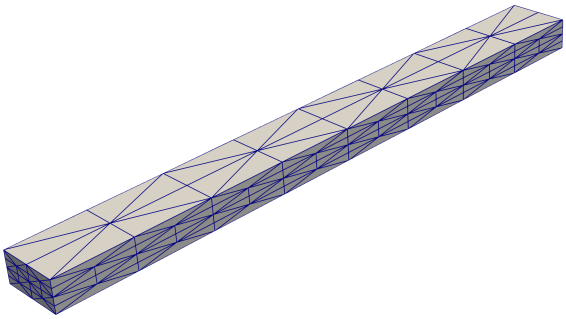

(c) Mesh for the GFEM-mERS

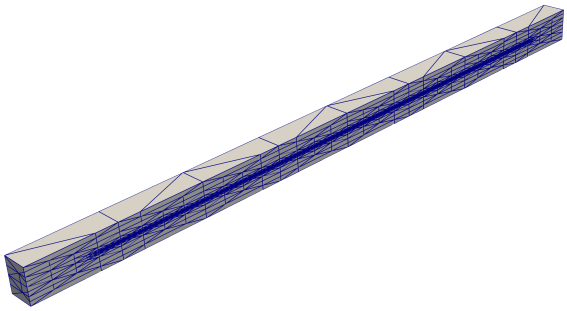

(d) Cut view for GFEM-mERS at the mid span of one of the fibers

Figure 5.26: Comparative between meshes for 3DFEM and GFEM-mERS

Figures 5.26(a) and (b) show the final deformed shape (green) compared to the original configuration of the bar (black) for this problem. It can be observed that mesh refinement is necessary to match the fiber and matrix meshes (for 3DFEM). In addition to that, a very refined mesh is also necessary near the fiber length in order to capture the nonlinearity of the problem (as discussed in Sec. 5.6.1). This adds some extra layer of complexity when solving the problem using a 3DFEM approach.

Figures 5.26(c) and (d) show the respective meshes for the problem solved using GFEM-mERS. Because the fiber mesh does not need to match the matrix mesh this problem can be highly refined without adding geometrical complexities for the mesh generation process.

Similarly to the study performed in Sec. 5.6.1, Fig. 5.27 shows the reaction forces at the domain edge for incrementally prescribed displacements. It can be observed that the values of GFEM-mERS agree well with the 3DFEM analysis performed in Abaqus (arrow indicating the nonlinearity at the interface).

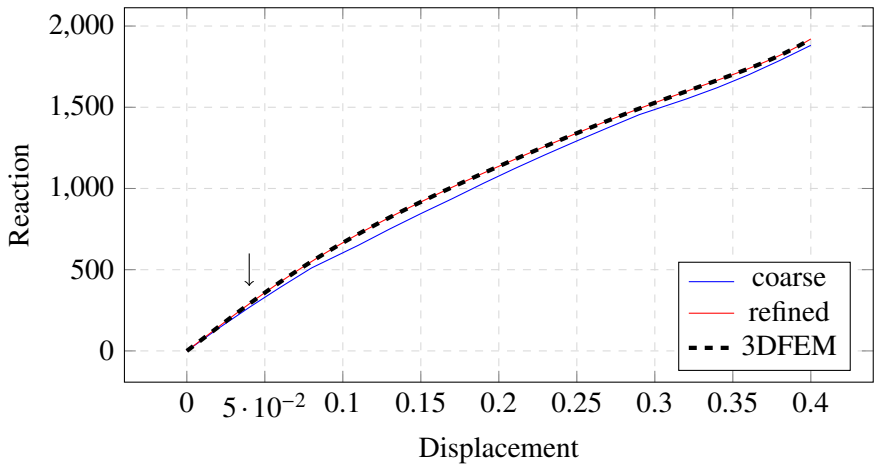

Figure 5.27: Comparative reactions between GFEM-mERS and 3DFEM analysis

Prismatic bar with diagonal fiber

The fiber-reinforced prismatic bar with diagonal fiber is considered again in this section. Figure 5.28 shows the fiber orientation for this problem. The fiber is defined by the segment $f_1 = [(0.2, 0.1, -0.1), (9.8, 0.4, -0.9)]$ embedded into the bar. The same material properties as in the previous section are adopted. The cohesive law at the fiber-matrix interface is also the same.

(a) Fiber orientation -view 1 **(b)** Fiber orientation - view 2

Figure 5.28: Prismatic bar with diagonal fiber

This problem is more complex than the previous one because the displacement is fully 3D. This produces a more complex fiber-matrix interaction. An extensive study on *hp* refinement of this problem using GFEM-mERS was previously performed by [51]. Figure 5.29 shows the mesh for this model. It can be seen that the mesh is highly refined around the fiber in order to reproduce the mechanical behavior at the matrix-fiber interface.

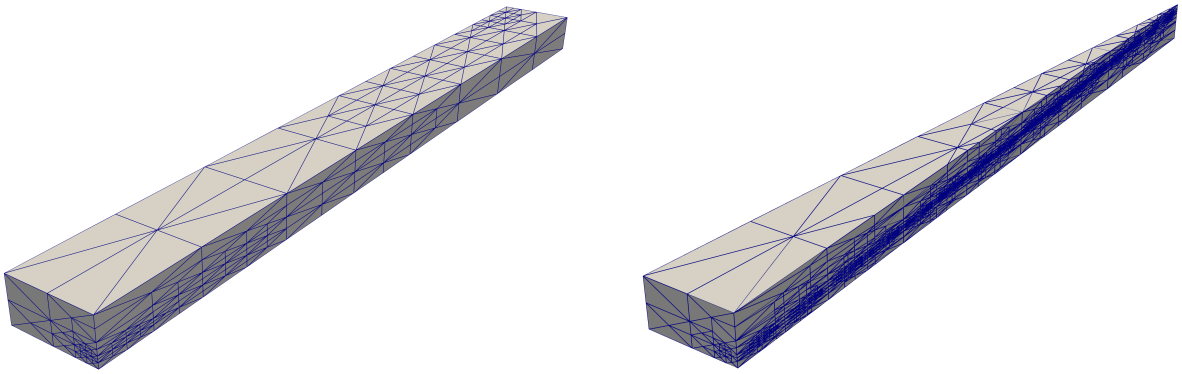

(a) Mesh for the GFEM-mERS mesh

(b) Cut view for GFEM-mERS at the mid span of the fiber

Figure 5.29: Mesh used for GFEM-mERS model

The GFEM-mERS approach is again compared with the 3DFEM model solved in Abaqus. Figure 5.30 shows the reaction forces at the edge for incremental displacements. It can be observed that the GFEM-mERS solution matches well the 3DFEM model.

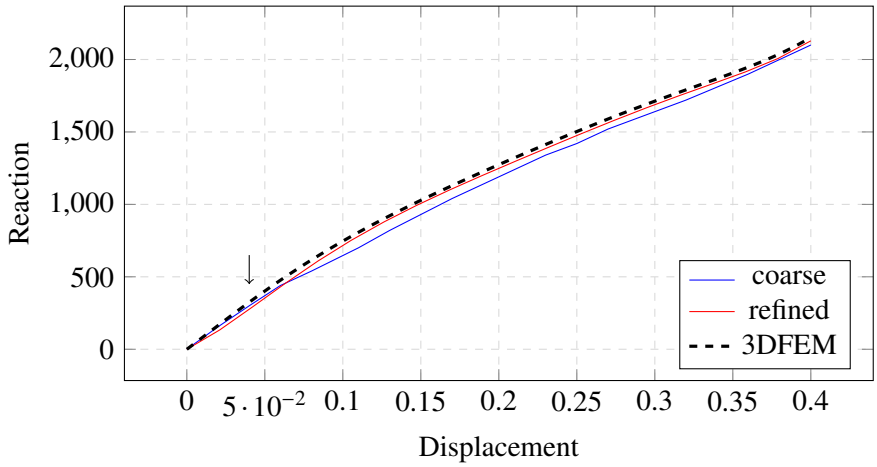

Figure 5.30: Comparative reactions between GFEM-mERS and 3DFEM analysis

5.6.3 Prismatic tensile specimen with a pre-defined crack

The cracked prismatic tensile specimen shown in Fig. 5.31 is analyzed in this section using the GFEM-mERS. The predefined crack is at the middle plane of the specimen. A single fiber bridges the crack faces. This problem was proposed and solved in Kang et al. [20] using a lattice method.

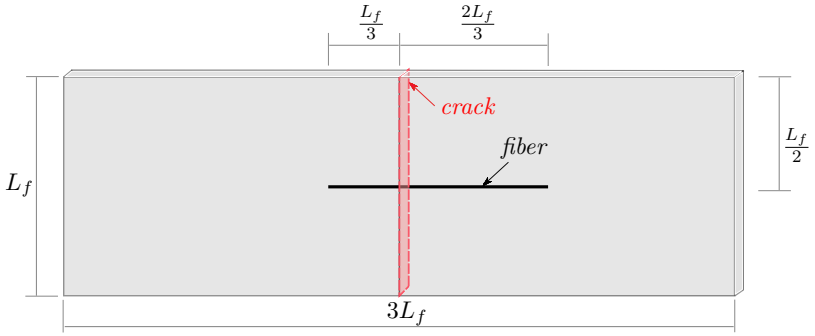

Figure 5.31: Prismatic tensile specimen with a pre-defined crack

A previous solution using the GFEM-mERS was also performed by [51]. Here, however, the problem uses a nonlinear debonding law between fiber and matrix. Fig. 5.32 shows the results for GFEM-mERS. This problem uses the same material parameters as in the previous sections (including those for the bilinear cohesive debonding law presented in Sec. 5.3.2).

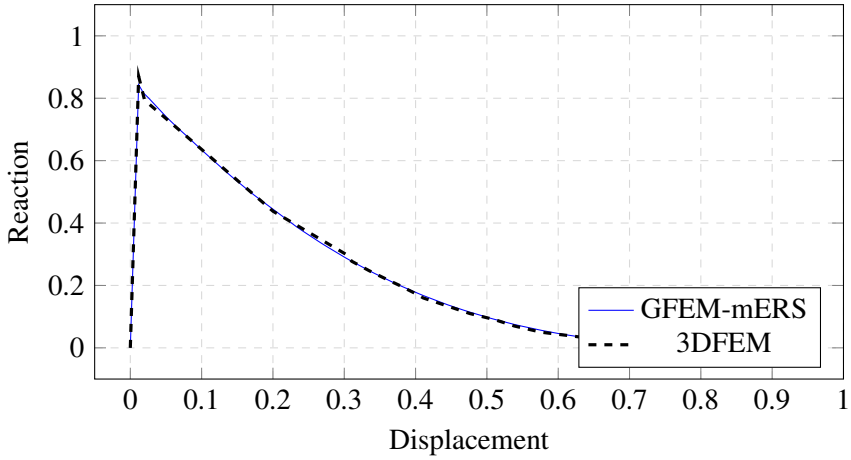

Figure 5.32: Comparative reactions between GFEM-mERS and 3DFEM

Figure 5.33 shows the mesh along the fiber length. This attests to the complexity of the problem solved using 3DFEM approach. It is necessary for a complex mesh generation fit interface between fiber and matrix. The stress of the problem is also shown in Fig. 5.33 indicating the difference in magnitude between fiber and matrix.

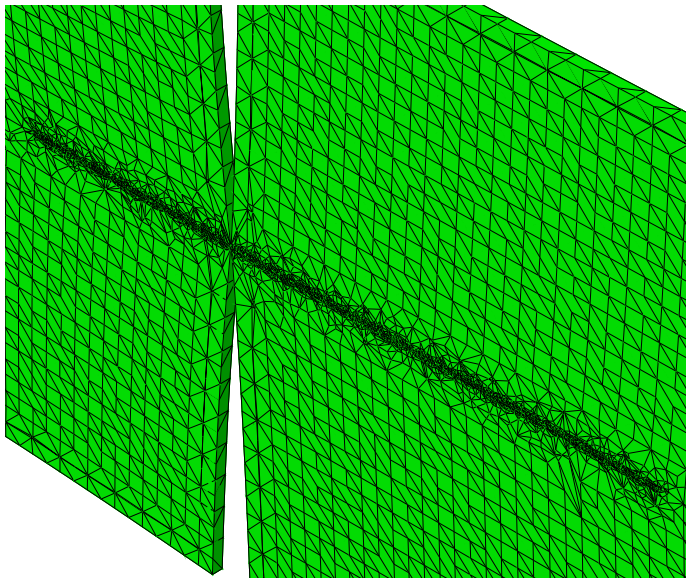

(a) Mesh along the fiber (cutting plane)

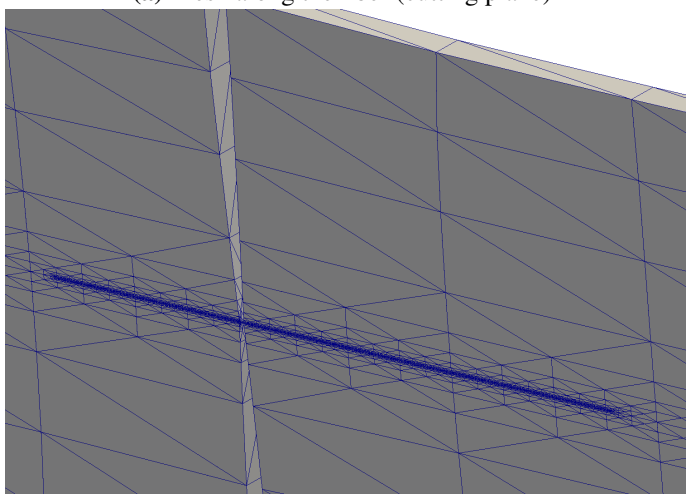

(b) Mesh along the fiber (cutting plane)

Figure 5.33: Mesh along the fiber for 3DFEM and GFEM-mERS

5.6.4 Fiber-reinforced compact tension specimen

This example consists of a composite specimen with discrete glass fiber tows in an epoxy matrix. The Compact Tension (CT) specimen geometry is based on the ASTM D5045 standard. Fibers tows are perpendicular to the crack plane as shown in Fig. 5.34. Each tow is idealized as a single fiber in the computational models adopted here.

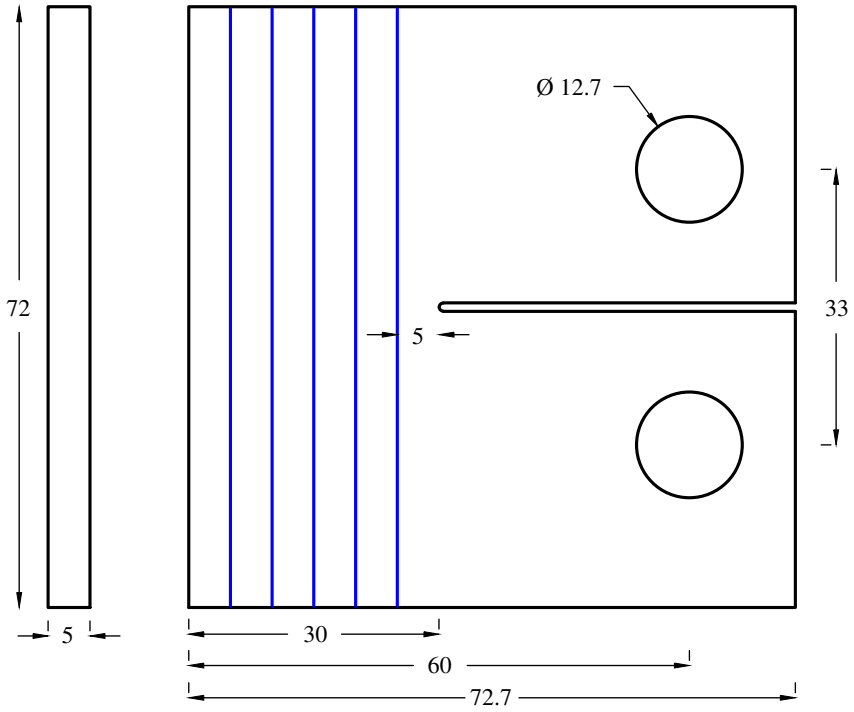

Figure 5.34: Compact Tension specimen with five fiber tows embedded in an epoxy matrix. All dimensions are in mm

The static crack version of this problem was studied in [51] where this problem is solved using the GFEM-mERS and 3DFEM and an extensive study of SIFs is performed. There, however, the interaction between fiber and matrix does not follow a nonlinear cohesive law. It was shown that a good match between experimental and numerical models is obtained for the peak load. The numerical models previously solved in [51] are considerably simpler compared to the one proposed here because crack propagation and nonlinear debonding law are not involved.

Here, the problem is studied with respect to the propagation point of view. The numerical simulation is compared to the laboratory results obtained from [69]. The simulation of this problem is complex and the accurate numerical simulation of the problem requires one to model the nonlinear interaction between fiber and matrix, crack propagation in the matrix material, and fiber breakage. Therefore the use of techniques such as the ones described in Sec. 5.3 (GFEM, mERS and computational geometry) and Sec. 5.4 (propagation algorithm), are essential to the accurate simulation of this experiment.

The following parameters are adopted for this problem: Modulus of elasticity of the epoxy matrix $E_{\mathrm{m}} = 0.82\,GPa$; Poisson's ratio of the matrix $\nu = 0.35$; Modulus of elasticity of fibers $E_{\mathrm{f}} = 72.4\,GPa$; Area of each fiber tow (type 158B-AA-675) $A_{\mathrm{f}} = 0.33\,mm^2$; Fracture toughness of the matrix $K_{\mathrm{Ic}} = 20\,N/\sqrt{mm}$; Ultimate tensile strength of the fiber $\sigma_{ult} = 2GPa$. The matrix-fiber interaction is described using the bond-slip law proposed by [81] as described in details in Sec. 5.3.2. The control points of the law are the following: $s^{ini}_{max} = 0.0001\,mm$, $\tau^{ini}_{max} = 6\,N/mm$, $s^{ini}_{res1} = 0.01\,mm$, $\tau^{ini}_{res1} = 1\,N/mm$, $s^{ini}_{res2} = 10\,mm$, and $\tau^{ini}_{res2} = 0.9\,N/mm$.

Figure 5.35 shows the mesh and boundary conditions of the specimen. Quadratic tetrahedral elements enriched with the Heaviside and singular functions defined in Sec. 3.2 are used to discretize the cracked specimen. The crack surface is defined using an explicit triangulation as shown in Fig. 4.25. Linear 1D elements are used for fiber elements. The prescribed nodal displacements at the opening of the CT specimen are incrementally increased to reproduce the experimental conditions.

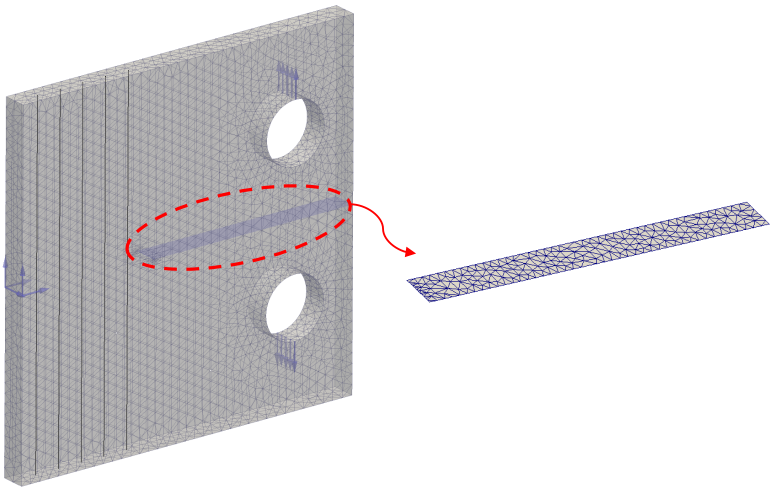

Figure 5.35: GFEM discretization of specimen. Fibers are discretized with GFEM-mERS and an explicit representation of the crack surface is adopted

Before simulating to the problem of the specimen with five fibers, the fracture behavior was studied for two simpler specimens: unreinforced and one-fiber specimen. Figure 5.36 shows the optical images of the experiment performed by [69]. It is observed that the crack propagates horizontally until the crack stop location (a small hole added to ensure the change in crack length was constant in the laboratory experiment). For the specimen with one fiber, the crack similarly advances to the crack stop in one step. During this event, the fiber tow is debonded (the dark region in Fig. 5.36 on the fiber surface).

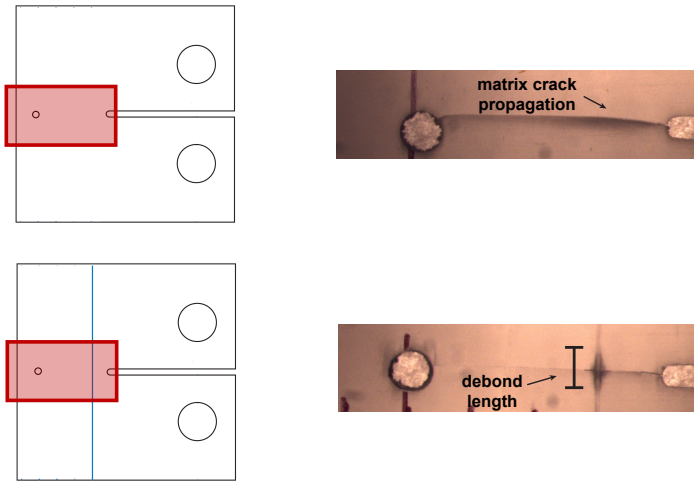

Figure 5.36: Optical images corresponding to unreinforced and specimen with one fiber, [69]

Representative experimental load-displacement curves for these specimens are shown in Fig. 5.37. The peak load can be observed for both unreinforced and reinforced specimen before the crack propagates in a single step. Fiber debonding is observed in the specimen with one fiber, as shown in Fig. 5.37. This is reflected in the load-displacement curve shown in Fig. 5.37(b). These two experiments are considerably simpler than the crack propagation for the specimen with five fibers and are used here to calibrate the material and fiber properties.

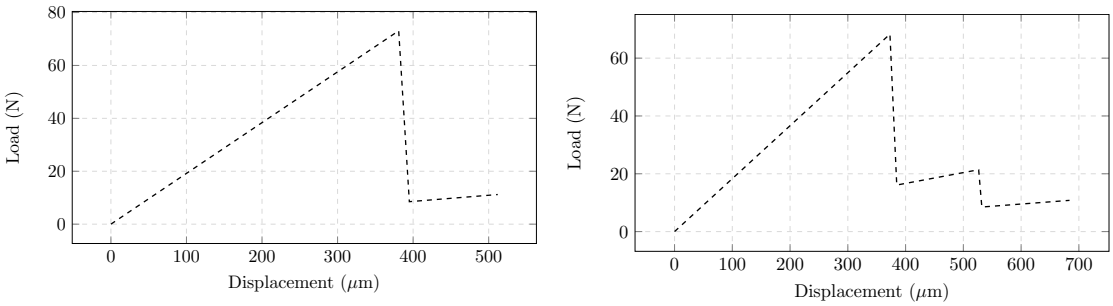

(a) Unreinforced specimen **(b)** Specimen with one fiber

Figure 5.37: Experimental load-displacement curve for the specimen with zero, and one fiber, [69]

For the problem with five fibers, multiple stages of crack propagation are observed. This is an indicative of the fiber tows slowing the crack growth. Three stages are shown in Fig. 5.38. The first stage shows the pre-crack without propagation. For the second stage, the crack progresses from the pre-crack to the second fiber while the first fiber is still not broken. Some additional debonding occurs in the first fiber until it breaks. In the third stage the crack progresses to the fourth fiber, which causes the breakage of the second fiber. Debonding in the third and fourth fibers is observed.

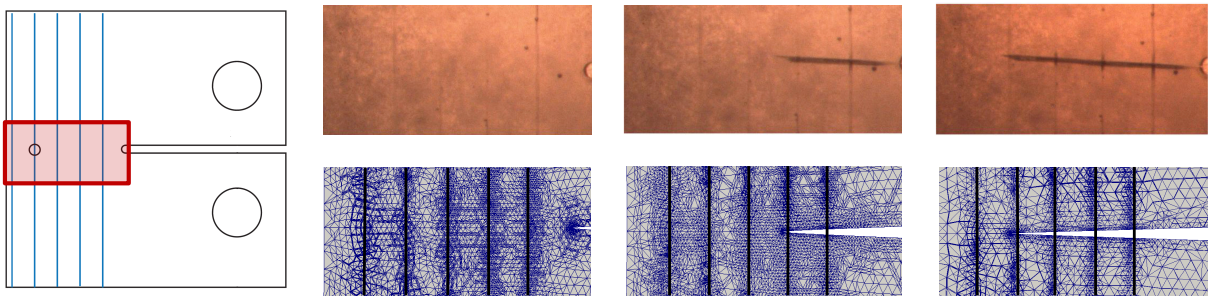

Figure 5.38: Comparative between experimental, [69], (on top) and numerical (below) models for the three stages of the crack propagation

As shown in Chapter 4 the static version of problem can predict with relative accuracy the peak load and when the crack propagation initiates. When combined with the crack propagation framework, that model can reproduce the peak load of this problem with some accuracy, but fails to reproduce later stages of the problem (Noncohesive curve in Fig. 5.39). This shows that the nonlinear debonding behavior plays an important hole for this problem and has to be taken into account.

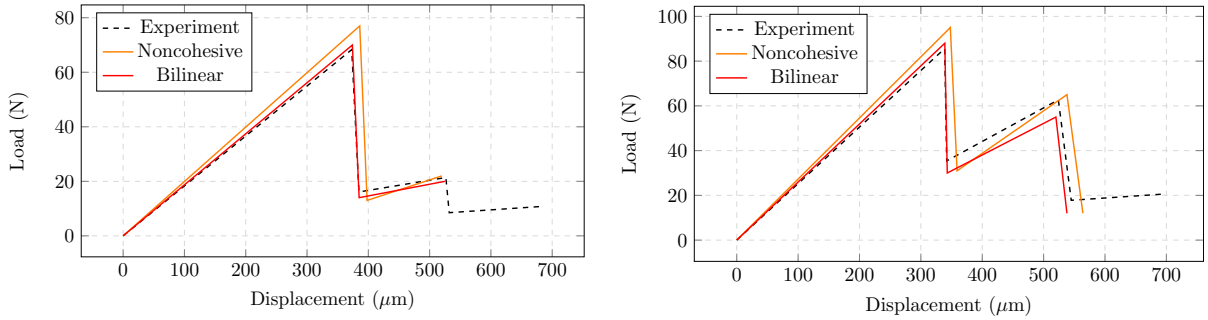

(a) Specimen with one fiber

(b) Specimen with five fibers

Figure 5.39: Load-displacement curve for the specimen with one and five fibers

The specimen with one and five fibers are solved again using the bilinear cohesive law of Sec. 5.3.2 with the parameters indicated earlier in this section. The nonlinear bilinear law can definitely approximate better the problem (peak load and stiffness of the specimen), but it fails at the later stage as can be seen in Fig. 5.39(b). This suggests that the frictional part of the law should be taken into account for this problem in order to correctly reproduce the experiment.

Finally, the GFEM-mERS results using the PCHIP cohesive law to describe the matrix-fiber interface are compared to experimental data provided by [69]. Figure 5.40 shows the load-displacement curve for the applied boundary condition described in Fig. 4.25. Displacement control is applied for the nonlinear process. This procedure is analogous to the one adopted for the experiments reported in [69]. The adopted parameter for crack propagation $\Delta a_{max} = 0.1mm$ and 300 steps were chosen based on the experience and have guaranteed the smoothness of this problem. A detailed explanation of these parameters and extra examples about crack propagation can be found in Appendix B.

The results show very good agreement between numerical and experimental results. The circled numbers in Fig. 5.40 show where the stages of crack propagation from Fig. 5.38 are located along the loads-displacement curve of the problem. From the beginning of the experiment until point ①, the first stage described in Fig. 5.38 is observed. From ① until ② the second stage is observed. It is important to note that the simulation was able to capture the stable crack propagation with several steps while for the laboratory experiment the crack grows as a single snap. This phenomenon is reflected in the first descending part of the interval ① - ② in Fig. 5.40. The load continue to increase until the second peak load is reached at point ②. After that, a second propagation is observed with similar characteristic as the first one. Again, the numerical crack propagation is captured with several steps while for the laboratory experiment the crack propagates in a big snap.

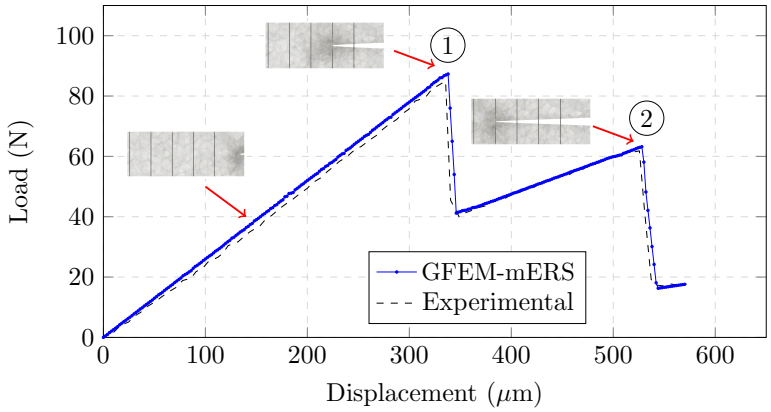

Figure 5.40: Comparative between GFEM-mERS and experimental analysis

The excellent match between GFEM-mERS and experimental was possible for this problem. It is important to note that high accuracy between models was obtained for an experiment under very controlled parameters. For this case, the adopted numerical framework clearly took advantage of the prior physical test of the specimens to calibrate the adopted material parameters. It was shown, however, that model (GFEM-mERS) combined with the appropriate cohesive law (PCHIP) can be used to described this class of problems with success.

Figure 5.41 shows the details for the propagation stages previously shown in Fig. 5.38. The matrix elements are made opaque in order to show where the fibers are located, this is the reason why the hazy effect is observed in the picture. It is important to highlight one more time that the fibers do not need to be meshed to fit the tetrahedrons (matrix material). They are introduced in the model using the GFEM-mERS

previously discussed. Together with the global view of the specimen, it is shown a zoomed lateral view of the specimen and the crack surface as the crack propagates.

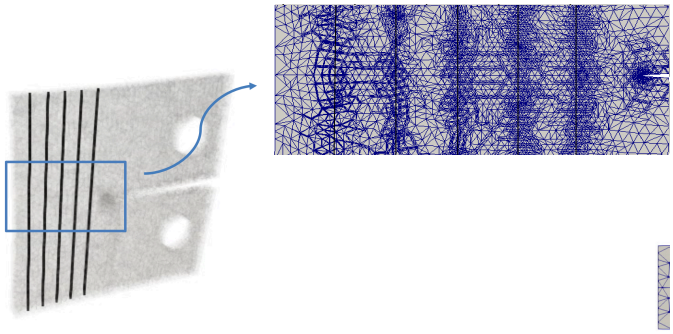

(a) Stage one: precrack

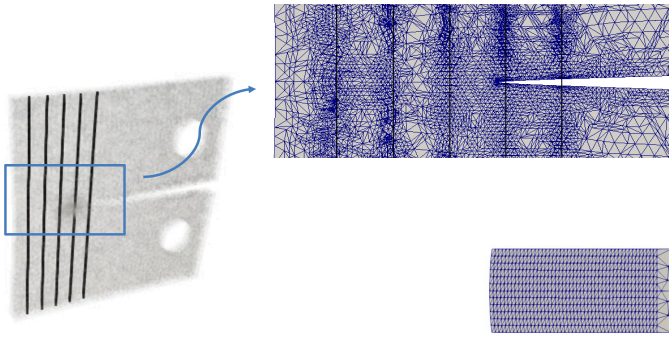

(b) Stage two: peak load is reached and propagation is initiated

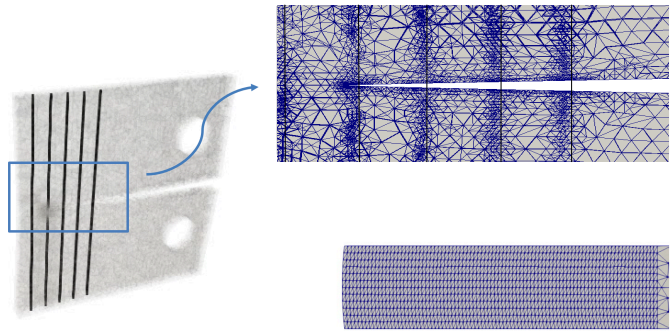

(c) Stage three: second propagation initiates

Figure 5.41: Three stages of crack propagation for the numerical simulation and their corresponding crack surface

5.6.5 Parametric studies for one inclined fiber

After validating the proposed method with experimental results, this section tests the methodology and algorithms for a more complex fiber orientation. The inclination of the fiber and their properties make the crack propagation more complex compared to the previous example.

The mesh of the matrix is shown in Figs. 5.42. The parameters of the model are the same as defined in the previous section, except for the fiber, which is now located at $f_1 = [(11.0, 4.0, 2.5), (31.0, 68.0, 2.5)]$.

A qualitative study is performed with respect to the crack path. The Young modulus of the fiber is increased concerning the original E_f^o adopted in Sec. 5.6.4. Five values for E_f are used here: $5E_f^o$, $10E_f^o$, $15E_f^o$, $20E_f^o$ and $25E_f^o$. The goal is to study how the crack path changes for different variables of the problem.

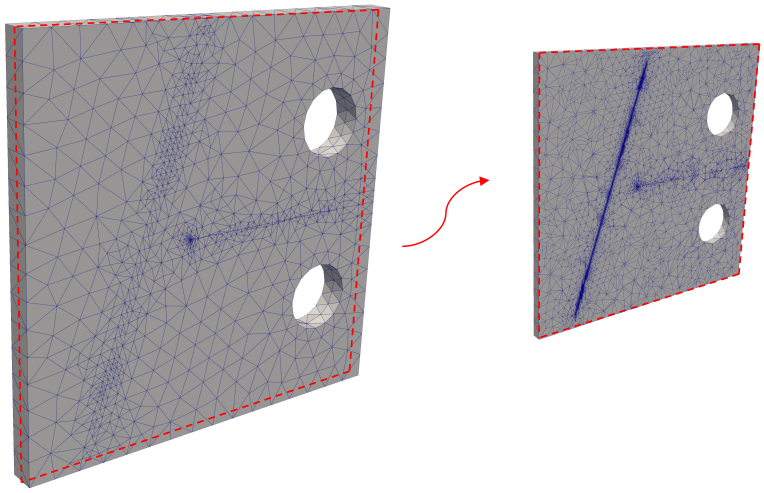

Figure 5.42: Mesh of the matrix material and corresponding cut showing the refinement at the mid plane of the specimen

In Fig. 5.43 it can be observed five different crack paths. Each path corresponds to a different value of E_f. For three of them ($5E_f^o$ dark green, $10E_f^o$ red and $15E_f^o$ yellow) the crack crosses the fiber. For two of them ($20E_f^o$ purple and $25E_f^o$ light green) the fiber is stiff enough to prevent the crack to continue the horizontal path, so it turns into another direction and continues to grow. This study, although qualitative, show the full three-dimensional capability of the developed framework. This experiment does not intent to validate the model since it was already done in the previous section. The goal here is to show the flexibility and robustness of the implementation on a more challenging problem.

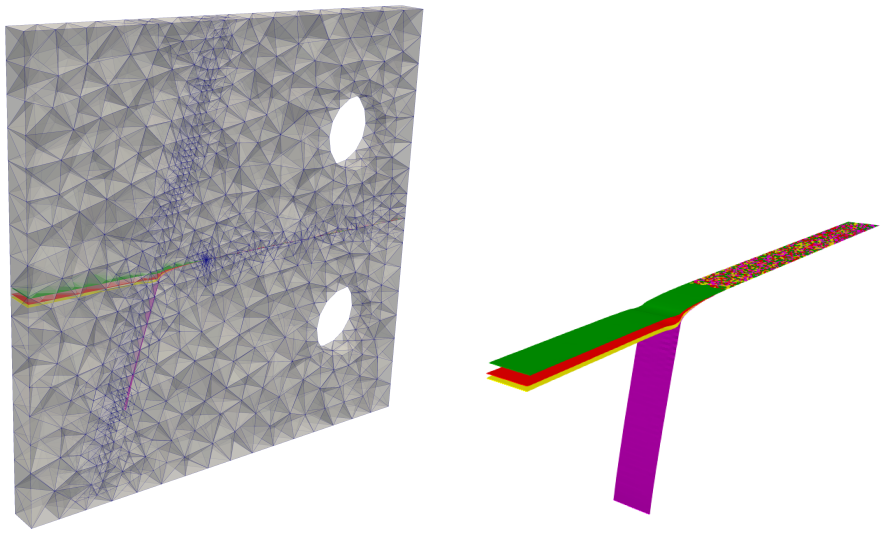

(a) Matrix mesh and crack surfaces **(b)** Crack surfaces

Figure 5.43: Crack surfaces for different values of E_f

Figure 5.44 shows in details the crack path for numerical experiments where cracks cross the fiber ($5E_f^o$, $10E_f^o$ and $15E_f^o$). It can be observed a small difference among them. The dark green path corresponds to the less stiffer fiber while the yellow path corresponds to the stiffer fiber (among these three listed moduli of elasticity).

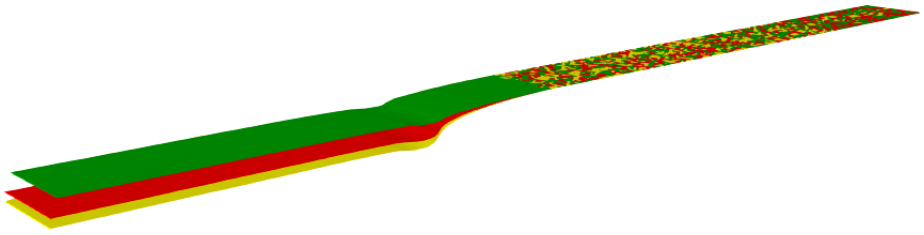

Figure 5.44: Crack propagation when cracks cross the fiber

Figure 5.45 shows the crack path when cracks do not cross the fiber. Cracks advance towards the fiber with a small turning and finally abruptly veer to an inclined direction. The light green crack surface, corresponding to $20E_f^o$, has a more brusque turning compared to the purple one.

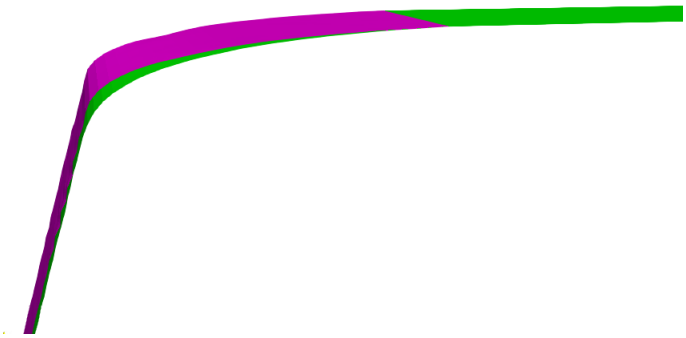

Figure 5.45: Crack propagation when cracks do not cross the fiber

Another interesting detail can be noted when green light and purple paths are compared as shown in Fig. 5.46. For the model with less stiffness (Fig. 5.46(a)) it can be observed a wiggle behavior at the borders of the crack surface. Since the higher stiffness of the specimen is concentrated on the mid-thickness plane (where the fiber is located), it suggests that the borders of the crack are more susceptible to follow the horizontal crack growth as observed in less stiff models. This shows that the difference in stiffness along the thickness can be captured by the model. This clearly shows the 3D crack propagation behavior. This behavior, of course, is more prominent for thicker specimens.

In contrast to the behavior presented in Fig. 5.46(a), the model with higher stiffness shown in Fig. 5.46(b) manifests a more definite path (without wiggly borders). This demonstrates that the overall stiffness provided by the system fiber-matrix in this region is big enough to make a clean and stable crack path.

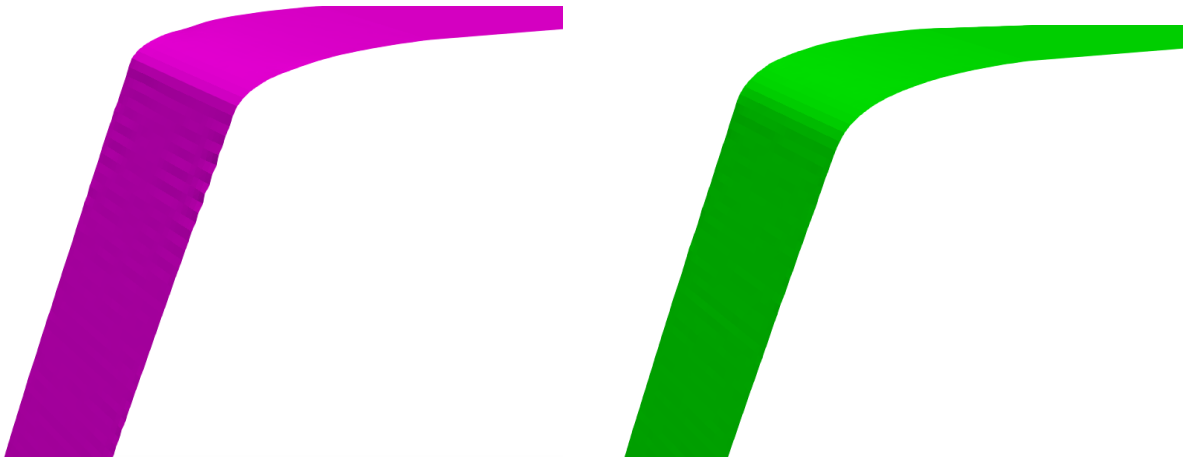

(a) Crack surface with wiggly borders

(b) Crack surfaces with stable path

Figure 5.46: Crack surfaces for different values of E_f

5.7 Summary

This chapter presents a methodology for the analysis of realistic three-dimensional crack propagation in fiber-reinforced materials. The GFEM-mERS method is improved to handle nonlinear bonding interactions between the matrix-fiber interface combined with a three-dimensional crack growth framework. The proposed framework simulates fiber-reinforced composites using meshes that fit neither the fractures nor the fibers and can handle complex three-dimensional crack propagation behavior.

Several problems and a large number of parametric studies for a range of fiber cross-section area, fiber stiffness, and fiber-matrix bond nonlinear laws are presented in Sec. 4.1. The examples compare the proposed approach with other numerical methods and laboratory experiments. A good agreement between the GFEM-mERS and reference solutions is observed for all parameter values considered.

The proposed method is verified against fully 2D/3D FEM solutions based on meshes that fit both the crack surfaces and fiber boundaries. The experiments presented in Sec. 5.6.1 are performed using parametric studies and intend to highlight important conceptual aspects of the method.

The simulations show that the mERS can capture the propagation phenomenon relative to the experiment. The mERS and experimental results have very close numerical and qualitative results. This is only allowed because of the new methodologies proposed by this research. In the end, a complex three-dimensional crack propagation is shown to highlight the flexibility and robustness of the proposed framework.

Chapter 6

Two-scale Analysis of Fiber-Reinforced Composites: Bridging Scales with the GFEM^{gl}

6.1 Introduction

This chapter [1] shows the two-scale analysis for fiber composites. For a long time the computational analysis of physical systems was restricted to one scale of observation and modeling. This procedure is acceptable for many classes of problems where the scale of analysis is relatively homogeneous for the entire analysis domain. The increase in computational power and the development of computational methods have sought for efficient methods bridging scales of complex problems. In this chapter, it is presented the idea of using the Generalized Finite Element Method with global-local enrichments (GFEM^{gl}).

A key idea of the GFEM^{gl} is to use numerically defined enrichment functions provided by the solution of auxiliary boundary or initial boundary value problems. A global-local analysis is then performed based on the so-called global-local enrichment functions. These functions are able to represent fine-scale responses on coarse macroscale finite element meshes and to fully account for interactions among scales. This method, originally proposed by [107] and presented in details in [61], combines the classical GFEM with the Global-Local strategy proposed by [108]. The GFEM^{gl} is suitable for many classes of problems, as described in details in [109]. The analysis is basically divided in three steps:

- *Initial global problem (step 1)*: A coarse FEM mesh is used for the analysis of the whole domain.
- *Local problem (step 2)*: A small portion of the global domain is selected. The mesh into this domain is refined and the results from step 1 are used as boundary conditions for this new domain.
- *Final global problem (step 3)*: The whole domain is solved again. Now, however, some nodes are enriched using numerical functions calculated in step 2.

[1] This chapter has been adapted from the paper "P. Alves, C. A. Duarte, A Multiscale Generalized FEM for Three-Dimensional Crack Propagation in Fiber-Reinforced Composites, conference paper awarded by the Engineering Mechanics Institute (EMI) - Ph.D. research competition on Computational Mechanics - MIT (2018), [106]"

In the GFEM^{gl}, the numerical solution produced by the local analysis can be easily introduced into the the global problem using enrichment functions. The local problem can be strongly refined and it does not affect the overall computational performance of the analysis (as measured in details by [110]). Therefore, the problem is performed using less memory and processing time than standard GFEM, as shown by [61], [109], and [111].

Another important feature of the GFEM^{gl} is its great potential to the parallel processing, as already observed by [112] and [110]. Each local problem can be solved individually and the amount of computational work can be easily distributed to the several processors of the system. For this reason some problems can be efficiently solved in parallel, since no communication among processors is required. Only a global scatter-gather communication is involved, leading to a highly scalable algorithm, as studied by [113] and [111].

6.2 Formulation

The formulation presented here follows the steps carefully developed by [114], [115], [61], and [116]. The GFEM^{gl} is presented in its generalized form. The next sections shows in details the mathematical formulation for each of the 3 steps of the method.

6.2.1 Initial global problem (step 1)

Consider a domain $\bar{\Omega}_G = \Omega_G \cup \partial\Omega_G$ in R^n. The boundary is decomposed in $\partial\Omega_G = \partial\Omega_G^u \cup \partial\Omega_G^\sigma$ with $\partial\Omega_G^u \cap \partial\Omega_G^\sigma = \oslash$, where u and σ refer to the Dirichlet and Neumann boundary conditions, respectively.

As an example, Fig. 6.1 shows a generic bidimensional problem discretized with triangular elements. The problem has an horizontal crack crossing the center of the specimen. The problem has a displacement applied at the right boundary (domain $\partial\Omega_G^u$) and has a load applied at the top and bottom boundaries $\partial\Omega_G^\sigma$. The highlighted region in green corresponds to its local domain, which will be formulated next.

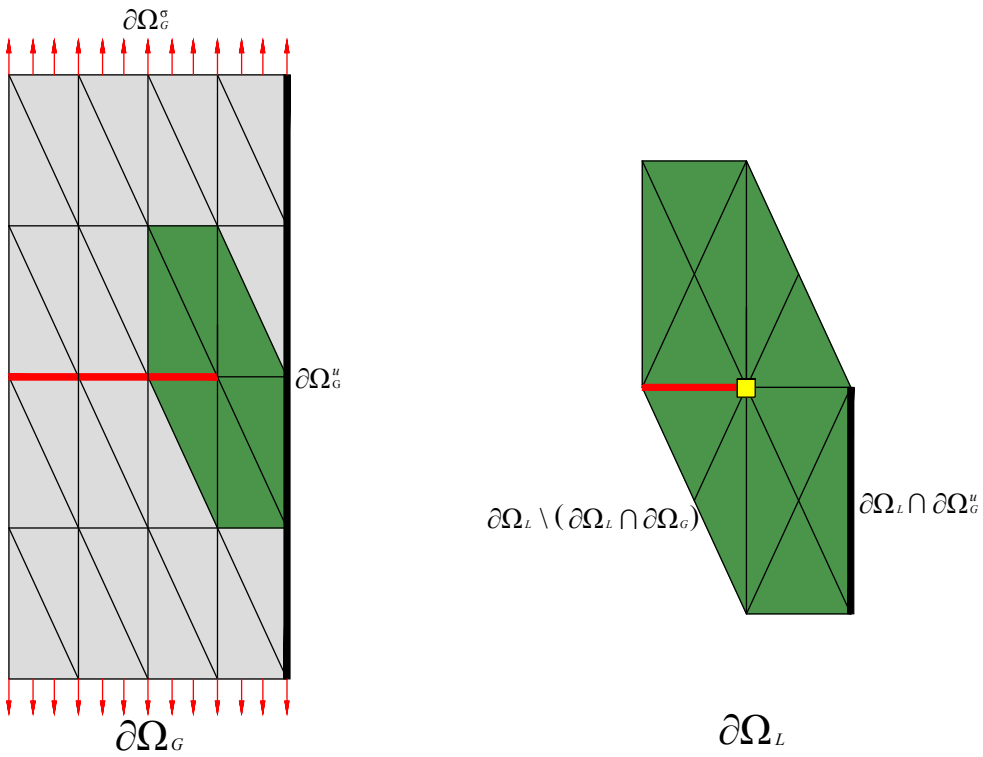

Figure 6.1: Global and local domains for a generic bidimensional problem

The equilibrium equations are given by:

$$\nabla \cdot \boldsymbol{\sigma} = \mathbf{0} \text{ in } \partial\Omega_G \tag{6.1}$$

The constitutive relations are given by the generalized Hooke's law, $\boldsymbol{\sigma} = \boldsymbol{C} : \boldsymbol{\varepsilon}$, where $\boldsymbol{C}$ is Hooke's tensor. The following boundary conditions are prescribed on $\partial\Omega_G$.

$$\boldsymbol{u} = \bar{\boldsymbol{u}} \text{ in } \partial\Omega_G^u \tag{6.2}$$

$$\boldsymbol{\sigma}\boldsymbol{n} = \bar{\boldsymbol{t}} \text{ in } \partial\Omega_G^\sigma \tag{6.3}$$

It is observed that $\boldsymbol{n}$ is the outward unit normal vector to $\partial\Omega_G^\sigma$ and $\bar{\boldsymbol{t}}$ and $\bar{\boldsymbol{u}}$ are prescribed tractions and displacements. Equations 6.1, 6.2 and 6.3 are the boundary value problem for Elasticity theory.

Let $\boldsymbol{u}_G^0$ denote a generalized FEM approximation of the problem at damage evolution step *0*. This approximation is the solution of Eq. 6.4 given by: Find $\boldsymbol{u}_G^0 \in \tilde{\mathcal{X}}_G^0(\Omega_G) \subset \mathcal{H}^1(\Omega_G) \quad \forall \quad \boldsymbol{v}_G^0 \in \tilde{\mathcal{X}}_G^0(\Omega_G)$.

$$\int_{\Omega_G} \boldsymbol{\sigma}(\tilde{\boldsymbol{u}}_G^0) : \boldsymbol{\varepsilon}(\boldsymbol{v}_G^0) d\boldsymbol{x} + \eta \int_{\partial\Omega_G^u} \tilde{\boldsymbol{u}}_G^0 \boldsymbol{v}_G^0 d\boldsymbol{s} = \int_{\partial\Omega_G^\sigma} \bar{\boldsymbol{t}} \boldsymbol{v}_G^0 d\boldsymbol{s} + \eta \int_{\partial\Omega_G^u} \bar{\boldsymbol{u}} v_G^0 d\boldsymbol{s} \tag{6.4}$$

Space $\tilde{\mathcal{X}}_G^0(\Omega_G)$ is the discretization of $\mathcal{H}^1(\Omega_G)$, a Hilbert space defined on Ω_G, built with FEM or GFEM. The representation in Eq. 6.4 assumes that the Dirichlet boundary conditions are imposed using Penalty method. The space for GFEM is given by:

$$\tilde{\mathcal{X}}_G^0(\Omega_G) = \left\{ \tilde{\boldsymbol{u}}_G^0(\boldsymbol{x}) = \sum_{\alpha=1}^{N} N_\alpha(\boldsymbol{x}) \hat{\boldsymbol{u}}_\alpha^E(\boldsymbol{x}) \;\mid\; \hat{\boldsymbol{u}}_\alpha^E(\boldsymbol{x}) = \sum_{i=1}^{D_L} \tilde{\boldsymbol{u}}_{\alpha i} E_{\alpha i}(\boldsymbol{x}) \right\} \tag{6.5}$$

In Eq. 6.5, $\tilde{\boldsymbol{u}}_{\alpha i}$, $\alpha = 1, ..., N$, $i = 1, ..., D_L$ are the generalized DOFs, where N are the number of nodes for the problem and D_L is the dimension of a set of enrichment functions $E_{\alpha i}(\boldsymbol{x})$. The space can also be define using standard polynomial FEM shape functions.

6.2.2 Local problem (step 2)

For this case, Ω_L is a sub-domain from Ω_G as shown in Fig. 6.1. This sub-domain may contain special features such as cracks and fibers. The corresponding local solution $\boldsymbol{u}_L \in \tilde{\mathcal{X}}_L$ is obtained solving Eq. 6.6 given by: Find $\boldsymbol{u}_L \in \tilde{\mathcal{X}}_L(\Omega_L) \subset \mathcal{H}^1(\Omega_L) \quad \forall \quad \boldsymbol{v}_L \in \tilde{\mathcal{X}}_L(\Omega_L)$.

$$\begin{aligned} &\int_{\Omega_L} \boldsymbol{\sigma}(\boldsymbol{u}_L) : \boldsymbol{\varepsilon}(\boldsymbol{v}_L) d\boldsymbol{x} + \eta \int_{\partial\Omega_L \cap \partial\Omega_G^u} \boldsymbol{u}_L \cdot \boldsymbol{v}_L d\boldsymbol{s} + \kappa \int_{\partial\Omega_L \setminus (\partial\Omega_L \cap \partial\Omega_G)} \boldsymbol{u}_L \cdot \boldsymbol{v}_L d\boldsymbol{s} \\ &= \int_{\partial\Omega_L \cap \partial\Omega_G^\sigma} \bar{\boldsymbol{t}} \boldsymbol{v}_L d\boldsymbol{s} + \eta \int_{\partial\Omega_L \cap \partial\Omega_G^u} \bar{\boldsymbol{u}} \cdot \boldsymbol{v}_L d\boldsymbol{s} + \int_{\partial\Omega_L \setminus (\partial\Omega_L \cap \partial\Omega_G)} (\boldsymbol{t}(\boldsymbol{u}_G^0) + \kappa \boldsymbol{u}_G^0) \cdot \boldsymbol{v}_L d\boldsymbol{s} \end{aligned} \tag{6.6}$$

Space $\tilde{\mathcal{X}}_L$ generated by GFEM functions described in Chapter 3, η is the penalty parameter and κ is the stiffness parameter to consider Cauchy boundary condition. The space $\tilde{\mathcal{X}}_L$ can be defined as:

$$\tilde{\mathcal{X}}_L(\Omega_L) = \left\{ \boldsymbol{u}_L(\boldsymbol{x}) = \sum_{j=1}^{N_L} N_j(\boldsymbol{x})[\hat{\boldsymbol{u}}_j^E(x) + \tilde{\boldsymbol{u}}_j^E(\boldsymbol{x}) + \check{\boldsymbol{u}}_j^E(\boldsymbol{x}) + \acute{\boldsymbol{u}}_j^E(\boldsymbol{x})] \right\} \tag{6.7}$$

The functions $\hat{\boldsymbol{u}}_j^E(\boldsymbol{x})$, $\tilde{\boldsymbol{u}}_j^E(\boldsymbol{x})$, $\check{\boldsymbol{u}}_j^E(\boldsymbol{x})$ and $\acute{\boldsymbol{u}}_j^E(\boldsymbol{x})$ are functions of continuous approximation, discontinuous, singulars or functions that can represent any feature as fibers or inclusions. The value N_L is the number of nodes of the refined domain.

The traction vector that appears in Eq. 6.6 is computed from the global scale using Cauchy relation.

$$\boldsymbol{t}(\boldsymbol{u}_G^0) = \hat{\boldsymbol{n}} \cdot \boldsymbol{\sigma}(\boldsymbol{u}_G^0) = \hat{\boldsymbol{n}} \cdot (\boldsymbol{C} : \boldsymbol{\varepsilon}(\boldsymbol{u}_G^0)) \tag{6.8}$$

The term $\hat{\mathbf{n}}$ is the outward unit normal vector to $\partial\Omega_L \backslash (\partial\Omega_L \cap \partial\Omega_G)$.

6.2.3 Enriched global problem (step 3)

For the step 3 of the problem, the initial domain is enriched with the results from step 2. The global enriched problem is enriched by the numerical solution $\boldsymbol{u}_L$. The new solution $\boldsymbol{u}_G^E \in \mathcal{S}_G^E(\Omega_G)$ is the following:

$$\boldsymbol{\phi}_j = N_j \boldsymbol{u}_L \tag{6.9}$$

The function N_j is used in the global problem and $\tilde{\boldsymbol{u}}_L$ is the numerical result found in the local problem. The enriched global problem is obtained solving Eq. 6.10: Find $\boldsymbol{u}_G^E \in \tilde{\mathcal{X}}_G^E(\Omega_G) \subset \mathcal{H}^1(\Omega_G) \quad \forall \quad \boldsymbol{v}_G^E \in \tilde{\mathcal{X}}_G^E(\Omega_G)$.

$$\int_{\Omega_G} \boldsymbol{\sigma}(\boldsymbol{u}_G^E) : \boldsymbol{\varepsilon}(\boldsymbol{v}_G^E) d\boldsymbol{x} + \eta \int_{\partial\Omega_G^u} \boldsymbol{u}_G^E \boldsymbol{v}_G^E d\boldsymbol{s} = \int_{\partial\Omega_G^\sigma} \bar{\boldsymbol{t}} \cdot \boldsymbol{v}_G^E d\boldsymbol{s} + \eta \int_{\partial\Omega_G^u} \bar{\boldsymbol{u}} v_G^E d\boldsymbol{s} \tag{6.10}$$

where $\tilde{\mathcal{X}}_G^E(\Omega_G)$ is the initial space $\tilde{\mathcal{X}}_G^0(\Omega_G)$ increased by $\boldsymbol{u}_k^{gl}(\boldsymbol{x})$ from local problem $\boldsymbol{u}_L$:

$$\mathcal{S}_G^E(\Omega_G) = \left\{ \boldsymbol{u}(\boldsymbol{x}) = \sum_{j=1}^{N} N_j(\boldsymbol{x}) \boldsymbol{u}_j^E(\boldsymbol{x}) + \sum_k N_k(\boldsymbol{x}) \boldsymbol{u}_k^{gl}(\boldsymbol{x}) \right\} \tag{6.11}$$

and k represents the nodes enriched by $\boldsymbol{u}_L$ in number of $\mathcal{I}_{gl}$ (set of enriched nodes).

Figure 6.2 shows schematically the 3 steps of GFEM^{gl} described in the previous sections.

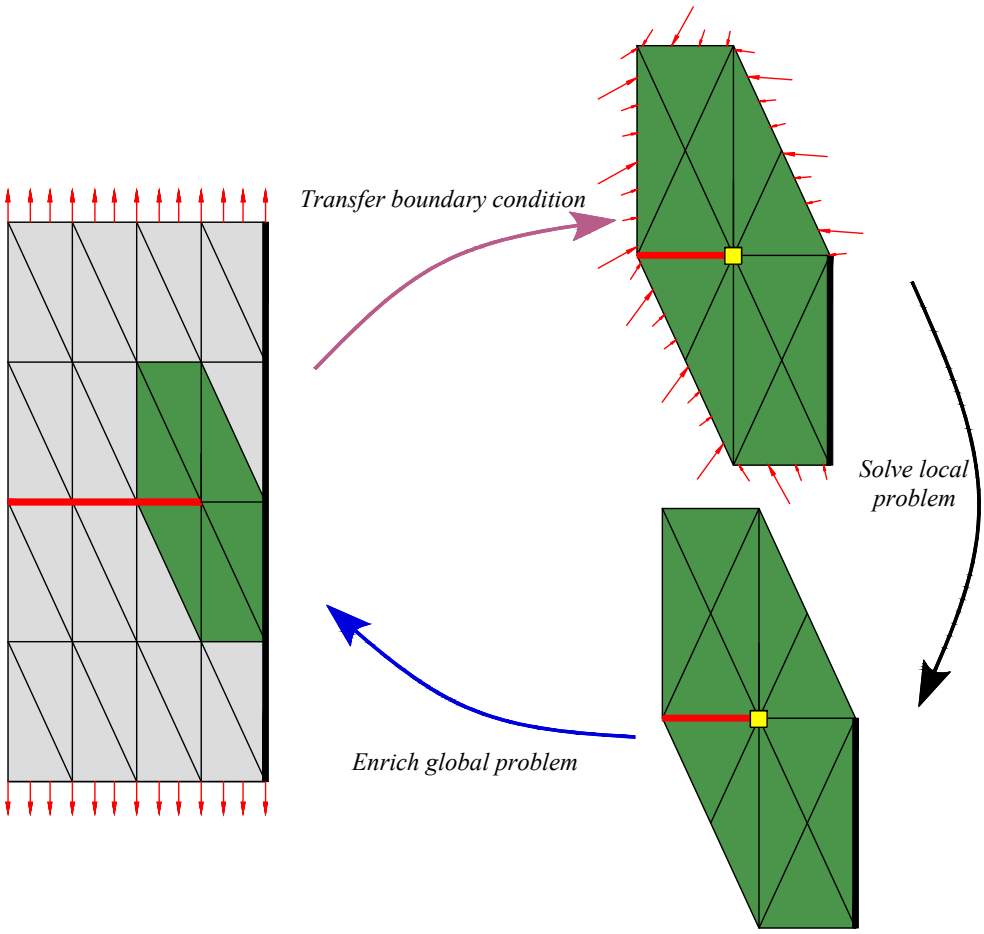

Figure 6.2: The three steps of the GFEM^{gl}

6.3 Multiscale and fibers

As discussed earlier, fiber-reinforced composites have interesting features that can only be studied using multiscale methods. Figure 6.3 shows schematically how the multiscale is applied in the context of the GFEM^{gl} for fibers. The 3 steps described in the last section (together with intermediate steps) are depicted in the figure below.

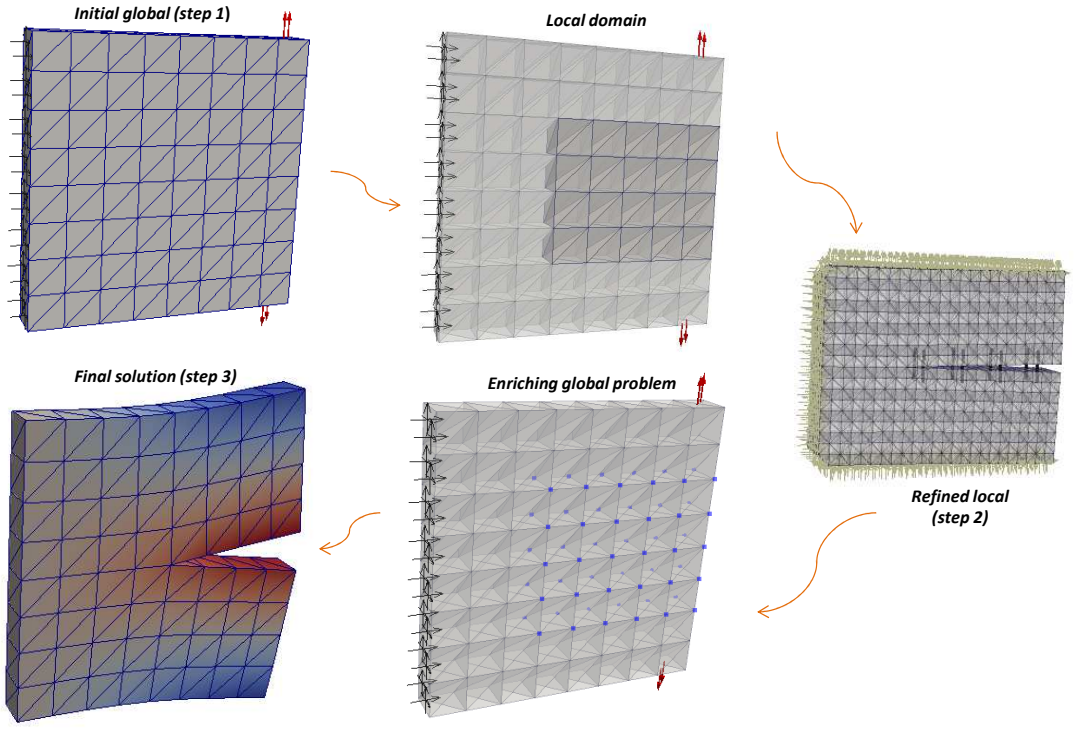

Figure 6.3: Global local scheme applied to fiber-reinforced materials

- *Initial global (step 1):* A coarse mesh is used to solve the initial global problem. For the example shown in Fig. 6.3, the fibers are concentrated in a small portion of the entire domain. This is considered the step 1 of the GFEM^{gl} analysis. The mathematical background of this step was described in details in Sec. 6.2.1.

- *Local domain:* A small portion of the domain is selected. The size of the local domain is a key factor for GFEM^{gl} analysis and will be studied in details in Sec. 6.5. Large local domains are preferable (because they provide a better boundary condition from the initial global problem), but are computationally expensive. Small local problems are computationally cheaper, but the accuracy of the boundary conditions provided by the initial global problem can affect the precision of the solution.

- *Refined local (step 2):* The local domain selected previously is largely refined using *hp* refinement. Cracks and fibers are modeled using *GFEM* functions (but not limited to). In fact, the framework is generic enough to support other methodologies to model the features. In this research, however, only *GFEM* is studied.

- *Enriching global problem:* The initial global mesh is enriched with the numerical results obtained from the local problem solution. For the examples reproduced in this report, all the nodes located in the "local domain region" are enriched with the numerical function obtained from the local analysis. It is important to note that the local behavior is captured using numerical define functions only (analytical functions to represent crack or fiber do not need to be used in step 3).

- *Final solution (step 3):* The enriched global problem is solved using the enrichment obtained from the local analysis. The global problem is now able to reproduce the special local features of the problem. Even for a very refined local domain, only a few new DOFs are added to the enriched global problem. The mathematical background of this step was described in details in Sec. 6.2.3.

Besides the advantage of using GFEM^{gl} in terms of flexibility (can be easily combined with legacy FEM codes, [117]), another important feature of using this method is the possibility of solving the problem using parallel processing. Since each local problem is independent of each other, they can be independently solved by different processors. See for example structural specimen described in Fig. 6.4. This hypothetical specimen has fibers distributed over the entire domain and three cracks as described in the figure. Each of these cracks can be represented by a local domain into the GFEM^{gl} scheme. Problems with multiple local domains were previously studied in [61].

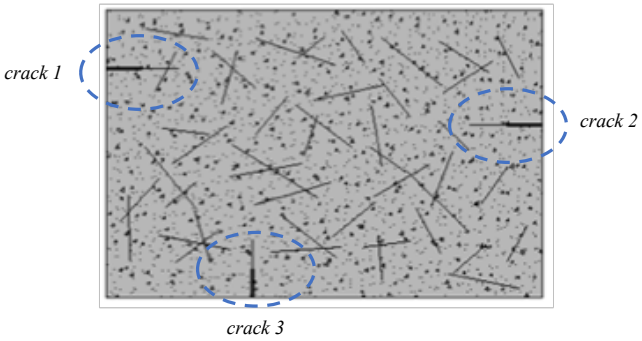

Figure 6.4: Hypothetical specimen with fibers over the entire domain and three cracks

For this hypothetical problem, three local domains are created and each of them can be individually solved. No communication among problems is required and each local problem is independently processed. These problems can be solved in parallel, since no communication among processors is required. Only a global scatter-gather communication is involved, leading to a highly scalable algorithm as recently studied by [111].

Figure 6.5 schematically shows the 3 local problems created for the Global-Local analysis. Each local domain does not communicate with other local problems and they are independent boundary value problems. At the local level (step 2) they are refined and fibers and crack are described using enrichment functions. The results from each local problem are later transferred to the enriched global problem (step 3) by using numerical enrichment functions. The local behavior generated by the local problems are introduced in the enriched global problem adding a few DOFs in the original global problem (now called enriched global problem).

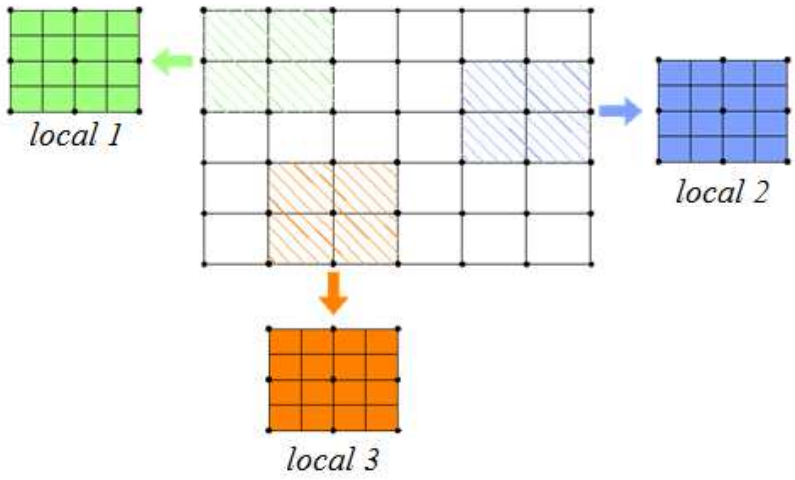

Figure 6.5: Schematic of the GFEM^{gl} for problems with multiple local problems

6.4 Multiscale simulations for a fiber-reinforced cracked specimen

This example simulates a cracked specimen with Mode I loading, as shown in Fig. 6.6. The crack is bridged by 8 fibers described as dashed lines in this figure. For non-reinforced materials cracks need to overcome the cracking resistance of the matrix in order to propagate. In fiber-reinforced composite materials, however, fibers can hold the crack together and increase crack opening resistance. The complete parametric study for the effect of the area of the fibers, its quantity, location and length are presented in Appendix C. Here the focus is on the multiscale approach using the GFEM^{gl}. The following parameters are assumed for this problem, with consistent units: Modulus of elasticity of matrix $E_{\mathrm{m}} = 1.0\times10^{4}\ N/mm^2$; Poisson's ratio of matrix $\nu = 0.2$; Modulus of elasticity of fiber $E_{\mathrm{f}} = 5.0\times10^{6}\ N/mm^2$; Area of the fiber $A_{\mathrm{f}} = 2.0\times10^{-4}\ mm^2$; Bond stiffness: $K_{\mathrm{b}} = 5.0\times10^{6}\ N/mm^3$; Traction: $\sigma = 1000.0\ N/mm^2$.

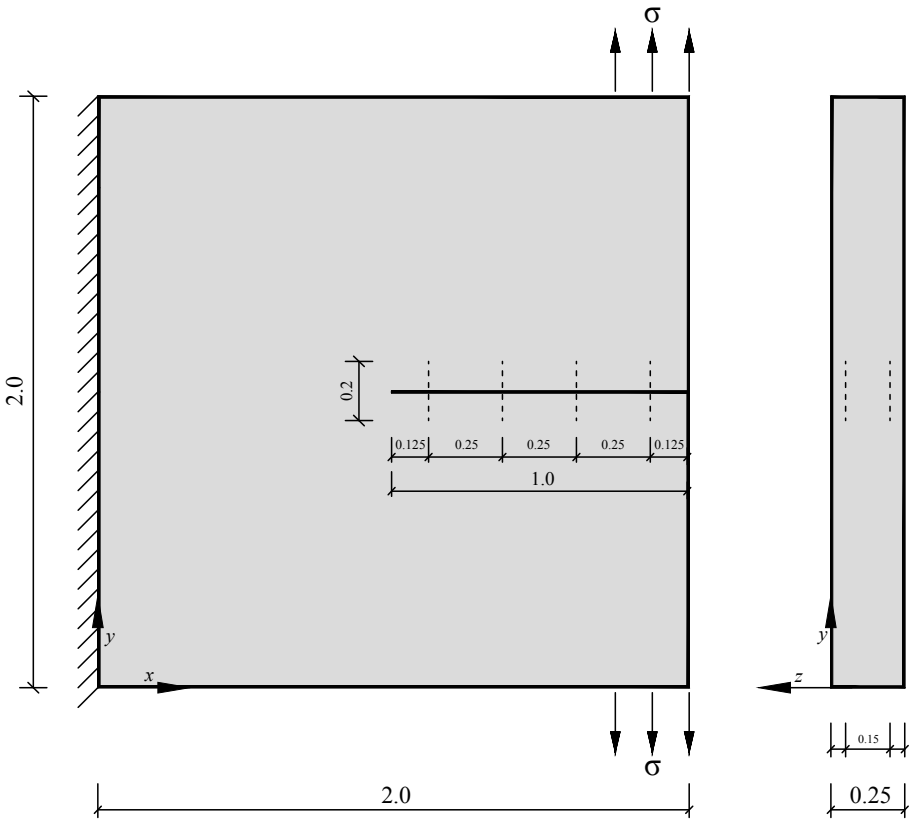

Figure 6.6: Cracked specimen bridged by fibers

The global domain uses the mesh shown in Fig. 6.7. Figure 6.7 also shows the Dirichlet $\partial\Omega_G^u$ and Neumann $\partial\Omega_G^\sigma$ boundary conditions applied to the problem. Crack and fibers are described only in the local domains as shown in Fig. 6.8.

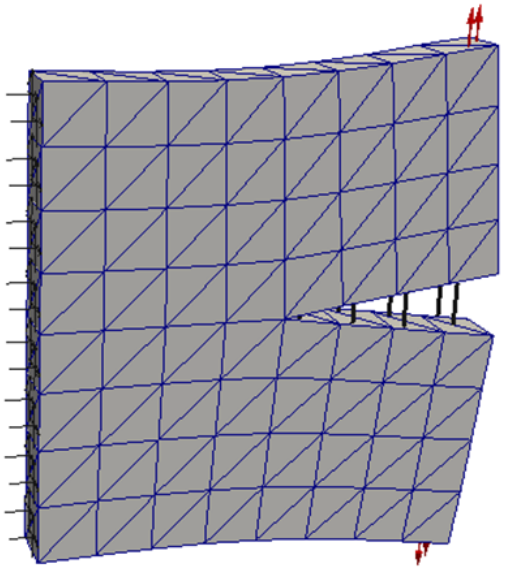

Figure 6.7: Boundary conditions and fiber configuration for the problem

First, the size of the local problem is studied. The cracked specimen is solved using 4 different local domains as shown in Fig. 6.8. Dirichlet boundary condition is used to transfer information from the initial global domain to the local problems (Neumann or Cauchy boundary conditions can be equally used as shown by [110]).

The quality of boundary conditions applied to local problems is investigated. Large local problems are computationally more expensive, but have better boundary conditions. Small local problems are computationally cheaper, but have worse boundary conditions. Comparative among the models is performed using the crack opening extracted at the enriched global problem (step 3).

Table 6.1 presents the crack opening extracted in step 3. The displacement d is measured as shown in Fig. 6.9. The displacement $d_{GFEM^{gl}}$ are compared to d_{GFEM}, which represents the solution performed without Global-Local strategy (same type of analysis performed in the previous chapters) and used here as reference solution. Fiber and cracks are described (using GFEM) only in the local domain (step 2). The enriched global domain uses global-local enrichment functions (step 3). There is no enrichment in the initial global problem (step 1). The error e is calculated as $e = \frac{|d_{GFEM^{gl}} - d_{GFEM}|}{|d_{GFEM}|}$

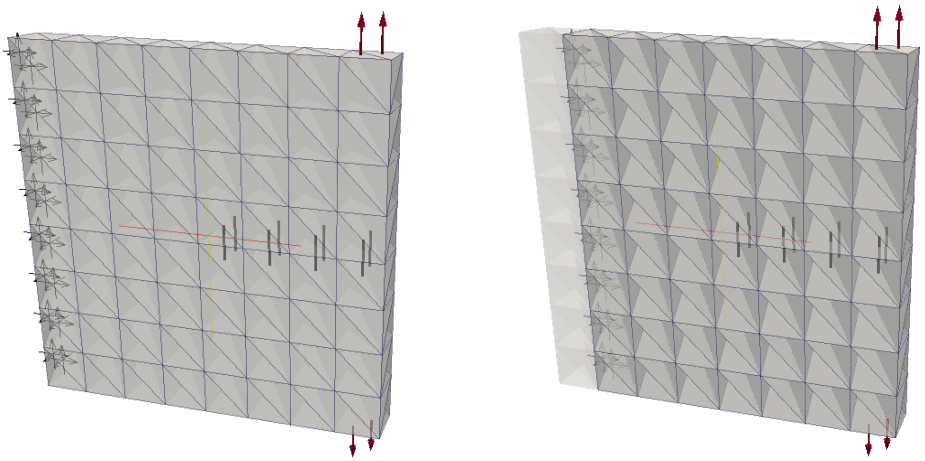

(a) Local domain 1 **(b)** Local domain 2

(c) Local domain 3 **(d)** Local domain 4

Figure 6.8: Local domains for the studied problem

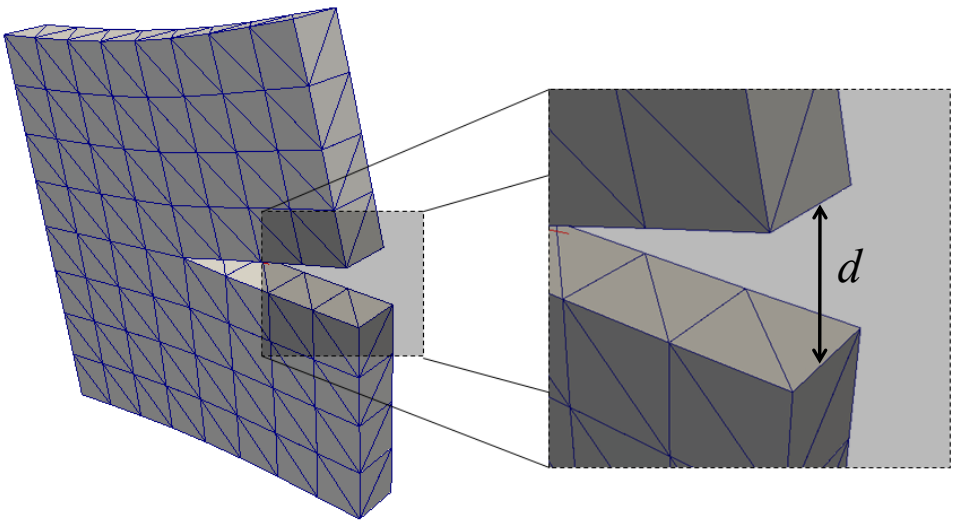

Figure 6.9: Opening d of the crack

Table 6.1: *Comparative crack opening among at the nodes*

	d	e
Reference	0.2165	0.0000
Local 1	0.2173	0.0034
Local 2	0.2218	0.0243
Local 3	0.2820	0.3023
Local 4	0.2828	0.3062

It can be observed that the solution using global-local framework is highly affected by the size of local problems. The framework using local problems 1 and 2 is able to reproduce the reference results with high accuracy. For local problems 3 and 4 the results have low accuracy (around 30% error). Next sections this effect is studied in details and alternatives are provided to address this issue.

6.5 Identifying the problem: effect of the size of local problems

Three similar boundary value problems are studied. The goal is to study how the ratio between local and global problems affects the behavior of the problem (opening d at step 3 is the value used as comparative). Figures 6.10(a) and 6.10(b) show the first boundary value problem. Figures 6.10(c) and 6.10(d) show the second boundary value problem. Figures 6.10(e) and 6.10(f) show the third boundary value problem. For each boundary value problem, two sizes for the local domain are analyzed. So, for example, problem value problem 1 is first analyzed using as a local problem the domain described in Fig. 6.10(a) and later the same global domain is analyzed using a bigger domain for the local problem (shown in Fig. 6.10(b)).

The combination of 3 boundary value problems (with 2 local domains for each global domain) produces six different "$\frac{Local}{Global}(\%)$" described in Tab. 6.2. The "$\frac{Local}{Global}(\%)$" is obtained by dividing the number of nodes in the local domain by the number of nodes in the global domain of the problem. The error $e(\%)$ shown in the table is calculated similarly as in the previous section.

For *Prob1* the fibers and crack represent a large portion of the domain. That means the influence of fibers and crack for the global behavior of the problem are relevant. Among all the 6 cases analyzed, "*Prob1Loc1*" represents the worst scenario for GFEM^{gl} since these features correspond to a large portion of the problem. The "*Prob3Loc2*" represents the best scenario for GFEM^{gl} since the features are localized in a small portion of the domain.

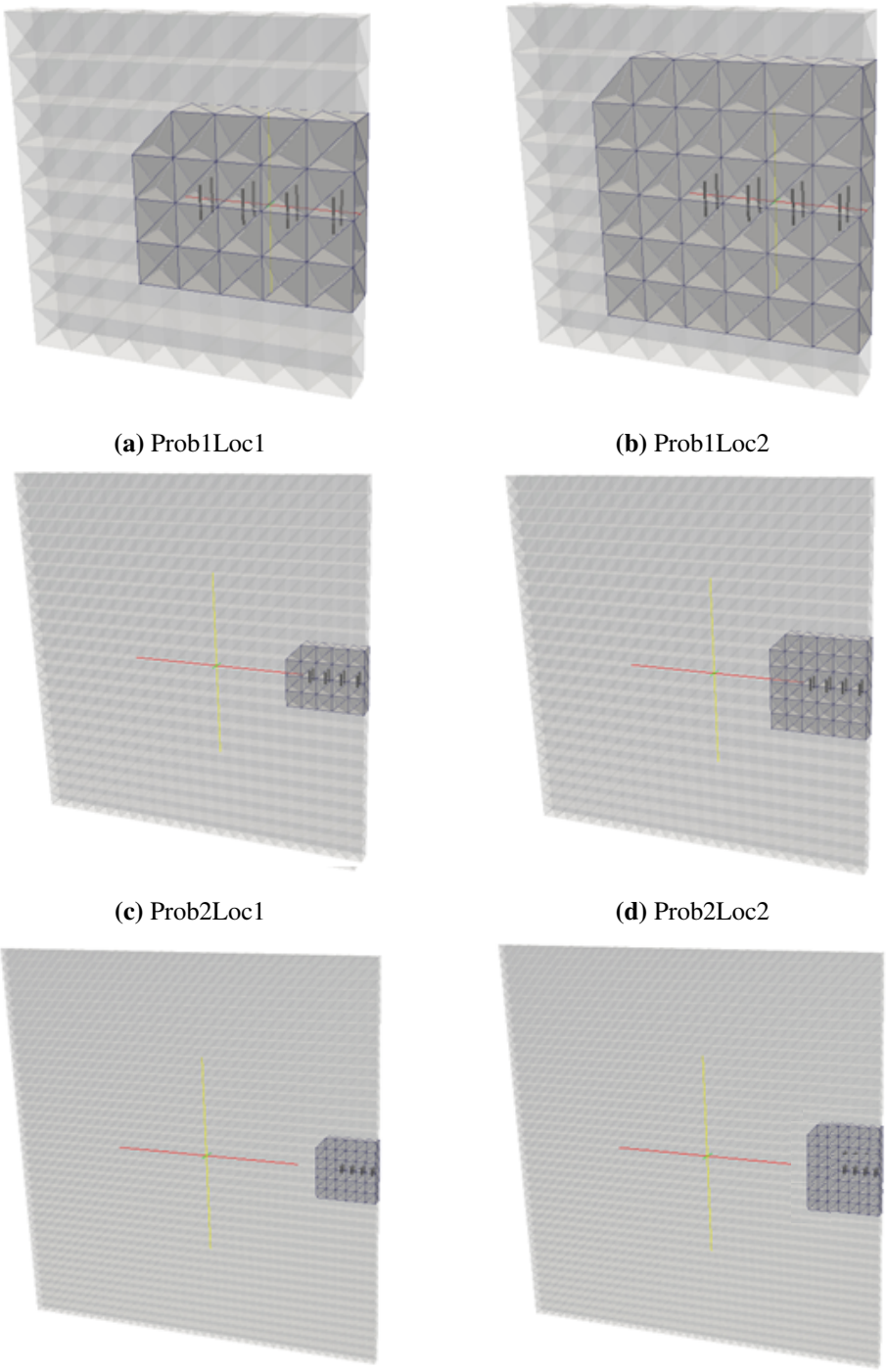

(a) Prob1Loc1

(b) Prob1Loc2

(c) Prob2Loc1

(d) Prob2Loc2

(e) Prob3Loc1

(f) Prob3Loc2

Figure 6.10: Global and local domains representation for the six cases analyzed

Table 6.2: *Impact of* $\frac{Local}{Global}$ *domain ratio for GFEM*^{gl} *solution*

Problem	*Global*		*Local*		$\frac{Local}{Global}$(%)	*e* (%)
	nodes	*elements*	nodes	elements		
Prob1Loc1	1536	384	468	117	30.47	30.62
Prob1Loc2	1536	384	852	213	55.47	30.23
Prob2Loc1	13824	3456	468	117	3.39	20.02
Prob2Loc2	13824	3456	852	213	6.16	19.82
Prob3Loc1	38400	9600	468	117	1.29	7.43
Prob3Loc2	38400	9600	852	213	2.22	6.73

Table 6.2 shows all six different cases analyzed. Boundary value problem 1 described in the table ("*Prob1Loc1*" and "*Prob1Loc2*") is the same problem studied in Sec. 6.4. The local features of this problem have considerable influence in its global behavior. The next two sections propose remedies in order to decrease the error of this framework.

6.6 Remedy 1: Refining global mesh

The goal of this section is to study how the refinement of the initial global problem can improve the transference of boundary conditions between step 1 and step 2 of GFEM^{gl}. The problem presented in Sec. 6.4 is studied again. Now, however, different levels of refinement are used for the initial global mesh (step 1). Table 6.3 shows all the six different levels of refinement for the corresponding problem. *Refining level* 0 represents the same mesh of the global domain used previously. The number of nodes and elements for *Global* and *Local* domains for each case is shown in Tab. 6.3. Figure 6.11 shows the mesh corresponding to the level of refinement "5" described in Tab. 6.3.

Table 6.3: Study of refinement of initial global problem

Refining level	*Global*		*Local*		*Relative error (%)*
	nodes	*elements*	*nodes*	*elements*	
0	1536	384	468	117	30.62
1	3072	768	1608	402	29.53
2	6144	1536	3032	758	29.04
3	12288	3072	5712	1428	28.68
4	24576	6144	11072	2768	28.38
5	49152	12288	21424	5356	28.05

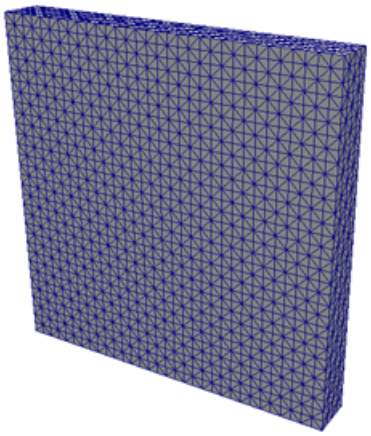

Figure 6.11: Level of refinement 5 for reinforced cracked plate

From Tab. 6.3 it can be observed that the refinement does not help decreasing the *e (%)* at step 3. This can be explained because the local feature of this problem (fibers and crack) corresponds to a large amount of the global domain. This strategy can be used for some classes of problems, but does not have an effect here. It can be concluded that the refinement alone can not always decrease the error for the GFEM^{gl}. Next section we study other alternative to reduce the error of using GFEM^{gl}.

6.7 Remedy 2: Iterative global-local analysis

As observed in previous sections, the size of the local domain are a key point for the quality of results of GFEM^{gl}. Large local domains have better boundary conditions, but are computationally expensive. A reasonable size of local domains are an important point in a multiscale analysis using GFEM^{gl} strategy. This is still an open field of in this area and has been studied recently by our research group for different types of problems, [61, 109–112, 118–122].

A remedy that successfully has been used for GFEM^{gl} is the so-called the *Iterative* GFEM^{gl}. For this strategy the interaction between global and local problems is performed multiple times. The goal of this iterative procedure is to improve the boundary conditions applied to the local domain using multiple steps.

As described in Fig. 6.12, for each iterative analysis of the local problem (step $k+1$) the boundary condition for this local domain is improved with results from iterative step k. The overall behavior of the problem converges to the correct solution, as suggests the studies from [111, 112, 119–122].

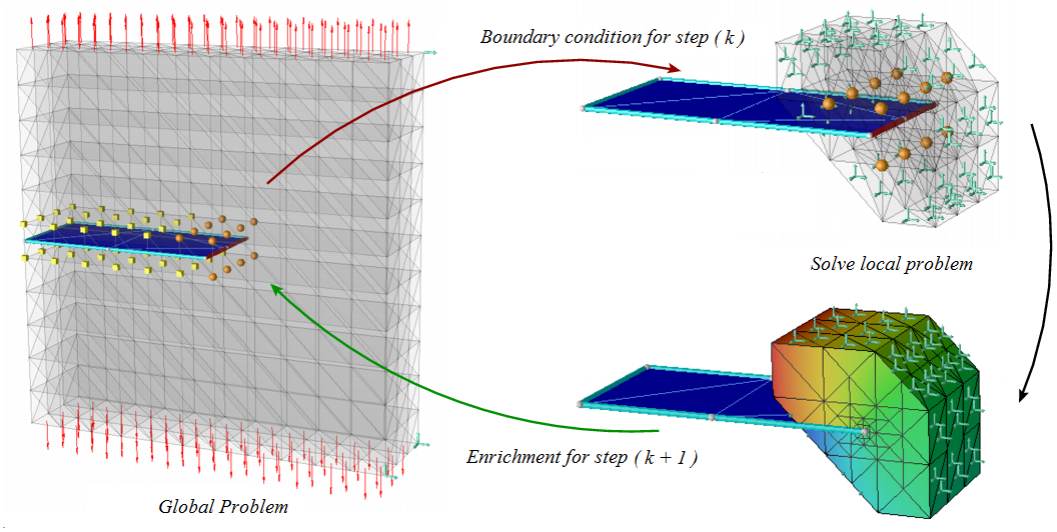

Figure 6.12: Iterative process for GFEM^{gl}, [110]

The problems previously analyzed in Sec. 6.5 are here performed again. Now, however, the iterative GFEM^{gl} process described earlier in applied. Although an unlimited number of iterative steps could be used, Tab. 6.4 shows that the second iterations already reduces the error by a considerable amount for each problem.

Table 6.4: Iterative process for GFEM^{gl}

Problem	*Global*		*Local*		$\frac{Local}{Global}$ (%)	*e*(%)	
	nodes	*elements*	*nodes*	*elements*		*iterat. 1*	*iterat. 2*
Prob1Loc1	1526	384	468	117	30.67	30.62	7.6
Prob1Loc2	1526	384	852	213	55.83	30.23	7.2
Prob2Loc1	13824	3456	468	117	3.39	20.02	4.6
Prob2Loc2	13824	3456	852	213	6.16	19.82	4.4
Prob3Loc1	38400	9600	468	117	1.22	7.43	1.8
Prob3Loc2	38400	9600	852	213	2.22	6.73	1.6

6.8 General observations for GFEM^{gl}

This chapter shows that GFEM^{gl} can be used as a potential framework bridging micro and macro scales. As seen, all the performed numerical simulations were able to reproduce the reference solution with acceptable accuracy. Although applied in a small specimen with only one local problem, the results show that the method has great potential to be employed to large problems with multiple local problems. In fact, the

efficiency of the method is still more salient when utilized in those types of problem. Another important tool not exploited here is the potential for parallel processing of local problems. This is an important feature of GFEM^{gl} that certainly can be used in future steps of this research.

For the problems performed in this chapter cracks and fibers are confined in a small portion of the problem (here called local domain). For realistic simulations of reinforced materials, however, fibers are usually spread all over the domains. For these types of problem, fibers can not simply be described only in the local domain. The initial global domain has to take account of the fibers in order to provide realistic boundary conditions to the local problem. A full discretization of fibers at step 1, however, is not necessary for our purpose and can be easily replaced by homogenization of its properties, as described by [123] and [124]. It is expected that the homogenized initial global problem will be able to capture the global structural behavior of the problem. Therefore, the local domain will be provided with accurate boundary conditions and be able to capture the local behavior of the problem (such as crack propagation, bond breakdown and slip of the fibers).

Chapter 7

Contributions and Future Work

Computational methods are crucial to model, simulate, and improve the understanding of reinforced materials. They remove one significant barrier hampering the broad use of advanced composites. The research presented in previous chapters is expected to impact the way fiber is modeled and analyzed by contributing to the ability to realistically model and understand the behavior of a broad range of new materials.

A novel computational method able to describe fractures and fibers in reinforced composites is proposed, implemented, verified, and validated against experimental data. The proposed methodology uses the GFEM-mERS for crack and fiber description and the GFEM^{gl} to bridge scales of interest. The preceding chapters discussed the main scientific challenges, objectives, methodology, and numerical experiments that validate the research. A summary of the main contributions of this dissertation and potential future extensions are given next.

7.1 Contributions

A methodology for the analysis of fiber-reinforced materials is presented. The GFEM-mERS combines a 3D GFEM with the mERS to simulate fractures in fiber-reinforced composites using meshes that fit neither the fractures nor the fibers. This computational framework is shown to be accurate and efficient based on the applications presented in this work. It can significantly reduce the user-time spent on the model generation and modification process.

The proposed mERS allows its integration with methods that use high-order polynomial or non-polynomial shape functions. This also allows the combination of the mERS with other advanced discretization methods such as, for example, the Discontinuity-Enriched FEM [125], Element-Free Galerkin Method [126], and

the Reproducing Kernel Particle Method [127]. The original ERS can only be used, in a consistent way, with low-order finite element approximations. Thus, the potential application of the proposed mERS goes beyond those presented in this research.

The GFEM-mERS is extended to handle advanced methodologies for crack propagation and fiber-matrix interaction. The method was developed within a LEFM crack propagation framework while adopting complex nonlinear fiber-matrix debonding laws. These features are necessary and attractive in real-world engineering practice where complex physical phenomena play an important role in the mechanics of the composite. The formulation is validated with laboratory experiments.

This work also demonstrates that the GFEM^{gl} framework can be used to bridge micro and macro scales for fiber-reinforced composites. This procedure performs well even for critical scenarios where the local features largely contribute to the overall behavior of the composite. This is achieved thanks to the iterative process between scales. The concepts shown here can be easily expanded to a large range of complex materials.

7.2 Future work

Several future directions are suggested based on the studies presented in this work. The goal here is to propose guidelines to the many fields where the current research can progress towards more realistic and practical applications of the methodology presented in previous chapters.

7.2.1 Combining the mERS with other discretization methods

The capability of mERS to be combined with methods that use high-order polynomial or non-polynomial shape functions, like the Discontinuity-Enriched FEM, Element-Free Galerkin Method, or Kernel Particle Method, potentialize the applications of these methods to a variety of problems involving fiber reinforcement. Problems where these methods perform well such as modeling rigid cohesive cracks, large deformation, and high modal density problems can be further explored in future research, [125, 128].

7.2.2 Biological materials

There is a growing demand for biological materials. The development of novel fiber composites for medical devices has largely required the integration of several concepts associated with material science and biophysics. The accurate representation of complex matrix and fibers phenomena associated with various biological components makes the numerical validation of these composites a difficult task. To adjust the mechanical properties at the macro and microscopic level, the spatial arrangement of fibers needs to be represented well through several spacial scales. Application of such composites has been limited by the poor numerical description of localized behavior, long setting time, and unsatisfactory biocompatibility between numerical and experimental tests. The proposed framework in this research is a reliable option to improve the understanding of this class of materials, [129, 130].

7.2.3 Sophisticated material models

For the numerical experiments presented in this work, homogeneous isotropic material properties are adopted for matrix and fibers. However, some more advanced material models, such as anisotropic materials, may be needed for practical simulations. The nonlinearity of the matrix and fiber is also observed and can be relevant for a growing number of applications. An extension of this research to account for these issues can be further developed using the concepts layed down by this research, [131].

7.2.4 Self healing materials

Interfacial microcracks in matrix composites are difficult to be detected and repaired. The self-healing concept provides opportunities to fabricate composites with unusual properties where microcracks can be easily repaired. However, the study of these materials involves complex mechanical and chemi-thermal analysis which are hard to be simulated using available computational tools. A reliable numerical method to describe fibers and cracks is a key aspect of studying these materials. The methods developed in this research can be helpful to model the localized and complex failure mechanisms of self healing materials, [69, 132, 133].

7.2.5 Topological optimization

The topological optimization of fiber composite structures has been widely used while tailoring materials to achieve the required engineering physical properties. A reliable multiscale approach and an accurate crack and fiber representation with a relatively low computational cost is still challenging. Currently, the design of these materials for advanced applications is still limited by the capacity to represent local failures due to fiber debonding and collapse. The methods developed in this research can be a useful tool to improve the numerical approaches commonly used in this field of study, [134, 135]

7.2.6 Randomly distributed fibers

The multiscale framework used to bridge different material scales plays an important role in describing composites where the fibers are randomly distributed over the domain. Homogenization techniques alone are not always able to accurately model complex localized crack and fiber interactions in these materials. However, the integration of these techniques into the multiscale framework developed in this work can be a relevant alternative to analyze this class of material, [123, 124].

7.2.7 Failure initiation

Modeling the failure initiation processes of fiber composite materials is an interesting challenge and has relevant applications in the industry. Phase-field and other material damage techniques can offer a powerful tool to model failure initiation and to improve the understanding of such materials. This can be further explored in the future research, [136–138].

7.2.8 Parallel computing

Realistic simulations of evolving crack surfaces in fiber composites require hundreds of small propagation steps and several different initial configurations. The numerical simulation of these problems is costly and leads to severe load balancing issues in parallel implementation. An improvement of the framework developed in this work under the parallel computing paradigm is necessary for large and complex material models and can be the subject of future work, [110, 111].

7.2.9 Additive manufacturing

Additive manufacturing has revolutionized advanced materials with customized features. It has been applied to aerospace, automotive, consumer, and biomedical fields. Its applicability to composites has attracted special attention due to its promise in improving, modifying, and diversifying the properties of generic materials through the introduction of reinforcements. A reliable and robust approach for three-dimensional analysis of these materials is crucial to provide valuable insight for their correct fabrication and usage. Volume redundancy and superposition of materials become a major problem for this class of problems. The numerical methods developed in this research can be an important tool to describe these materials, [139–142].

7.2.10 Multiphysics

Several applications of composites requires that they can resist thermo-structural loads. Multiphysics models with coupled thermo-mechanical physics are therefore a necessary tool for more accurate analysis of a broad range of realistic problems. An extension of the current computational implementation is a potential field of study. It is indeed largely facilitated by the object-oriented design of the code where this research was developed, [143, 144].

7.2.11 Artificial intelligence, machine learning and big data

The adoption of composite materials in the industry has allowed greater freedom in design and their respective components. However, this freedom of material choice has resulted in increased complexity for numerical simulation and manufacturing. The ability to discretely describe crack and fibers is crucial for this analysis. The approach here developed combined with machine learning and artificial intelligence can be explored for a large number of advanced manufacturing applications. Big data in reinforced fibers can be improved through advanced methods to describe fibers. The material properties estimated by complex approaches are helped by an optimized neural network for accurate modeling of the fibers which can be used for later goals of optimization and design, [145, 146].

References

[1] J. Reddy and D. Robbins Jr, "Theories and computational models for composite laminates," *Applied Mechanics Review*, vol. 47, no. 6, pp. 147–169, Jun 1994.

[2] J. J. Kruzic, J. P. Campbell, and R. O. Ritchie, "On the fatigue behavior of g-based titanium aluminides: Role of small cracks," *Acta Materialia*, vol. 47, pp. 801–816, 1999.

[3] J. J. Kruzic, "Predicting fatigue failures," *Science*, vol. 325, pp. 156–158, 2009.

[4] J. Melenk and I. Babuška, "The partition of unity finite element method: Basic theory and applications," *Computer Methods in Applied Mechanics and Engineering*, vol. 139, pp. 289–314, 1996.

[5] C. Duarte, I. Babuška, and J. Oden, "Generalized finite element methods for three dimensional structural mechanics problems," *Computers and Structures*, vol. 77, pp. 215–232, 2000.

[6] J. Oden, C. Duarte, and O. Zienkiewicz, "A new cloud-based *hp* finite element method," *Computer Methods in Applied Mechanics and Engineering*, vol. 153, pp. 117–126, 1998.

[7] T. Strouboulis, K. Copps, and I. Babuška, "The generalized finite element method," *Computer Methods in Applied Mechanics and Engineering*, vol. 190, pp. 4081–4193, 2001.

[8] Market, "Composite market size, share and trend analysis report," *Advanced Interior Materials*, 2020.

[9] Owenscorning, *Manual properties glass fiber 158B-AA-675*, 2018 (accessed March, 2018). [Online]. Available: https://www.owenscorning.com/

[10] F. W. Zok, "Developments in oxide fiber composites," *Journal of the American Ceramic Society*, vol. 89, pp. 3309–3324, 2006.

[11] M. Ortiz and A. Pandolfi, "Finite-deformation irreversible cohesive elements for three-dimensional crack propagation analysis," *International Journal for Numerical Methods in Engineering*, vol. 44, pp. 1267–1282, 1999.

[12] D. S. Beyerle, S. M. Spearing, and A. G. Evans, "Damage mechanisms and the mechanical properties of a laminated 0/90 ceramic/matrix composite," *Journal of the American Ceramic Society*, vol. 75, pp. 3321–3330, 1992.

[13] R. O. Ritchie, "Mechanisms of fatigue-crack propagation in ductile and brittle solids," *International Journal of Fracture*, vol. 100, pp. 55–83, 1999.

[14] J. J. Kruzic, R. M. Cannon, J. W. Ager, and R. O. Ritchie, "Fatigue threshold r-curves for predicting reliability of ceramics under cyclic loading," *Acta Materialia*, vol. 53, pp. 2595–2605, 2005.

[15] J. J. Kruzic, R. M. Cannon, and R. O. Ritchie, "Crack-size effects on cyclic and monotonic crack growth in polycrystalline alumina: Quantification of the role of grain bridging," *Journal of the American Ceramic Society*, vol. 87, pp. 93–103, 2004.

[16] C. E. Harris and M. J. Shuart, "An assessment of the state-of-the-art for the design and manufacturing of large composite structures for aerospace vehicles," *22nd SAMPE Europe International Conference*, vol. 1, p. 2729, 2001.

[17] A. Bensoussan, J. L. Lions, and G. Papanicolaou, "Asymptotic analysis for periodic structures," *Studies in Mathematics and its Applications*, vol. 5, 1978.

[18] S. Ghosh, K. Lee, and P. Raghavan, "A multi-level computational model for multi-scale analysis in composite and porous materials," *International Journal of Solids and Structures*, vol. 38, pp. 2335–2385, 2001.

[19] F. K. F. Radtke, "Computational modeling of fibre-reinforced cementitious composites: An analysis of discrete and mesh-independent techniques," PhD Thesis, Delft University of Technology, December 2012.

[20] J. Kang, K. Kim, Y. Lim, and J. Bolander, "Modeling of fiber-reinforced cement composites: Discrete representation of fiber pullout," *International Journal of Solids and Structures*, vol. 51, pp. 1970–1979, 2014.

[21] K. Visalvanich and A. E. Naaman, "Fracture model for fiber reinforced concrete," *J. Am. Concr. Inst.*, vol. 80, pp. 128–138, 1983.

[22] F. C. Caner, Z. P. Bazant, and R. Wendner, "Microplane model m7f for fiber reinforced concrete," *J. Am. Concr. Inst.*, vol. 105, pp. 41–57, 2013.

[23] S. C. Lee, J. Y. Cho, and F. J. Vecchio, "Diverse embedment model for steel fiber-reinforced concrete in tension: model verification," *ACI Materials J.*, vol. 108, pp. 526–535, 2011.

[24] S. C. Lee, J. Y. Cho, and F. J. Vecchio, "Simplified diverse embedment model for steel fiber-reinforced concrete elements in tension," *ACI Mater. J.*, vol. 110, pp. 403–412, 2013.

[25] S. H. Park, D. J. Kim, G. S. Ryu, and K. T. Koh, "Tensile behavior of ultra high performance hybrid fiber reinforced concrete," *Cement and Concrete Composites*, vol. 34, pp. 172–184, 2012.

[26] B. Shen and G. H. Paulino, "Identification of cohesive zone model and elastic parameters of fiber-reinforced cementitious composites using digital image correlation and a hybrid inverse technique," *Cement and Concrete Composites*, vol. 33, pp. 572–585, 2011.

[27] M. Carvalho, J. Barros, Y. Zhang, and D. Dias-da-Costa, "A computational model for simulation of steel fibre reinforced concrete with explicit fibres and cracks," *Computer Methods in Applied Mechanics and Engineering*, vol. 363, p. 112879, 2020.

[28] G. Ruiz, "Propagation of a cohesive crack crossing a reinforcement layer," *Int. J. Fract.*, vol. 111, pp. 265–282, 2001.

[29] L. Bouhala, A. Makradi, S. Belouettar, H. Kiefer-Kamal, and P. Fréres, "Modelling of failure in long fibres reinforced composites by X-FEM and cohesive zone model," *Composites B*, vol. 55, pp. 352–361, 2013.

[30] L. Zhao, J. Zhi, J. Zhang, Z. Liu, and N. Hu, "XFEM simulation of delamination in composite laminates," *Composites A*, vol. 80, pp. 61–71, 2016.

[31] M. Karimi, H. Bayesteh, and S. Mohammadi, "An adapting cohesive approach for crack-healing analysis in SMA fiber-reinforced composites," *Computer Methods in Applied Mechanics and Engineering*, vol. 349, pp. 550–575, 2019.

[32] J. M. Guedes and N. Kikuchi, "Preprocessing and postprocessing for materials based on the homogenization method with adaptive finite element methods," *Computer Methods in Applied Mechanics and Engineering*, vol. 83, no. 2, pp. 143–198, 1990.

[33] H. Lusti and A. Gusev, "Finite element predictions for the thermoelastic properties of nanotube reinforced polymers," *Modelling and Simulation in Materials Science and Engineering*, vol. 12, pp. 107–119, 2004.

[34] B. Mortazavi, M. Baniassadi, J. Bardon, and S. Ahzi, "Modeling of two-phase random composite materials by finite element," *Composites Part B: Engineering*, vol. 45, pp. 1117–1125, 2013.

[35] W. Tian, L. Qi, C. Su, J. Zhou, and Z. Jing, "Numerical simulation on elastic properties of short-fiber-reinforced metal matrix composites: Effect of fiber orientation," *Composite Structures*, vol. 152, pp. 408–417, 2016.

[36] S. Balakrishnan and D. W. Murray, "Finite element prediction of reinforced concrete behavior," Department of Civil Engineering, The University of Alberta, Tech. Rep. Structural Engineering Report No. 138, July 1986.

[37] A. E. Elwi and T. M. Hrudey, "Finite element model for curved embedded reinforcement," *Journal of Engineering Mechanics*, vol. 115, no. 4, pp. 740–754, 1989.

[38] M. G. Pike and C. Oskay, "XFEM modeling of short microfiber reinforced composites with cohesive interfaces," *Finite Elements in Analysis and Design*, vol. 106, pp. 16–31, 2015.

[39] M. G. Pike and C. Oskay, "Three-dimensional modeling of short fiber-reinforced composites with extended finite-element method," *Journal of Engineering Mechanics*, vol. 142, pp. 11–16, 2016.

[40] J. E. Bolander and S. Saito, "Discrete modeling of short-fiber reinforcement in cementitious composites," *Advanced Cement Based Materials*, vol. 6, no. 3, pp. 76–86, 1997.

[41] J. Kozicki and J. Tejchman, "Effect of steel fibres on concrete behavior in 2D and 3D simulations using lattice model," *Archives of Mechanics*, vol. 62, pp. 1–28, 2010.

[42] M. Kunieda, H. Ogura, N. Ueda, and H. Nakamura, "Tensile fracture process of shcc by means of three-dimensional meso-scale analysis," *Cem. Concr. Compos.*, vol. 33, pp. 956–965, 2011.

[43] E. A. Schauffert and G. Cusatis, "Lattice discrete particle model for fiber-reinforced concrete. I: Theory," *Journal of Engineering Mechanics.*, vol. 138, no. 7, pp. 826–833, 2012.

[44] E. A. Schauffert and G. Cusatis, "Lattice discrete particle model for fiber-reinforced concrete. II: Tensile fracture and multiaxial loading behavior," *Journal of Engineering Mechanics.*, vol. 138, no. 7, pp. 834–841, 2012.

[45] J. E. Bolander, S. Choi, and S. R. Duddukuri, "Fracture of fiber-reinforced cement composites: Effects of fiber dispersion," *International Journal of Fracture*, vol. 154, no. 1–2, pp. 73–86, 2008.

[46] G. Cusatis, D. Pelessone, and A. Mencarelli, "Lattice Discrete Particle Model (LDPM) for failure behavior of concrete. I: Theory," *Cement and Concrete Composites*, vol. 33, no. 9, pp. 881–890, 2011.

[47] H. Hartl, "Development of a continuum-mechanics-based tool for 3d finite element analysis of reinforced concrete structures and application to problems of soil-structure interaction," PhD Thesis, Graz University of Technology, 2002.

[48] O. Zienkiewicz, D. Owen, D. Phillips, and G. Nayak, "Finite element methods in the analysis of reactor vessels," *Nuclear Engineering and Design*, vol. 20, no. 2, pp. 507–541, 1972.

[49] C. Octávio, D. D. da Costa, J. Alfaiate, and E. Júlio, "Modelling the behaviour of steel fibre reinforced concrete using a discrete strong discontinuity approach," *Engineering Fracture Mechanics*, vol. 154, pp. 12–23, 2016.

[50] D. Dias-da-Costa, J. Alfaiate, L. Sluys, P. Areias, and E. Júlio, "An embedded formulation with conforming finite elements to capture strong discontinuities," *International Journal for Numerical Methods in Engineering*, vol. 93, no. 2, pp. 224–244, 2013.

[51] P. Alves, A. Simone, and C. A. Duarte, "A generalized finite element method for three-dimensional fractures in fiber-reinforced composites," *Mechanica*, 2020.

[52] F. Radtke, A. Simone, and L. Sluys, "A partition of unity finite element method for obtaining elastic properties of continua with embedded thin fibres," *International Journal for Numerical Methods in Engineering*, vol. 84, no. 6, pp. 708–732, 2010.

[53] P. Alves and C. A. Duarte, "A GFEM for three-dimensional crack propagation in fiber reinforced composites," *EMI research competition - UCSD*, 2017.

[54] I. Babuška, G. Caloz, and J. Osborn, "Special finite element methods for a class of second order elliptic problems with rough coefficients," *SIAM Journal on Numerical Analysis*, vol. 31, no. 4, pp. 945–981, 1994.

[55] I. Babuška and J. Melenk, "The partition of unity method," *International Journal for Numerical Methods in Engineering*, vol. 40, pp. 727–758, 1997.

[56] C. Duarte and J. Oden, "An *hp* adaptive method using clouds," *Computer Methods in Applied Mechanics and Engineering*, vol. 139, pp. 237–262, 1996.

[57] C. Duarte and J. Oden, "*Hp* clouds – An *hp* meshless method," *Numerical Methods for Partial Differential Equations*, vol. 12, pp. 673–705, 1996.

[58] T. Belytschko and T. Black, "Elastic crack growth in finite elements with minimal remeshing," *International Journal for Numerical Methods in Engineering*, vol. 45, pp. 601–620, 1999.

[59] T.-P. Fries and T. Belytschko, "The generalized/extended finite element method: An overview of the method and its applications," *International Journal for Numerical Methods in Engineering*, vol. 84, no. 3, pp. 253–304, 2010.

[60] M. Schweitzer, "Generalizations of the finite element method," *Central European Journal of Mathematics*, vol. 10, pp. 3–24, 2012.

[61] C. A. Duarte and D. J. Kim, "Analysis and applications of a generalized finite element method with global-local enrichment functions," *Comput. Methods Appl. Mech. Eng.*, vol. 197, pp. 487–504, 2008.

[62] G. Wells and L. Sluys, "A new method for modeling cohesive cracks using finite elements," *International Journal for Numerical Methods in Engineering*, vol. 50, pp. 2667–2682, 2001.

[63] N. Moës, J. Dolbow, and T. Belytschko, "A finite element method for crack growth without remeshing," *International Journal for Numerical Methods in Engineering*, vol. 46, pp. 131–150, 1999.

[64] J. Oden and C. Duarte, "Chapter: Clouds, Cracks and FEMs," in *Recent Developments in Computational and Applied Mechanics*, B. Reddy, Ed. Barcelona, Spain: International Center for Numerical Methods in Engineering, CIMNE, 1997, pp. 302–321, http://gfem.cee.illinois.edu/papers/jMartin_color.pdf.

[65] A. Sanchez-Rivadeneira, N. Shauer, B. Mazurowski, and C. Duarte, "A stable generalized/extended p-hierarchical fem for three dimensional linear elastic fracture mechanics," *Computer Methods in Applied Mechanics and Engineering*, 2019, submitted.

[66] Abaqus, "Version 6.14 Documentation. Dassault Systemes Simulia Corporation, Providence, RI, USA," 2014.

[67] J. Pereira, C. Duarte, D. Guoy, and X. Jiao, "*Hp*-Generalized FEM and crack surface representation for non-planar 3-D cracks," *International Journal for Numerical Methods in Engineering*, vol. 77, no. 5, pp. 601–633, 2009.

[68] M. Heath, *Scientific Computing: An Introductory Survey*, ser. McGraw-Hill series in computer science. Boston, Mass.: McGraw-Hill, 1997.

[69] A. Jones, "Solvent-based self-healing approaches for fiber-reinforced composites," PhD Thesis, University of Illinois at Urbana-Champaign, 2015.

[70] D. Zhao and J. Botsis, "Experimental and numerical studies in model composites part I: Experimental results," *International Journal of Fracture*, vol. 82, pp. 153–174, 1989.

[71] J. Zhang, S. Deng, Y. Wang, L. Ye, L. Zhou, and Z. Zhang, "Effect of nanoparticles on interfacial properties of carbon fibre-epoxy composites," *Composites Part A: Applied Science and Manufacturing*, vol. 55, pp. 35–44, 2013.

[72] Miller-Stephenson, *Manual properties EPON*, 2018 (accessed March, 2018). [Online]. Available: miller-stephenson.com

[73] B. Blaiszik, M. Baginska, S. White, and N. Sottos, "Autonomic recovery of fiber/matrix interfacial bond strength in a model composite," *Advanced functional materials*, vol. 20, pp. 3547–3554, 2010.

[74] B. V. Farahani, P. J. Tavares, J. Belinha, and P. M. G. P. Moreira, "A fracture mechanics study of a compact tension specimen: Digital image correlation, finite element and meshless method," *2nd International Conference on Structural Integrity, ICSI 2017*, vol. 5, pp. 920–927, 2017.

[75] Y. Lei, "Finite element crack closure analysis of a compact tension specimen," *International Journal of Fatigue*, vol. 30, pp. 21–31, 2008.

[76] J. Garzon, P. O'Hara, C. Duarte, and W. Buttlar, "Improvements of explicit crack surface representation and update within the generalized finite element method with application to three-dimensional crack coalescence," *International Journal for Numerical Methods in Engineering*, vol. 97, no. 4, pp. 231–273, 2014.

[77] M. G. Pike and C. Oskay, "Modeling random short nanofiber- and microfiber-reinforced composites using the extended finite-element method," *Journal of Nanomechanics and Micromechanics*, vol. 5, no. 1, p. A4014005, 2015.

[78] P. Gupta, C. Duarte, and A. Dhankhar, "Accuracy and robustness of stress intensity factor extraction methods for the generalized/eXtended Finite Element Method," *Engineering Fracture Mechanics*, vol. 179, pp. 120–153, June 2017.

[79] P. Alves and C. A. Duarte, "Three-dimensional crack propagation in fiber-reinforced composites using a nonlinear debonding law for fiber-matrix interface," *In preparation to be submitted to Computer and Structures*, 2020.

[80] F. M. Mukhtar, P. D. Alves, and C. A. Duarte, "Validation of a 3-d adaptive stable generalized/extended finite element method for mixed-mode brittle fracture propagation," *Engineering Fracture Mechanics*, 2020.

[81] J. Hartig, U. Haußler-Combe, and K. Schicktanz, "Influence of bond properties on the tensile behaviour of textile reinforced concrete," *Cement and Concrete Composites*, vol. 30, no. 10, pp. 898 – 906, 2008.

[82] R. Barhum and V. Mechtcherine, "Influence of short dispersed and short integral glass fibres on the mechanical behaviour of textile-reinforced concrete," *Materials and Structures*, vol. 46, pp. 557 – 572, 2013.

[83] Y. Qin, X. Zhang, J. Chai, Z. Xu, and S. Li, "Experimental study of compressive behavior of polypropylene-fiber-reinforced and polypropylene-fiber-fabric-reinforced concrete," *Construction and Building Materials*, vol. 194, pp. 216 – 225, 2019.

[84] F. K. F. Radtke, A. Simone, and L. J. Sluys, "A partition of unite finite element method for simulating non-linear debonding and matrix failure in thin fibre composites," *International Journal for Numerical Methods in Engineering*, vol. 86, pp. 453–476, 2011.

[85] F. N. Fritsch and R. E. Carlson, "Monotone piecewise cubic interpolation," *Society for Industrial and Applied Mathematics*, 1980.

[86] J. Pereira, C. Duarte, X. Jiao, and D. Guoy, "Generalized finite element method enrichment functions for curved singularities in 3D fracture mechanics problems," *Computational Mechanics*, vol. 44, no. 1, pp. 73–92, 2009.

[87] J. Pereira, C. Duarte, and X. Jiao, "Three-dimensional crack growth with *hp*-generalized finite element and face offsetting methods," *Computational Mechanics*, vol. 46, no. 3, pp. 431–453, 2010.

[88] P. Gupta and C. Duarte, "Simulation of non-planar three-dimensional hydraulic fracture propagation," *International Journal for Numerical and Analytical Methods in Geomechanics*, vol. 38, pp. 1397–1430, 2014.

[89] C. Duarte, *ISET-An Adaptive Generalized Finite Element Solver, Reference Manual*, ISET Developers, http://gfem.cee.illinois.edu, 2016.

[90] CGAL, "Computational Geometry Algorithms Library," 2012. [Online]. Available: http://www.cgal.org

[91] M. Schöllmann, H. Richard, G. Kullmer, and M. Fulland, "A new criterion for the prediction of crack development in multiaxially loaded structures," *International Journal of Fracture*, vol. 117, no. 2, pp. 129–141, 2002.

[92] F. Erdogan and G. Sih, "On the crack extension in plates under plane loading and transverse shear," *Journal of Basic Engineering*, vol. 85, pp. 519–527, 1963.

[93] H. A. Richard, M. Fulland, and M. Sander, "Theoretical crack path prediction," *Fatigue & Fracture of Engineering Materials & Structures*, vol. 28, no. 1–2, pp. 3–12, 2005.

[94] J. Pereira, "Generalized finite element methods for three-dimensional crack growth simulations," PhD Dissertation, University of Illinois at Urbana-Champaign, 2010, urbana, IL, USA.

[95] M. Kuna, *Finite elements in fracture mechanics: theory numerics applications*. Dordrecht: Springer, 2013.

[96] A. Paris and F. Erdogan, "A critical analysis of crack propagation laws," *Journal of Basic Engineering*, vol. 85, pp. 528–534, 1963.

[97] A. A. Griffith, "The phenomena of rupture and flow in solids," *Philosophical Transactions of the Royal Society of London. Series A, Containing Papers of a Mathematical or Physical Character*, vol. 221, pp. pp. 163–198, 1921.

[98] R. Nuismer, "An energy release rate criterion for mixed mode fracture," *International Journal of Fracture*, vol. 11, pp. 245–250, 1975.

[99] V. Lazarus, "Brittle fracture and fatigue propagation paths of 3D plane cracks under uniform remote tensile loading," *International Journal of Fracture*, vol. 122, no. 1-2, pp. 23–46, 2003.

[100] J. Rungamornrat, M. Wheeler, and M. Mear, "A numerical technique for simulating nonplanar evolution of hydraulic fractures," in *Proceedings of the SPE Annual Technical Conference and Exhibition*, Dallas, TX, USA, October 9–12, 2005, sPE-96968-MS. p. 9.

[101] S. Chan, I. Tuba, and W. Wilson, "On the finite element method in linear fracture mechanics," *Engineering Fracture Mechanics*, vol. 2, pp. 1–17, 1970.

[102] L. Banks-Sills and D. Sherman, "Comparison of methods for calculating stress intensity factors with quarter-point elements," *International Journal of Fracture*, vol. 32, pp. 127–140, 1986.

[103] A. Dhankhar, "A comparative study of stress intensity factor extraction techniques for the generalized finite element method," M.S. thesis, University of Illinois at Urbana-Champaign, May 2016. [Online]. Available: http://hdl.handle.net/2142/90968

[104] M. Goudarzi and A. Simone, "Fiber neutrality in fiber-reinforced composites: Evidence from a computational study," *International Journal of Solids and Structures*, vol. 156-157, pp. 14–28, 2019.

[105] M. K. Bannister, "Development and application of advanced textile composites," *Proceedings of the Institution of Mechanical Engineers, Part L: Journal of Materials: Design and Applications*, vol. 1, pp. 253–260, 2004.

[106] P. Alves and C. A. Duarte, "A multiscale generalized FEM for three-dimensional crack propagation in fiber reinforced composites," *EMI research competition - MIT*, 2018.

[107] C. A. Duarte and I. M. Babuska, "A global-local approach for the construction of enrichment functions for the generalized fem and its application to propagating three-dimensional cracks," ECCOMAS Thematic Conference on Meshless Methods, Technical Report, 2005, technical Report 06.

[108] A. K. Noor, "Global-local methodologies and their application to nonlinear analysis," *Finite Elements in Analysis and Design*, vol. 2, pp. 333–346, 1986.

[109] D. J. Kim, J. P. Pereira, and C. A. Duarte, "Analysis of three-dimensional fracture mechanics problems: A two-scale approach using coarse-generalized fem meshes," *International Journal for Numerical Methods in Engineering*, vol. 81, pp. 335–365, 2010.

[110] D. J. Kim, C. A. Duarte, and N. A. Sobh, "Parallel simulations of three-dimensional cracks using the generalized finite element method," *Computational Mechanics*, 2011.

[111] H. Li, "A multiscale computational framework for the simulation of local features in large structures," PhD Thesis, University of Illinois at Urbana-Champaign, May 2020.

[112] J. P. A. Pereira, D. J. Kim, and C. A. Duarte, "A two-scale approach for the analysis of propagating three-dimensional fractures," *Computational Mechanics*, 2011.

[113] G. Hager, *Introduction to high performance computing for scientists and engineers*, 1st ed. CRC computational science series, 2011.

[114] P. D. Alves, "Global-local strategy applied to the generalized finite element method," M.S. thesis, Federal University of Minas Gerais, 2012.

[115] P. D. Alves, F. B. Barros, and R. L. S. Pitangueira, "An object-oriented approach to the generalized finite element method," *Iberian Latin American Congress on Computational Methods*, vol. 1, pp. 1–21, 2013.

[116] M. Malekan, F. Barros, R. Pitangueira, and P. Alves, "An object-oriented class organization for global-local generalized finite element method," *Latin American Journal of Solids and Structures*, vol. 13, 2016.

[117] P. Gupta, J. Pereira, D.-J. Kim, C. Duarte, and T. Eason, "Analysis of three-dimensional fracture mechanics problems: A non-intrusive approach using a generalized finite element method," *Engineering Fracture Mechanics*, vol. 90, pp. 41–64, 2012.

[118] D. J. Kim, C. A. Duarte, and J. P. Pereira, "Analysis of interacting cracks using the generalized finite element method with global-local enrichment functions," *ASME Journal of Applied Mechanics*, vol. 75, pp. 763–813, 2008.

[119] V. Gupta, D. Kim, and C. Duarte, "Extensions of the two-scale generalized finite element method to nonlinear fracture problems," *International Journal for Multiscale Computational Engineering*, vol. 11, pp. 581–596, 2013.

[120] J. A. Plews and C. A. Duarte, "Bridging multiple structural scales with a generalized finite element method," *International Journal for Numerical Methods in Engineering*, vol. 102(3-4), pp. 180–201, 2015.

[121] J. A. Plews and C. A. Duarte, "Generalized finite element approaches for analysis of localized thermo-structural effects," *International Journal for Numerical Methods in Engineering*, vol. 1, pp. 1–1, 2015.

[122] J. Kim and C. A. Duarte, "A new generalized finite element method for two-scale simulations of propagating cohesive fractures in 3-d," *International Journal for Numerical Methods in Engineering*, vol. 1, pp. 1–1, 2015.

[123] V. Lefevre and O. Lopez-Pamies, "The overall elastic dielectric properties of fiber-strengthened/weakened elastomers," *Journal of Applied Mechanics*, vol. 82, pp. 111 009–111 009–21, 2015.

[124] Z. Hashin and B. W. Rosen, "The elastic moduli of fiber-reinforced materials," *Journal of Applied Mechanics*, vol. 31, pp. 223–232, 1964.

[125] A. Aragon and A. Simone, "The discontinuity-enriched finite element method," *International Journal for Numerical Methods in Engineering*, vol. 112, no. 11, pp. 1589–1613, 2017.

[126] T. Belytschko, Y. Lu, and L. Gu, "Element-free Galerkin methods," *International Journal for Numerical Methods in Engineering*, vol. 37, pp. 229–256, 1994.

[127] W. Liu, S. Jun, and Y. Zhang, "Reproducing kernel particle methods," *International Journal for Numerical Methods in Fluids*, vol. 20, pp. 1081–1106, 1995.

[128] W. K. Liu, Y. Chen, S. Jun, T. Belytschko, C. Pan, R. A. Uras, and C. T. Chang, "Overview and applications of the reproducing kernel particles methods," *Archives of Computational Methods in Engineering*, vol. 3, pp. 3–80, 1996.

[129] H. Fabritius, C. Sachs, P. R. Triguero, and D. Raabe, "Influence of structural principles on the mechanics of a biological fiberbased composite material with hierarchical organization: The exoskeleton of the lobster homarus americanus," *Advanced Materials*, vol. 21, 2009.

[130] X. Wang, X. Peng, P. Yue, H. Qi, J. Liu, L. Li, C. Guo, H. Xie, X. Zhou, and X. Yu, "A novel cpc composite cement reinforced by dopamine coated scpp fibers with improved physicochemical and biological properties," *Materials Science and Engineering: C*, vol. 109, 2020.

[131] T. Yokozeki, T. Ogasawara, and T. Ishikawa, "Effects of fiber nonlinear properties on the compressive strength prediction of unidirectional carbonfiber composites," *Composites Science and Technology*, vol. 65, 2005.

[132] Z. Hu, Q. Shao, Y. Huang, L. Yu, D. Zhang, X. Xu, J. Lin, H. Liu, and Z. Guo, "Light triggered interfacial damage self-healing of poly(p-phenylene benzobisoxazole) fiber composites," *Nanotechnology*, vol. 29, 2018.

[133] M. R. Kessler, N. R. Sottos, and S. R. White, "Self-healing structural composite materials," *Composites Part A: Applied Science and Manufacturing*, vol. 34, pp. 743–753, 2003.

[134] A. V. Krysko, J. Awrejcewicz, S. P. Pavlov, K. S. Bodyagina, and V. A. Krysko, "Topological optimization of thermoelastic composites with maximized stiffness and heat transfer," *Composite Part B: Engineering*, vol. 158, pp. 319–327, 2019.

[135] Z. Sun, D. Li, W. Zhang, S. Shi, and X. Guo, "Topological optimization of biomimetic sandwich structures with hybrid core and cfrp face sheets," *Composite Science and Technology*, vol. 142, pp. 79–90, 2017.

[136] A. Dean, J. Reinoso, N. K. Jha, E. Mahdi, and R. Rolfes, "A phase field approach for ductile fracture of short fibre reinforced composites," *Theoretical and Applied Fractures Mechanics*, vol. 106, 2020.

[137] A. Dean, P. K. Kumar, J. Reinoso, C. Gerendt, M. Paggi, E. Mahdi, and R. Rolfes, "A multi phase-field fracture model for long fiber reinforced composites based on the puck theory of failure," *Composite Structures*, vol. 251, 2020.

[138] F. A. Denli, O. Gultekin, G. A. Holzapfel, and H. Dal, "A phase-field model for fracture of unidirectional fiber-reinforced polymer matrix composites," *Computational Mechanics*, vol. 65, pp. 1149–1166, 2020.

[139] G. Goh, Y. Yap, S. Agarwala, and W. Yeong, "Recent progress in additive manufacturing of fiber reinforced polymer composite," *Advanced Materials Technologies*, vol. 4, 2018.

[140] Z. Li, L. Wang, and G. Ma, "Mechanical improvement of continuous steel microcable reinforced geopolymer composites for 3d printing subjected to different loading conditions," *Composites Part B: Engineering*, vol. 187, 2020.

[141] S. Tabatabaei and S. Lomov, "Eliminating the volume redundancy of embedded elements and yarn interpenetrations in mesofinite element modelling of textile composites," *Computers and structures*, vol. 152, 2015.

[142] O. Vorobiov, S. Tabatabaei, and S. Lomov, "Mesh superposition applied to meso-fe modelling of fibre-reinforced composites: cross-comparison of implementations," *International Journal for Numerical Methods in Engineering*, vol. 111, 2016.

[143] Z. Andleeb, C. Strand, S. Malik, G. Hussain, H. Khawaja, G. Boiger, and M. Moatamedi, "Multiphysics analysis of cfrp charpy tests by varying temperatures," *International Journal of Multiphysics*, vol. 14, 2020.

[144] Y. Ni, S. Zhu, J. Sun, Z. Tong, Z. Zhou, and X. Xu, "Analytical buckling solution of magneto-electro-thermo-elastic cylindrical shells under multi-physics fields," *Composite Structures*, vol. 239, 2020.

[145] C. Sacco, A. B. Radwan, A. Anderson, R. Harik, and E. Gregory, "Machine learning in composite manufacturing: a case study of automated fiber placement inspection," *Composite Structures*, vol. 250, 2020.

[146] M. Jalal, R. M. Dastjerdi, and M. Bidram, "Big data in nanocomposites: Onn approach and mesh-free method for functionally graded carbon nanotube-reinforced composites," *Journal of Computational Design and Engineering*, vol. 6, pp. 209–223, 2018.

[147] T. Belytschko, R. Gracie, and G. Ventura, "A review of extended/generalized finite element methods for material modeling," *Modelling and Simulations in Materials Science and Engineering*, vol. 17, pp. 1–24, 2009.

[148] J. Dolbow, N. Moës, and T. Belytschko, "Discontinuous enrichment in finite elements with a partition of unity method," *Finite Elements in Analysis and Design*, vol. 36, pp. 235–260, 2000.

[149] R. Henshell and K. Shaw, "Crack tip finite elements are unnecessary," *International Journal for Numerical Methods in Engineering*, vol. 9, no. 3, pp. 495–507, 1975.

[150] R. Barsoum, "On the use of isoparametric finite elements in linear fracture mechanics," *International Journal for Numerical Methods in Engineering*, vol. 10, no. 1, pp. 25–37, 1976.

[151] I. Babuška and U. Banerjee, "Stable generalized finite element method (SGFEM)," *Computer Methods in Applied Mechanics and Engineering*, vol. 201–204, pp. 91–111, 2012.

[152] Q. Zhang, I. Babuška, and U. Banerjee, "Robustness in stable generalized finite element methods (SGFEM) applied to Poisson problems with crack singularities," *Computer Methods in Applied Mechanics and Engineering*, vol. 311, pp. 476–502, 2016.

[153] Q. Zhang, U. Banerjee, and I. Babuška, "Higher order stable generalized finite element method," *Numerische Mathematik*, vol. 128, no. 1, pp. 1–29, 2014.

[154] K. Kergrene, I. Babuška, and U. Banerjee, "Stable generalized finite element method and associated iterative schemes; application to interface problems," *Computer Methods in Applied Mechanics and Engineering*, vol. 305, pp. 1–36, 2016.

[155] I. Babuška, U. Banerjee, and K. Kergrene, "Strongly stable generalized finite element method: Application to interface problems," *Computer Methods in Applied Mechanics and Engineering*, vol. 327, pp. 58–92, 2017.

[156] M. Ndeffo, P. Massin, N. Moës, A. Martin, and S. Gopalakrishnan, "On the construction of approximation space to model discontinuities and cracks with linear and quadratic extended finite elements," *Advanced Modeling and Simulation in Engineering Sciences*, vol. 4, no. 1, 2017.

[157] D. Grégoire, H. Maigre, J. Réthoré, and A. Combescure, "Dynamic crack propagation under mixed-mode loading – comparison between experiments and X-FEM simulations," *International Journal of Solids and Structures*, vol. 44, no. 20, pp. 6517–6534, 2007.

[158] A. Bergara, J. Dorado, A. Martin-Meizoso, and J. Martínez-Esnaola, "Fatigue crack propagation in complex stress fields: Experiments and numerical simulations using the extended finite element method (XFEM)," *International Journal of Fatigue*, vol. 103, pp. 112–121, 2017.

[159] E. Ferrie, J.-Y. Buffiere, W. Ludwig, A. Gravouil, and L. Edwards, "Fatigue crack propagation: In situ visualization using X-ray microtomography and 3D similation using the extended finite element method," *Acta Materialia*, vol. 54, pp. 1111–1122, 2006.

[160] J. Shi, D. Chopp, J. Lua, N. Sukumar, and T. Belytschko, "Abaqus implementation of extended finite element method using a level set representation for three-dimensional fatigue crack growth and life predictions," *Engineering Fracture Mechanics*, vol. 77, no. 14, pp. 2840–2863, 2010.

[161] M. Nikfam, M. Zeinoddini, F. Aghebati, and A. Arghaei, "Experimental and XFEM modelling of high cycle fatigue crack growth in steel welded T-joints," *International Journal of Mechanical Sciences*, vol. 153-154, pp. 178–193, 2019.

[162] R. Tian, L. Wen, and L. Wang, "Three-dimensional improved XFEM (IXFEM) for static crack problems," *Computer Methods in Applied Mechanics and Engineering*, vol. 343, pp. 339–367, 2019.

[163] I. Varfolomeev, M. Burdack, S. Moroz, D. Siegele, and K. Kadau, "Fatigue crack growth rates and paths in two planar specimens under mixed mode loading," *International Journal of Fatigue*, vol. 58, pp. 12–19, 2014.

[164] E. Giner, N. Sukumar, J. E. Tarancón, and F. J. Fuenmayor, "An Abaqus implementation of the extended finite element method," *Engineering Fracture Mechanics*, vol. 76, no. 3, pp. 347–368, 2009.

[165] G. Ventura, E. Budyn, and T. Belytschko, "Vector level sets for description of propagating cracks in finite elements," *International Journal for Numerical Methods in Engineering*, vol. 58, no. 10, pp. 1571–1592, 2003.

[166] Z. Shabir, E. Van der Giessen, C. Duarte, and A. Simone, "On the applicability of linear elastic fracture mechanics scaling relations in the analysis of intergranular fracture of brittle polycrystals," *International Journal of Fracture*, 2019, accepted.

[167] K. Pham, K. Ravi-Chandar, and C. Landis, "Experimental validation of a phase-field model for fracture," *International Journal of Fracture*, vol. 205, no. 1, pp. 83–101, 2017.

[168] B. Szabo and I. Babuška, *Finite Element Analysis*. New York: John Wiley and Sons, 1991.

[169] A. Kumar and O. Lopez-Pamies, personal Communication.

[170] C. Duarte, "Report 2013-2014 NSF: Validated multiscale simulations of ceramic matrix composites," University of Illinois at Urbana-Champaign, Technical Report, 2014.

[171] N. Sakakibara, "Finite element method in fracture mechanics," The University of Texas at Austin, Technical Report, 2008.

[172] M. Kuna, *Finite Element in Fracture Mechanics*. Spring, 2013.

[173] S. Mohammadizadeh, "A novel augmented fem for modeling arbitrary cracking in solids," PhD Thesis, University of Miami, November 2013.

[174] S. Li and S. Ghosh, "Modeling interfacial debonding and matrix cracking in fiber reinforced composites by the extended voronoi cell fem," *Finite Element in Analysis and Design*, vol. 43, pp. 397–410, 2007.

[175] E. Jongejans, "FEM modeling of fiber reinforced composites," MSc Thesis, Delft University of Technology, 2012.

[176] A. Simone, "Personal communication," unpublished.

Appendix A

Object-Oriented Project

The methods described in the previous chapters are implemented and performed using the Illinois Scientific and Engineering Toolkit (ISET), a numeric implementation of the Generalized Finite Element Method. ISET is a research code under development by a research team supervised and guided by its creator, Professor Carlos Armando Duarte from the Department of Civil and Environmental Engineering at the University of Illinois at Urbana-Champaign. The implementation of this research project is facilitated by its highly modularized and object oriented architecture.

As a part of this research project, ISET was augmented to implemented a LFEM problem with fibers embedded in a background mesh. For this purpose fibers are idealized as two noded truss elements. This implementation uses an existing framework of four noded linear tetrahedrons as background mesh elements. Only linear elastic, isotropic matrix materials are considered in this research, but all the capabilities can be easily expanded to other materials types or modules already implemented in ISET. A nonlinearity is considered at the interface of the matrix-fiber.

A.1 General aspects

The fiber framework is composed by three main applications:

- *fiber engine*: group of classes responsible for finding intersections between fibers and elements.
- *fiber manager*: group of classes responsible for the interface between fiber engine and ISET. Create one dimensional elements representing fibers, enrich three dimensional elements, manage fiber materials, etc.
- *fiber material*: group of classes responsible for calculating the terms depicted in Chapters 2 and 3.

A.2 *Fiber engine*

The model described in Ch. 3 requires the knowledge of the matrix elements that are in the neighborhood of the fibers. The exact intersection with each background element is also required to integrate functions that have discontinuous derivatives across element boundaries, such as the shape functions of these matrix elements. This gives rise to the need for an efficient three-dimensional intersection calculation algorithm, capable of handling the typically large number of fibers that might intersect a given mesh.

Fiber engine was created in order to deal with the multiple fibers intersecting the matrix. Figure A.1 shows an overview of geometric engine algorithm. The follow steps are highlighted:

- The user provides 2 input files: one for mesh (.grf) and one for fiber distribution (.frf).
- *FiberGeoEng3d* creates a temporary *FiberBuilderType* and reads the input file.
- *FiberGeoEng3d* creates a *GeoMesh* and reads data from input mesh file.
- *fiberContainerType* is created from *FiberBuilderType*.
- *GeoEl* are extracted from *GeoMesh* and intersections for each fiber is stored in *IntersectionWithTet*.
- *FibCutelinfo* is created and linked with associated *GeoEl*.

The fiber geometric engine, after computation of intersections between fiber distribution and background mesh, generates sets of objects of two classes: *FibCutelinfo* and *IntersectionWithTet*. They both are used by the fiber manager in the next step of analysis.

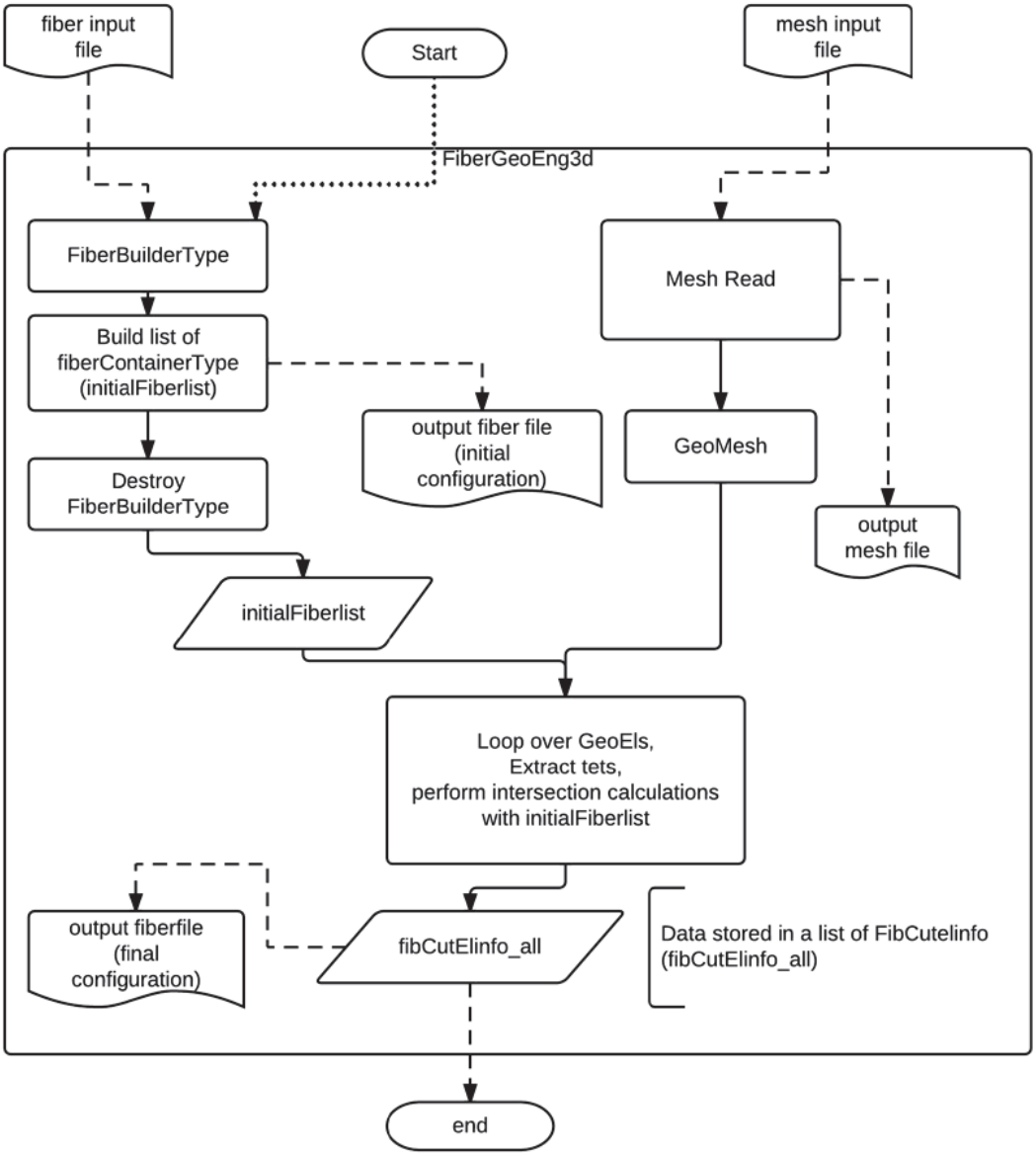

Figure A.1: Overview of Geometric Engine

A.3 *FiberManager3d*

In order to use existing algorithms of ISET, the objects generated by *FiberEng3d* need to be converted. *FibCutelinfo* and *IntersectionWithTet* are converted to *GeoElTet* for the intersected background and *GeoEl1D* for fiber intersection. Figure A.2 depicts the overall algorithm of the class.

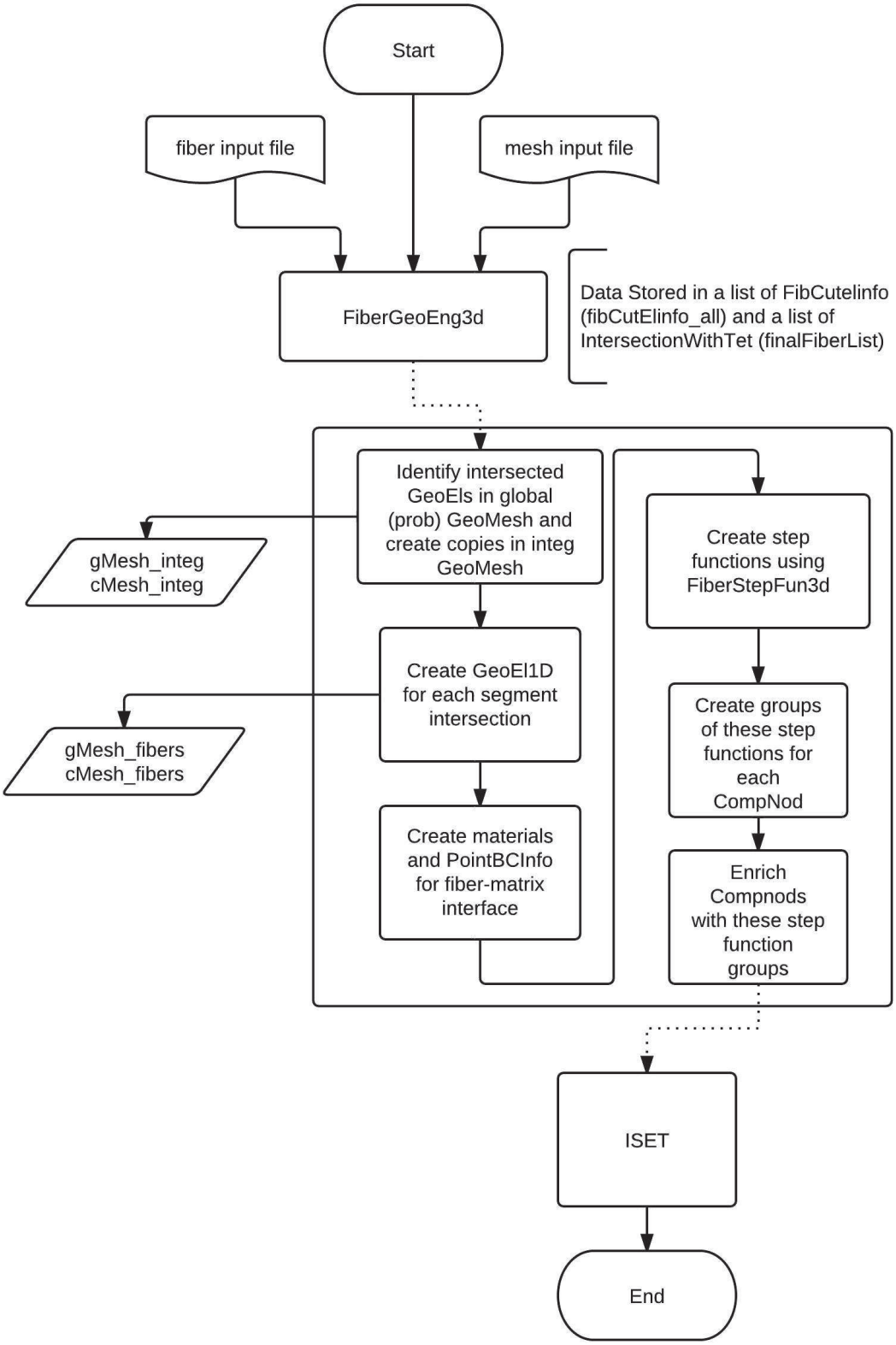

Figure A.2: Overview of FiberManager3d algorithm

A.4 Statement of the problem

The set of equations developed in Ch. 3 are here written in a more suitable way to be implemented into ISET. Since ISET numbers FEM DOFs and enrichments DOFs in a nodal level (or, in other words, the coeficients due to the enrichment are not concentrated in a certain region of the final stiffness matrix), our formulation can be more easily implemented using the expressions depicted in the next 3 sections. Figure A.3 shows an example of a linear tetrahedron enriched by one fiber. The total stiffness K_{total} is composed by three contributions.

- K_1: representing the contribution due to the matrix.
- K_{2a}: representing the contribution due to the fiber.
- K_{2b}: representing the contribution due to the bond slip between fiber and matrix.

The original linear tetrahedron used in this example is originally composed by 4 nodes and has a total of 12 DOFs (each node has 3 DOFs). When enriched with 1 fiber the total number of DOFs is changed to 24, since 3 new DOFs are added to each node. Each additional fiber increases in 3 DOFs the total number of DOFs in each node.

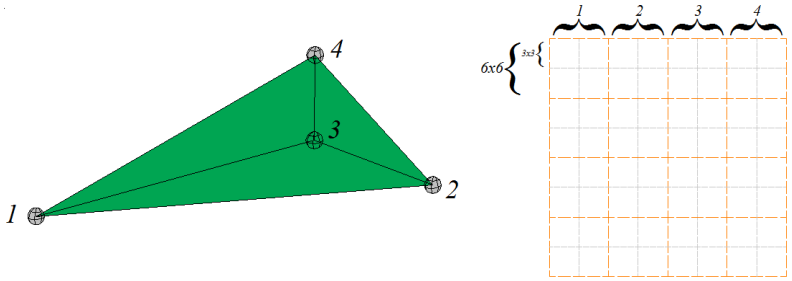

$$K_{total} = K_1 + K_{2a} + K_{2b}$$

Figure A.3: Contributions for the stiffness matrix

A.4.1 Stiffness due to the matrix (K_1)

It corresponds to contribution due to the stiffness of the matrix. The calculation is performed over volume and coordinated by the method *contributeDescend* from *CompEl* class. Figure A.4 shows discrete equation responsible for this stiffness as well where the data are localized in the final stiffness matrix of the element. All the values related to fiber enrichment are zero in this case, since the fiber step functions are zero for volume integration (see Fig. A.5).

$$K_{1_{24x24}} = \int_{\Omega} B^T_{m_{24x6}} \cdot \mathcal{D}_{m_{6x6}} \cdot B_{m_{6x24}} d\Omega$$

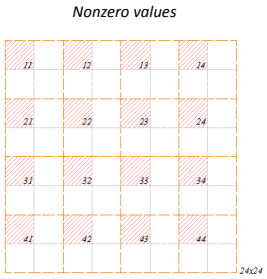

Figure A.4: Entries related to K_1 in the stiffness matrix of an element

We can observe that the integral in Figs. A.4 and A.5 are equal to the equations to the fiber GFEM. Here, however, B_m includes coefficients related to FEM and enrichments DOFs. The purpose of this change in notation is to make compatible the formulation with what was effectively implemented in ISET. Figure A.5 shows the details for each term of K_1 .

$$K_{1_{24x24}} = \int_{\Omega} B^T_{m_{24x6}} \cdot \mathcal{D}_{m_{6x6}} \cdot B_{m_{6x24}} d\Omega$$

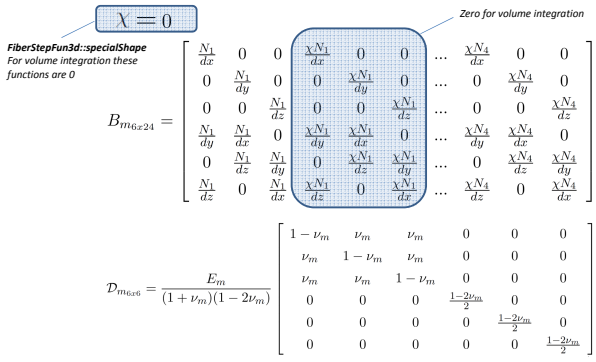

Figure A.5: Details for each term of K_1

A.4.2 Stiffness due to the fiber (K_{2A})

It corresponds the contribution due to the stiffness of the fiber. The calculation is performed over the line and also coordinated by the method *contributeDescend* from *CompEl* class. Figure A.6 shows discrete equation responsible for this stiffness. The nonzero values fulfill all the stiffness matrix, as shown in Fig. A.6.

$$K_{2a_{24x24}} = A_f \int_l B^T_{m_{24x6}} \cdot \mathcal{D}_{f_{6x6}} \cdot B_{m_{6x24}} dl$$

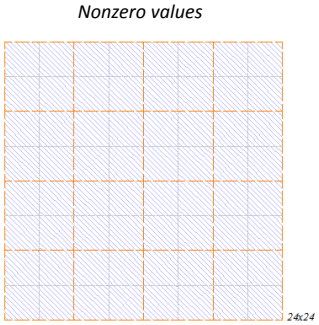

Figure A.6: Contributions due to the fiber

We can observe that this term corresponds to the coupled matrix/fiber: B_m comes from the matrix (volume) and $\mathcal{D}_f$ from the material properties of the fiber. Figure A.7 shows in details the terms for our example.

$$K_{2a_{24x24}} = A_f \int_l B^T_{m_{24x6}} \cdot \mathcal{D}_{f_{6x6}} \cdot B_{m_{6x24}} dl$$

$$B_{m_{6x24}} = \begin{bmatrix} \frac{N_1}{dx} & 0 & 0 & \frac{\chi N_1}{dx} & 0 & 0 & \dots & \frac{\chi N_4}{dx} & 0 & 0 \\ 0 & \frac{N_1}{dy} & 0 & 0 & \frac{\chi N_1}{dy} & 0 & \dots & 0 & \frac{\chi N_4}{dy} & 0 \\ 0 & 0 & \frac{N_1}{dz} & 0 & 0 & \frac{\chi N_1}{dz} & \dots & 0 & 0 & \frac{\chi N_4}{dz} \\ \frac{N_1}{dy} & \frac{N_1}{dx} & 0 & \frac{\chi N_1}{dy} & \frac{\chi N_1}{dx} & 0 & \dots & \frac{\chi N_4}{dy} & \frac{\chi N_4}{dx} & 0 \\ 0 & \frac{N_1}{dz} & \frac{N_1}{dy} & 0 & \frac{\chi N_1}{dz} & \frac{\chi N_1}{dy} & \dots & 0 & \frac{\chi N_4}{dz} & \frac{\chi N_4}{dy} \\ \frac{N_1}{dz} & 0 & \frac{N_1}{dx} & \frac{\chi N_1}{dz} & 0 & \frac{\chi N_1}{dx} & \dots & \frac{\chi N_4}{dz} & 0 & \frac{\chi N_4}{dx} \end{bmatrix}$$

$$\mathcal{D}_{f_{6x6}} = \frac{E_f}{(1+\nu_f)(1-2\nu_f)} \begin{bmatrix} 1-\nu_f & \nu_f & \nu_f & 0 & 0 & 0 \\ \nu_f & 1-\nu_f & \nu_f & 0 & 0 & 0 \\ \nu_f & \nu_f & 1-\nu_f & 0 & 0 & 0 \\ 0 & 0 & 0 & \frac{1-2\nu_f}{2} & 0 & 0 \\ 0 & 0 & 0 & 0 & \frac{1-2\nu_f}{2} & 0 \\ 0 & 0 & 0 & 0 & 0 & \frac{1-2\nu_f}{2} \end{bmatrix}$$

Figure A.7: Details of each term of K_{2a}

A.4.3 Stiffness due to the bond slip (K_{2b})

It corresponds the stiffness contribution due to the bond slip between fiber and matrix. As K_{2A}, the calculation is performed over the line and also coordinated by the method *contributeDescend* from *CompEl* class. Figure A.8 shows discrete equation responsible for this stiffness. The nonzero values are shown in Fig. A.8.

$$K_{2b_{24x24}} = C_f \int_l [[\mathcal{N}_m^T]]_{24x3} \cdot {R^T}_{3x3} \cdot \mathcal{D}_{b_{3x3}} \cdot R_{3x3} \cdot [[\mathcal{N}_m]]_{3x24} dl$$

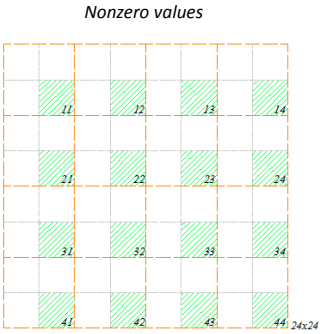

Figure A.8: Contributions due to the bond slip of the fiber

It is important to observe the presence of the term $[[\mathcal{N}_m]]$ in this integral. This term can be understood by the difference between the displacement field from matrix and fiber. As an example, see the an element and a fiber shown in Fig. A.9. The cross section between matrix and fiber is shown in details.

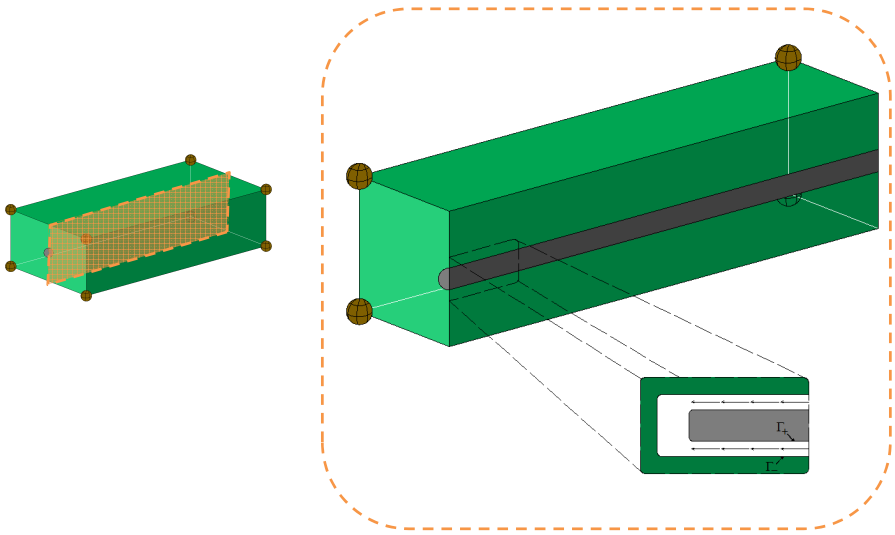

Figure A.9: Details of the bond slip

There is clearly an discontinuous approximation between the boundaries from the fiber side Γ_+ and matrix side Γ_-. As shown in Fig. A.10, the approximation at the fiber side Γ_+ is given by $\mathcal{N}_{m\Gamma_+}$. On the other hand, the approximation of the matrix side Γ_- is given by $\mathcal{N}_{m\Gamma_-}$. The difference $\mathcal{N}_m = \mathcal{N}_{m\Gamma_+} - \mathcal{N}_{m\Gamma_-}$ gives the approximation $[[\mathcal{N}_m]]$.

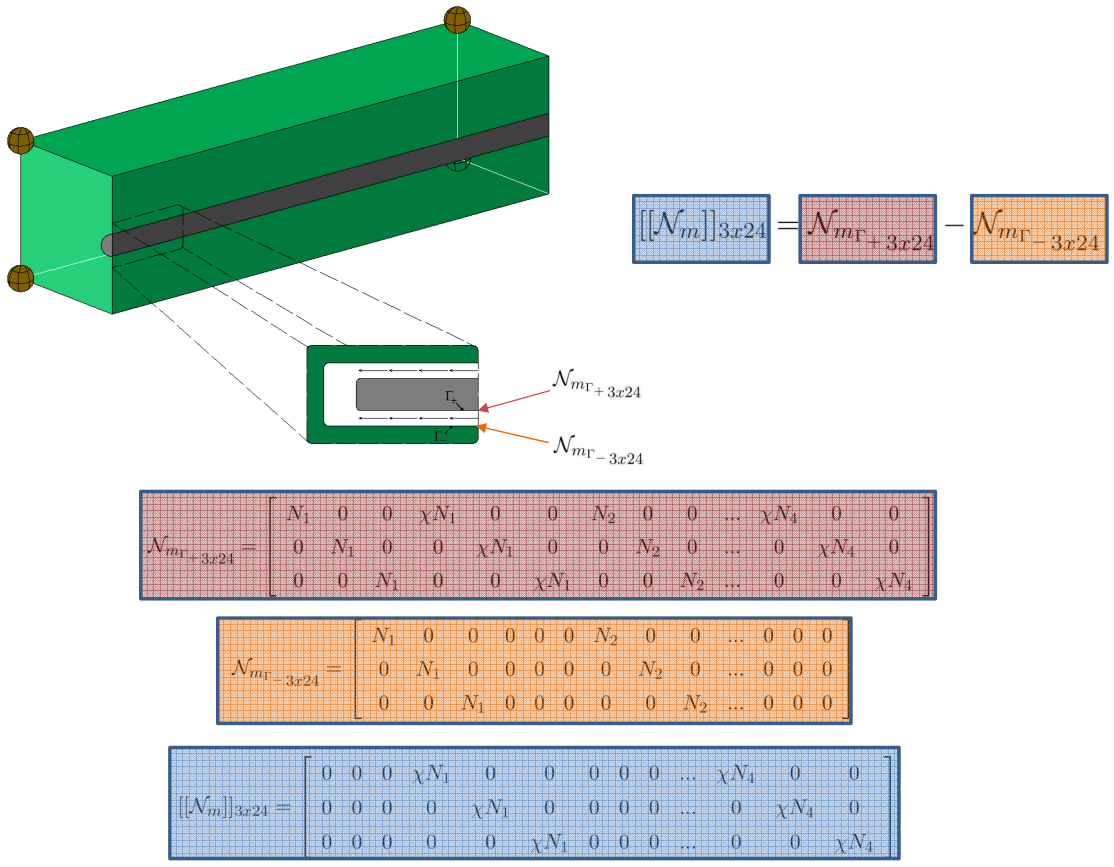

Figure A.10: Contributions for the stiffness matrix

Figure A.11 shows the terms for the line integral corresponding to K_{2b}. Special attention is given to the bond slip term $\mathcal{D}_b$, which is the second order tensor and represents the bond parameters between matrix and fiber. The R matrix just changes the coordinates of $\mathcal{D}_b$.

$$K_{2b_{24x24}} = C_f \int_l [[\mathcal{N}_m^T]]_{24x3} \cdot {R^T}_{3x3} \cdot \mathcal{D}_{b_{3x3}} \cdot R_{3x3} \cdot [[\mathcal{N}_m]]_{3x24} dl$$

$$[[\mathcal{N}_m]]_{3x24} = \mathcal{N}_{m_{\Gamma+\,3x24}} - \mathcal{N}_{m_{\Gamma-\,3x24}}$$

$$[[\mathcal{N}_m]]_{3x24} = \begin{bmatrix} 0 & 0 & 0 & \chi N_1 & 0 & 0 & 0 & 0 & 0 & \dots & \chi N_4 & 0 & 0 \\ 0 & 0 & 0 & 0 & \chi N_1 & 0 & 0 & 0 & 0 & \dots & 0 & \chi N_4 & 0 \\ 0 & 0 & 0 & 0 & 0 & \chi N_1 & 0 & 0 & 0 & \dots & 0 & 0 & \chi N_4 \end{bmatrix}$$

MatFiberElas3d::contribute
If element has MatFiberElas3d material, these terms are 0

$$\mathcal{D}_{b3x3} = \begin{bmatrix} k_{bt} & 0 & 0 \\ 0 & k_{bn} & 0 \\ 0 & 0 & k_{bn} \end{bmatrix}$$

$$R_{3x3} = \begin{bmatrix} \cos(\theta_x^{x'}) & \cos(\theta_y^{x'}) & \cos(\theta_z^{x'}) \\ \cos(\theta_x^{y'}) & \cos(\theta_y^{y'}) & \cos(\theta_z^{y'}) \\ \cos(\theta_x^{z'}) & \cos(\theta_y^{z'}) & \cos(\theta_z^{z'}) \end{bmatrix}$$

Figure A.11: Details for the bond slip contribution

A.4.4 Total contribution

The total stiffness matrix is given by the contribution of these three terms (K_1 + K_{2a} + K_{2b}). Figure A.12 shows how these contribution look like in the final stiffness matrix.

$$K_{total} = K_1 + K_{2a} + K_{2b}$$

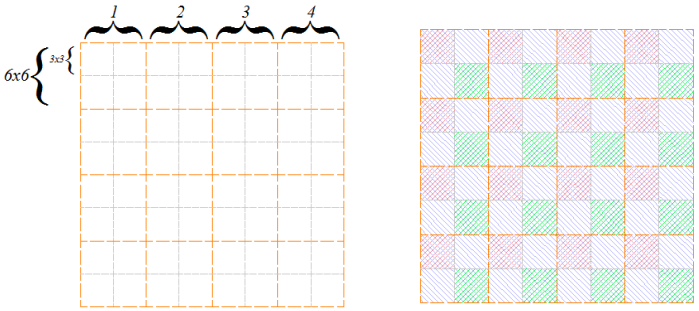

Figure A.12: Contributions for the stiffness matrix

Figure A.13 shows an UML activity diagram for the calculation of the stiffness matrix presented in Fig. A.12. It describes the method *calcStiff* from *CompMesh* class. An overview of the algorithm is given below:

- At the beginning of the method, the algorithm asks if there is at least one fiber embedded in the model. Methods *calcStiff* or *calcStiffLocGl* are performed (depending on the type of the problem which is being analyzed).

- *getDescendentList* gets a list of descendents of the element (using same procedure performed from Global-Local GFEM analysis). The first element of the list of the descendents corresponds the three-dimensional element (background matrix). The other elements of the list correspond to the one-dimensional element (fibers).

- A loop of each descendent is performed. For each descendent the algorithm asks if the descendent corresponds to a three-dimensional or one-dimensional element. For three-dimensional elements the fiber enrichment function is zero.

- If the descendent is a three-dimensional element, conventional method *contributeDescend* is called (in order to calculate *Stiffness (1)*). Otherwise, *Stiffness (2)* (integral over the line) must be performed. Fibers have an specific material.

- Contribution related to the fiber can be divided in two parts: *Stiffness (2A)* which is related to the coupled fiber-matrix problem, and *Stiffness (2B)* related to the fiber contribution. It is performed by the fiber material.

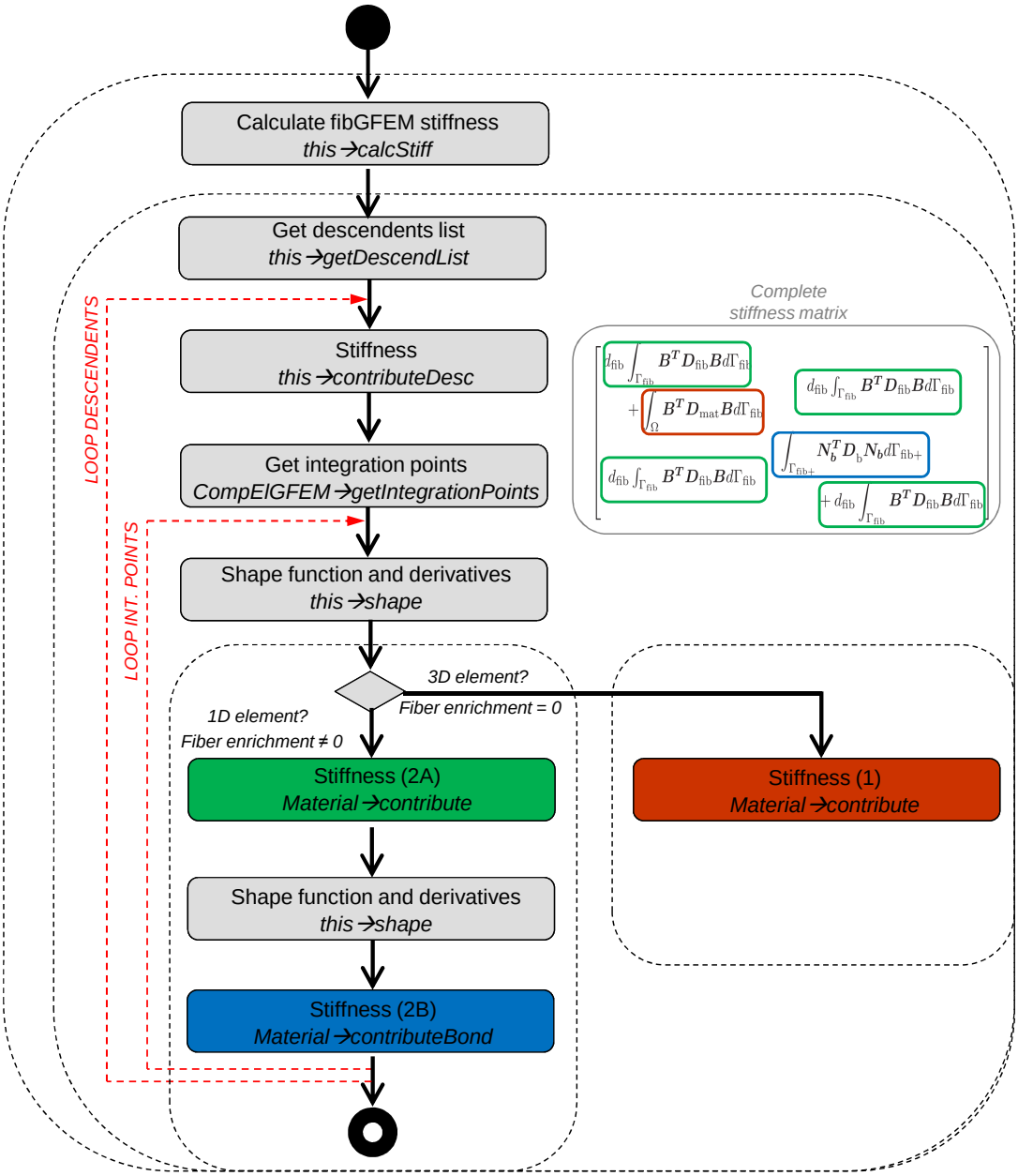

Figure A.13: UML activity diagram for stiffness matrix

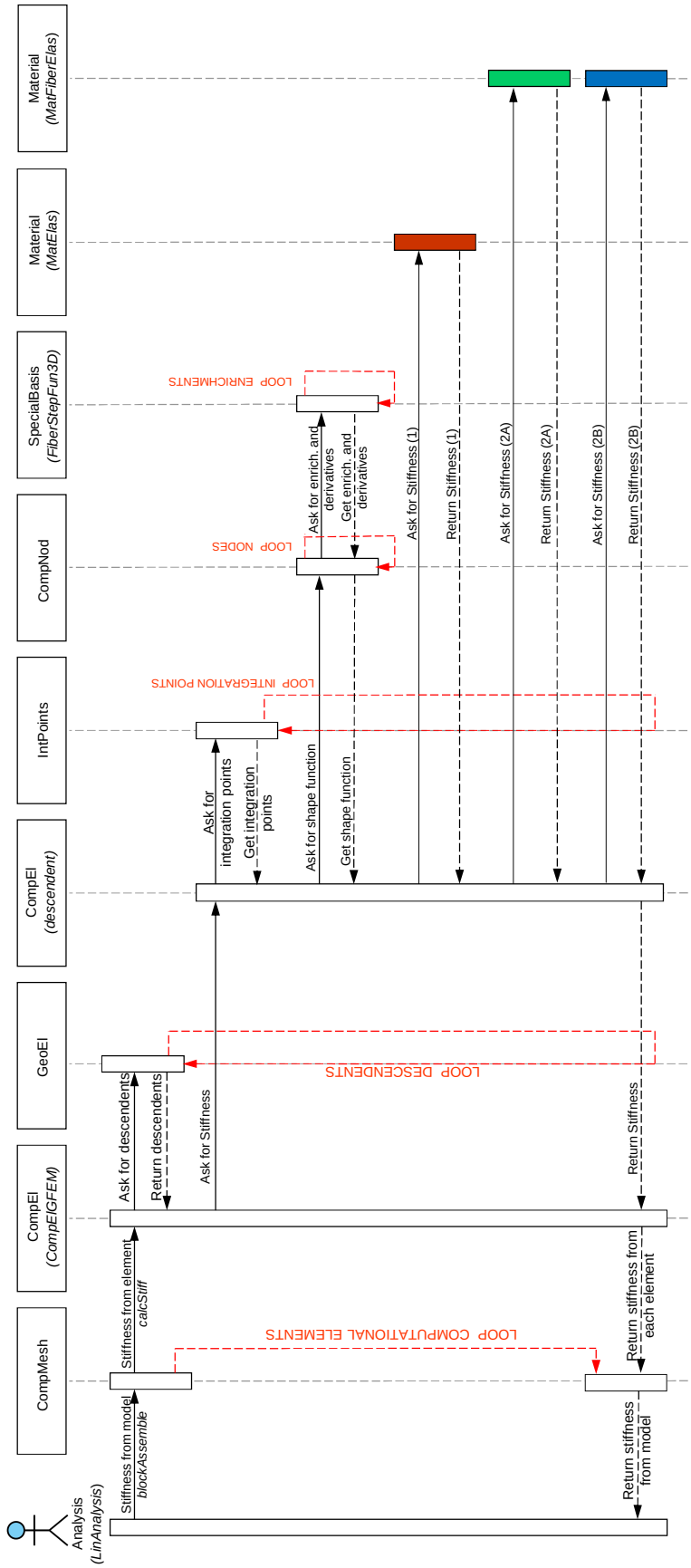

Figure A.14: UML sequence diagram for stiffness matrix

One important information observed in Fig. A.14 is related to the *CompEl* descendents objects. The red *CompEl* object corresponds to the integral over the volume using three-dimensional shape functions (*Stiffness (1)*). The green objects corresponds to the integral over the line, but using three-dimensional shape functions (coupled problem matrix-fiber *Stiffness (2a)*). Finally, the blue object corresponds to the integral over the line using one-dimensional shape functions (*Stiffness (2b)*).

Figure A.14 shows a UML sequence diagram for stiffness matrix. Differently from Fig. A.13, the focus here is on the relation between objects. This diagram shows how processes operate with one another and in what order. It is arranged in time sequence and depicts the classes involved in the scenario performed in Fig. A.13.

Appendix B

Validation of a 3D Adaptive Stable GFEM for Mixed-Mode Brittle Fracture Propagation

B.1 Introduction

This appendix [1] shows recent advances on GFEM for solution of fracture mechanics problems. The GFEM (or XFEM, [147]) has been developed and improved for more than two decades for the solution of fracture mechanics problems [5, 6, 58, 64, 148] and currently is available in several mainstream commercial software such as Abaqus, ANSYS, LS-DYNA, OptiStruct, etc. The GFEM [4–6, 54, 55, 58, 63] can be interpreted as a FEM with an enriched test/trial space which is obtained by hierarchically augmenting a standard finite element approximation space, $\mathbb{S}_{FEM}$, with an enrichment space, $\mathbb{S}_{ENR}$ derived from a priori knowledge about the solution of a problem.

The enrichment space used in the GFEM enables the use of finite element meshes that do not fit crack surfaces or their fronts. This flexibility of the method is particularly appealing in the case of 3-D simulations of crack propagation, like those considered in this appendix. Furthermore, the convergence rate of the GFEM presented in [65] is at least three times higher than quadratic finite elements with quarter-point elements [149, 150] around the crack front, which are broadly used to solve fracture problems. However, the condition number of the GFEM stiffness matrix grows much faster than in the classical FEM as the mesh is refined.

There is a considerable amount of work on approaches to address the conditioning issue of the method [151–156]. The approach adopted here is the so-called Stable GFEM (SGFEM) with a discontinuous interpolant enrichment modification and a p-hierarchical FEM basis – the pFEM-DSGFEM introduced in [65] for 3-D fracture problems.

[1] This appendix has been adapted from the paper by "F. Mukhtar, P. Alves and C. A. Duarte, Validation of a 3-D Adaptative Stable Generalized/eXtended Finite Element Method for Mixed-Mode Brittle Fracture Propagation, International Journal of Fracture (2020), [80]"

This SGFEM, with the proper choice of singular enrichments, leads to stiffness matrices with a scaled condition number of the same order as in the standard FEM. The *p*FEM-GFEM and its well-conditioned counterpart *p*FEM-DSGFEM is presented in [65].

The goal of this section is the validation of an adaptive *p*FEM-DSGFEM for a Compact tension specimen. Additional validation problems can be found in the full paper [80]. For the example shown here crack propagation is assumed to be governed by Griffith's criterion [97, 98]. The GFEM and some of the algorithms adopted here have been extensively verified [65, 67, 76, 87, 88] but not systematically validated.

The literature on GFEM for fracture propagation is quite extensive but most of the works have focused on the development of the method and its verification against analytical or reference solutions. Examples of works dedicated to the validation of the method for problems governed by LEFM include the works of Grégorie et al. [157] on 2D dynamic crack propagation, the work of Bergata et al. [158], Ferrié et al. [159], Shi et al. [160], Nikfam et al. [161], Tian et al. [162], and Varfolomeev et al. [163] on 3-D fatigue crack propagation. The work of Giner et al. [164], and Ventura et al. [165] on 2-D simulations of brittle crack propagation.

Several of the algorithmic aspects of the GFEM adopted here have been presented in [67, 76, 87, 88]. They include the representation and update of non-planar fracture surfaces, the integration of the weak form over element intersected by the fracture, etc. The complete computational geometry strategies and crack propagation algorithm with mesh adaptivity is presented in [80]

The satisfaction of a brittle fracture propagation criterion in 3-D may require an iterative procedure to find loading scaling factors or the crack size that meets the criterion. In this section, LEFM scaling relations are used to back calculate scaling factors that lead to the satisfaction of the propagation criterion. These scaling factors are also used to compute other quantities of interest such as reaction forces and Crack Opening Displacement (COD). These are low-cost post-processing operations performed on the GFEM solution of each crack propagation step. They involve no iterations or recalculation of the GFEM solution.

This is a novel strategy to solve 3-D mixed-mode brittle fracture propagation problems. Similar ideas are used by Shabir et al. [166] to find load-displacement curves for crack propagation in polycrystalline specimen and by Gupta and Duarte [88] to solve a Mode I hydraulic fracture propagation problem.

The simulations presented in this section validate not only an adaptive GFEM for brittle fracture propagation but also the algorithmic aspects of the method and the adopted computational fracture growth model for LEFM.

B.2 Validation with Experimental Results

The GFEM and algorithms presented earlier are validated against three experimental data sets. The experiments involve mode I and mode I+II fracture propagation problems with increasing complexity in crack path. Here it is shown one of the validation examples presented in [80], the reader is invited to follow this reference for further examples. For this simulation the Stress Intensity Factors (SIFs) are extracted using the Displacement Correlation Method (DCM). A brief review of the DCM formulation adopted in this work is given in Chapter 5.

B.2.1 Mode I+II fracture propagation: Modified CT Specimen CT31 of Pham et al. [167]

The systematically designed experiments conducted by Pham et al. [167] consists of two groups of specimens. The first one includes six compact tension (CT) specimens while the second one adopts three specimens and a modified CT specimen geometry. Here is presented the validation of the adaptive GFEM and the fracture propagation algorithm against data sets from a mode I+II fracture propagation problem. The experimental data are from Specimen CT31 of Pham et al. [167] unless stated otherwise.

The material of the specimen is a thermoplastic polymer, polymethylmethacrylate (PMMA), whose elastic material properties and fracture parameters, as determined in [167], are: Modulus of elasticity $E = 2.98\,GPa$; Poisson's ratio $\nu = 0.35$; and Fracture energy $G_c = 0.285\,kJ/m^2$ that resulted in an estimated fracture toughness $K_{Ic} = 0.98\,MPa \cdot m^{1/2}$.

The initial sharp crack is generated in the specimen ahead of the U-notch, using a wedge impact along with a blade. The top and bottom holes are loaded monotonically, with displacements $\boldsymbol{u}_y^+$ and $\boldsymbol{u}_y^-$, respectively, as illustrated in Fig. B.2.

Figure B.1 shows the setup used in the experiments of Pham et al. [167]. It consists of an Instron testing machine, cameras, and loading grips. The test proceeds using a displacement-controlled loading whose magnitude, and the displacement of the load-points are monitored. At the same time, a set of two cameras are placed on opposite sides of the specimen to capture the images used for calculating the crack opening displacement (COD) at the load line, using DIC analysis, and tracking the crack front location. The COD corresponding to each load step is determined using time correlation between the image and loading time sequences. More details about the experiment and a summary about the image analysis can be found in [167].

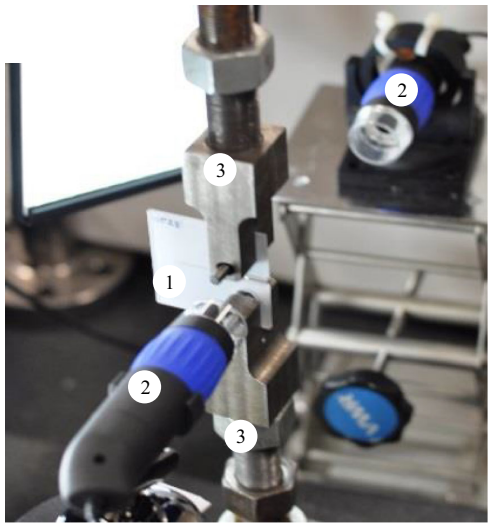

Figure B.1: Experimental setup showing the CT specimen (1), cameras (2), and loading grips (3), [167]

Figure B.2 shows the geometry and dimensions of the specimens of Pham et al. [167] tested under mixed-mode conditions. Each specimen is created by drilling a third hole in a CT specimen as shown in the figure. This hole influences the crack path as shown later on, leading to mode I+II fracture propagation.

The displacements imposed by loading pins on the top and bottom holes of the specimen are modeled as displacements prescribed to nodes located along the load lines shown in Fig. B.2. These nodes are equally spaced in the thickness direction of the specimen. Both vertical and lateral movements of the so defined nodes in the bottom hole are prevented in the GFEM model. Vertical upward displacement of magnitude $1.5\,mm$ is applied to the nodes of the top hole while its lateral movement is restricted. To prevent rigid body motion, one node in each of the top and bottom loaded lines is restricted from movement in all directions. A discussion on the influence of these modeling assumptions is presented in Section B.2.1.

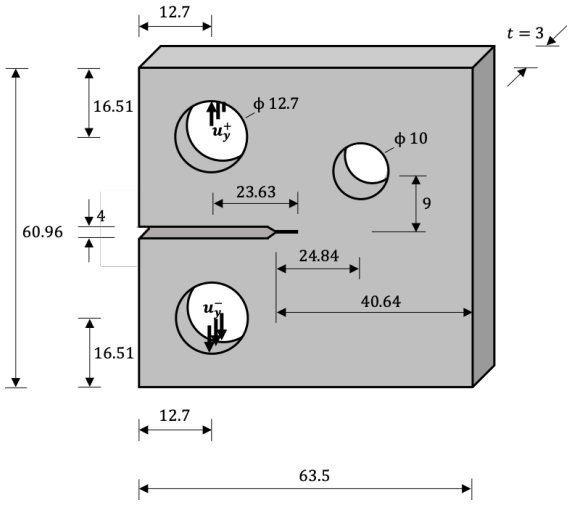

Figure B.2: Dimensions (in *mm*) of the modified CT specimen of [167]

It is well known that point displacement boundary condition is inconsistent in elasticity problems, except to prevent rigid body motion [168]. Numerical experiments not presented here were performed to check the sensitivity of computed reaction forces at the nodes with prescribed displacements. They show that, as long as a reasonably coarse mesh is used at the specimen holes, the results are not sensitive with respect to discretization parameters adopted in this section, such as the polynomial order of the GFEM approximation or element size at the holes.

Mesh refinement and enrichment studies are presented next. The effect of crack advancement magnitude, Δa_{max}, is also investigated. The actual geometry of the initial crack front in Specimen CT31 is not available. Thus, its effect on the GFEM results is not considered — the initial crack front is assumed to be straight in all simulations presented in this section. The initial crack surface, however, is slightly curved and the sharp crack does not start exactly from the U-notch tip. This happens due to fabrication imperfections, and it results in both the initial crack tail and front having some offset away from the intended nominal initial crack surface location.

Hence, the mixed-mode simulations presented in this section model the initial crack surface as non-planar with a vertical off-set estimated from the experimental results of [167]. The adopted crack front is given by the segment $(x = 13.221, y = 0.374, -1.5 \leq z \leq 1.5)\,mm$, with the origin of the coordinate system at U-notch "tip" (located at the middle plane of the specimen and at a distance of $40.64\,mm$ from the right face of the specimen).

Mesh refinement and enrichment study

Figures B.3(a) and B.3(c) show the two user-provided meshes used in the convergence studies presented in this section. Hereafter, the sequence of meshes based on them and used for the simulation of crack growth are denoted by "coarse" and "fine" meshes. The meshes ignore the initial crack ahead of the specimen notch as in the previous section. The nearly uniform meshes provided by the user are automatically refined around the propagating crack front as shown in figures B.3(b) and B.3(d) such that the maximum edge length of elements intersected by the crack front, $h_{\max}$, is close to $0.1\,mm$. This same $h_{\max}$ is used in all simulations presented in this section. The problem size using the coarse meshes and GFEM approximations of degree $p = 2$ ranges between 36,597 and 87,381 equations. In the case of simulations with fines meshes and $p = 2$, the problem size ranges between 262,572 and 309,360.

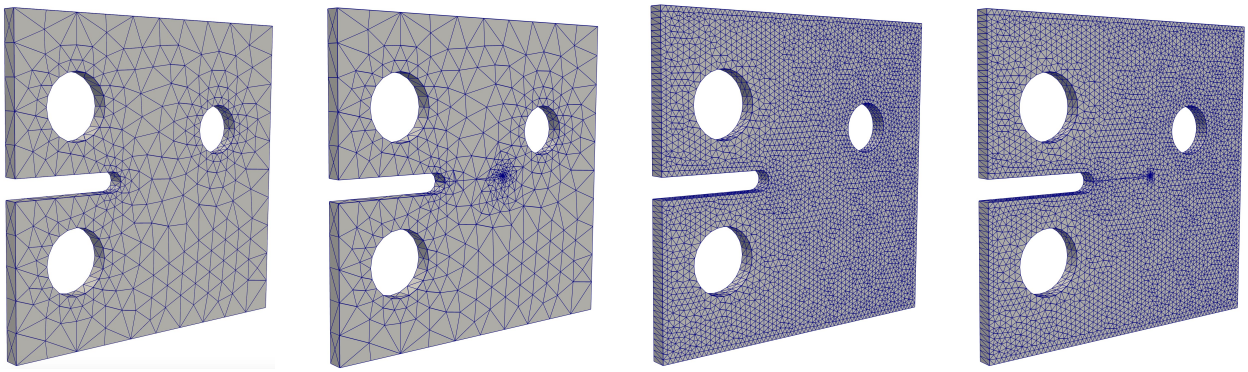

(a) **(b)** **(c)** **(d)**

Figure B.3: Discretization using coarse and fine meshes (a and c) and the corresponding typical automatic mesh refinement around the crack front during the fracture propagation (b and d) for the modified CT specimen used for mixed-mode fracture

Figure B.4 shows plots of load versus COD and the predicted crack path. The load is the reaction force at the nodes with prescribed displacement as explained earlier. These quantities are computed at each crack propagation step using the scaling relations. GFEM results for the sequence of coarse and fine meshes with $p = 2$ basis functions and $\Delta a_{\max} = 0.1\,mm$ are shown in the figure, together with the experimental results from [167].

The stiffness of the specimen before the crack propagates is matched very well by the GFEM model. The predicted critical load for crack propagation is slightly higher than the measured one but the GFEM curves match reasonably well the experimental data. The observed difference in Figure B.4(a) between the

GFEM curves and experimental data for COD greater than $\approx 0.32\,mm$ is related to the model adopted for the boundary conditions at the holes of the specimen. This is further discussed in Section B.2.1.

The two GFEM curves in each plot shown in Figure B.4 are nearly identical. This is the case since, as in the previous problem, the same element size is adopted near the crack front for both sequences of meshes. Based on this, hereafter only the coarse mesh is used in the simulations.

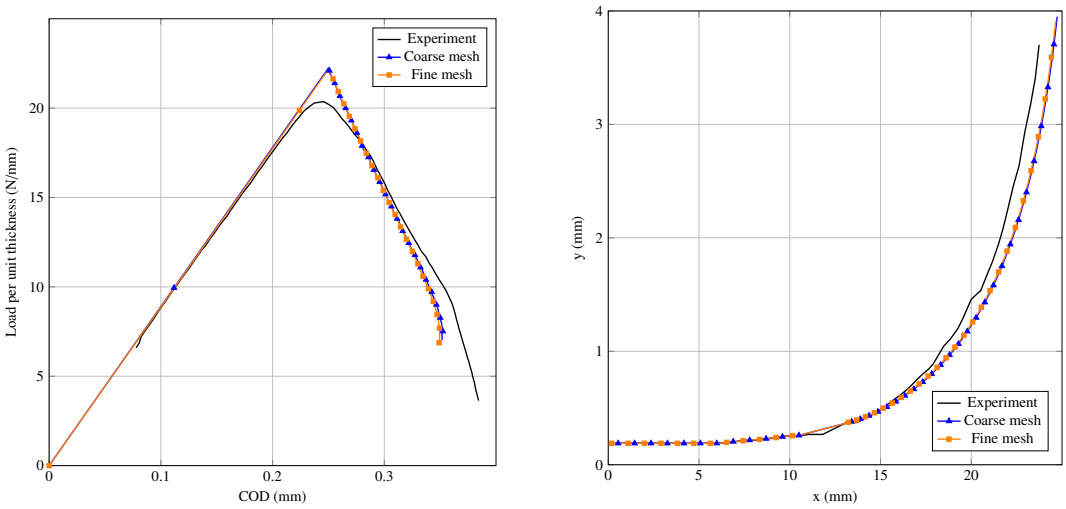

(a) Load variation **(b)** Crack path

Figure B.4: Mesh convergence in the GFEM simulation of Specimen CT31 using $\Delta a_{\max} = 0.1\,mm$, and $p = 2$ (a) Load variation (b) Crack path

Figure B.5 show GFEM results for the sequence of coarse meshes with approximations of degree $p = 2$ and $p = 3$, and $\Delta a_{\max} = 0.1\,mm$. The GFEM curves, again, match reasonably well the experimental data and show that a quadratic basis suffices for the sequence of coarse meshes adopted for this problem. Figure B.6 shows contour plots of von Mises stress field on the deformed configuration (with magnification) at crack propagation steps 20 and 120. Figure B.7 compares the crack path predicted by the GFEM with the experiment of Pham et al. [167]. The GFEM simulation adopts coarse meshes, $\Delta a_{\max} = 0.1\,mm$, and $p = 2$. It is clear that the GFEM path agrees well with the experimental one.

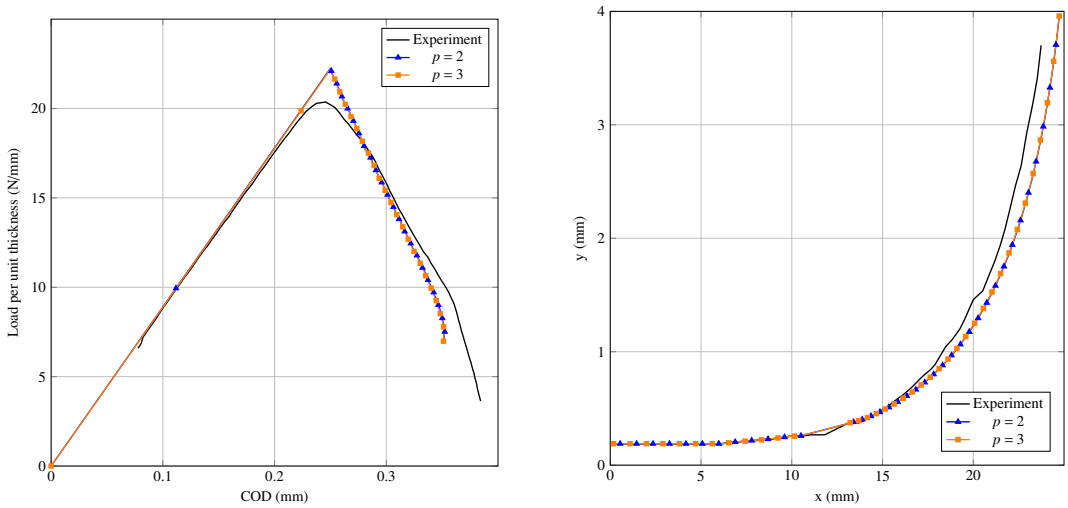

(a) Load variation **(b)** Crack path

Figure B.5: p-adaptivity in the GFEM simulation of Specimen CT31 using coarse meshes and $\Delta a_{\max} = 0.1\,mm$ (a) Load variation (b) Crack path

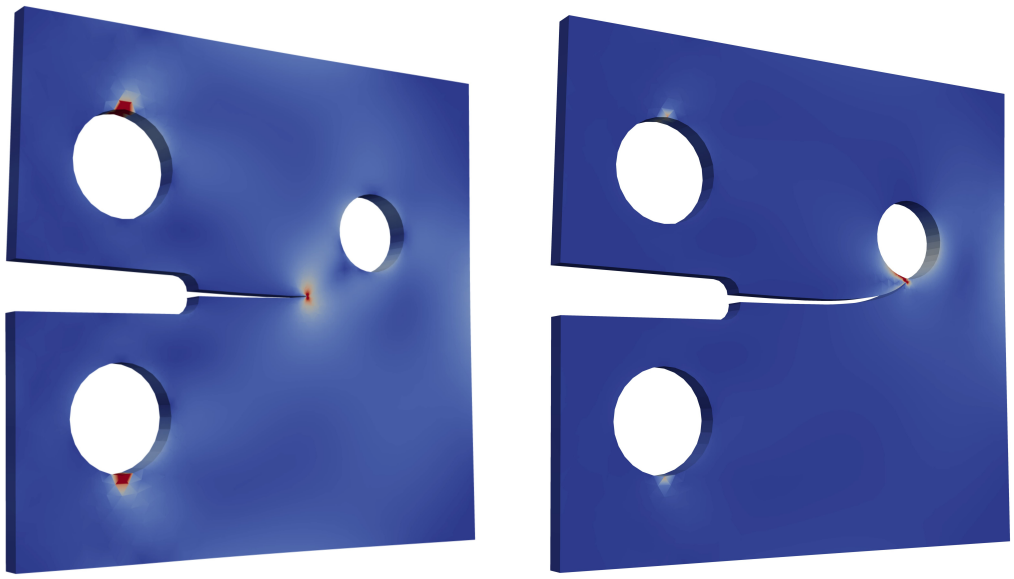

(a) **(b)**

Figure B.6: Contour plots of von Mises stress field on the deformed configuration (with magnification) for two crack propagation steps

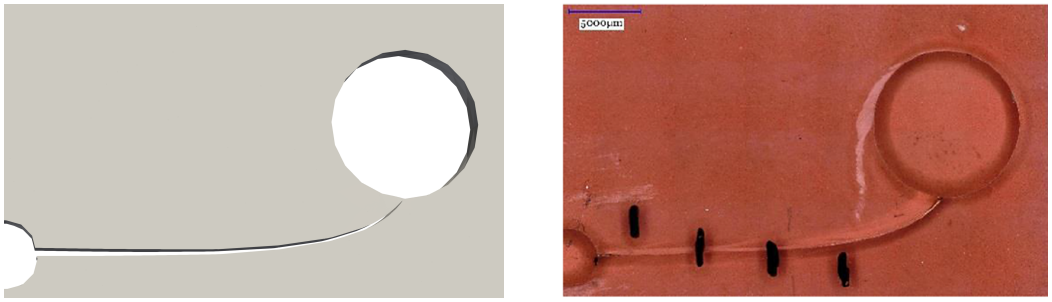

(a) **(b)**

Figure B.7: Final crack path for Specimen CT31 (a) GFEM simulation with coarse meshes, $\Delta a_{\max} = 0.1\,mm$, and $p = 2$ (b) Experiment of Pham et al. [167]

Effect of crack advancement magnitude Δa_{max}

The effect of crack advancement magnitude Δa_{max} is considered in this section. Figure B.8 shows plots of load versus COD and the crack path for the coarse mesh with $p = 2$ GFEM basis functions, and $\Delta a_{\max} = 0.3, 0.1$ and $0.035\,mm$. Good agreement with the experimental data is observed in all cases. This justifies the adopted $\Delta a_{\max} = 0.1\,mm$ in the simulations presented earlier.

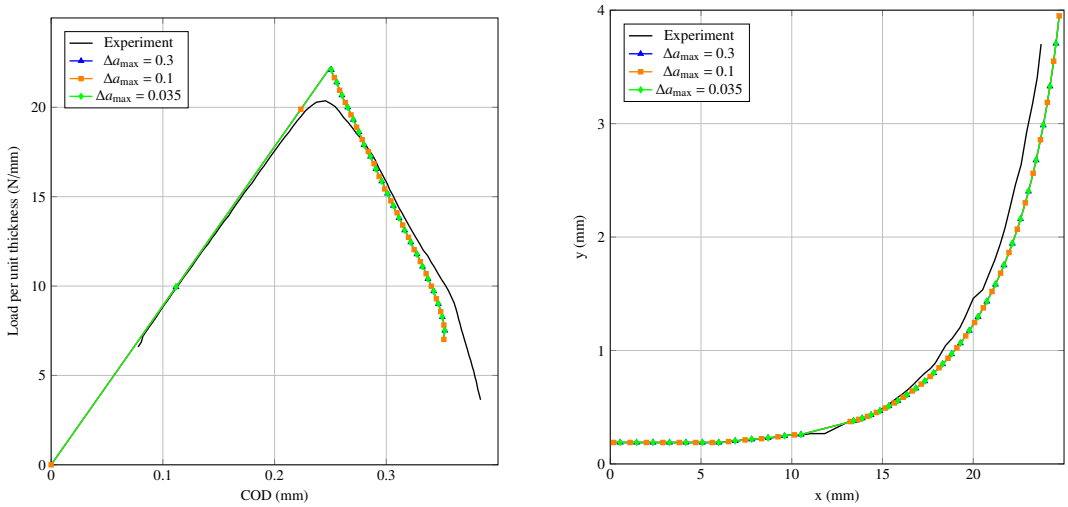

(a) Load variation **(b)** Crack path

Figure B.8: GFEM simulation of Specimen CT31 versus experimental results for different crack increments using coarse meshes and $p = 2$ (a) Load variation (b) Crack path

Comparison with other specimens and phase-field FEM

Figure B.9 compares the GFEM simulation of Specimen CT31 (using coarse meshes, $\Delta a_{\max} = 0.1\,mm$, and $p = 2$) with experimental results from specimens CT31, CT32, and CT33 of Pham et al. [167]. It can be observed that the load versus COD curve for Specimen CT33 deviates from the curves for specimens CT31 and CT32. The crack path from all experiments are, however, close for $x > 17\,mm$. The GFEM results are compared in Fig. B.10 with phase-field FEM simulations of Specimen CT31 by Pham et al. [167] and by Kumar and Lopez-Pamies [169].

Phase-field results from [167] are for two choices of the ratio l_0/h where l_0 is an intrinsic size scale for the damage model in the phase-field simulation and h is the element size in the region that contains the expected crack path. Unstructured meshes with small elements ($h = 25\,\mu m$ and $h = 6.25\,\mu m$) are used [167].

The GFEM and phase-field load versus COD curves agree very well with the experimental results of Specimen CT31. The crack paths predicted by GFEM is close to the phase-field results of Pham et al. [167] and nearly identical to the phase-field results of Kumar and Lopez-Pamies [169].

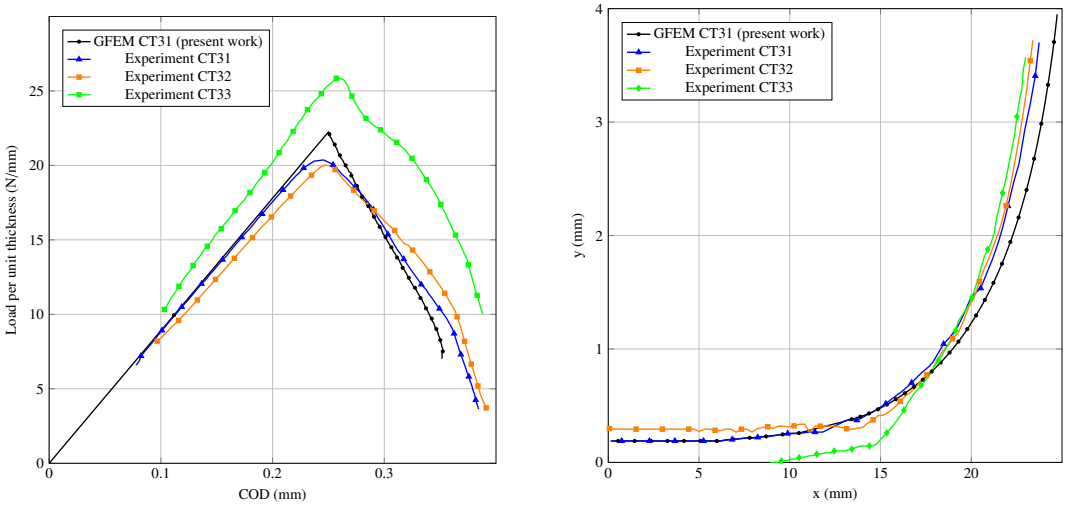

(a) Load variation **(b)** Crack path

Figure B.9: GFEM simulation of Specimen CT31 (with coarse meshes, $\Delta a_{\max} = 0.1\,mm$, and $p = 2$) compared with data from three specimens of the modified CT test of Pham et al. [167]. (a) Load variation (b) Crack path

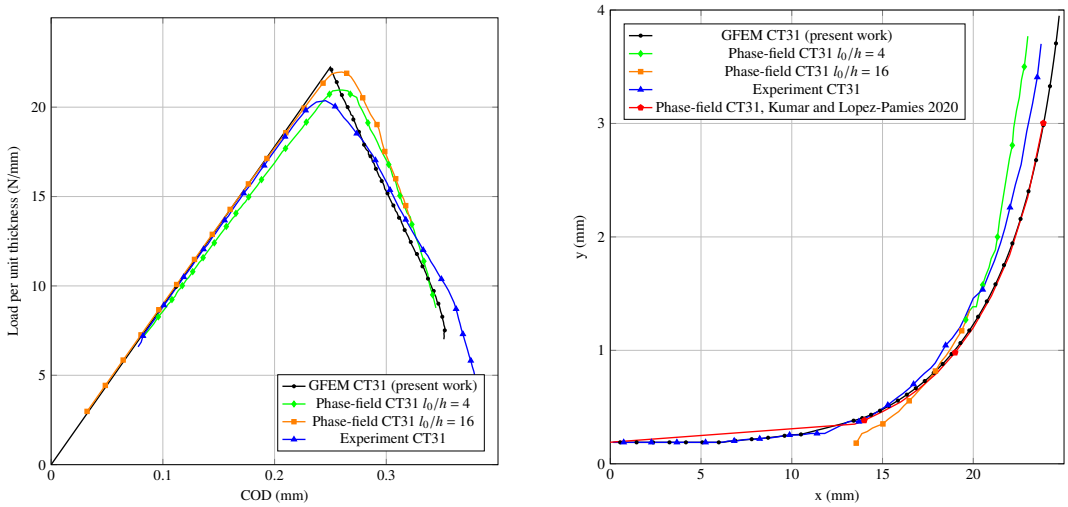

(a) Load variation **(b)** Crack path

Figure B.10: GFEM simulation of Specimen CT31 (with coarse meshes, $\Delta a_{\max} = 0.1\,mm$, and $p = 2$) compared with phase-field FEM simulations by Pham et al. [167] and by Kumar and Lopez-Pamies [169] (a) Load variation (b) Crack path

Computational performance

The GFEM simulation of Specimen CT31 on the sequence of coarse meshes using $\Delta a_{max} = 0.1\,mm$ and $p = 2$ took about 27.5 minutes on a 2018 MacBook Pro with 8 cores. The average number of tetrahedron elements in these meshes is 12,581. The average time spent to solve one propagation step was 13 sec. and 127 propagation steps were solved during the entire simulation.

The reduced cost of a propagation step compared to Specimen CT24 is due to the smaller problem size at each propagation step. Fewer propagation steps are required for the simulation of Specimen CT31 than Specimen CT24 since the initial (final) crack of Specimen CT31 is longer (shorter) than for Specimen CT24.

Effects of model adopted for boundary conditions at CT specimen holes

The observed difference in, for example, Figure B.4(a) between the GFEM load versus COD curves and experimental data is discussed in this section. The displacements imposed by the loading pins on the top and bottom holes of the CT and modified CT specimens are modeled as displacements prescribed to nodes located along the load lines.

The actual loading is, however, a contact problem where one of the contacting surfaces (the specimen's circular surfaces of the hole faces) rotates relative to the vertically moving cylindrical loading pin. As such, the location of the effective loaded zone changes during the experiment. The adopted model, on the other hand, assumes that the loaded/contacting surfaces remain the same throughout the test.

The loading pins do not prevent rotation of the specimen. This motivated the adoption of point constraints in our model. If, however, displacements were instead prescribed on element faces, the relative rolling movement between the loading pins and the holes would be prevented, leading to an excessively constrained model. In the first case the crack propagates along a plane of symmetry and the specimen rotation is small [167].

The turning of the crack in the Mode I+II problem causes a rotation of the specimen larger than in the Mode I problem. The relative motion between the loading pins and the modified CT specimen holes is illustrated in Fig. B.11. The locations of the contact on the hole surfaces change from A to $A'$and A'' at the top and bottom holes, respectively, as the specimen deforms. This movement is prevented by the adopted boundary conditions.

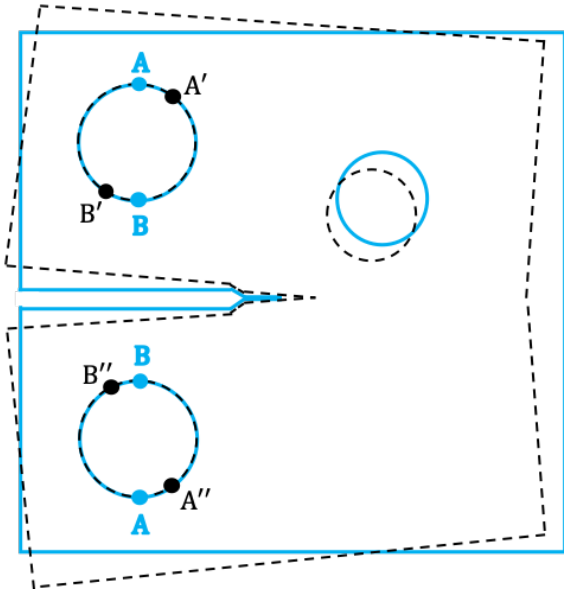

Figure B.11: Illustration of the deformed (black dashed line) and undeformed (solid blue line) configurations of the modified CT specimen showing the rotations of points along the loaded holes

B.3 Conclusions

An adaptive Generalized FEM for the simulation of mixed-mode brittle fracture propagation is presented and validated against several experimental data sets for mode I and mode I+II fracture propagation problems. Very good agreement between the GFEM and experimental results is observed. These include fracture path, Crack Opening Displacement (COD), and load and fracture length versus COD curves.

The computational efficiency of the method is also assessed. The simulation cost of the GFEM is shown to be significantly smaller than state-of-the-art phase-field FEMs. This is due to (i) smaller problem size since in the GFEM refinement is required only along a line (crack front) while in the phase-field FEM the mesh needs to be refined along the entire crack surface; (ii) At each crack propagation step, a linear problem is solved by the GFEM and a highly non-linear one is solved by the phase-field FEM.

A benchmark problem is a mode I+II fracture propagation simulation in a modified CT specimen. Other problems can be accessed in [80]. The effects of the model adopted for boundary conditions at CT specimen holes are discussed in details. They show that the contact between the loading pins and the specimen needs to be modeled in order to remove observed inconsistencies of the adopted model.

Appendix C

Numerical Experiments for Fracture Mechanics in Composite Materials

Fibers are added to composites and other brittle matrix materials for a variety of reasons, including improvements in cracking resistance and material toughness. As part of these efforts, the effects of fiber distribution on the cracking performance need to be understood and quantified using computational simulations.

Many advanced materials like CMCs rely on crack bridging mechanisms to hold cracks together and resist crack growth. Cracks in CMCs components are initially very small (micrometer scale). These cracks can behave in a way that is vastly different from that of the millimeter-scale cracks studied in laboratory tests using standardized techniques developed for traditional metal alloys. This difference is a notable problem in predicting fatigue failures in modern advanced materials.

In crack bridging, as shown in Fig. C.1, a small crack situated between reinforcing fibers or layers needs only to overcome the cracking resistance of the matrix in order to propagate. However, once the crack has propagated around the reinforcing phase, that phase can hold the crack together and increase crack propagation resistance.

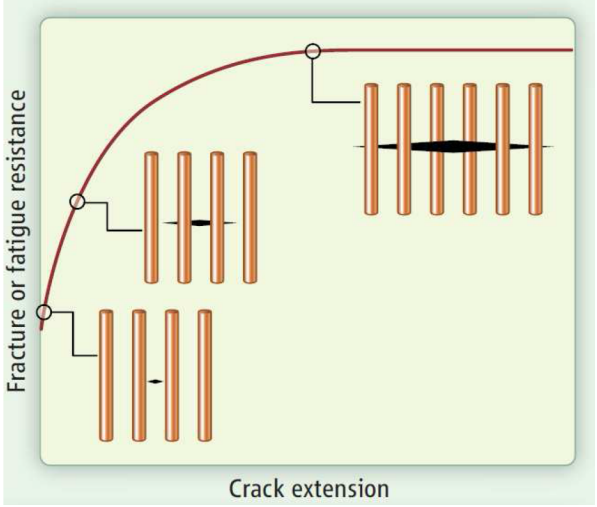

Figure C.1: *R-curve and failure mechanism in CMCs, by [3]*

C.1 Fiber reinforced cracked specimen

C.1.1 Introduction

This appendix simulates a cracked specimen with Mode I loading, as shown in Fig. C.2. The crack is bridged by 8 fibers described as dashed lines in this figure. For non-reinforced materials cracks need to overcome the cracking resistance of the matrix in order to propagate. In fiber-reinforced composite materials, however, fibers can hold the crack together and increase crack opening resistance.

This example simulates a cracked specimen with axial stress, as shown in Fig. C.2. In modern advanced materials the shape, orientation and size of these fibers are usually chosen to produce specific structural responses. In crack bridging, for example, a small crack needs only to overcome the cracking resistance of the matrix in order to propagate. However, in fiber composite materials a fiber can hold the crack together and increase crack propagation resistance. The goal of this problem is to show how the different geometric properties and configurations of fibers can affect the structural behavior of the composite.

A complete parametric study for the effect of the area of the fibers, its quantity, location and length are presented here. The following parameters are assumed for this problem, with consistent units: Modulus of elasticity of matrix $E_{\mathrm{m}} = 1.0 \times 10^4$; Poisson's ratio of matrix $\nu = 0.2$; Modulus of elasticity of fiber $E_{\mathrm{f}} = 5.0 \times 10^6$; Area of the fiber $A_{\mathrm{f}} = 2.0 \times 10^{-4}$; Bond stiffness: $K_{\mathrm{b}} = 5.0 \times 10^6$; Traction: $\sigma = 1000.0$.

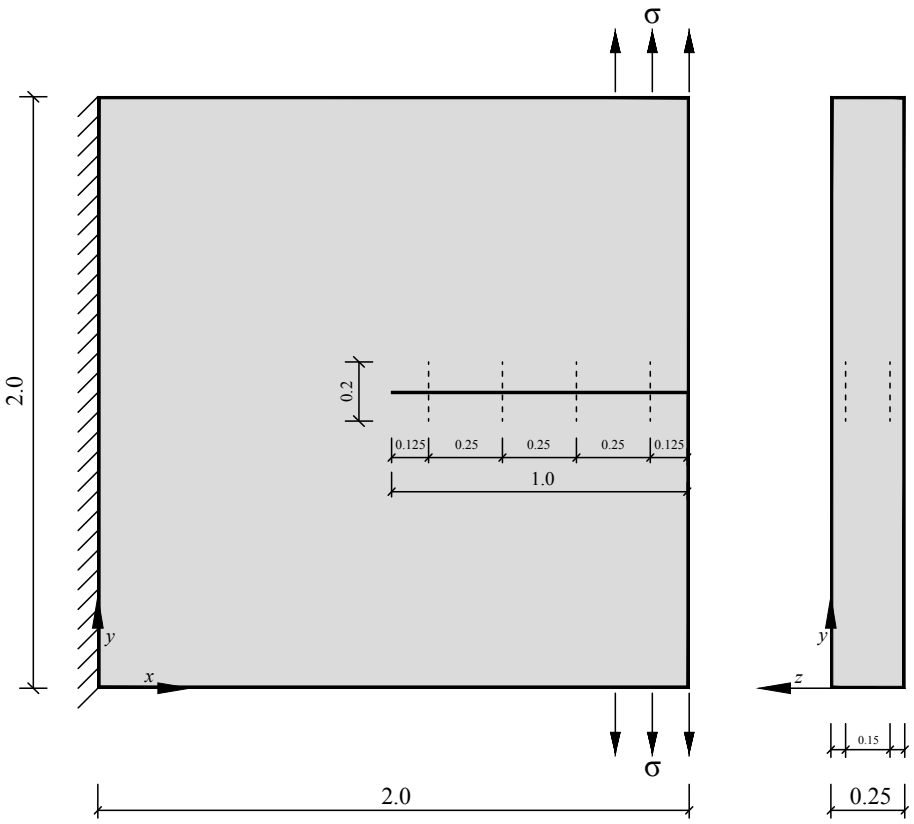

Figure C.2: Specimen submitted to axial load

C.1.2 Mesh definition

Figure 6.6 depicts the finite element mesh used by ISET for the problem presented in section C.1. The sample is *2 x 2 x 0.25* in dimension and is discretized using linear tetrahedral elements. The left face is constrained against translation along X, Y and Z directions. Traction σ is applied to the top and bottom surface in order to allow mode I opening in the sample.

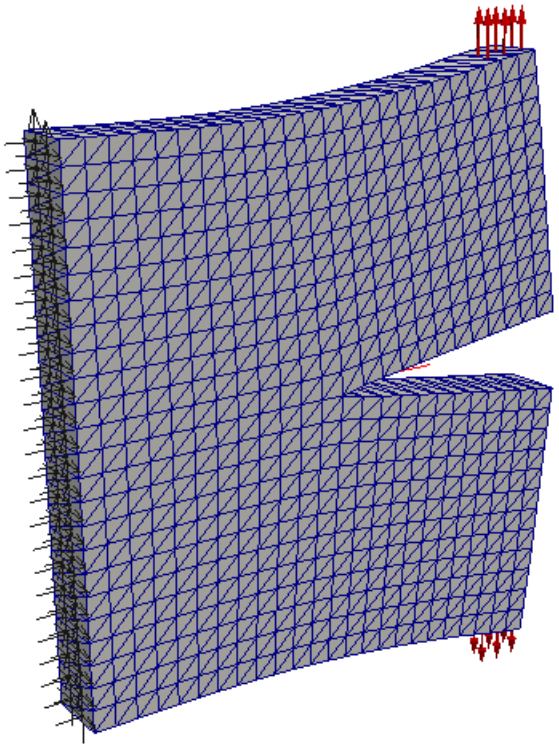

Figure C.3: Boundary conditions and displacement

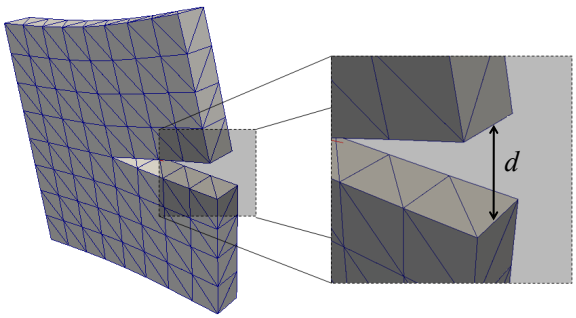

Figure C.4: Opening of the crack

C.1.3 Effect of the area of the fiber

The specimen is reinforced with fibers placed at $x = 0.875$ and with length equal to 0.7. The centroid of their cross-sections are located at $z = -0.05$ and $z = -0.20$. Figure C.5 describes the problem.

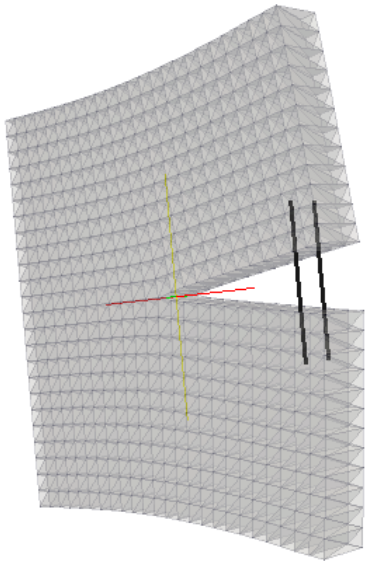

Figure C.5: Reinforced cracked specimen bridged by two cracks

Table C.1 shows that as the area increases the opening d between the crack faces is reduced. The fiber can bridge the crack and increase crack propagation resistance.

Table C.1: Opening d of the crack with respect to the area of the fibers

Area of each fiber	d
1.00E-8	0.3500
1.00E-4	0.3068
2.00E-4	0.2334
3.00E-4	0.1838
4.00E-4	0.1506

C.1.4 Effect of the number of fibers

The effect of the number of fibers is studied here. The constitutive properties are the same as earlier stated in this section. Fibers are added in pairs and distanced each other by 0.25 (on x axis). Figure C.6 shows the 4 different configurations analyzed in this section.

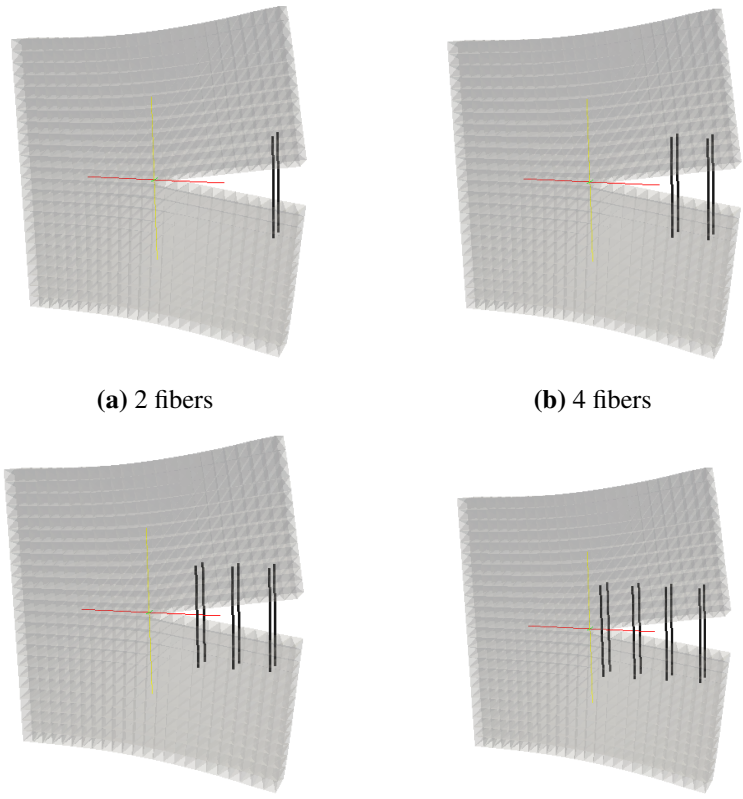

(a) 2 fibers **(b)** 4 fibers

(c) 6 fibers **(d)** 8 fibers

Figure C.6: Fiber configuration to study the effect of the number of fibers

Table C.2 shows that as the number of fibers increases, the d is reduced. It can be observed that this relationship is not linear. Fibers located at $x = 0.875$ contribute more effectively than the fibers located at $x = 0.125$ for the variable d. The effect of the position of the fibers is investigated in the next section.

Table C.2: Opening of the crack with respect to the number of fibers

Number fibers	d
2	0.2334
4	0.1805
6	0.1641
8	0.1600

C.1.5 Effect of the position of fibers

The setup of the problem solved in this section is similar to the one solved in the previous section. Here, however, only 2 fibers are solved each time.The position of the fibers is described in Fig. C.7.

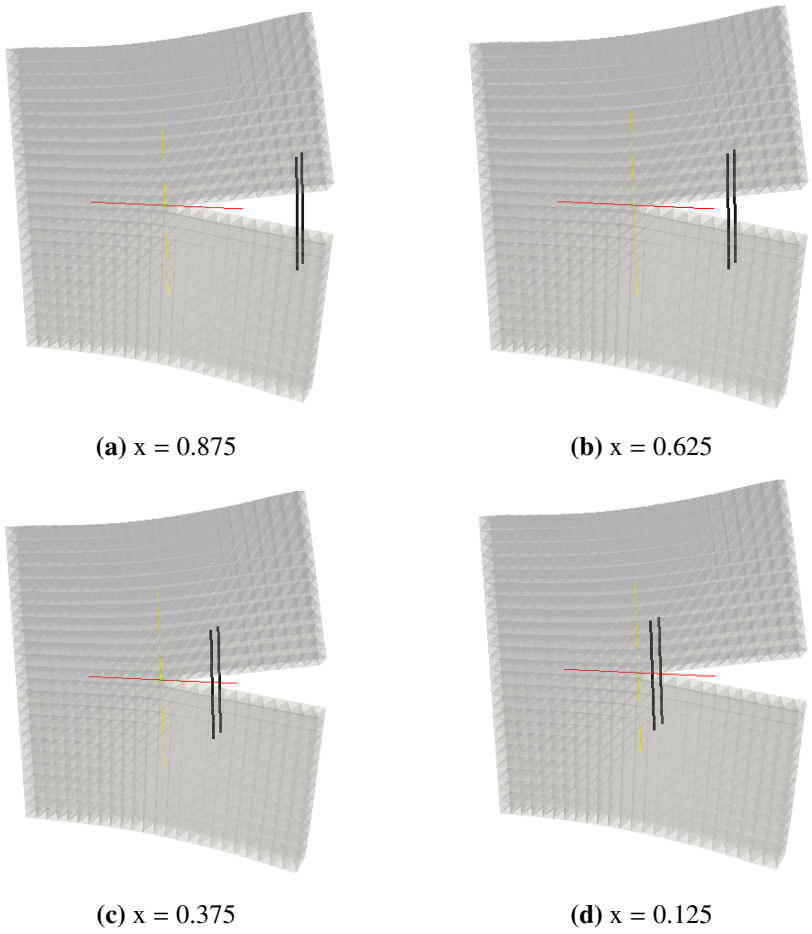

(a) x = 0.875 **(b)** x = 0.625

(c) x = 0.375 **(d)** x = 0.125

Figure C.7: Variation of the position of the fibers

Table C.3 shows that crack opening d for the specimens indicated in Fig. C.7. lt can be observed that fibers further to the crack tip contribute more effectively to the reduction of the d.

Table C.3: Opening of the crack with respect to the position of fibers

Position	d
0.875	0.2334
0.625	0.2961
0.375	0.3369
0.125	0.3473

C.1.6 Effect of the length of the fiber

The setup of the problem solved in this section is similar to the one solved in the previous section. Here, however, the length of the fibers varies from 0.2 to 1.7 (before was fixed to 0.7).

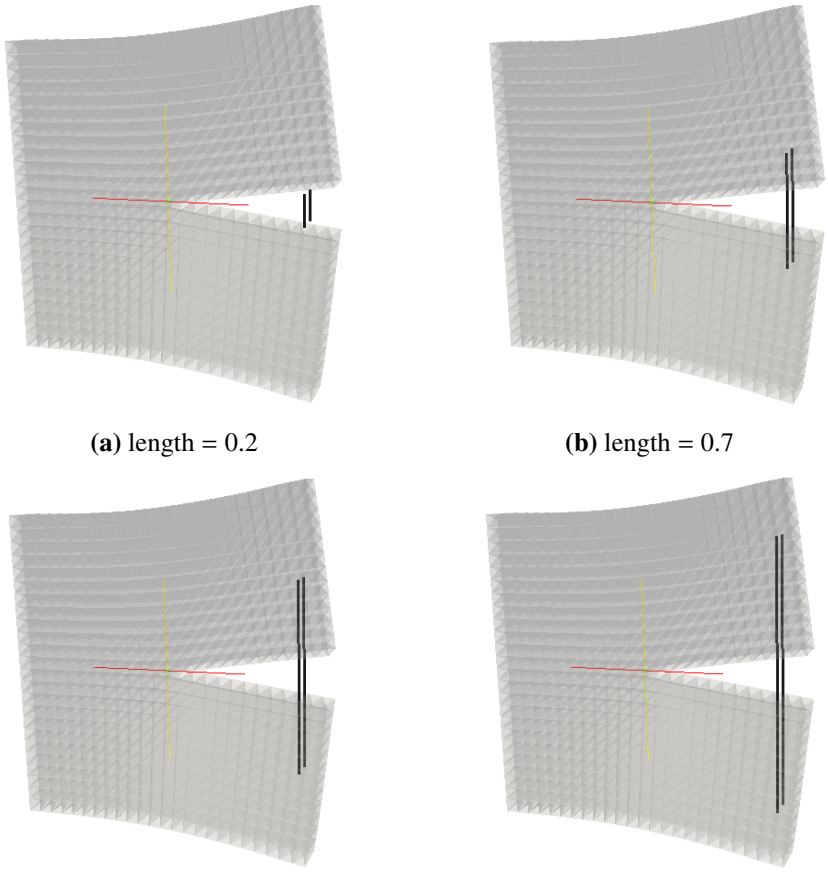

(a) length = 0.2 **(b)** length = 0.7

(c) length = 1.2 **(d)** length = 1.7

Figure C.8: Variation of the length of the fibers

Table C.4 shows the crack opening d for the specimens indicated in Fig. C.8. It can be observes that an increase in the length of the fibers leads to a stiffer behavior of the specimen.

Table C.4: Opening of the crack with respect to the length of fibers

Length	d
0.2	0.3347
0.7	0.2334
1.2	0.1735
1.7	0.1356

C.2 General observations

The fiber description using GFEM was able to capture the behavior for fracture mechanics for reinforced cracks. Similar problems solved by [170], [171], [172], [173] and [174] using different numerical methods have been shown similar behavior for the problems reproduced here. The use of GFEM, however, has the powerful feature of being meshless. This important tool adds flexibility to mesh description and will be fully exploited for the crack propagation analysis performed later in this project.

The linear dependency for GFEM observed for certain problems and reported by [175] did not affect the solution of problems solved in this appendix. The solver in ISET was able to handle the system of equations and the results are comparable to the reference solutions found in literature. As shown by [175], the linear dependency is caused by the integration over the fiber volume and the bond of the fiber. Improvements reported by [176] has been shown that this problem can be overcame using volume of surface integration instead of a line integration over the one dimensional elements of the mesh.